Mathematical modelling of platelet production

Helen Min Saville
University College
University of Oxford

A thesis submitted for the degree of
Doctor of Philosophy

October 2022

For my parents

Acknowledgements

Firstly, I would like to thank my supervisors, Prof Sarah Waters and Prof Jim Oliver: for teaching me how to do research in such a patient and encouraging way, for always providing help, insights, and enthusiasm, and for bringing a healthy dose of humour to supervisions. I feel fortunate to have been supervised by two such excellent mathematicians. I am furthermore grateful for the rewarding collaboration with Profs Cédric Ghevaert, Ruth Cameron, and Serena Best, and Dr Daniel Howard, and for their original instigation of the project with Sarah and Jim.

I would also like to thank Dr Benjamin Walker for supervising the work on the method of regularised Stokeslets, for contributing many hours and insights, and for generously sharing his code with me. I am grateful to Profs Bindi Brook and Derek Moulton for examining this thesis, and to Profs Andreas Münch, Colin Please, and Ian Griffiths for their helpful comments during my transfer and confirmation vivas. Further thanks are due to the encouraging and inspiring maths teachers and lecturers I've had over the years, particularly to Prof Irene Moroz for giving me a chance to try research during my undergraduate degree and encouraging me to pursue a PhD.

My experience as a PhD student has been brightened by sharing an office with Eddy, Michael, Matt, and (honorarily) Amy, whose friendship I am extremely thankful for. These past four years wouldn't have been half as good without the solidarity, laughter, and lunches together. I have also very much appreciated the company of members of the Maths Institute, particularly the friendly conversation with the OCIAM research group at coffee each day.

I am grateful to Lacey and Sharon, whose in-person friendships got me through the lockdowns. A big thank you also to all the wonderful friends and family in Oxford or far away, whose presence or voice feels like home. I feel lucky to have a brother who is as kind and funny as Tim, and to have parents, Juliet and Jian Ping, who have always been a rock of love and support to me. Thank you to my husband Luke for making me laugh every day, for cheering me on, and for being the best person I could walk through life with. Finally, I thank God for His grace and immeasurable love.

Abstract

Hospitals sometimes experience shortages of donor blood platelet supplies, motivating research into *in vitro* production of platelets. We use mathematical modelling to study platelet production.

First, we model the flow in a novel platelet bioreactor described by our collaborators in Shepherd et al. [137]. The bioreactor consists of an upper channel, a lower channel, and a cell-seeded porous collagen scaffold situated between the two. Flow is driven by gravity, and controlled by valves on the four inlets and outlets. The bioreactor is long relative to its width, a feature which we exploit to derive a lubrication reduction of the Navier-Stokes equations in the channels coupled to Darcy flow in the scaffold.

We first consider the quasi-steady regime, with slowly-moving valves, before incorporating inertia in two regimes: one to study small amplitude valve oscillations, and one to study order one amplitude valve oscillations. The former is a systematic reduction; the latter incorporates a phenomenological approximation for the cross-sectional flow profile. To achieve clinically and commercially viable yields of platelets, our collaborators will need to be able to finely control the fluxes and shear stresses in the bioreactor. Thus we use our model to predict how fluxes and shear stresses may be controlled using bioreactor valve dynamics and geometrical parameters.

Next, we study platelet production at the cellular level, modelling an intermediate stage of proplatelet formation. During this stage, pseudopodia (called proplatelets) elongate from the body of the platelet-producing cell, and platelets form along the proplatelets. Shear stress from external flow enhances both the proplatelet elongation and platelet formation rates, though it is unknown whether this enhancement is due to purely mechanical effects, or whether mechanotransductive effects are involved. We construct two models to investigate the dynamics

of proplatelet elongation and to compare these two possible mechanisms, by assessing their effects on the shape and elongation rate of a single proplatelet. The first model uses active gel theory to model the cytoskeleton-powered proplatelet elongation, and resistive force theory to model the drag between external flow and the proplatelet. The second model uses the method of regularised Stokeslets to characterise the flow around proplatelets tethered to a wall in a half-space, with each proplatelet described as an inextensible elastic rod. The models provide computationally-light bases into which future experimental hypotheses may be incorporated.

Contents

Chapter 1

Introduction

1.1 Platelet production

Platelets are cell fragments that circulate in the blood of mammals, with each microlitre of blood containing approximately $150000 - 400000$ platelets. Platelets play a key role in wound healing and blood clot formation in blood vessels, by adhering to a site of vessel injury, aggregating with red blood cells to form a clot, and releasing signals to recruit more platelets to the site [100]. Platelet transfusions are often given to patients undergoing surgical procedures, patients with haematological diseases, and patients receiving chemotherapy or stem cell treatment for cancer [28, 32]. More broadly, platelets are multifunctional, being involved in inflammatory and immune responses by releasing pro-inflammatory, anti-inflammatory, and angiogenic factors into the circulatory system [144], and playing critical roles in diseases such as atherosclerosis, stroke, peripheral vascular disease, and diabetes [101]. There are several disorders directly related to platelets. These fall within the broad categories of thrombocythemia and thrombocytosis, both of which result in an over-production of platelets; thrombocytopenia, which involves an under-production of platelets; and platelet dysfunction, where platelet numbers may be normal but platelet functioning is impaired [86]. It is important to understand the production and function of platelets to aid the development of therapies for the aforementioned diseases and disorders.

Platelets are produced by cells called megakaryocytes. *In vivo*, at the point of platelet production, megakaryocytes migrate to sit in the vascular niche, exterior

to vascular sinusoids in the bone marrow [96, 97], separated from the fluid flow by the endothelial wall as shown in Figure 1.1. Once *in situ*, megakaryocytes form pseudopodia, called proplatelets, which are long filaments that protrude through the endothelial wall into a blood vessel. Proplatelets use an extensive membrane reservoir contained within the megakaryocyte to elongate into the bloodstream. Platelets form at the tips of proplatelets, and possibly along their lengths too. Both proplatelets and platelets may be released into the bloodstream, where any proplatelets will further fragment into platelets, as shown in Figure 1.1 [78]. The above description of platelet production is considered to be the dominant mode of platelet production, though alternative sites and modes of platelet production have been observed: whole megakaryocytes or fragments of megakaryocytes have been found to produce platelet-like structures while circulating in the bloodstream [13]; megakaryocytes have been seen to travel to the lungs, where they lodge in capillary beds and produce platelets [93]; and platelet release has been observed to occur via megakaryocytes undergoing cytoplasmic rupture, in response to inflammatory stimuli [109].

Currently, platelets for transfusion are obtained solely from blood donors. When stored outside of the body, platelets must be kept at 18^oC to preserve their functionality. However, this temperature is not sufficiently low to prevent contamination by bacteria, and the shelf life of platelets obtained from donors is therefore limited to $5 - 7$ days [68]. As a result, hospitals commonly experience platelet shortages, especially during public holidays, major weather disasters, or pandemics [42]. Additionally, donor-derived platelets often have high immunogenicity, provoking an undesired immune response in the patient [150]. These factors motivate the need for *in vitro* production of platelets to provide a reliable supply of platelets that have low immunogenicity. *In vitro* platelet production occurs within bioreactor systems, which are devices used in tissue engineering to provide an environment in which cell constructs can be produced and studied. Platelet bioreactors harvest platelets from megakaryocytes seeded onto a biomaterial scaffold, as an alternative to platelets obtained from donors.

Both *in vitro* and *in vivo*, fluid shear stress has been recognised as an important factor influencing platelet production and is the focus of ongoing experimental research. *In vivo*, shear stress is provided by the flow of blood past megakaryocytes

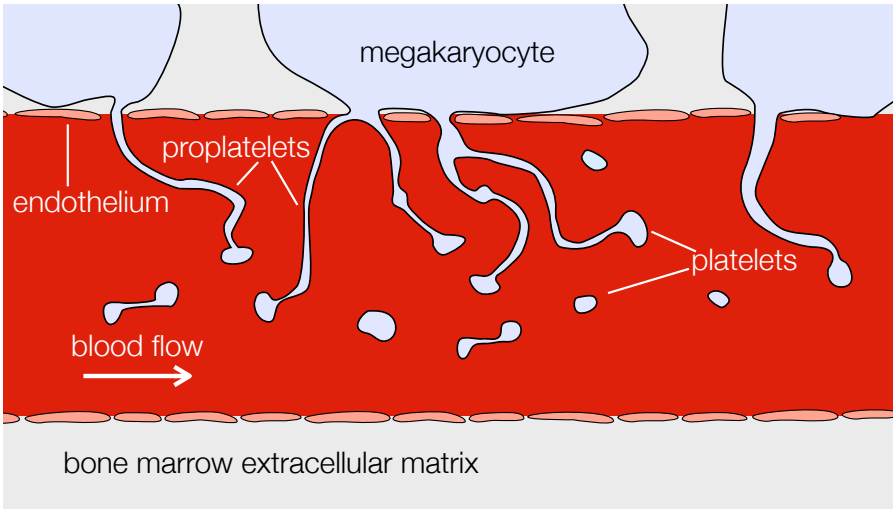

Figure 1.1: *In vivo*, megakaryocytes sit exterior to bone marrow sinusoids. They extend proplatelets into the sinusoid flow, which exerts shear stress on proplatelets, aiding their release into the bloodstream and further fragmentation into platelets.

and proplatelets, while *in vitro* it is provided by the flow of cell culture media through tubing in the bioreactor. To investigate the effect of shear stress on platelet production, Bender et al. [14] used an *in vitro* set-up designed by Thon et al. [154], with two parallel microfluidic channels separated by a row of pillars, and megakaryocytes lodged between the pillars. Flow passing from one channel to another then exerted a shear stress on the megakaryocytes. With this set-up, Bender et al. found that proplatelet extension occurred at $30\,\mu$m/min under a flow rate of $12.5\,\mu$l/hr. In contrast, in static culture proplatelets were found to elongate at only $0.85\,\mu$m/min [14]. *In vitro* experiments have also shown that exposing megakaryocytes to shear flow results in megakaryocytes starting the platelet production process earlier, and in platelet yields per megakaryocyte being higher as compared to static culture [14, 43, 117]. For example, a shear rate of $1800\,\mathrm{s}^{-1}$ triggered 30% – 45% of megakaryocytes to produce platelets in 20 minutes in the rectangular perfusion chamber of Dunois-Lardé et al. [43], whereas Balduini et al. [9] found that in the absence of shear a maximum of 25% of megakaryocytes produced platelets in $24 - 72$ hours.

In this thesis we use mathematical modelling to study platelet production from two angles, focusing on the effect of fluid shear stress on platelet production. First,

we study the fluid dynamics of a bioreactor system used for platelet production. After this, we look at the cell-scale process of proplatelet elongation.

1.2 Bioreactors for tissue engineering and platelet production

In vitro bioreactor systems can be used to grow biological cells and tissues in cell culture media. They are developed with the aim of engineering cell products of sufficient quantity and quality to replace organs, tissues, and blood products sourced from donors [10]. When cell products are engineered using cells derived from the patient, the potential negative impacts of the immunological response can be avoided [108].

To engineer functional cell products, bioreactors enable precise control of the operating conditions, with the aim of mimicking *in vivo* conditions within the bioreactor. Bioreactors can control the flux of cell culture medium into the system, delivering nutrients to the cells, whilst transporting away waste products. In addition to exploiting fluid flow to enhance mass transport by advection, thereby overcoming diffusive transport limitations, fluid flow can provide mechanical cues to cells via, for example, pressure and shear stress [136, 142]. Some popular types of bioreactors that exploit fluid-enhanced mass transport and fluid-induced stress include [31]: stirred-tank and spinner-flask bioreactors, where rotor-attached paddles or magnetic rods stir the cell culture media in a tank (e.g. [141, 149]); rotating wall bioreactors, where the wall rotation of a cylindrical chamber creates a balance between hydrodynamic, centrifugal, and gravitational forces on cell culture media and cell constructs inside the chamber (e.g. [49, 120]); and perfusion bioreactors, where a flow of cell culture media into and out of the bioreactor is driven by for example a peristaltic pump, and ensures nutrient replenishment, waste removal, and mechanical stress throughout the scaffold (e.g. [29, 154]). In bioreactor systems, cells are often seeded on substrates designed to enhance cell and tissue growth. The substrate often takes the form of a biocompatible porous scaffold [26]. The scaffold geometry and its material properties can be designed to further control the local mechanical and biochemical environment experienced by the cells.

To mimic the local mechanical environment of megakaryocytes *in vivo*, platelet bioreactors often seed megakaryocytes on biomaterial substrates which facilitate the elongation of proplatelets into an adjoining pore or channel. Once the proplatelets have fragmented into platelets, they are collected in solution at the bioreactor outlet. Platelet bioreactors are relatively novel in that their product is delicate cells that are washed out of the system, rather than tissue growing on a construct. Balduini et al. [9, 41, 115] have developed a bioreactor that seeds megakaryocytes into a porous silk scaffold, surrounding a single biocompatible silk microtube, representing a blood vessel. Platelets are released into the microtube and washed out of the system. In the bioreactor of Thon et al. [154] mentioned earlier, the row of pillars separating the two microfluidic channels emulates the endothelium, while the channel into which proplatelets extend mimics a blood vessel. Even with designs that go some way in mimicking the bone marrow microenvironment, at present platelet bioreactors do not produce platelets at sufficient rates to be able to replace supplies from donors. For example, Thon et al. achieved a production rate of approximately 30 functionally viable platelets per megakaryocyte which, though relatively high when compared to other *in vitro* studies, is still much lower than the $\sim 10^4$ platelets produced by a single megakaryocyte over the few hours of its platelet-producing lifespan *in vivo* [79, 96].

The critical challenges in the operation of platelet bioreactors are to control flow to ensure the megakaryocytes experience a sufficient level of shear stress, while keeping the product concentration as high as possible, so as to minimise the amount of expensive post-procedure concentration of suspended platelets that is required. Additionally, excessive back-flow in the direction of outlet to inlet should be avoided, to reduce the risk of transporting cells into the wrong parts of the bioreactor and disrupting platelet production.

Our focus is an *in vitro* perfusion bioreactor designed by Shepherd et al. [137] for platelet production. The bioreactor has wide potential applications as a model for the bone marrow microenvironment, useful not only for *in vitro* production of blood cells, but also for studying the role of microenvironment parameters in the differentiation and renewal of stem cells, and for investigating disease mechanisms for haematopoeitic disorders [21]. The mathematical model presented in Chapters $2-4$ may be viewed as a framework for any bioreactor built from long thin

tubes, porous scaffolds, and pinch valves; thus may readily be adapted to similar bioreactors, such as those used by [24], [74], and [99].

The bioreactor has a collagen scaffold with graduated porosity, to retain the megakaryocyte cells ($16.4\,\mu$m$-22.4\,\mu$m in diameter [145]) for continual platelet production, and allow the smaller platelets ($1.6\,\mu$m$-3.9\,\mu$m in diameter [110]) to exit the scaffold once they have broken off from megakaryocytes [137]. Flow is driven by gravity and controlled by valves near the inlets and outlets of the bioreactor, which are all closed to the atmosphere. Damage, activation, and aggregation of platelets are minimised by the passive nature of gravity-driven flow, with a lack of contact between platelets and mechanical pumping devices [137]. Given this bioreactor setup, the question is how to control and synchronise the opening and closing of the values to ensure the megakaryocytes are exposed to sufficient levels of fluid shear stress while minimising excessive dilution of the collected cell product.

1.2.1 Mathematical modelling in bioreactor design

To address this question, we employ mathematical modelling. The use of mathematical and computational modelling to inform experimental bioreactor design in tissue engineering is well established and has been reviewed in [26, 112, 162]. Mathematical models provide insights into the characteristics of bioreactor systems that are quicker and cheaper to obtain than performing numerous, time-consuming experiments. Once calibrated, the theoretical models can be validated via detailed comparison of the theoretical model predictions with experimental data, and used to inform bioreactor operating conditions. Typical model outputs include flow velocities and pressure, nutrient and waste product distributions, and cell growth and distributions.

Commonly, flow is described by combinations of the Navier-Stokes equations; Darcy's law, incorporating a rigid scaffold; Darcy-Brinkman flow, including viscous shear effects; and Biot's equations of poroelasticity, coupling Darcy flow to the solid mechanics of the extra-cellular matrix [26]. The last three of these are volume-averaged equations used for flow through porous scaffolds, containing parameters describing the macroscale properties of the scaffold. Multiscale modelling methods may be used to incorporate the microscale geometrical and material properties

of the scaffold, by inputting properties in a representative volume element in a microscale model. Then techniques such as homogenisation or volume averaging are used to describe bulk material properties in the macroscale model in terms of the microscale solution [46, 50, 119, 140].

Cells can be included as an additional continuous phase, resulting in a multiphase model, where conservation of mass and momentum equations track the volume fractions of fluid, cell, and extra-cellular matrix phases, and incorporate interphase forces, diffusion, convection, mechanotaxis, and chemotaxis of each phase. Analysis of continuum models is often simplified through asymptotic reductions exploiting disparate length and time-scales, see for example [40]. It is also possible to model cells discretely [33, 56] to track individual cells, incorporate intercellular interactions, preserve the stochasticity of cell-level processes, and include detailed information on scaffold geometries, obtained from micro-tomography scans. When using discrete cell models, fluid flow is usually solved using the lattice Boltzmann method [26], which is a computationally efficient alternative to solving the Navier-Stokes equations in complex domains using finite element or other computational methods.

Nutrient and waste product distributions are described by advection-reaction-diffusion equations. The chemical species are advected with the flow, and either consumed or produced by cells according to prescribed reaction kinetics. Diffusion coefficients can be chosen to account for tissue growth reducing the permeability of the construct through which the species are diffusing [55].

The bioreactor of Shepherd et al. [137] that we are modelling is a perfusion bioreactor with a relatively complex geometry. Other models of perfusion bioreactors have typically focused on a single subregion of a bioreactor, such as the scaffold region permeated by flow, or a single channel or tank with fluid and/or a scaffold. Within the former category, Guyot et al. [63] used the immersed boundary method to compute the shear stress on a single deformable cell in a scaffold pore perfused by flow with a prescribed inlet rate, in five different pore geometries. Comparing shear stresses in a pore with and without a cell, they found that shear stress on a cell in the former case could be up to two times greater than the wall shear stress in the latter case.

Porter et al. [122] used microtomography imaging of cylindrical porous scaffolds with varying microarchitectures to define $3D$ computational flow domains. Using a lattice Boltzmann method and prescribing the inlet flow rate at one end of the cylinder, they solved for the flow through the scaffold, and explored the dependence of scaffold shear stress on four inlet flow rates and on the scaffold microarchitecture. By making comparisons with companion bone tissue engineering experiments that related flow rate to cell function (proliferation, death, and bone marker gene expression), Porter et al. were then able to relate scaffold shear stress to cell function.

Multiple studies of perfusion bioreactors have considered macroscale modelling of the scaffold and/or tissue constructs through single channels. O'Dea et al. [111] neglected the scaffold and modelled a perfusion bioreactor comprising a two-dimensional channel containing two viscous phases, with the cell culture media modelled as one phase, and the combined cells and extracellular matrix forming the other phase. In the large interphase drag limit, they quantified the dependence of cell growth on the pressure-driven flow, and on the inclusion of cell density or pressure-dependent cell growth and death rates.

Zhao et al. [167] also modelled flow in a two-dimensional channel, with a prescribed inlet flow rate and a pressure condition at the outlet. In their stem cell bioreactor the channel interfaced a scaffold, parallel to and directly underneath the channel. Zhao et al. solved Stokes flow in the channel and Darcy-Brinkman in the scaffold, using a lattice Boltzmann method, and computed the shear stress in the scaffold. They also solved an advection-reaction-diffusion equation for the oxygen concentration, and conducted experiments in the physical bioreactor, where flow through the channels was driven by a peristaltic pump. The companion experimental results revealed a discrepancy in stem cell differentiation and growth between two different flow rates. Mathematical modelling was used to explain this discrepancy as arising from differences in the scaffold shear stress when using the two flow rates, rather than from differences in nutrient distribution.

Whittaker et al. [163] modelled flow through a cylindrical scaffold using Darcy's law, with flow entering the scaffold through an inlet, and exiting through an outlet. The scaffold additionally contained two porous-walled fibres whose tips met the walls of the cylinder, with cell culture media pumped from an external source

into the fibre tips to improve the distribution of cell culture media in the scaffold. Darcy's law was used to model the fibre walls and the steady Navier-Stokes equations were used to model flow through the fibre cores. By exploiting the small aspect ratio of the fibres and the relative impermeability of their walls, the authors derived an asymptotically-reduced system of equations and characterised the dependence of scaffold shear stress on the prescribed inlet flow rates.

Hyndman et al. [70] also used modelling to characterise shear stress dependence on inlet flow rate, in a simple perfusion bioreactor consisting of a tank of cell culture media, with a single inlet and outlet. They solved the Navier-Stokes equations and nutrient transport advection-reaction-diffusion equations in the tank for ten inlet flow rates using the commercial finite element software COMSOL. We similarly aim to characterise the dependence of shear stress experienced by cells on the bioreactor operating conditions and the bioreactor geometry.

Modelling of perfusion bioreactors with more complex geometries than those described above has been performed, but typically makes use of computationally expensive methods to solve the systems. For example, Thon et al. [154] used COMSOL to solve for flow and compute the shear stress in their microfluidic bioreactor, consisting of multiple inlet and outlet channels, and a central channel divided by a perforated barrier. An approach using computational fluid dynamics may possibley fail altogether for the bioreactor of Shepherd et al., due to the extreme aspect ratios in parts of the bioreactor. Instead, we exploit dimensionless parameters characterising the bioreactor system of Shepherd et al. to derive reduced models that are amenable to efficient numerical solution, allowing us to perform parameter sweeps and gain mechanistic insight.

1.3 Proplatelet elongation

All cells contain a dynamic network of protein filaments called the cytoskeleton, providing structure, strength, and motility [2]. The cytoskeleton is made up of three kinds of filaments: microtubules, actin, and intermediate filaments. There is evidence that the first two of these play major roles in proplatelet formation [19], in the form of microtubule bundles and the actomyosin cortex. The actomyosin cortex is a largely isotropic network situated under the cell membrane and comprised of

actin filaments cross-linked by the motor protein myosin [58]. Myosin molecules hydrolyse ATP to allow them to walk along actin filaments, in a process which has been largely observed to result in network contraction [83]. Microtubule bundles on the other hand have been observed to cause extensile forces. Each bundle lining the shaft of a proplatelet is made of approximately ten microtubules, cross-linked by the motor protein dynein [71]. Dynein uses ATP hydrolysis to walk along microtubules, and studies have shown that this causes axial sliding of microtubules apart from each other [14].

The combination of contractile actomyosin cortex and extensile microtubules bundles gives rise to periods of elongation, pause, and contraction within the overall elongation of proplatelets [19], and additionally contributes to the formation of beaded structures along the proplatelet [8, 154]. As mentioned in §1.1, an external shear flow speeds up proplatelet elongation, and may contribute to bead formation [8]. It is unclear whether this speeding up is due to the purely mechanical stretching of the proplatelet by the flow, or whether it also involves mechanotransductive processes whereby a mechanical stimulus (external flow) is converted to a biochemical signal, that may for example recruit more dynein to microtubules. In Chapter 5 we construct mathematical models of the cell-scale process of proplatelet elongation to use as tools for studying interactions between proplatelets and external flow. We postpone a review of relevant cytoskeletal modelling and fluid-structure interaction modelling to Chapter 5.

1.4 Thesis outline

In Chapters 2-4 we construct a model for the platelet bioreactor of Shepherd et al. [137]. The full model is introduced in Chapter 2. The quasi-steady regime is explored in Chapter 3, while in Chapter 4 we include the effects of inertia. Throughout, we exploit disparities in the sizes of dimensionless parameters governing the system to derive reduced models that are computationally inexpensive to solve. We use modelling to characterise the dependence of fluxes in the bioreactor and scaffold shear stress on the bioreactor's geometrical parameters and valve dynamics.

In Chapter 5 we move to cell-scale modelling of platelet formation, and construct two models to explore the effect of an external flow on the stresses experienced by a proplatelet. The first model incorporates extensile microtubule bundle forces through active stress in the proplatelet bulk, and incorporates the contractile actomyosin cortical forces through active surface tension. Forces from the external fluid are modelled using leading-order slender body theory, and the proplatelet is assumed to be axisymmetric. In the second model we simplify the description of the proplatelet material but include more accurate computations of the forces exerted by the external fluid on the proplatelet. We discuss the potential to combine elements of both models, to build a model that captures the key biomechanical and biochemical effects in proplatelet formation.

We conclude with a discussion in Chapter 6 on the results of Chapters 2-5, and the outlook for the use of mathematical modelling to complement experiment, to drive advances in our understanding of platelet formation.

1.5 Statement of originality

The models of the bioreactor of Shepherd et al. [137] in Chapter 2-4 are the first models of this bioreactor (or ones of similar design) that we know of. The work in Chapter 3 has been published in Frontiers in Mechanical Engineering [134]. The models in Chapter 5 are some of the first mathematical models of proplatelet mechanics (the only previous example we are aware of is [8]). The chapter contains the first proplatelet model that involves an extensional flow reduction of the proplatelet modelled as an active gel, and the first that uses the method of regularised Stokeslets to model interaction between the proplatelet and external flow.

Chapter 2

Model for the platelet bioreactor

In this chapter we develop a mathematical model for the platelet bioreactor of Shepherd et al. [137]. The bioreactor design and operation are detailed §2.1. In §2.2 we discuss the ranges of shear stress suitable for platelet production. The model for flow in the bioreactor is stated and non-dimensionalised in §2.3 − 2.6. To model flow in the scaffold we use Darcy's law, which tells us the volume-averaged Darcy velocity in the scaffold, and in §2.7 we describe a method for estimating the scaffold shear stress from the Darcy velocity. Finally §2.8 outlines the various parameter regimes that we study in Chapters 3 and 4.

2.1 Bioreactor design and operation

We describe the bioreactor design of Shepherd et al. [137]. A schematic of the perfusion bioreactor setup is shown in Figure 2.1. Flow is driven by gravity and controlled by valves near the inlet and outlet reservoirs, which are all enclosed, and large in volume relative to the rest of the bioreactor. Damage, activation, and aggregation of platelets is minimised by the passive nature of gravity-driven flow, as the set-up ensures that there is no contact between platelets and mechanical pumping devices.

The megakaryocytes are seeded in a porous collagen scaffold, inside a cuboid chamber that is sandwiched between two channels, as shown in the inset of Figure 2.1. Fluid flows into each channel from a reservoir of cell culture media, and out of each channel into a reservoir, controlled in each case by a sequence of valve tubing,

valves, and resistor tubing. Fluid can also flow freely between the channels and the scaffold. The pressure head due to gravity drives fluid into the channels, causing differences in pressure in the channels that can result in flow through the scaffold. Each valve is controlled by a solenoid pinch mechanism, whose speed is set by the user, and opens and shuts periodically to control the fluid flow.

The poroelastic collagen scaffold has two layers, each of which is fairly homogeneous and highly interconnected. As described in [137], the upper layer has a higher average pore size and porosity than the lower layer, so that the megakaryocytes are trapped in the upper layer, while the smaller platelets that are produced are able to move through both layers, with the aim of them being flushed through the system and collected in the lower outlet reservoir. To give an idea of the cross-sectional structure of a single layer, Figure 2.2 a) depicts a cross-sectional micro-computed tomography scan [104] of a collagen scaffold that has been constructed in the same way as the scaffold used by Shepherd et al. The schematic in Figure 2.2 b) illustrates a megakaryocyte caught in the scaffold, with platelets being washed away. Flow from the lower inlet to the lower outlet can wash platelets out of the system, so that it is not necessary to rely on cross-flow from the upper inlet to lower outlet to facilitate platelet washout. Flow from the upper inlet to upper outlet may deliver nutrients to cells via diffusion from the upper channel into the scaffold, as an alternative to advective nutrient transport via the cross-flow from upper inlet to lower outlet.

To seed the bioreactor scaffold with megakaryocytes, Shepherd et al. [137] delivered $400,000$ megakaryocytes suspended in 5 ml of culture media over a 5 minute period, with the suspension entering the system through the (fully open) upper valve tubing. Approximately 80% of the megakaryocytes are retained in the scaffold. Three doses of 5 ml of culture media were then passed through the system to remove unbound megakaryocytes from the upper channel. After seeding, the bioreactor was in operation for the next 20 hours.

Shepherd et al. chose the valves to be open for approximately one in every twenty seconds, with the opening and closing of valves occurring over milliseconds. This allowed some flow to pass through the bioreactor system, so as to exert shear stress on megakaryocytes and wash platelets out of the system, while avoiding an

excessively dilute product. The four valves had staggered timings, rather than opening and closing in unison, so as to reduce the chance of air bubbles forming.

2.2 Target shear stresses

We construct a mathematical model of the bioreactor to investigate how geometrical parameters and valve timings affect the flow and shear stresses in the bioreactor. The aim is to choose geometrical parameters and valve timings to reach a target shear stress in the scaffold, while avoiding back-flow and an excessively dilute product concentration.

The target shear stress ranges we consider are informed by those measured *in vivo* and those used *in vitro*. The shear rate *in vivo* in mouse bone marrow sinusoids has been measured to be in the range $50.5 - 165$ s^{-1} [98]. Equivalent measurements for human bone marrow sinusoids do not appear to be available in the literature, although studies showing that shear rates in mouse arteries are an order of magnitude larger than human artery shear rates [116] suggest that human bone marrow shear rates may be lower than in mice. Using the viscosity 1.7×10^{-3} Pa s for blood in tubes of diameter $40\,\mu$m [135] (which is approximately the diameter of bone marrow sinusoids), we estimate the shear stress in bone marrow sinusoids to be in the range $0.086 - 0.28$ Pa.

However, *in vitro* some platelet bioreactors have used higher shear stresses, for example Dunois et al. [43] and Thon et al. [154] have used shear rates of 1800 s^{-1} at the location of megakaryocytes, which with a cell culture media viscosity of 1.2×10^{-3} Pa gives a shear stress of 2.2 Pa. In these flow conditions, Dunois et al. found that $30\% - 45\%$ of megakaryocytes converted into proplatelets and platelets within 20 mins, which was much quicker than the multiple hours required for proplatelets to form in static culture. Thon et al. found that 90% of megakaryocytes converted into proplatelets within 2 hrs, whereas in static culture only 50% of megakaryocytes had converted to proplatelets in the same time period. Ito et al. [73] tested a range of shear stresses up to 4.2 Pa, and found that in their bioreactor system the greatest number of functional platelets were obtained at 2 Pa. Thus, it may be that platelet production can be enhanced under shear stresses exceeding physiological values.

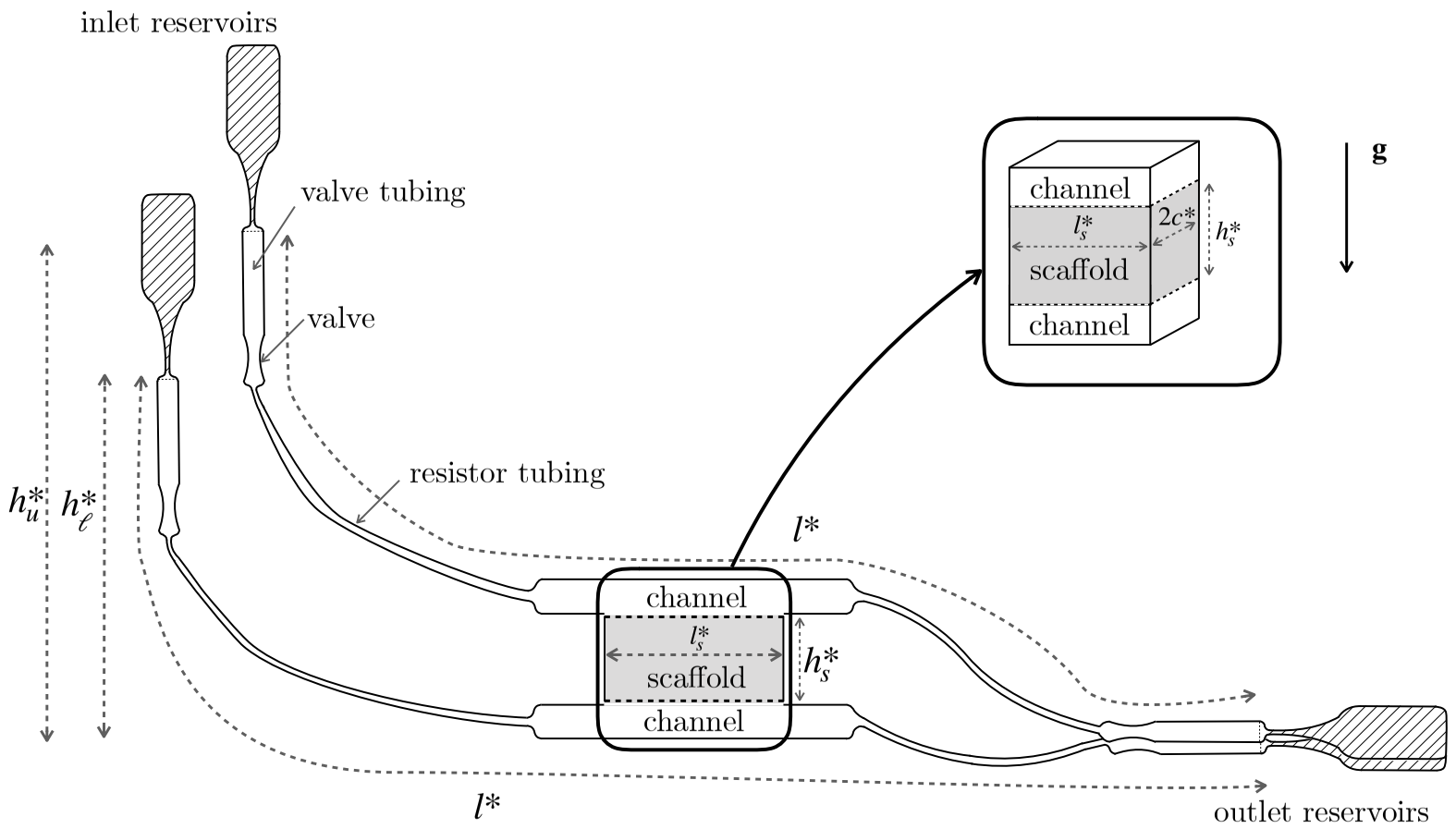

Figure 2.1: Schematic of the valve-controlled, gravity-driven platelet bioreactor designed by [137], showing the inlet and outlet reservoirs, joined by valve tubing, valves, resistor tubing, channels, and a collagen scaffold. The inset shows the scaffold and channels in 3D. Megakaryocytes sit in the collagen scaffold and produce platelets, which are washed out into the lower outlet reservoir. The upper and lower tubing systems have equal axial lengthscales, l^*; the heights of the inlet reservoirs above the base of the bioreactor are h_u^* and h_ℓ^* respectively; the scaffold height is h_s^*; and the scaffold length is l_s^*.

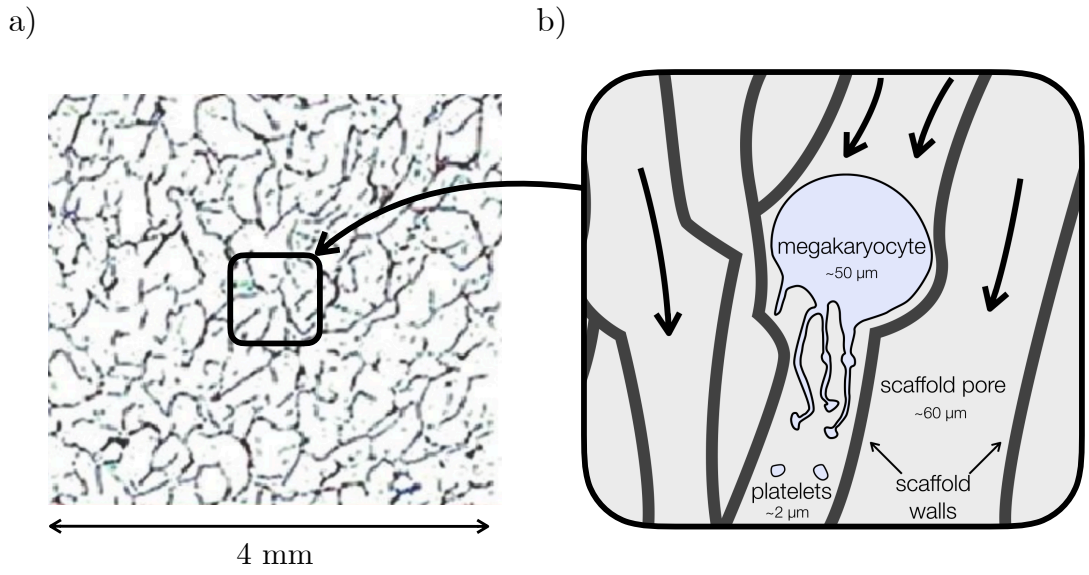

Figure 2.2: a) Micro-computed tomography image of a collagen scaffold, reprinted with permission from [104], and similar to those used by Shepherd et al. [137]. b) Schematic of a megakaryocyte that has been captured in a pore and is producing platelets. The larger black arrows indicate the direction of the culture media flow. The lengths indicate typical diameters of a megakaryocyte, platelet [153], and scaffold pore (see Table 2.1).

However, if platelets are exposed to too high a shear stress for too long, they will become activated. This must be avoided in the bioreactor, because activated platelets are able to aggregate and are therefore unsuitable for blood transfusion. The shear stress required for activation is inversely related to the exposure time of platelets to shear stress, as shown by Hellums [67]. If we assume that the maximum continuous exposure time of platelets to stress is on the order of 100 s (which for example includes the valve operating condition in Shepherd et al. [137], where valves were open for one in twenty seconds), then approximately 10 Pa is required to activate platelets [67]. We therefore look at shear stress ranges with upper bounds less than 10 Pa.

Specifically, we look at three target shear stress ranges:

$$0.086 < \Sigma < 0.28\,\text{Pa}, \quad 1.1 < \Sigma < 3.3\,\text{Pa}, \quad \text{and} \quad 0.086 < \Sigma < 3.3\,\text{Pa} \tag{2.1}$$

which correspond respectively to the approximate *in vivo* range, a range close to shear stresses found to be most effective *in vitro* (and still well below the activation shear stress for platelets) and lastly a combination of the two ranges. The bioreactor can induce both spatial and temporal variation in scaffold shear stress. If we are aiming to reflect the *in vivo* situation where megakaryocytes and proplatelets are exposed to a relatively constant shear stress provided by the blood stream in bone marrow sinusoids, then we may seek to achieve scaffold shear stresses within a target range continuously for seconds or minutes. However, it has not been shown whether continuous shear stress (perhaps at lower levels) or instantaneously high shear stresses are most important for improving platelet yields *in vitro*. We will therefore compute both instantaneous and integrated shear stresses in the scaffold. As we will see later, there is also spatial variation in the shear stress distribution in the bioreactor scaffold. Ideally, the scaffold shear stress should lie within the chosen target range throughout the entire scaffold, however this may be incompatible with other requirements, such as a restriction on back-flow in the scaffold. We will therefore measure the proportion of the scaffold volume that experiences shear stresses within the target ranges.

2.3 Model overview

Throughout we use *tube system* to mean the combined channel, resistor tubing, valve and valve tubing. To model the bioreactor, we use the Navier-Stokes and continuity equations for flow in the tube systems, and Darcy's law and the continuity equation for flow in the scaffold. These have both been widely used in bioreactor modelling, see for example [139, 149]. Darcy-Brinkman is another option for modelling flow in the scaffold, being similar to Darcy's law but including an extra Laplacian term. However, as there is not a clear consensus on its applicability or clear definition of the effective viscosity parameter it introduces, we do not use Darcy-Brinkman [91]. Darcy's law is appropriate for a rigid scaffold in which the pores are connected and inertia is negligible, and is therefore a good choice for a simplest-first modelling approach. We check that it is valid to neglect inertia in the scaffold *a posteriori* by computing the pore Reynolds number, which must be sufficiently small for inertia to be negligible [11].

A challenge in models involving both tube flow and scaffold flow is imposing appropriate coupling conditions at interfaces between the two types of flow. In the tube systems, the Navier-Stokes are derived directly by applying mass and momentum conservation to fluid motion, whereas the extra step of volume averaging involved in obtaining Darcy flow in the scaffold contains length-scale assumptions that break down as the interface between regions is approached. The incompatibility of the two systems can be seen in the difference in the orders of the partial differential equations. Before we discuss interface conditions between a tube flow and scaffold flow, we remark that the three accepted conditions imposed at a fixed interface between two regions of viscous flow are continuity of normal stress, normal velocity, and tangential velocity. The first may be justified through for example a pillbox stress balance argument; the second is due to conservation of mass: both of these conditions can also be used at the interface between tube flow and scaffold flow [91, 94].

In modifying the third condition to be applied at the interface between tube flow and scaffold flow, an initial suggestion might be to take zero tangential velocity at very low scaffold permeability, and continuity of tangential velocity at

high scaffold permeabilities. However, either extreme is inadequate, as shown experimentally by Beavers and Joseph [12] for Poiseuille flow through a tube with an impermeable upper wall and a permeable lower wall, where the lower wall adjoins a porous scaffold. They instead proposed a widely-used condition relating the shear stress in the tube flow to the discontinuity in slip velocities of the tube and scaffold flows, through a slip coefficient that depends on the geometric properties of the interface and the permeability of the scaffold. This slip coefficient can be measured experimentally [12] or determined through numerical simulation [102]. Since its initial empirical justification, the Beavers-Joseph slip condition has been analytically justified for laminar flow over a porous scaffold, which is close to our physical set-up, most notably by Saffman [132]. Saffman additionally showed through a combination of averaging techniques and *ad hoc* assumptions that the scaffold slip velocity in the Beavers-Joseph slip condition can be neglected. This version of the slip condition is called the Beavers-Joseph-Saffman condition, and we employ this condition in our bioreactor model.

2.4 Model geometry

The (equal) centreline arclengths of the upper and lower tube systems are denoted l^*. Throughout, the upper and lower tube systems are labelled by subscripts $i = u, \ell$ respectively. We denote by h_u^* (h_ℓ^*) the height of the inlet of the upper (lower) tube system above that of its outlet, g as gravitational acceleration, and ρ as the density of the cell culture media, so that gravity generates a pressure head of $\rho g h_u^*$ ($\rho g h_\ell^*$) across the upper (lower) tube system; see Figure 2.1. We adopt an orthogonal curvilinear coordinate system (x^*, y^*, z^*) in each of the two tube systems, with the z^*-axis running along the axial centreline from inlet to outlet, and x^* and y^* being cross-sectional coordinates.

The upper and lower tube systems have four regions differing in their cross-sections, shown in Figure 2.3: channels, with fixed, rectangular cross-sections of width $2c^*$ and height $2b_c^*$; resistor tubing, with fixed, circular cross-sections of radius b_r^*; valve tubing, with fixed, circular cross-sections of radius b_v^*, and valves, with time-dependent cross-sections. Valve cross-sections are idealised for modelling purposes to be elliptical, as shown in Figure 2.3. (In the physical bioreactor of

Shepherd et al. [137] the valve cross-sections are asymmetric, due to the valve mechanism that pinches the valves with a relatively flat edge from above and a sphere from below.)

We denote by z_j^* for $j = 0, ..., 9$ the z-coordinate of the junctions between the components, as illustrated in Figure 2.3. Valve tubing occupies $z^* \in (z_0^*, z_1^*) \cup (z_8^*, z_9^*)$ and each piece has length l_t^*; valves occupy $z^* \in (z_1^*, z_2^*) \cup (z_7^*, z_8^*)$ and each valve has length l_v^*; resistor tubing occupies $z^* \in (z_2^*, z_3^*) \cup (z_6^*, z_7^*)$ and each piece has length l_r^*; and channels occupy $z^* \in (z_3^*, z_6^*)$ and have length l_c^*. Thus, the cross-sectional areas in the valve tubing, resistor tubing, and channel regions of the bioreactor are given by

$$A_i^* = \begin{cases} \pi b_v^{*2} & \text{for} \quad z^* \in (z_0^*, z_1^*) \cup (z_8^*, z_9^*), \\ \pi b_r^{*2}, & \text{for} \quad z^* \in (z_2^*, z_3^*) \cup (z_6^*, z_7^*), \\ 4 b_c^* c^* & \text{for} \quad z^* \in (z_3^*, z_6^*). \end{cases} \tag{2.2}$$

The elliptical valve cross-sections have semi-major axes $a_{ij}^*(z^*, t^*)$ and semi-minor axes $b_{ij}^*(z^*, t^*)$, where $i = u, \ell$, $j = 1, 7$. We parameterise the valve walls as

$$(x^*, y^*, z^*) = (a_{ij}^* \cos\phi, b_{ij}^* \sin\phi, z^*), \text{ for } \phi \in [0, 2\pi), \ z^* \in (z_j^*, z_{j+1}^*), \tag{2.3}$$

where $j = 1, 7$, so that the cross-sectional valve areas are $A_i^* = \pi a_{ij}^* b_{ij}^*$. The semi-major a_{ij}^* and semi-minor b_{ij}^* axes are determined by prescribing the area and circumference of the valve cross-section at each axial location and time, and then fix the position of valve walls via equation (2.3).

The ellipses' circumferences are set to be constant throughout and equal to the circumference of the valve tubing, via

$$2\pi b_v^* = 4 a_{ij}^* E(e_{ij}), \tag{2.4}$$

where $e_{ij} = \sqrt{1 - b_{ij}^{*2}/a_{ij}^{*2}}$ is the eccentricity, and E is the complete elliptic integral of the second kind.

The cross-sectional area $A_i^* = \pi a_{ij}^* b_{ij}^*$ of each valve is prescribed to be

$$A_i^* = \pi b_v^{*2} \left\{ 1 - \frac{a}{2} \left(1 - \cos\left(\frac{2\pi(z^* - z_j^*)}{z_{j+1}^* - z_j^*} \right) \right) c_v(t^*; \tau) \right\}, \tag{2.5}$$

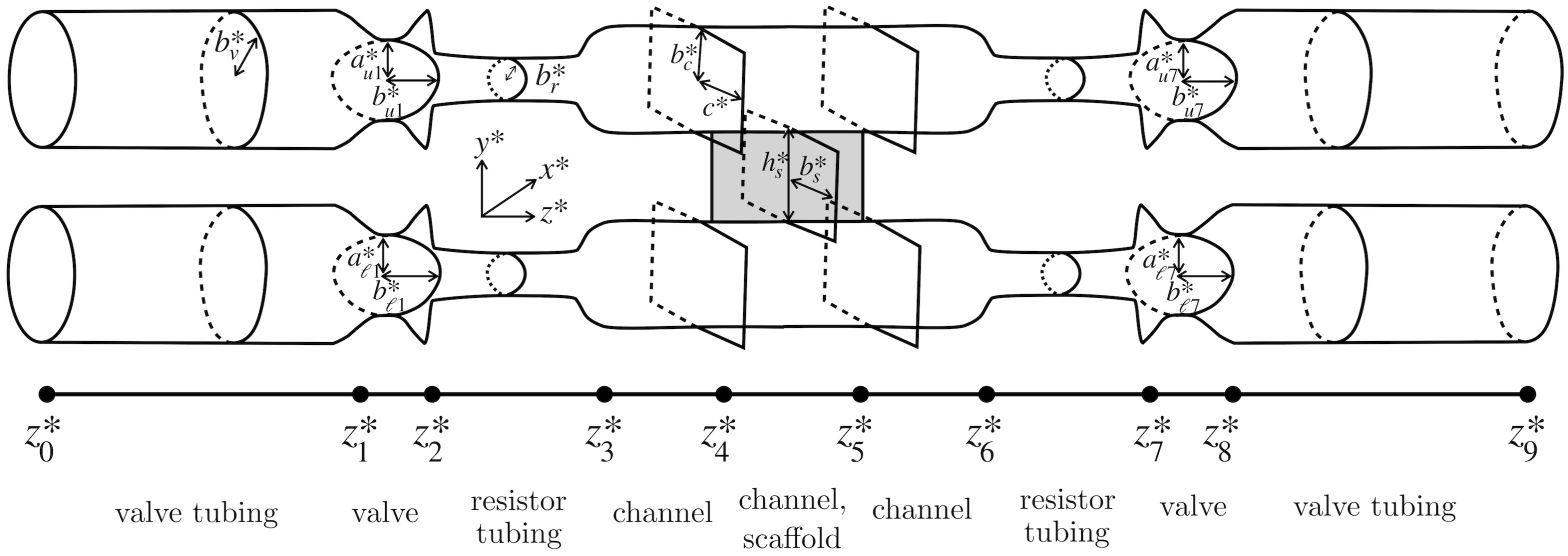

Figure 2.3: Simplified modelling domain, showing cross-sectional shapes of each of the valve tubing, valve, resistor tubing, channel, and scaffold regions.

in $z^* \in (z_j^*, z_{j+1}^*)$. Here the dimensionless valve amplitude a controls how completely the valve can close: $a = 0$ is a valve that is always open, and $a = 1$ is a valve that can close completely. For numerical convenience the valves are prevented from closing completely ($0 \leq a < 1$), so as to avoid dividing by zero area when computing solution coefficients. The valve period τ is the time taken for a valve to either open and then close, or close and then open; either of these sequences is henceforth referred to as a valve pulse. We prescribe τ within the range given in Table 2.1. The valve closure function $c_v(t^*; \tau)$, given in Appendix A, prescribes the time-dependency of the valve area, and always takes values in $[0, 1]$. The valve area is modelled as varying sinusoidally in the axial direction, shown by the cosine term in equation (2.5). Thus a valve is most heavily constricted at its centre, where A_i^* varies between πb_v^{*2} (fully open) when $c_v = 0$, and $(1 - a)\pi b_v^{*2}$ (closed) when $c_v = 1$. Using the choice of c_v given in equations (A.3) and (A.4), Figure 2.4 plots both c_v and A_i^* midway along the valve, for the scenarios of a valve that opens and then closes (solid lines) with amplitudes $a = 0.95$ and $a = 0.2$, an open valve (dotted line), and a closed valve (dashed line). In the model, each valve can be made to pulse as many times as desired, and to stay (partially) open or closed for as long as desired.

The scaffold has centreline arclength, l_s^*, and rectangular cross-section with height h_s^* and width $2b_s^*$. It occupies $z_4^* < z^* < z_5^*$.

The cross-sections of the upper tube system, lower tube system, and scaffold are labelled as Ω_u, Ω_ℓ and Ω_s respectively, with boundaries $\partial\Omega_u, \partial\Omega_\ell, \partial\Omega_s$, and interfaces $\Gamma_i = \partial\Omega_i \cap \partial\Omega_s$ between scaffold and channel cross-sections.

Typical values for h_i^*, l^*, l_v^*, l_c^*, l_t^*, c^*, b_c^*, b_v^*, b_r^* and b_s^* are given in Table 2.1. The values reflect those of the particular bioreactor set-up in [137], and the wider literature on the permeability of collagen scaffolds [104].

2.5 Model formulation

We model the cell culture medium as a Newtonian viscous fluid of viscosity μ and density ρ, which is a widely used and justified assumption in the field of bioreactors [26]. Neglecting the effects of centreline curvature, as the ratio of transverse lengthscale to radius of curvature of the tube centreline is small, the flow

Table 2.1: Model parameters, chosen to match the bioreactor of [137]. Where a range is give, values or ranges in brackets have been used in simulations. The values without a citation are reported here for the first time, having been measured by Daniel Howard (an author on [137]).

Name	Symbol	Bioreactor value(s)	Units	Source
upper reservoir height	h_u^*	$0-3$ (0.5)	m	–
lower reservoir height	h_ℓ^*	$0-0.5$ (0.25)	m	–
scaffold height	h_s^*	0.004	m	[137]
tube system length	l^*	1.4	m	–
scaffold length	l_s^*	0.01	m	[137]
valve tubing length	l_t^*	0.5	m	–
valve length	l_v^*	0.005	m	–
resistor tubing length	l_r^*	0.15	m	–
channel length	l_c^*	0.09	m	–
scaffold half-width	b_s^*	7.5×10^{-4}	m	[137]
valve tubing radius	b_v^*	0.001	m	–
resistor tubing radius	b_r^*	2×10^{-4}	m	–
channel half-height	b_c^*	7.5×10^{-4}	m	–
channel half-width	c^*	0.0025	m	–
valve timescale	τ	$10^{-5}-10$	s	–
typical valve timescale	T	$0.04, 10$	s	–
interface slip coefficient	ζ	$1.3-7$ (4)	–	[152]
cell culture viscosity	μ	0.001	Pa s	[85]
scaffold permeability	K	$10^{-15}-10^{-9}$ (10^{-11})	m^2	[104]
scaffold tortuosity	η	$1.49-1.99$ (1.74)	–	[104]
scaffold porosity	ϕ	$0.88-0.91$ (0.9)	–	[137]
average pore diameter	d	$4\times10^{-5}-8\times10^{-5}$ (6×10^{-5})	m	[104]
ambient pressure	p_{amb}	1.025×10^5	Pa	–
cell culture density	ρ	1000	kg/m^3	[156]
gravitational acceleration	g	9.8	m/s^2	–

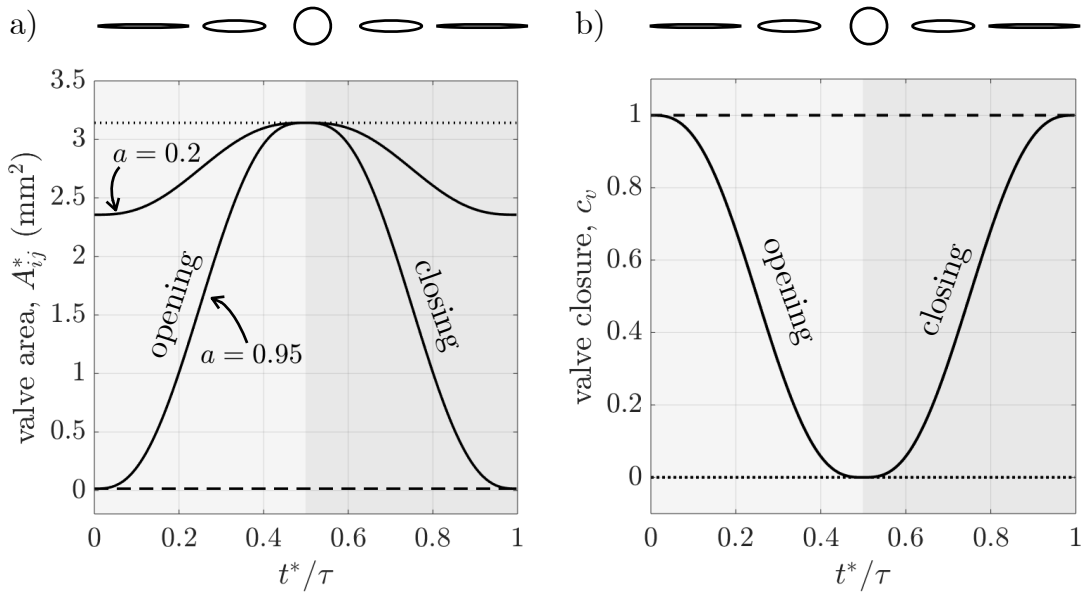

Figure 2.4: a) Area A^*_{ij} of a valve cross-section, halfway along the valve and b) the valve closure function c_v, computed using (A.3) and (A.4). The solid lines indicate a valve that opens and then closes, with dimensionless amplitudes $a = 0.95$ and $a = 0.2$; note c_v does not depend on a. The dotted line is an open valve, and the dashed line is a closed valve. The diagrams on the top sketch the valve cross-sectional shape as the valve opens and closed. Parameters are given in Table 2.1.

in the upper and lower tube systems, $\Omega_i \times (z^*_0, z^*_9)$, is governed by the incompressible Navier-Stokes equations

$$\rho\left(\frac{\partial \boldsymbol{u}^*_i}{\partial t^*} + \boldsymbol{u}^*_i \cdot \nabla \boldsymbol{u}^*_i\right) = -\nabla p^*_i + \mu \nabla^2 \boldsymbol{u}^*_i, \tag{2.6a}$$

$$\nabla \cdot \boldsymbol{u}^*_i = 0, \tag{2.6b}$$

where $\boldsymbol{u}^*_i$ and p^*_i are fluid velocities and the reduced pressure in region i, and $\boldsymbol{u}^*_i$ has components (u^*_i, v^*_i, w^*_i) in the (x, y, z)-directions. The reduced pressure p^*_i is related to the absolute pressure P^*_i, the elevation in the lab frame Y^*, and the ambient pressure p_{amb} by $p^*_i = -p_{\text{amb}} + \rho g Y^* + P^*_i$.

The flow in the scaffold, $\Omega_s \times (z^*_4, z^*_5)$ is governed by Darcy's law together with the incompressibility condition appropriate for the constant porosity scaffold, *viz.*

$$\boldsymbol{u}^*_s = -\frac{K}{\mu}\nabla p^*_s, \qquad \nabla \cdot \boldsymbol{u}^*_s = 0. \tag{2.7a, 2.7b}$$

where the velocity in the scaffold is $\boldsymbol{u}_s^*$, with components (u_s^*, v_s^*, w_s^*) in the (x, y, z) directions, the reduced pressure in the scaffold is $p_s^* = -p_{\text{amb}} + \rho g Y^* + P_s^*$, and the scaffold permeability is K. We treat the porosity as constant throughout the bioreactor runtime, because the volume of megakaryocytes is small relative to the scaffold volume: an idealised spherical megakaryocyte with radius $10\,\mu$m has volume $4 \times 10^{-15}\,\text{m}^3$, so that the volume of the 3.2×10^5 megakaryocytes in the scaffold is approximately $10^{-9}\,\text{m}^3$, which represents just under 2% of the scaffold volume. Any platelets exiting the scaffold, and therefore increasing scaffold porosity, must have been converted from megakaryocyte mass, hence there is at most 2% decrease in scaffold porosity over the bioreactor runtime. In Chapters 3 and 4 we check *a posteriori* that it is valid to neglect inertia in the scaffold and therefore use Darcy's law, by computing the pore Reynolds number [163],

$$\mathcal{R}_p = \frac{\rho d \eta |\boldsymbol{u}_s^*|}{\mu \phi}, \tag{2.8}$$

where d is the typical pore diameter, η is the scaffold tortuosity, and ϕ is the scaffold porosity, all given in Table 2.1. In the literature, there are a number of choices for the lengthscale used to compute the pore Reynolds number: some use the average pore diameter, while others use the square root of the scaffold permeability [11]. We use the average pore diameter, which in our case provides a slightly more conservative estimate of the pore Reynolds number. The systematic derivation of Darcy's law from homogenisation of Stokes flow at the porescale requires that the pore Reynolds number is much less than one, however a variety of experiments have shown that Darcy's law is generally valid for higher pore Reynolds numbers, even as high as 10 [11], thus we will present results for pore Reynolds numbers of up to 10.

At the solid walls of the tube systems we impose the usual no-slip and no-flux conditions given by

$$\boldsymbol{u}_i^* = \boldsymbol{U}_i^* \quad \text{on} \quad \partial\Omega_i, \tag{2.9}$$

where the velocities $\boldsymbol{U}_i^*$ of the walls in the bioreactor are

$$\boldsymbol{U}_i^* = \begin{cases} (0,0,0) & \text{for } z^* \in (z_0^*, z_1^*) \cup (z_2^*, z_7^*) \cup (z_8^*, z_9^*), \\ \dfrac{\partial}{\partial t^*}\left(a_{ij}^* \cos\phi, b_{ij}^* \sin\phi, z^*\right) & \text{for } z^* \in (z_j^*, z_{j+1}^*) \quad \text{for} \quad j = 1, 7. \end{cases} \tag{2.10}$$

We prescribe normal stress and no tangential velocity at the inlet and outlet of the upper and lower tube systems, *viz.*

$$\boldsymbol{u}_u^* \cdot \boldsymbol{t} = 0, \qquad \boldsymbol{n} \cdot \sigma_u^* \cdot \boldsymbol{n} = -p_u^{in*} \qquad \text{at } z^* = 0, \tag{2.11a}$$

$$\boldsymbol{u}_u^* \cdot \boldsymbol{t} = 0, \qquad \boldsymbol{n} \cdot \sigma_u^* \cdot \boldsymbol{n} = 0 \qquad \text{at } z^* = l^*, \tag{2.11b}$$

$$\boldsymbol{u}_\ell^* \cdot \boldsymbol{t} = 0, \qquad \boldsymbol{n} \cdot \sigma_\ell^* \cdot \boldsymbol{n} = -p_\ell^{in*} \qquad \text{at } z^* = 0, \tag{2.11c}$$

$$\boldsymbol{u}_\ell^* \cdot \boldsymbol{t} = 0, \qquad \boldsymbol{n} \cdot \sigma_\ell^* \cdot \boldsymbol{n} = 0 \qquad \text{at } z^* = l^*, \tag{2.11d}$$

where $\boldsymbol{t}$ is any tangent to the cross-section and $\sigma_i^* = -p_i^* \boldsymbol{I} + \mu(\nabla \boldsymbol{u}_i^* + (\nabla \boldsymbol{u}_i^*)^T)/2$ is the stress tensor in the pipe. The upper and lower inlet pressure heads are $p_i^{in*} = \rho g h_i^*$ for $i = u, \ell$. On the impermeable scaffold walls we have the no-flux condition, so that

$$\boldsymbol{u}_s^* \cdot \boldsymbol{n} = 0 \quad \text{on} \quad \partial\Omega_s \setminus (\Gamma_u \cup \Gamma_\ell). \tag{2.12}$$

At the interfaces Γ_u and Γ_ℓ between scaffold and channels, we prescribe continuity of normal flux, continuity of normal stress, and the Beavers-Joseph-Saffman condition:

$$\boldsymbol{u}_i^* \cdot \boldsymbol{n} = \boldsymbol{u}_s^* \cdot \boldsymbol{n} \qquad \text{on} \quad \Gamma_i, \tag{2.13a}$$

$$\boldsymbol{n} \cdot \sigma_i^* \cdot \boldsymbol{n} = -p_s^* \qquad \text{on} \quad \Gamma_i, \tag{2.13b}$$

$$\boldsymbol{n} \cdot \left(\nabla \boldsymbol{u}_i^* + (\nabla \boldsymbol{u}_i^*)^T\right) \cdot \boldsymbol{t} = \frac{\zeta}{\sqrt{K}} \boldsymbol{u}_i^* \cdot \boldsymbol{t} \qquad \text{on} \quad \Gamma_i, \tag{2.13c}$$

where ζ is the Beaver-Joseph slip coefficient, and $\boldsymbol{t}$ is any tangent to the interface. The system is closed by imposing the initial fluid velocities everywhere except in the scaffold region:

$$\boldsymbol{u}_i^* = \boldsymbol{u}_b^* \quad \text{at} \quad t^* = 0. \tag{2.14}$$

2.6 Non-dimensionalisation

There are two mechanisms driving flow in the bioreactor: the gravitational pressure heads of the inlet reservoirs, and the motion of the valves. We therefore define two velocity scales for axial flow in the tube systems,

$$U_g = \frac{\epsilon^2 l^* p_u^{in*}}{\mu}, \quad \text{and} \quad U = \frac{a l^*}{T}, \tag{2.15}$$

which are, respectively, flow driven by the gravitational pressure head $p_u^{in*} = \rho g h_u^*$ of the upper inlet reservoir (which is never less than that of the lower inlet reservoir), and flow driven by the valves. Here the bioreactor aspect ratio $\epsilon = b_r^*/l^* \ll 1$ is the ratio of the smallest transverse lengthscale to the largest axial lengthscale, T is a typical valve period, and a is the dimensionless valve amplitude appearing in equation (2.5) for the valve area. We assume $U/U_g = \mathrm{O}(1)$ or $U \gg U_g$, and non-dimensionalise axial velocities using the valve-driven velocity scale U. (In the model limit where the gravity-driven velocity scale is much larger than the valve-driven velocity scale, $U_g \gg U$, the kinematic boundary condition (2.9) reduces to zero valve wall velocity at leading-order, hence the problem is the same as when there is no valve motion and contained within the cases we look at, so that we do not treat this case separately.)

There are three timescales in the system: that of gravity-driven axial flow, l^*/U_g, valve-driven axial flow, $l^*/U = T/a$, and the typical valve period T. The gravity-driven timescale is never shorter than the valve-driven timescale, because $U/U_g = \mathrm{O}(1)$ or $U \gg U_g$; and the valve-driven timescale is never shorter than the typical valve period, because $a \in [0, 1]$. We therefore choose the typical valve period T as the non-dimensionalisation timescale.

The governing equations (2.6), and boundary conditions (2.9), (2.11) and (2.13) in the upper and lower tube systems are non-dimensionalised using the following scalings

$$(x^*, y^*, z^*) = l^*(\epsilon x, \epsilon y, z), \quad p_i^* = \frac{\mu U}{\epsilon^2 l^*} p_i, \tag{2.16a}$$

$$(u_i^*, v_i^*, w_i^*) = U(\epsilon u_i, \epsilon v_i, w_i), \quad t^* = Tt, \tag{2.16b}$$

The above scalings assume that transverse velocities are an order of magnitude smaller than axial velocities. We note that these scalings are not valid near the junctions between different types of tubing, where there may be a jump discontinuity in the cross-sectional area, and we therefore expect the flow to be three-dimensional at leading-order. We defer discussion of this issue to Chapters 3 and 4. The governing equations (2.7) and boundary conditions (2.12) and (2.13) in the scaffold are non-dimensionalised using the scalings

$$(x^*, y^*, z^*) = l^*(\epsilon x, \epsilon y, z), \quad p_s^* = \frac{\mu U}{\epsilon^2 l^*} p_s, \quad (u_s^*, v_s^*, w_s^*) = U_s(u_s, v_s, \epsilon w_s). \tag{2.17}$$

The scale $\mu U/(\epsilon^2 l^*)$ for the scaffold pressure in (2.17) is the same as in the tube systems, motivated by the continuity of stress condition (2.13b) at the interfaces $\Gamma_{u,\ell}$ between the scaffold and upper/lower channels. Darcy's law (2.7a) sets the cross-sectional velocity scaling as

$$U_s = \frac{KU}{\epsilon^2 l^* h_s^*}. \tag{2.18}$$

The velocity scaling (2.18) provides an upper bound on scaffold flow velocity, because it scales pressure with the viscous pressure drop scaling $\mu U/(\epsilon^2 l^*)$ across the tubing systems. Its accuracy as an estimate for scaffold velocity depends on the permeability of the scaffold and which valves are open or closed. For example, if all of the valves are open, we would expect the scaffold velocity to be much smaller than if only the upper inlet and lower outlet valves are open, forcing all the flow to pass through the scaffold.

In addition to the aspect ratio ϵ, the dimensionless valve period τ/T, the valve amplitude a, and the various dimensionless lengths in the bioreactor (see Table 2.2 for a list), the resulting dimensionless governing equations are characterised by the dimensionless parameters

$$\mathcal{R} = \frac{\epsilon^2 \rho U l^*}{\mu}, \quad \mathcal{S} = \frac{l^*}{UT} = \frac{1}{a}, \quad \mathcal{A} = \frac{\sqrt{K}}{\zeta l^*}, \tag{2.19a}$$

$$\mathcal{B} = \frac{h_s U_s}{\epsilon U} = \frac{K}{\epsilon^4 l^{*2}}, \quad p_u^{in} = \frac{\epsilon^2 l^* p_u^{in*}}{\mu U} = \frac{U_g}{U} \tag{2.19b}$$

The reduced Reynolds number, $\mathcal{R}$, represents the ratio of inertia to viscous effects based on the transverse velocity and lengthscale in the tube systems. The Strouhal number, $\mathcal{S}$, is the ratio of the timescale l^*/U for flow to travel from the bioreactor inlet to outlet (i.e. the axial flow timescale), to the typical valve period T. The dimensionless Beavers-Joseph slip coefficient, $\mathcal{A}$, is the ratio of the slip length $\sqrt{K}/\zeta$ to the system length l^*. The dimensionless permeability, $\mathcal{B} = h_s U_s/(\epsilon U)$, measures the ratio of the transverse scaffold velocity scale, U_s, to the size of transverse tubing velocities, ϵU. As will be shown in §3.2, $1/\mathcal{B}$ is the dimensionless pressure drop $(p_u - p_\ell)$ across the scaffold that drives a flux vertically down the scaffold comparable in size to the flux along the channel. The dimensionless upper

Table 2.2: Dimensionless parameters corresponding to the bioreactor geometry of [137], given to 2 s.f. Values in brackets are used in simulations unless otherwise stated. The ranges are computed separately using the maximum and minimum values of U and T used (and stated) in the following chapters, and the maximum ranges are given.

Name	Symbol	Formula	Value(s)
upper reservoir height	h_u	h_u^*/h_u^*	1
lower reservoir height	h_ℓ	h_ℓ^*/h_u^*	0.5
scaffold height	h_s	h_s^*/b_r^*	20
tube system length	l	l^*/l^*	1
scaffold length	l_s	l_s^*/l^*	0.0071
valve tubing length	l_t	l_t^*/l^*	0.36
valve length	l_v	l_v^*/l^*	0.0036
resistor tubing length	l_r	l_r^*/l^*	0.11
channel length	l_c	l_c^*/l^*	0.064
scaffold half-depth	b_s	b_s^*/b_r^*	7.5
valve tubing radius	b_v	b_v^*/b_r^*	5
resistor tubing radius	b_r	b_r^*/b_r^*	1
channel half-breadth	b_c	b_c^*/b_r^*	3.25
channel half-depth	c	c^*/b_r^*	12.5
dimensionless valve timescale	$-$	τ/T	$0.05 - 250$
valve amplitude	a	$-$	$0 - 1$
reduced Reynolds number	$\mathcal{R}$	$\epsilon^2\rho l^* U/\mu$	$0.0041 - 1$
Strouhal number	$\mathcal{S}$	$l^*/(UT)$	$1 - 1000$
dimensionless slip coefficient	$\mathcal{A}$	$\sqrt{K}/(\zeta l^*)$	1.8×10^{-7}
dimensionless permeability	$\mathcal{B}$	$K/(\epsilon^4 l^{*2})$	$20 - 2.0 \times 10^7$ (1.2×10^4)
aspect ratio	ϵ	b_r^*/l^*	1.4×10^{-4}
dimensionless upper inlet pressure	p_u^{in}	U_g/U	$0.0038 - 1$

inlet pressure p_u^{in} is the ratio of the gravity-driven axial velocity scale U_g to the valve-driven velocity scale U.

We work in the physically relevant regime in which $\mathcal{A} = \mathrm{o}(\epsilon)$. Using parameter values in Table 2.1, the dimensionless slip coefficient lies in the range $\mathcal{A} \in (5.6 \times 10^{-9}, 5.6 \times 10^{-6})$. We also check that the equivalent slip parameter computed using scaffold length scales is small, by computing the ratio of the slip length to the *scaffold* length, $\mathcal{A}_s = \sqrt{K}/(\zeta l_s^*)$, and comparing it to the scaffold aspect ratio, $\epsilon_s = h_s^*/l_s^*$. The parameter values in Table 2.1 show that $\mathcal{A}_s$ is at most 0.002, while $\epsilon_s = 0.4$, confirming that we are indeed in the regime where slip is negligible. The dimensionless permeability $\mathcal{B}$ varies between 20 for lower permeabilities and 2.0×10^7 for higher permeabilities, reflecting the fact that for highly permeable scaffolds, only a tiny pressure drop $1/\mathcal{B}$ is required to drive comparable flows through the scaffold as along the channel, because of the relatively long length of the tube system. As we shall describe in §2.8, in Chapters 3 and 4 we will work in three different regimes for $\mathcal{R}$, $\mathcal{S}$, and p_u^{in}.

The dimensionless cross-sectional areas (2.2) in the channels, valve tubing, and resistor tubing are the same with stars dropped:

$$A_i = \begin{cases} \pi b_v^2 & \text{for} \quad z \in (z_0, z_1) \cup (z_8, z_9), \\ \pi b_r^2, & \text{for} \quad z \in (z_2, z_3) \cup (z_6, z_7), \\ 4 b_c c & \text{for} \quad z \in (z_3, z_6). \end{cases} \tag{2.20}$$

The dimensionless version of equation (2.4) for the circumference of elliptical cross-sections of each valve is

$$2\pi b_v = 4 a_{ij} E(e_{ij}), \tag{2.21}$$

and the dimensionless version of equation (2.5) prescribing the cross-sectional area, $A_{ij} = \pi a_{ij} b_{ij}$, of each valve is

$$A_i = \pi b_v^2 \left\{ 1 - \left(\frac{1-\delta}{4} \right) \left(1 - \cos \frac{2\pi(z - z_j)}{z_{j+1} - z_j} \right) c_v \left(t; \frac{\tau}{T} \right) \right\}, \quad j = 1, 7. \tag{2.22}$$

Here the dimensionless valve tubing radius is $b_v = b_v^*/b_r^*$, given in Table 2.2, the ellipses' eccentricities are e_{ij}, the dimensionless valve period is τ/T, and c_v is the valve closure function controlling time-dependence of the valve area, given in Appendix A.

The dimensionless Navier-Stokes equations (2.6) in the fluid domain Ω_i are

$$\epsilon^2\mathcal{R}\left(\mathcal{S}\frac{\partial u_i}{\partial t}+u_i\frac{\partial u_i}{\partial x}+v_i\frac{\partial u_i}{\partial y}+w_i\frac{\partial u_i}{\partial z}\right)= -\frac{\partial p_i}{\partial x}+\epsilon^2\frac{\partial^2 u_i}{\partial x^2}+\epsilon^2\frac{\partial^2 u_i}{\partial y^2}+\epsilon^4\frac{\partial^2 u_i}{\partial z^2}, \tag{2.23a}$$

$$\epsilon^2\mathcal{R}\mathcal{S}\frac{\partial v_i}{\partial t}+\epsilon^2\mathcal{R}\left(u_i\frac{\partial v_i}{\partial x}+v_i\frac{\partial v_i}{\partial y}+w_i\frac{\partial v_i}{\partial z}\right)= -\frac{\partial p_i}{\partial y}+\epsilon^2\frac{\partial^2 v_i}{\partial x^2}+\epsilon^2\frac{\partial^2 v_i}{\partial y^2}+\epsilon^4\frac{\partial^2 v_i}{\partial z^2}, \tag{2.23b}$$

$$\mathcal{R}\mathcal{S}\frac{\partial w_i}{\partial t}+\mathcal{R}\left(u_i\frac{\partial w_i}{\partial x}+v_i\frac{\partial w_i}{\partial y}+w_i\frac{\partial w_i}{\partial z}\right)= -\frac{\partial p_i}{\partial z}+\frac{\partial^2 w_i}{\partial x^2}+\frac{\partial^2 w_i}{\partial y^2}+\epsilon^2\frac{\partial^2 w_i}{\partial z^2}, \tag{2.23c}$$

$$\frac{\partial u_i}{\partial x}+\frac{\partial v_i}{\partial y}+\frac{\partial w_i}{\partial z}=0. \tag{2.23d}$$

After non-dimensionalisation, Darcy's law and the continuity equation (2.7) in the scaffold domain Ω_s are

$$(u_s,v_s,w_s)=-h_s\left(\frac{\partial p_s}{\partial x},\frac{\partial p_s}{\partial y},\frac{\partial p_s}{\partial z}\right), \tag{2.24a}$$

$$\frac{\partial u_s}{\partial x}+\frac{\partial v_s}{\partial y}+\epsilon^2\frac{\partial w_s}{\partial z}=0, \tag{2.24b}$$

where $h_s=\mathrm{O}(1)$. The dimensionless prescribed tubing wall velocities (2.9) are

$$(u_i,v_i,w_i)=(U_i,V_i,W_i)\quad\text{on}\quad\partial\Omega_i, \tag{2.25}$$

where $\boldsymbol{U}_i$ is given by equation (2.10) with stars dropped. The dimensionless boundary conditions of unidirectional flow and prescribed normal stress at inlets and outlets (2.11) are

$$u_u=0=v_u,\ p_u-\epsilon^2\frac{\partial w_u}{\partial z}=p_u^{in}\quad\text{at } z=0, \tag{2.26a}$$

$$u_u=0=v_u,\ p_u-\epsilon^2\frac{\partial w_u}{\partial z}=0\quad\text{at } z=1, \tag{2.26b}$$

$$u_\ell=0=v_\ell,\ p_\ell-\epsilon^2\frac{\partial w_\ell}{\partial z}=p_\ell^{in}\quad\text{at } z=0, \tag{2.26c}$$

$$u_\ell=0=v_\ell,\ p_\ell-\epsilon^2\frac{\partial w_\ell}{\partial z}=0\quad\text{at } z=1, \tag{2.26d}$$

where $p_u^{in} = \epsilon^2 l^* p_u^{in*}/(\mu U)$, as stated in equation (2.19), and $p_\ell^{in} = \epsilon^2 l^* p_\ell^{in*}/(\mu U)$. The dimensionless zero normal flux condition (2.12) on scaffold walls is

$$w_s = 0 \quad \text{on} \quad \partial\Omega_s \setminus (\Gamma_u \cup \Gamma_\ell). \tag{2.27}$$

The dimensionless conditions (2.13) on the scaffold-channel interfaces Γ_i are

$$v_i = -\mathcal{B}\frac{\partial p_s}{\partial y}, \qquad \epsilon^2 \frac{\partial v_i}{\partial y} - p_i = -p_s, \tag{2.28a}$$

$$\mathcal{A}\left(\frac{\partial v_i}{\partial x} + \frac{\partial u_i}{\partial y}\right) = \epsilon u_i, \qquad \mathcal{A}\left(\epsilon^2 \frac{\partial v_i}{\partial z} + \frac{\partial w_i}{\partial y}\right) = \epsilon w_i. \tag{2.28b}$$

The initial condition (2.14) for flow in the tube systems $\Omega_{u,\ell}$ is

$$(u_i, v_i, w_i) = (u_b, v_b, w_b), \tag{2.29}$$

where $(u_b^*, v_b^*, w_b^*) = U_v(\epsilon u_b, \epsilon v_b, w_b)$.

2.7 Shear stress

To estimate the shear stress distributions throughout the scaffold from predictions of the Darcy velocity we follow Whittaker et al. [163]. In this model, the pores are assumed to be cylindrical tubes and the geometry of the scaffold enters only via the average pore size d and the scaffold tortuosity η, so that the model does not account for scaffold deformability and elasticity.

While we choose this model for its simplicity, more detailed pore-scale approaches have also been employed to compute shear stress in tissue engineering scaffolds. Within these, various methods have been used to obtain a model scaffold domain that is close to the physical scaffold domain, for example micro-computed tomography has been used [128] to computationally reconstruct a section of scaffold. Others [62] have used a computationally-aided design template for a scaffold, and updated the flow domain during simulations to account for tissue growth on the scaffold. Common to these more detailed approaches has been the use of computational fluid dynamics simulations to solve Stokes flow in the scaffold domain. In contrast, the much more computationally light approach of [163] gives a simple analytical expression for shear stress in terms of the Darcy velocity.

In detail, to approximate the shear stress in the scaffold, we idealise the scaffold pores as cylinders of diameter d through which there is a Poiseuille flow. Then the dimensional axial pore velocity is $u_{\text{pore}}(r) = 2U_{\text{pore}}(1 - (2r/d)^2)$ where r is the local radial coordinate in a pore and U_{pore} is the average pore fluid velocity. The dimensional shear stress is then $\Sigma \coloneqq \mu \left|\partial u_{\text{pore}}/\partial r\right|_{r=d/2} = 8\mu\, U_{\text{pore}}/d$. The dimensional Darcy velocity is related to U_{pore} via $|\boldsymbol{u}_s^*| = \phi\, U_{\text{pore}}/\eta$. We therefore estimate the dimensional scaffold shear stress to be

$$\Sigma(z,t) = \frac{8\mu\eta}{\phi d}\,|\boldsymbol{u}_s^*|\,. \tag{2.30}$$

2.8 Parameter regimes

In Chapters 3 and 4 we consider the three parameter regimes outlined below. These cover the range of physically-realistic operating conditions for the bioreactor.

Chapter 3 looks at the case where valve-driven and gravity-driven axial flow are of comparable size, $p_u^{in} = U_g/U = \mathrm{O}(1)$; axial flow is sufficiently slow that the reduced Reynolds number is small, $\mathcal{R} = \epsilon^2\rho U l^*/\mu = \mathrm{o}(1)$; and the dimensionless valve amplitude is order one, $a = \mathrm{O}(1)$, meaning the Strouhal number is order one, $\mathcal{S} = 1/a = \mathrm{O}(1)$. Since $p_u^{in} = \mathrm{O}(1)$, the inlet pressure boundary conditions (2.26a) and (2.26c) are non-zero at leading-order. The small reduced Reynolds number and order one Strouhal number imply that inertia is negligible at leading-order in the Navier-Stokes equations (2.23).

In §4.2-§4.7 we move to the regime where axial flow may be fast enough for the reduced Reynolds number to be $\mathcal{R} = \mathrm{O}(1)$; as before the dimensionless valve amplitude is order one, so that $\mathcal{S} = \mathrm{O}(1)$; and valve-driven flow dominates gravity-driven flow, $p_u^{in} = \mathrm{o}(1)$. We do not however exploit this last constraint, but always keep p_u^{in} in the model, as gravity-driven flow (i.e. when valves are static and flow is only driven by p_u^{in}) is used as a baseline for comparisons when presenting results. Additionally, retaining p_u^{in} does not make solving the system any more difficult. With order one reduced Reynolds and Strouhal numbers, inertia appears at leading-order in the Navier-Stokes equations (2.23).

Finally, in §4.8, as in Chapter 3 we have small reduced Reynolds number, $\mathcal{R} = \mathrm{o}(1)$, however we now assume that the dimensionless valve amplitude is

small, $a = \mathrm{o}(1)$, meaning that there is a disparity in timescales of axial-driven flow, $l^*/U = T/a$, and the valve period, T, so that the Strouhal number is large, $\mathcal{S} \gg 1$. We therefore have $\mathcal{RS} = \mathrm{O}(1)$, so that linear inertia appears at leading-order in the Navier-Stokes equations (2.23), while because $\mathcal{R} = \mathrm{o}(1)$, non-linear inertia is negligible at leading-order. For the valves to drive a flow with $\mathcal{RS} = \mathrm{O}(1)$, we are in the regime where $p_u^{in} = \mathrm{o}(1)$, however as in §4.2-§4.7 we do not exploit this fact.

A summary of the parameters that vary between modelling regimes is provided in Table 2.3. The key parameters that control which terms are retained or neglected in the Navier-Stokes equations (2.23) are the reduced Reynolds number $\mathcal{R}$ and the Strouhal number $\mathcal{S}$. We will see that the governing equations obtained in Chapter 3 and §4.8 are sublimits of those of §4.2-§4.7. The three regimes are solved and presented separately because the equations of Chapter 3 and §4.8 are simple enough to be solved systematically, while the extra complication of the non-linear inertia term in §4.2-§4.7 motivates the use of a method involving *ad hoc* assumptions.

In the following two chapters we reduce the dimensionless system of §2.6 in each of the regimes described above, and explore how the scaffold shear stress and bioreactor fluxes may be controlled using the valve dynamics and the various geometric parameters in the bioreactor.

Parameter name	Symbol	Formula	Chapter 3	§4.2-4.7	§4.8
Strouhal number	$\mathcal{S}$	$l^*/(UT)$	$\mathrm{O}(1)$	$\mathrm{O}(1)$	$\mathrm{O}(1/\mathcal{R})$
reduced Reynolds number	$\mathcal{R}$	$\epsilon^2\rho U l^*/\mu$	$\mathrm{o}(1)$	$\mathrm{O}(1)$	$\mathrm{o}(1)$
dimensionless valve amplitude	a	$-$	$\mathrm{O}(1)$	$\mathrm{O}(1)$	$\mathrm{o}(1)$
dimensionless upper inlet pressure	p_u^{in}	U_g/U	$\mathrm{O}(1)$	$\mathrm{o}(1)$	$\mathrm{o}(1)$

Table 2.3: Dimensionless parameters and scalings varying between the three modelling regimes of Chapter 3, §4.2-4.7, and §4.8.

Chapter 3

Quasi-steady model of the platelet bioreactor

To investigate the bioreactor model formulated in Chapter 2, we start with the simplest regime, where the axial flow is sufficiently slow and the valve amplitude is large enough that the effects of inertia may be neglected in equation (2.23). As explained in §2.8, this corresponds to the reduced Reynolds number $\mathcal{R} = \mathrm{o}(1)$ and the Strouhal number $\mathcal{S} = \mathrm{O}(1)$ as $\epsilon \to 0$. This lubrication regime includes configurations where the valves are static, which as described in §2.1 are used by Shepherd et al. [137] for the majority of the bioreactor run-time. The regime also includes configurations where the valves are moving, but both the valve-driven and gravity-driven axial flow are slow enough to ensure $\mathcal{R} = \mathrm{o}(1)$. While the valves in this chapter move more slowly than those used by Shepherd et al. (see §2.1), it is worth investigating whether using slower valves may be suitable for platelet production. This regime can also provide indications of trends in bioreactor fluxes and scaffold shear stress as we increase the valve speed.

In §3.1 we see that the leading-order bioreactor model is quasi-steady in the present regime, allowing us in §3.2 to solve for the pressure and fluxes throughout the bioreactor with little computational expense. In §3.5.1 we first use the model to investigate the bioreactor system when the valves are static, and each of the four valves may be open or closed. Specifically, we look at the dependence of bioreactor fluxes and scaffold shear stresses on the valve configuration (which valves are open, and which are closed), the scaffold permeability, and the lengths of each of the channel, resistor tubing, and valve tubing regions. We then investigate in

Table 3.1: Parameters used for the the regime $\mathcal{R} = \mathrm{o}(1)$ and $\mathcal{S} = \mathrm{O}(1)$. Composite parameters are given to 2 d.p. Where two values are given, the first is used in §3.5.1 and the second is used in §3.5.2.

Name	Symbol	Formula	Value(s)
bioreactor aspect ratio	ϵ	b_r^*/l^*	1.4×10^{-4}, 7.1×10^{-5}
valve amplitude	a	–	0.9995
valve period	τ	–	$0.5 - 40$ s
typical valve period	T	–	9.8 s, 40 s
valve-driven axial velocity scale	U	al^*/T	0.14 m/s, 0.036 m/s
gravity-driven axial velocity scale	U_g	$\epsilon^2 \rho g h_u^* l^*/\mu$	0.14 m/s, 0.036 m/s
dimensionless upper inlet pressure	p_u^{in}	U_g/U	1
dimensionless valve period	–	τ/T	$0.013 - 4.1$
reduced Reynolds number	$\mathcal{R}$	$\epsilon^2 \rho l^* U/\mu$	0.0041, 2.6×10^{-4}
Strouhal number	$\mathcal{S}$	$l^*/(UT) = 1/a$	1.0

§3.5.2 how moving the valves affects bioreactor fluxes and scaffold shear stresses, and determine whether there are ways to move the valves that will enhance the scaffold shear stress above levels achieved with static valves. A summary of the chapter is given in §3.6

3.1 Leading-order equations

Table 3.1 gives parameter values that are used in this chapter. In §3.5.2 we use radial lengthscales (stated later) that are slightly less than those used by Shepherd et al., to enable the investigation of shorter valve periods while remaining within the small Reynolds number regime. Where two values are given in Table 3.1, the first is used in the results of §3.5.1 and the second is used in §3.5.2. All other parameter values are as given in Table 2.1.

In the lubrication regime where $\mathcal{R} = \mathrm{o}(1)$ and $\mathcal{S} = \mathrm{O}(1)$ as $\epsilon \to 0$, the Navier-Stokes equations (2.23) for the fluid velocity, (u_i, v_i, w_i), and reduced pressure, p_i, in the fluid domain, Ω_i, are, at leading-order,

$$\frac{\partial p_i}{\partial x} = 0, \tag{3.1}$$

$$\frac{\partial p_i}{\partial y} = 0, \tag{3.2}$$

$$\frac{\partial^2 w_i}{\partial x^2} + \frac{\partial^2 w_i}{\partial y^2} - \frac{\partial p_i}{\partial z} = 0, \tag{3.3}$$

$$\frac{\partial u_i}{\partial x} + \frac{\partial v_i}{\partial y} + \frac{\partial w_i}{\partial z} = 0. \tag{3.4}$$

In the scaffold domain, Ω_s, we drop the $\mathrm{O}(\epsilon^2)$ in Darcy's equation (2.24):

$$\frac{\partial^2 p_\mathrm{s}}{\partial x^2} + \frac{\partial^2 p_s}{\partial y^2} = 0 \tag{3.5}$$

Continuity of normal stress and normal flux (2.28) at the scaffold-channel interfaces Γ_i, and no flux (2.27) on the scaffold walls $\partial\Omega_s \setminus (\Gamma_u \cup \Gamma_\ell)$ are

$$p_u = p_s, \quad v_u = -\mathcal{B}\frac{\partial p_s}{\partial y} \qquad \text{on} \quad \Gamma_u, \tag{3.6a}$$

$$p_\ell = p_s, \quad v_\ell = -\mathcal{B}\frac{\partial p_s}{\partial y} \qquad \text{on} \quad \Gamma_\ell, \tag{3.6b}$$

$$\frac{\partial p_s}{\partial n} = 0 \qquad \text{on} \quad \partial\Omega_s \setminus (\Gamma_u \cup \Gamma_\ell). \tag{3.6c}$$

The leading-order boundary and interface conditions are no-slip on the tube walls and the scaffold-channel interfaces,

$$w_i = 0 \quad \text{on} \quad \partial\Omega_i. \tag{3.7}$$

The kinematic condition (2.25) on the tubing walls is

$$(u_i, v_i, w_i) = \begin{cases} (0,0,0) & \text{for} \quad z \in (z_0, z_1) \cup (z_2, z_7) \cup (z_8, z_9), \\ \dfrac{\partial}{\partial t}\left(a_{ij}\cos\phi, b_{ij}\sin\phi, z\right), & \text{for} \quad z \in (z_1, z_2) \cup (z_7, z_8), \end{cases} \tag{3.8}$$

where $a_{ij} = a^*_{ij}/b^*_r$ and $b_{ij} = b^*_{ij}/b^*_r$, $j = 1, 7$ are the dimensionless semi-major and semi-minor axes of the elliptical valve cross-sections. These are computed

by solving equations (2.21) and (2.22) prescribing the ellipses' circumferences and areas, respectively. We use the valve closure function c_v given by equation (A.1) for a closing valve, and (A.2) for an opening valve, which is qualitatively the same as that in Figure 2.4 b).

Taking the leading-order stress conditions in (2.26) with $p_i^{in} = \epsilon^2 l^* \rho g h_i^*/(\mu U_g)$, inlet and outlet pressures are specified as

$$p_u(0,t) = 1, \quad p_u(1,t) = 0, \quad p_\ell(0,t) = h_\ell, \quad p_\ell(1,t) = 0. \tag{3.9}$$

3.2 Solution

We reduce the system to a network of pressure – cross-sectional area – flux relations at leading-order as follows. Integrating the continuity equation (3.4) over the cross-sections Ω_i, imposing the kinematic boundary conditions (3.8) and the interface flux condition (3.6a),(3.6b), and using Reynolds transport theorem, we find that the relationship between the axial flux and cross-sectional areas in the upper and lower tube systems is given, for $0 < z < 1$, by

$$\frac{\partial A_i}{\partial t} + \frac{\partial q_i}{\partial z} = J_i. \tag{3.10}$$

Here, the cross-sectional area, axial flux and net flux out of the adjoining scaffold are given by

$$A_i(z,t) = \iint_{\Omega_i} dx\, dy, \tag{3.11a}$$

$$q_i(z,t) = \iint_{\Omega_i} w_i\, dx\, dy, \tag{3.11b}$$

$$J_i(z,t) = \begin{cases} -\mathcal{B} \displaystyle\int_{\Gamma_i} \frac{\partial p_s}{\partial n}\, ds & \text{for} \quad z \in (z_4, z_5), \\ 0, & \text{otherwise}, \end{cases} \tag{3.11c}$$

with $\partial/\partial n$ being the derivative in the direction of the outward unit normal to the scaffold cross-section, so that positive J_i indicates flux from the scaffold into the tube system.

We solve Poisson's equation (3.3) subject to the no-slip condition (3.7) to determine w_i in terms of the pressure gradient, and use equation (3.11b) to obtain

the following flux-pressure relation

$$q_i = -C_i \frac{\partial p_i}{\partial z}, \tag{3.12}$$

where C_i are the tube system conductivities, determined by the various cross-sectional geometries, in the valve tubes, valves, resistor tubes, and channels respectively:

$$C_i(z,t) = \begin{cases} \dfrac{b_v^4 \pi}{8} & \text{for} \quad z \in (z_0, z_1) \cup (z_8, z_9), \\ \dfrac{\pi a_{ij}^4 (1-e_{ij}^2)^{3/2}}{4 e_{ij}^4 (2-e_{ij}^2)}, & \text{for} \quad z \in (z_j, z_{j+1}), \quad j = 1, 7, \\ \dfrac{b_r^4 \pi}{8} & \text{for} \quad z \in (z_2, z_3) \cup (z_6, z_7), \\ \displaystyle\sum_{n,m=0}^{\infty} \frac{16}{b_c c \lambda_n^2 \nu_m^2 (\lambda_n^2 + \nu_m^2)} & \text{for} \quad z \in (z_3, z_6), \end{cases} \tag{3.13}$$

where $\lambda_n = (n + 1/2)\pi/b_c$, $\nu_m = (m + 1/2)\pi/c$, $z_i = z_i^*/l^*$ for $i = 0, ..., 9$, and the dimensionless lengthscales $b_r = b_r^*/b_r^*$, $b_c = b_c^*/b_r^*$, and $c = c^*/b_r^*$ are given in Table 2.2. Figure 3.1 shows a plot of conductivities when the valves are closed: the valve conductivities dip very low, the resistor tubing conductivities are relatively low, and the channels and valve tubing have relatively high conductivities.

To determine the scaffold pressure, and hence the net flux, J_i, out of the scaffold into the adjoining channel, we solve equation (3.5) subject to (3.6). Since we have assumed that the scaffold cross section is a rectangular domain with Dirichlet and Neumann boundary conditions holding on horizontal and vertical sides respectively, the solution is simply

$$p_s(y, z, t) = (p_u(z,t) - p_\ell(z,t)) \frac{y}{h_s} + p_\ell(z,t), \tag{3.14}$$

and hence

$$J_u = -J_\ell = \begin{cases} -\dfrac{2c\mathcal{B}}{h_s}\big(p_u - p_\ell\big) & \text{for} \quad z_4 < z < z_5 \\ 0 & \text{otherwise.} \end{cases} \tag{3.15}$$

The dimensionless cross-sectional areas in each of the valve tubing, resistor tubing, channel, and valve regions are given in equations (2.20) and (2.22). The

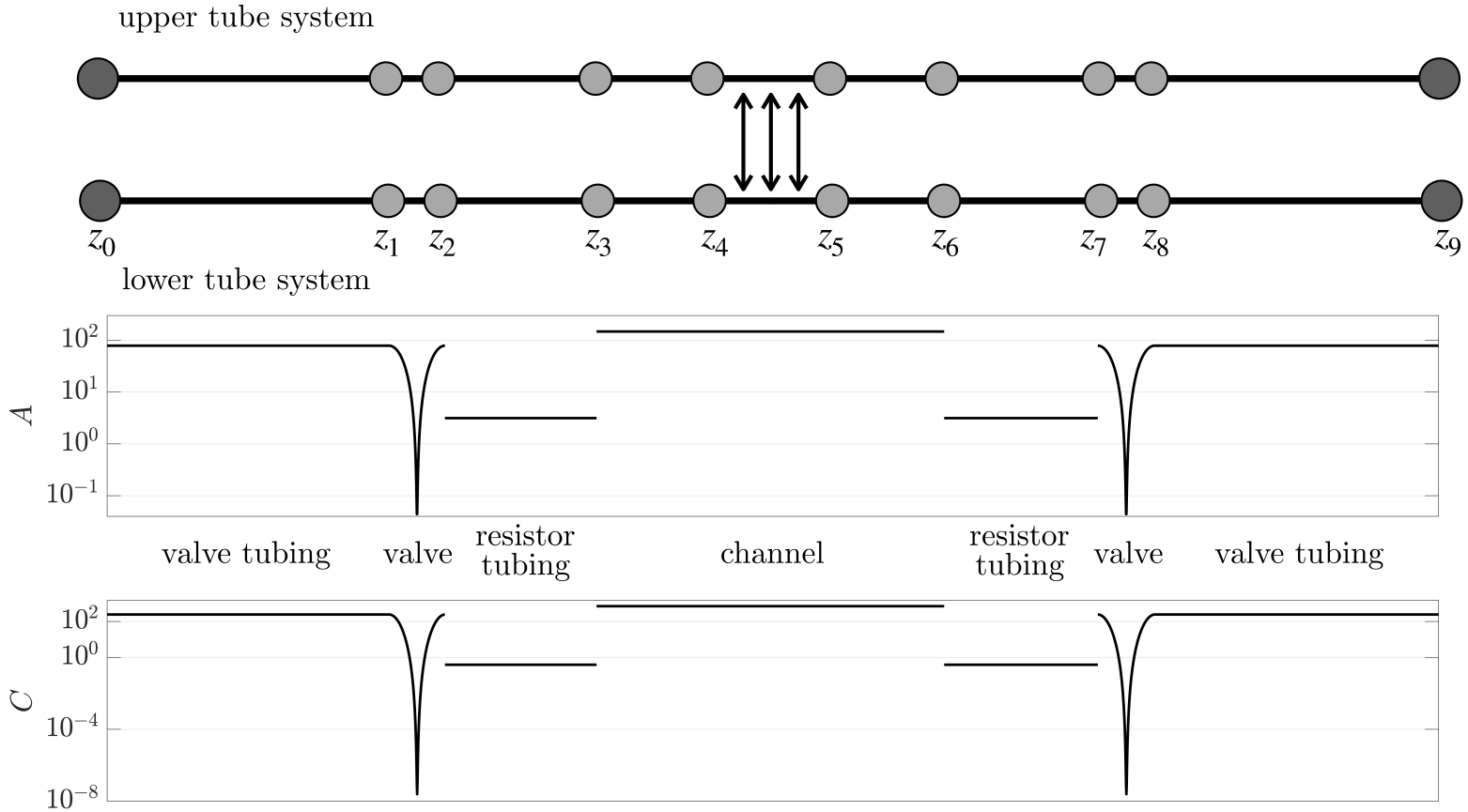

Figure 3.1: Network diagram of the reduced bioreactor system. Along the bioreactor centreline represented by black edges we impose the reduced system (3.10) and (3.12) with (2.20), (2.22), (3.13), and (3.15). The edges are joined by continuity of flux and pressure at the light grey nodes, representing junctions between regions. Pressure is prescribed at inlets and outlets at the dark grey nodes. The upper and lower tube systems are coupled due to the scaffold in $z \in (z_4, z_5)$, see equations (3.10), (3.15). Below are plots of the cross-sectional areas (A) and conductivities (C) of each region, when the valve regions are closed (z-axis not to scale). Parameters are in Tables 2.2 and 3.1.

cross-sectional area along the centreline, when the valves are closed, is plotted in Figure 3.1.

To summarise, the pressure – cross-sectional area – flux relations are given by equations (3.10) and (3.12), with tube conductivities (3.13), flux (3.15) from scaffold to channels, tube cross-sectional area (2.20), and valve cross-sectional areas (2.22). This system of second-order linear differential equations is solved (see below) subject to the specification of inlet and outlet tube system pressures (3.9), and continuity of pressures p_i and fluxes q_i ($i = u, \ell$) at the junctions between the valves, resistor tubing and channels. This is illustrated in the network diagram of Figure 3.1, where edges represent the tube system centrelines, light grey nodes are junctions, dark grey nodes are inlets or outlets, and the arrows indicate coupling between the upper and lower tube systems through the scaffold.

When there is a jump discontinuity in the cross-sectional area, these conditions can be derived systematically using a matched asymptotic analysis, as follows. We rescale the governing equations (2.23) in an inner region $\mathcal{V}$ around each junction such that the axial and transverse lengthscales are of O(ϵ), while the axial and transverse velocity scales are of O(1):

$$\mathcal{R}\left(\epsilon\mathcal{S}\frac{\partial\hat{\boldsymbol{u}}_i}{\partial t} + \hat{u}_i\cdot\hat{\nabla}\hat{\boldsymbol{u}}_i\right) = -\hat{\nabla}\hat{p}_i + \epsilon\hat{\nabla}^2\hat{\boldsymbol{u}}_i, \quad \text{and} \quad \hat{\nabla}\cdot\hat{\boldsymbol{u}}_i = 0, \tag{3.16}$$

where the hatted velocities are $\boldsymbol{u}_i^* = U\hat{\boldsymbol{u}}_i$, the hatted derivative is $\nabla = \hat{\nabla}/\epsilon$, and all other quantities are defined in equations (2.16) and (2.19). The resulting leading-order momentum equations then show that there is continuity in the leading-order outer pressure across each junction. Integrating the incompressibility condition over the inner region $\mathcal{V}$ around the junction,

$$\iiint_{\mathcal{V}} \hat{\nabla}\cdot\hat{\boldsymbol{u}}_i = 0, \tag{3.17}$$

and using the divergence theorem with no-flux on the tubing walls additionally implies continuity of the leading-order outer flux across each junction:

$$\iint_{\Omega_i(z_{in})} w_i\,dxdy = \iint_{\Omega_i(z_{out})} w_i\,dxdy, \tag{3.18}$$

where z_{in} and z_{out} are the $z-$bounds of $\mathcal{V}$. Hence, although the lubrication scalings do not apply in the inner region around each junction, we do not need to solve

for the full 3D flow equations but rather can apply the leading-order continuity conditions.

Using the parameters given in Table 2.1, the lower inlet pressure is $h_\ell = 0.5$. Having computed the pressures in the tube systems, the flux through the scaffold can be computed from equation (3.15).

We solve analytically the system of second order differential equations for the velocities and pressures in each of the 18 regions, with each pair of velocities and pressures having two degrees of freedom. Specifically, in the valve tubing, resistor tubing, and regions of channel that do not interface with the scaffold, the pressure is linear in z. In the regions of channel that do interface with the scaffold we have

$$p_u = B_1 e^{\gamma z} + B_2 e^{-\gamma z} - B_3 z + B_4, \tag{3.19a}$$

$$p_\ell = -\left(B_1 e^{\gamma z} + B_2 e^{-\gamma z}\right) - B_3 z + B_4, \tag{3.19b}$$

$$p_s = \left(B_1 e^{\gamma z} + B_2 e^{-\gamma z}\right)\left(\frac{2y}{h_s} - 1\right) - B_3 z + B_4, \tag{3.19c}$$

where $\gamma = \sqrt{4b_s\mathcal{B}/(h_s C)}$, and B_1, B_2, B_3, B_4 depend on time. There is no subscript on the channel conductivity C (see equation (3.13)) because the cross-sections of the upper and lower channels are the same. In the valves the pressure is

$$p_i = D_i \int_{z_j}^{z} \frac{1}{C_i}\, dz + \int_{z_j}^{z} \frac{1}{C_i} \int_{z_j}^{\hat{z}} \frac{\partial A_i}{\partial t}\, d\hat{z}\, dz + E_i, \quad j = 1, 7, \tag{3.20}$$

for valve conductivity C_i, and time-dependent coefficients D_i and E_i, $i = u, \ell$.

By imposing the conditions at the inlets, outlets, and junctions between regions, as described above, we obtain a system of 36 linear algebraic equations relating the 36 degrees of freedom. These are readily solved numerically in MATLAB using the backslash command.

3.3 Aside: exploiting the small scaffold length

In all of the above, we have not exploited the fact that the scaffold length l_s^* may be small compared to the bioreactor length l^*. Using the parameters in Table 2.2, this is indeed the case: $l_s = l_s^*/l^* = 0.0071$. We may therefore seek to simplify the

system presented in §3.2 by rescaling $z = l_s\hat{z}$ in the scaffold and adjacent channels, $z \in (z_4, z_5)$, and seeking series solutions

$$q_i = q_{i0} + l_s q_{i1} + \mathrm{O}(l_s^2), \qquad p_i = p_{i0} + l_s p_{i1} + \mathrm{O}(l_s^2). \tag{3.21}$$

Substituting expansions (3.21) into the flux-pressure relation (3.12) and equating terms of $\mathrm{O}(1/l_s)$, we find the leading-order p_{i0} is independent of $\hat{z}$. Equating terms of $\mathrm{O}(1)$ gives

$$q_{i0} = -C_i \frac{\partial p_{i1}}{\partial \hat{z}}, \tag{3.22}$$

which when combined with equation (3.10) using the scaffold flux expression (3.15) yields

$$\frac{\partial^2 p_{i1}}{\partial \hat{z}^2} = -\frac{2cl_s\mathcal{B}}{h_s C_i}\left(p_{i0} - p_{j0} + \mathrm{O}(l_s)\right) \quad \text{for} \quad z_4 < z < z_5 \tag{3.23}$$

where $(i, j) = (u, \ell), (\ell, u)$.

If $l_s\mathcal{B}/C_i = \mathrm{O}(1)$, then the upper and lower tube systems are fully coupled. We must proceed via the solution method described in §3.2, with the difference that the pressures p_{i1} are quadratic in z in $z_4 < z < z_5$ rather than involving exponentials, and the leading-order pressures p_{i0} are constants to be determined through imposing continuity of pressure and flux conditions (as for the coefficients B_i in equations (3.19c)).

If $l_s\mathcal{B}/C_i \ll 1$, then equation (3.23) shows that the pressure p_{i1} is linear in $z \in (z_4, z_5)$. In this regime, the upper and lower tube systems may decouple in certain valve configurations: for example, if all of the valves are open, then the two tube systems are decoupled from each other. In this configuration we can solve for the pressure along each tube system separately before computing the scaffold flux (3.15) as proportional to the pressure drop $p_u - p_\ell$. However, in a valve configuration where the upper inlet valve is open and the upper outlet valve is closed, we are effectively prescribing a no-flux condition on q_u at the boundary $z = z_7$ of the upper outlet valve. Additionally, equations (3.12) and (3.23) show that the pressure is linear in $z \in (z_2, z_7)$. Using continuity of flux between regions, this translates to zero leading-order flux in at least $z \in (z_2, z_7)$. Therefore in such a valve configuration, to find the flux we must go to higher order and solve with full coupling between the tube systems.

With the parameters in Table 2.2, $l_s\mathcal{B}/C_i = 0.12$, which is small, though it is physically plausible that the scaffold permeability, length, or channel dimensions could result in $l_s\mathcal{B}/C_i$ being larger than this value. We will be interested in valve configurations where the upper outlet valve is closed, as we expect these configurations to drive higher scaffold flows and possibly provide shear stresses suitable for platelet production. For these reasons, rather than rescaling into the small-l_s regime, we will solve the full system derived in §3.2.

3.4 Pore Reynolds number

As mentioned in §2.3, to justify the assumption that inertia is negligible in the scaffold, and that the use of Darcy's law is therefore valid, we must check that the pore Reynolds number is small in the scaffold [11].

We compute the pore Reynolds number *a posteriori* using scaffold velocities from the simulation rather than the scaffold velocity scaling (2.18) because, as we scaled the scaffold pressure with the pressure drop across the entire bioreactor in §2.6, in some valve configurations (2.18) may not be an accurate estimate for scaffold velocity. We compute the pore Reynolds number via

$$\mathcal{R}_p = \max_{\substack{z^*\in(z_4^*,z_5^*)\\ t^*\in(0,t_f^*)}} \frac{\rho\eta|\boldsymbol{u}_s^*|d}{\mu\phi}, \tag{3.24}$$

where d is the average pore diameter, and $\eta|\boldsymbol{u}_s^*|/\phi$ is the pore velocity, and t_f^* is the simulation run time. Values for d, η and ϕ are in Table 2.1. At leading-order, $|\boldsymbol{u}_s^*| = |v_s^*|$ because from equations (2.24a) and (3.14), $u_s^* = 0$, while $w_s^* = \mathrm{O}(\epsilon)$ is lower order than $v_s^* = \mathrm{O}(1)$. To compute $\mathcal{R}_p$, we therefore use values of scaffold velocity v_s^* obtained from simulations.

We use the valve configuration expected to give the greatest value for v_s^*, namely we move the upper inlet and lower outlet valves, closing the former while opening the latter, and keeping the other two valves closed. We use the shortest dimensionless valve period $\tau/T = 0.0125$ that also satisfies the requirement $\mathcal{S} = \mathrm{O}(1)$ and $\mathcal{R} = \mathrm{o}(1)$ (when using τ in place of the typical valve period T in the expressions for $\mathcal{S}$ and $\mathcal{R}$). The pore Reynolds number is computed to be $\mathcal{R}_p = 0.0073$, justifying our use of Darcy's law in this regime.

3.5 Results

3.5.1 Static valves

The fluid flow generated within the bioreactor fulfils three functions: to provide the cross-flow through the scaffold that exerts shear stress on megakaryocytes; to wash platelets out of the system to be collected; and to supply nutrients to the megakaryocytes in the scaffold and to remove their waste products. These three functions can be promoted by choosing which valves are open or shut. To understand how the valves influence each of these aspects, we first consider valves in different combinations of static configurations: fully open, partially open, or shut. For static valves, we first use the parameters of [137] given in Table 2.1 for illustration, and then vary the the bioreactor length and permeability to give a fuller characterisation of this class of bioreactor. Next we consider dynamic scenarios in which a single valve is periodically opened and shut, while the others remain static, before considering scenarios with multiple valves moving.

3.5.1.1 Shear stress and scaffold flux

At leading order, $|\boldsymbol{u}_s^*| = |v_s^*|$ because from Darcy's law (2.7a) and its solution (3.14) we have $u_s^* = 0$, while $w_s^* = \mathrm{O}(\epsilon)$ is lower order than $v_s^* = \mathrm{O}(1)$ (as reflected in the scalings (2.17)). The shear stress estimate (2.30) is therefore

$$\Sigma(z,t) = \frac{8\mu\tau U_s}{\phi d}\,|v_s|\,. \tag{3.25}$$

We compute the spatial mean of the scaffold shear stress,

$$\sigma = \frac{1}{l_s}\int_{z_4}^{z_5} \Sigma(z,t)\,dz, \tag{3.26}$$

where $\Sigma(z,t)$ is given in equation (2.30), and the scaffold flux

$$q_s = -2b_s\int_{z_4}^{z_5} v_s\,dz \tag{3.27}$$

for all the possible static configurations involving two, three, or four open valves, with the remaining valves closed. In Figure 3.2 a i) and a ii), we plot the spatial mean shear stress and the scaffold flux. We order the configurations by decreasing scaffold flux, and shade the combined physiological/experimental target shear

stress range of equation (2.1) in grey. As expected, configurations with the upper inlet valve open and a lower valve open give a non-negative scaffold flux, i.e. flow from the upper to the lower channel, because the upper inlet pressure is double the lower inlet pressure. Backflow, i.e. flow from the lower to upper channel, occurs when the upper inlet valve is closed, and the upper outlet and lower inlet valves are both open. Figure 3.2 a i) shows that mean shear stress is maximised by closing the upper outlet and lower inlet valves, while leaving the upper inlet and lower outlet valves open. As seen in Figure 3.2 a ii), this same configuration also maximises scaffold flux q_s^*, which promotes advective nutrient transport into the scaffold.

In Figure 3.2 b) we consider the shear-maximising configuration and explore how opening either one, or both, of the shut valves modulates the scaffold shear stress. Note that opening either one, or both, of the closed valves results in scenarios that have downward scaffold flux and open lower outlet valves, which we anticipate will promote platelet collection (see below). Recall that the degree of valve opening is controlled by the dimensionless parameter δ in (2.5), which varies between 10^{-4} (almost fully shut) and 1 (fully open). We see that either opening the upper outlet valve, or both the upper outlet and lower inlet valves, by as little as 3%, at $\delta = 0.03$, reduces shear stress by 44% and 31%, respectively.

We compute the average shear stress σ as we vary the scaffold permeability, K, for all the valve configurations shown in Figure 3.2 a ii) that have positive scaffold flux. For all of these configurations, Figure 3.2 c) shows that increasing K from 10^{-15} m^2 to 10^{-11} m^2 increases the shear stress σ by approximately three orders of magnitude, but increasing K further has minimal effect on the shear stress, as the limiting factor is no longer permeability but tube system geometry. Additionally, within the range of permeabilities $K = 10^{-12}$ m^2 to 10^{-9} m^2 for the scaffold used by [137] (see [104]), the shear stress for the two shear-maximising configurations always fall within the target shear stress range shaded in grey (see equation (2.1)), as shown by the dark and light blue lines in Figure 3.2 c). In the bioreactor operation of Shepherd et al., the configurations with all valves open (grey line), and with all but the lower inlet valve open (dark red line) were used. Figure 3.2 c) shows that these configurations just reach the target shear stress range for the

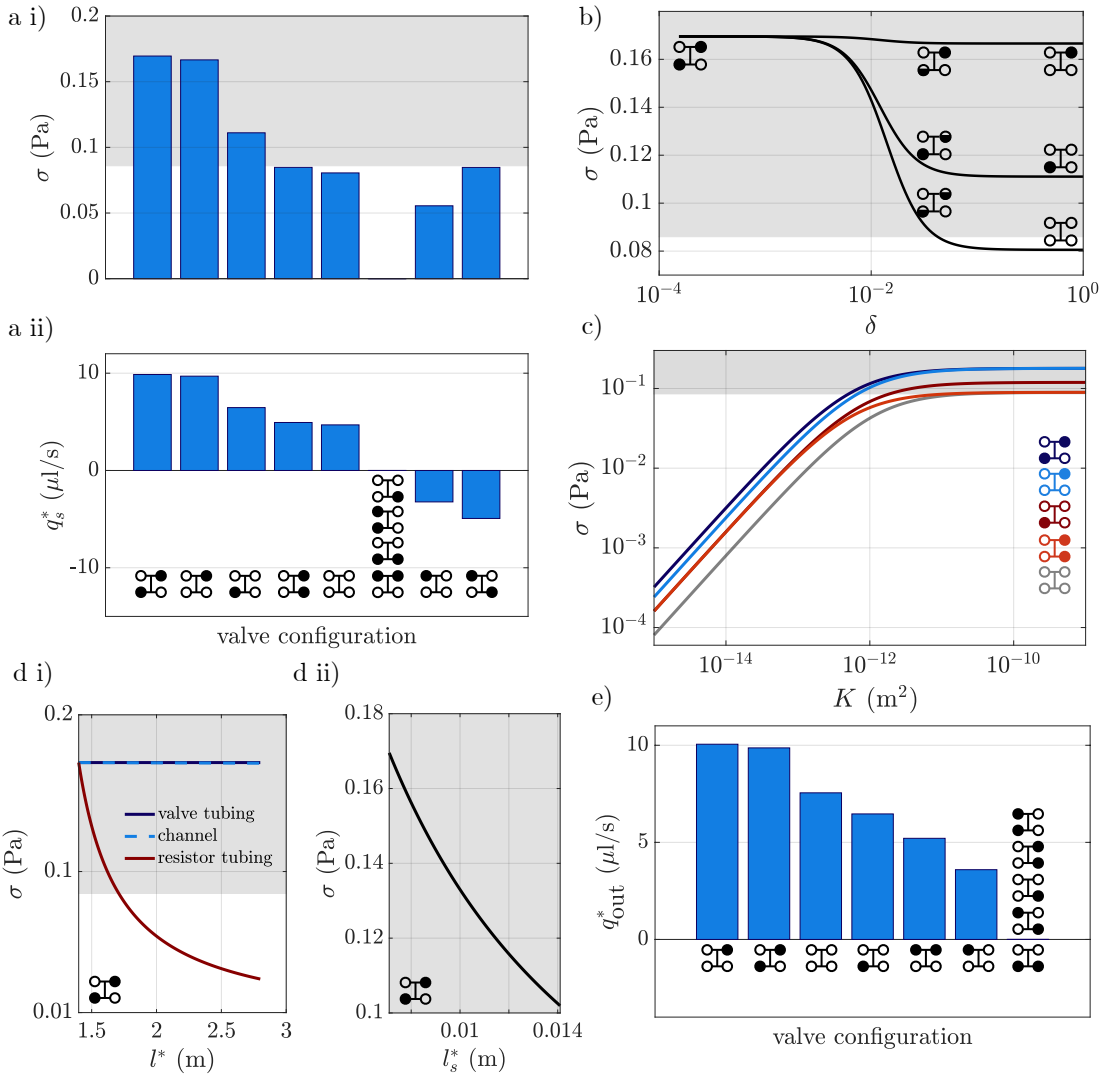

Figure 3.2: Trends in fluxes and shear stress for static valves, with the target shear stress range $0.086 < \sigma < 3.3$ Pa (from equation (2.1)) shaded grey throughout. a i) Mean scaffold shear stress and a ii) scaffold flux under different static valve configurations with two, three, or four valves open. The diagram(s) under the bars in a ii) show which valves are open (white) or closed (black). The sixth columns have $|q_s^*| < 0.0011\,\mu$l/s, and $\sigma < 4 \times 10^{-5}$ Pa, i.e. small compared to the other columns. b) Changes in shear stress when varying the fraction δ of a valve that is open; diagrams indicate which valves are being opened. The effect of c) scaffold permeability, K, and d) tube system length, l^*, on scaffold shear stress, σ, for the shear-maximising static configuration with open upper inlet and lower outlet, and closed upper outlet and lower inlet. In d) we lengthen either of the i) valve tubing, resistor, channels, or ii) scaffold and adjoining channels. e) Flux out of the lower outlet, for static configurations with 2, 3, or 4 valves open. Parameters are in Table 2.1 and 3.1.

permeability ranges $K = 2 \times 10^{-11} - K = 10^{-9}$ m^2 and $K = 2 \times 10^{-11} - 10^{-9}$ m^2, respectively.

For scaffold permeabilities between 10^{-15} m^2 and 10^{-12} m^2, opening the lower inlet valve, in addition to the upper inlet and lower outlet valves, significantly decreases scaffold shear stress, as shown by the mid-blue line in Figure 3.2 c) being visibly lower than the dark blue line. This is because, for small enough scaffold permeabilities, flow in the lower tube system dominates flow through the scaffold, in that allowing flow in through the lower inlet substantially increases pressure in the lower tube, relative to its value when the lower inlet is closed. In contrast, for large scaffold permeabilities, opening the lower inlet valve barely increases the pressure in the lower tube system, so that the shear stress is only slightly less than when the lower inlet valve is closed.

The average scaffold shear stress is also affected by varying the tube system length l^*. In Figure 3.2 d), we plot the change in scaffold shear stress as we increase the overall tube length by lengthening each of the regions: valve tubing, channels, resistor tubing, and the scaffold with its adjoining channel regions. We only present results for the shear-maximising valve configuration depicted in the bottom left inset, as we obtain the same qualitative results for all the valve configurations shown in Figure 3.2 a ii) that have non-negligible scaffold flux (i.e. all but those in the sixth column). Varying l^* by lengthening one particular region affects the model in three places. First, increasing l^* acts to decrease velocities in the tube systems, because the pressure drop $\rho g h_u^*$ now has to drive flow over a longer length. Second, increasing l^* increases the dimensionless permeability $\mathcal{B}$ in equation (2.19), representing an increase in scaffold velocity relative to tube system velocities. Lastly, increasing l^* by lengthening valve tubing or channels increases the proportion of the system with relatively wide tubing, decreasing resistance to flow and acting to increase velocities in the tube systems. Conversely, adding resistor tubing will increase the proportion of the system with relatively narrow tubing, increasing resistance to flow in the tube systems. To determine the net effect of these competing factors, we must solve the system.

Figure 3.2 d i) shows that doubling l^* from 1.4 m to 2.8 m by increasing either the valve tubing or channels reduces the scaffold shear stress by less than 1%. This is because the increase in axial length is approximately balanced out by the

increase in proportion of relatively wide tubing in the tube systems, so that flow rates in the upper and lower channels change by less than 1%. Thus there is little change in the flux through the scaffold, so that the scaffold velocity, and therefore shear stress, are virtually unchanged. In contrast, increasing the resistor tubing from 1.4 m to 2.8 m reduces the shear stress by 81%. This is because the axial lengthscale increases and the proportion of the system with relatively narrow tubing increases, so that the velocity in the upper channel decreases, as does the velocity in the scaffold.

Figure 3.2 d ii) shows that doubling the scaffold length (and also the section of channel adjoining the scaffold) reduces shear stress by 40%. The flow rates in the upper and lower channels change by less than 3%, as the increase in proportion of relatively wide tubing in the tube systems again approximately balances the increase in axial length. Thus the volume of media that passes from upper to lower channels at each instant in time stays roughly constant. As the length of the scaffold increases, the velocity in the scaffold therefore decreases, as does the shear stress.

Next we consider the effect of the upper inlet reservoir height h_u^* on scaffold shear stress. From equation (2.30) we see that the scaffold shear stress is linearly proportional to U, which is equal to $U_g = \epsilon^2 l^* \rho g h_u^* / \mu$ in this chapter. As this is the only place in the model where h_u^* appears, it follows that the shear stress increases linearly with the upper inlet reservoir height. The ceiling of the room the bioreactor is situated in provides an upper bound for the upper inlet reservoir height, thereby limiting the extent to which we can use the reservoir height to control the shear stress.

3.5.1.2 Platelet collection and diffusive nutrient transport

After platelets break off from their parent cell, they should be washed out of the system quickly, so as to minimise risk of damage or activation. This requires sufficient flux down the scaffold and out of the lower outlet. In Figure 3.2 e), we measure the flux $q_{\text{out}} = q_l(z_9, t)$ out of the lower outlet, for different valve configurations. The greatest flux is obtained when the upper inlet valve and both of the lower valves are open, as shown in the left column of Figure 3.2 e). In this configuration flow goes from scaffold to lower outlet and from lower inlet to

lower outlet. The same figure shows that the configuration with the upper inlet and lower outlet valves open has only slightly lower outlet flux, and as discussed above additionally promotes scaffold shear stress and advective nutrient transport. Thus we may use this configuration to achieve sufficient shear stress and nutrient transport, and then should we need more flux for platelet collection, use flow generated with only lower valves open to wash platelets out, for the following reasons. As seen in Figure 3.2 e), a reasonably high outlet flux of $5.2\,\mu$l/s is achieved when only lower valves are open, and from Figure 3.2 a ii) we additionally see that backflow in the scaffold is avoided. By keeping the upper inlet closed, we also avoid unnecessarily using nutrient-rich media from the upper reservoir to wash platelets out. Note that the duration of opening the lower valves should still be minimised as far as possible, to avoid excessive dilution of the product, which would then require expensive reconcentration procedures.

To facilitate diffusive transport of nutrients from the upper channel into the scaffold, while avoiding excessive collection volume at the lower outlet (i.e. dilute product), the configuration with the upper valves open and lower valves closed can be used, for reasons as follows. As seen in Figure 3.2 e), there is no flow out of the lower outlet when the lower valves are closed. Furthermore, we compute the velocity in the upper channel to be 1.3×10^{-4} m/s, which with a scaffold lengthscale of $l_s^* = 0.01$ m and nutrient diffusivity of $\mathrm{O}(10^{-9})$ (e.g. for oxygen or glucose [47, 169]), gives a Peclet number of $\mathrm{O}(10^3)$. Thus we are in the high Peclet number limit, so that at leading-order in the Peclet number, advection in the upper tube system maintains the concentration at the inlet value throughout the upper tube system. This allows diffusion across the scaffold to deliver the oxygen or nutrient to the cells, on a timescale much longer than the advective timescale.

3.5.2 Dynamic valves

To move between static configurations, valves must be opened and closed. This should be done by optimising some combination of shear stress, nutrient supply, and platelet collection, and without inducing backflow in the scaffold, upper channel, or lower channel.

Throughout this section, we use slightly narrower tubing radial lengthscales, $b_v^* = 4.9 \times 10^{-4}$ m, $b_c^* = 4.9 \times 10^{-4}$ m, and $b_r^* = 10^{-4}$ m, than were used by Shepherd et al., to allow us to investigate smaller dimensionless valve periods τ/T while remaining within the regime $\mathcal{R} = \mathrm{o}(1)$. The values of the dimensionless parameters for this section are the second values listed in Table 3.1.

In Figure 3.3 we illustrate the effect of each individual valve on the dimensionless fluxes $q_{u,\ell}^m = q_{u,\ell}(1/2, t)$ through the channel midpoints, and on the dimensionless scaffold flux q_s. Three valves are left open, while one pulses once: it closes and then opens, as illustrated in the plots of the cross-sectional valve area and shape in the left panel of Figure 3.3. We investigate two regimes: fast valves, with dimensionless valve period $\tau/T = 0.013$, and slow valves, with $\tau/T = 1$. The former case sits near the limit of our modelling regime, and we note that 'fast' valves here are still orders of magnitude slower than is possible in the physical bioreactor (see Table 2.1). In both regimes the valves are moved more slowly than in the specific experimental setup of [137] by a factor of approximately $10^3 - 10^4$. Thus our model clarifies the benefits or disadvantages of using slow valves. These insights can potentially be exploited by experimentalists in future studies. Additionally, the model can justify (or otherwise) the decision to use fast valves.

Although we impose the valve area to vary sinusoidally in time, as shown in the lower left plot in Figure 3.3 (or see equations (2.22), (A.1), (A.2)), changes in fluxes occur almost exclusively when the valve is at least 90% closed, in the interval $0.4 < t^*/\tau < 0.6$, so we plot fluxes in this interval. At $t^*/\tau = 0, 1$ the fluxes in Figure 3.3 return to the resting values when all valves are open, indicated by the grey dotted line.

3.5.2.1 Fast valves

Broadly, Figures 3.3 a i) and b ii) show that while a valve is closing (opening), the resistance of the valve increases (decreases), and the flux away from (towards) the valve is enhanced. Flux down the scaffold is therefore enhanced (diminished) during most of the time that an upper valve is closing (opening) or a lower valve is opening (closing), as illustrated by Figures 3.3 a iii) and b iii). Figures a i), a iii), b ii) and b iii) all contain negative fluxes. This indicates that backflow, where channel flow is from outlet to inlet, or scaffold flow is from bottom to top, can be

induced when outlets are closing or inlets are opening. As seen in Figures 3.3 a ii) and b i), the movement of upper (lower) valves has minimal effect on the lower (upper) channel flux, because contribution from the change in scaffold flux is small relative to the lower (upper) channel flux induced by the prescribed pressure drop across the lower (upper) tube system.

3.5.2.2 Slow valves

When the valves move with a slow period $\tau/T = 1$, Figures 3.3 c) and d) show that all of the fluxes vary monotonically either side of a local extremum that approximately coincides with the valve being closed. When a valve closes, the flux in its channel drops, and then increases when the valve reopens. In contrast to fast valves, where the flux extrema depend on the valve period, when valves are moved slowly the drop in flux depends only on the pressure boundary conditions. For instance, when the lower inlet valve closes, there is just a small drop in lower channel flux q_ℓ^m, as shown by the dark blue line in Figure d ii). This is because the prescribed pressure drop from upper inlet to lower outlet is one, i.e. high enough to compete with the prescribed pressure drop of one from upper inlet to upper outlet. On the other hand, the light blue line in Figure d ii) shows that closing the lower outlet valve, with lower inlet valve open, reduces the lower channel flux q_ℓ^m nearly to zero, as the prescribed pressure drop from upper inlet to lower inlet is only a half, i.e. less than the drop of one from upper inlet to lower outlet.

3.5.2.3 Controlling fluxes and shear stresses using valve synchronisation

The above principles seen from moving individual valves can be applied to determine what valve combinations should be used in transitioning between static configurations. There is freedom to choose the ordering of valve movements, and the extent to which different valves move in sync with each other, by choosing when each valve starts opening or closing. We first discuss valve ordering for fast valves, and then examine slow valves.

To illustrate valve ordering for fast valves, suppose we wish to maximise shear stress in the scaffold when transitioning from the configuration with only upper valves open (promoting diffusive nutrient transport) to the configuration with only

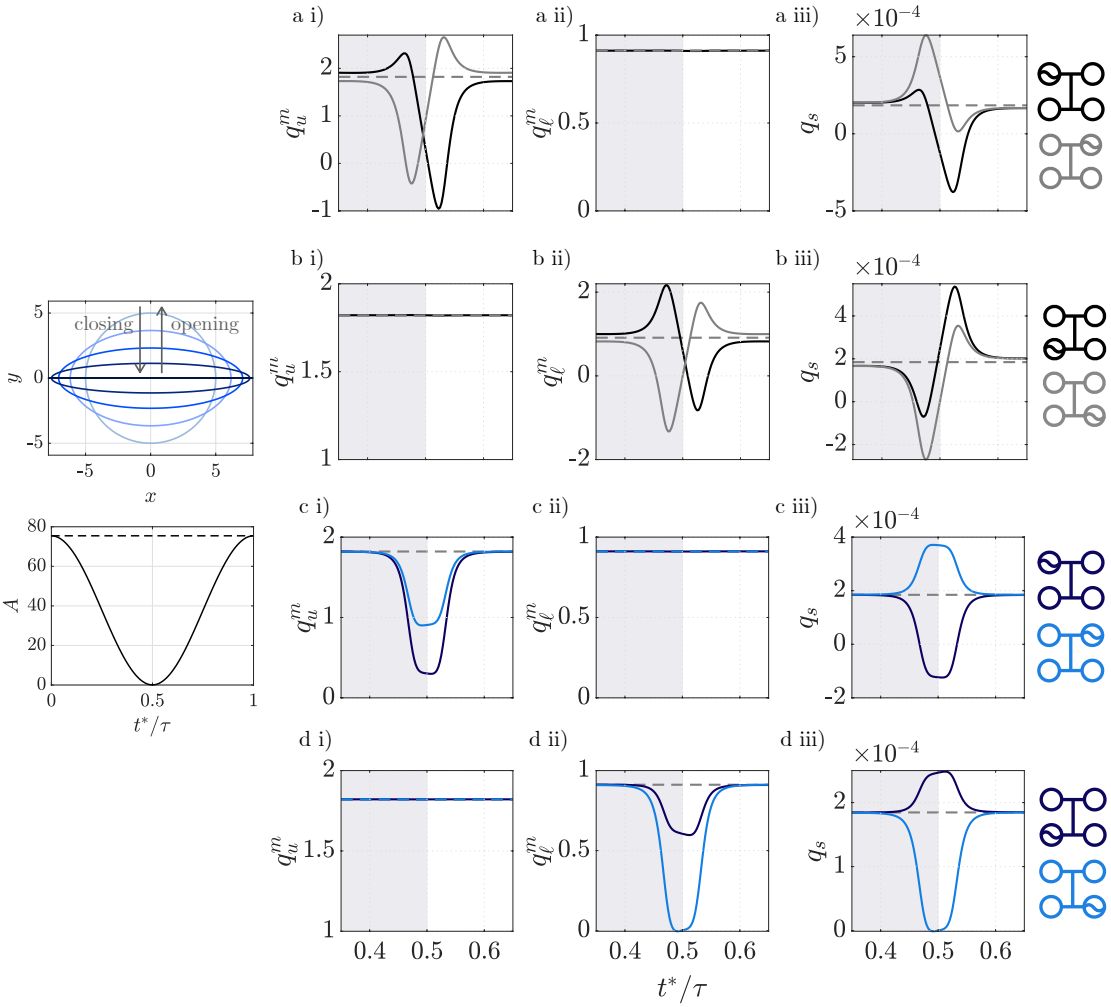

Figure 3.3: Dimensionless fluxes $q^m_{u,\ell}$ through the channel midpoints, and dimensionless flux q_s down the scaffold, when three valves are open. Lower left shows the area of the moving valve varying in time: initially, it is open, then closes in $t^*/\tau \in (0, 0.5)$ (shaded grey in a)-d)), and reopens in $t^*/\tau \in (0.5, 1)$ (unshaded in a)-d)) . The dotted line is the area when open. Upper left shows the valve cross-section closing, light to darker blue correspond to $t^*/\tau = 0, 0, 0.1, 0.2, 0.3, 0.5$. Subfigures a) and b) show valves moving quickly, with a period of $\tau = 0.5$ s, so that $\tau/T = 0.013$. Subfigures c) and d) show valves moving slowly, with a period of $\tau = 40$ s, so that $\tau/T = 1$. The tilde in the far-right diagrams show which valve is moving: in the first and third rows, upper valves are moving; in the second and fourth rows, lower valves are moving. The dotted grey line is the flux when all valves are open. Note that plots show $t^*/\tau \in (0.35, 0.65)$. Lengthscales are $b_v^* = 4.9 \times 10^{-4}$ m, $b_c^* = 4.9 \times 10^{-4}$ m, $b_r^* = 10^{-4}$ m, and other parameters are as in Tables 2.1 and 3.1.

lower valves open (promoting platelet collection). Then, to take advantage of the enhanced scaffold fluxes shown in Figure 3.3 a iii) while upper valves are closing and b iii) while lower valves are opening, the upper valves should be closed simultaneously with the lower valves opening. Closing both of the upper valves simultaneously additionally reduces backflow in the upper channel, as the increase in upper channel flux caused by closing the inlet valve (black line Figure 3.3 a i)) counteracts the backflow in the upper channel caused by closing the upper outlet valve (grey line Figure 3.3 a i)).

If the aim is relatively simple, then the principles explained above may be sufficient to pinpoint an appropriate set of valve configurations. More generally, when moving between any two static configurations, we may wish to optimise some function of q_u^m, q_ℓ^m, q_s and σ. As our model is computationally inexpensive, a large subset of the space of dynamic configurations that transition between any two static configurations may be simulated in seconds, enabling optimal configurations to be explored. We will illustrate how this might be done with two examples.

Suppose we move from the static configuration promoting shear stress, advective nutrient transport, and platelet collection, to the static configuration promotive diffusive nutrient transport, as shown in the upper right panel of Figure 3.4 a). The upper outlet valve must open and the lower outlet valve must close. The two valves move with a relative delay time of $\theta \in [-0.5, 0.5]$, where $\theta = 0$ corresponds to valves in-sync, $\theta = 0.5$ is the upper outlet valve opening completely, then the lower outlet valve closing, and $\theta = -0.5$ is the lower outlet valve closing completely, then the upper outlet valve opening (with no pause in between). Here θ is a time non-dimensionalised by the valve period, τ. In Figure 3.4 a) we predict the proportion of time above an illustrative threshold shear stress of 6.5×10^{-3} Pa, the total scaffold flux

$$\text{total}(q_s) = \int_0^{T_1} q_s \, dt \tag{3.28}$$

and the minimum instantaneous scaffold flux

$$\min(q_s) = \min_{t \in [0, T_1]} q_s(t) \tag{3.29}$$

while varying the synchronisation of valves. The total time T_1 is the time during which valve(s) are moving. We note that, as mentioned in §2.2, it is unclear

whether integrated or instantaneous shear stress is most important for enhancing platelet production; if the latter then we would replace the proportion of time in the shear stress range with the maximum shear stress. From Figure 3.4 a), we see we can for example choose θ to maximise the proportion of time that the shear stress is above the chosen threshold, under the constraint that $\min(q_s)$ is above some value, so that instantaneous backflow is sufficiently weak, and the constraint that $\text{total}(q_s)$ is below some chosen value, so that collection volume is sufficiently low.

In moving from the lower outlet valve closing first ($\theta = -0.5$), to the upper outlet valve opening first ($\theta = 0.5$), we see from Figure 3.4 a i) that the proportion of time spent above the threshold shear stress slightly increases in $\theta \in (-0.5, -0.44)$, then decreases in $\theta \in (-0.44, 0)$, before increasing in $\theta \in (0, 0.5)$. This is because the earlier (later) the lower outlet valve is closed, the less (more) time there is during which flow can pass from an upper valve, to a lower valve, exerting shear stress on the scaffold. Figure 3.4 a ii) shows that the total scaffold flux is smallest when the upper and lower outlet valves are in-sync, at $\theta = 0$. Opening the upper outlet valve and closing the lower outlet valve promotes backflow through the scaffold, in competition with the externally imposed pressure drop from upper inlet to lower outlet. Figure 3.4 a iii) shows that the highest degree of instantaneous backflow, captured via $\min(q_s)$, occurs for $\theta = -0.5$, where the upper outlet valve only starts opening after the lower outlet has fully closed. Away from $\theta = -0.5$, there is little variation in $\min(q_s)$.

In Figures 3.4 b), we show the proportion of time above the threshold shear, the total scaffold flux, and minimum instantaneous scaffold flux when moving from the shear-promoting static configuration, to the collection-promoting static configuration depicted on the right panel. Now $\theta = -0.5$ is opening the lower inlet valve first, and $\theta = 0.5$ is closing the upper inlet valve first. As predicted earlier, closing the upper inlet valve and opening the lower inlet valve pushes fluid down the scaffold, and from Figure 3.4 b iii) we see that backflow never occurs. Closing the upper inlet valve simultaneously with opening the lower inlet valve ($\theta = 0$) gives a high proportion of time above the threshold shear, but a lower total scaffold flux than first opening the lower inlet ($\theta = -0.5$), as seen in Figures 3.4 b i) and b ii), respectively. The total flux is lower because the time during which at least one

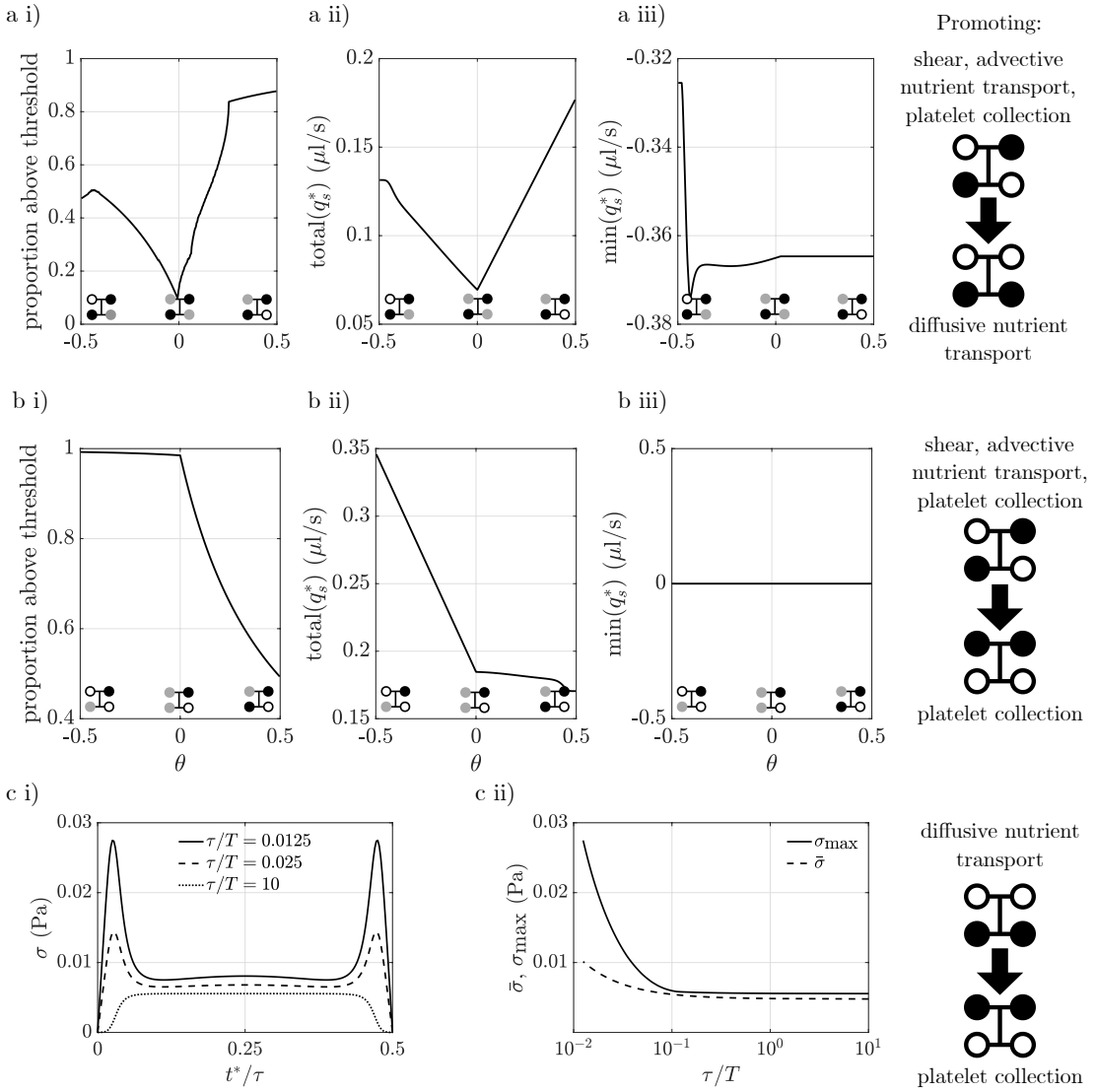

Figure 3.4: a, b i) Proportion of the total time the valves are moving, for which the shear stress is above an illustrative threshold value of 6.5×10^{-3} Pa; a, b ii) total scaffold flux over the time at least one valve is moving; and a, b iii) minimum instantaneous scaffold flux. Here the relative delay time θ between valves is varied while transitioning between two static configurations, shown on the right panels. The grey dots in the valve diagrams indicate which valve(s) starts moving first at that value of θ. c) Shear stress dependence on the dimensionless valve period τ/T. c i) Shear stress while closing upper valves and opening lower valves, with valves moving in sync, for $\tau/T = 10, 0.025, 0.013$. c ii) Maximum instantaneous shear stress σ_{max}, and time-averaged shear stress $\bar{\sigma}$ for $\tau/T \in [0.013, 10]$. Lengthscales are $b_v^* = 4.9 \times 10^{-4} = b_c^*$, $b_r^* = 10^{-4}$, and other parameters are as in Tables 2.1 and 3.1.

valve is moving is only half a period (i.e. the time for either closing or opening) for $\theta = 0$, but is one full period for $\theta = -0.5$.

We have so far studied advantages and disadvantages arising from varying the synchronisation of valves when the valves are moving quickly ($\tau/T = 0.013$); we check whether valve synchronisation matters in slow valves ($\tau/T = 1$). Specifically, when moving between any two of the three configurations depicted in the right panel of Figure 3.4, we vary the synchronisation θ between valves and measure σ, q_u^m, q_ℓ^m and q_s. We find that by varying θ, we cannot increase σ, q_u^m, q_ℓ^m and q_s by more than 1% above the maximum values they attain on the static configuration in Figure 3.2 a), nor is backflow induced. Thus with slow valves there are virtually no advantages/disadvantages to be had from varying the synchronisation of valves. Valve speeds are too slow to contribute to fluid velocity, and only valve position effects fluid velocity.

Finally, we examine how valve period affects shear stress, illustrated in Figure 3.4 c) using the transition from the valve configuration with only upper valves open, to only lower valves open, with valves moving simultaneously. Figure 3.4 c i) shows the instantaneous spatially-averaged shear stress σ during transition for three valve periods, and Figure 3.4 c ii) shows the maximum

$$\sigma_{\max} = \max_{t^* \in [0, \tau/2]} \sigma(t^*) \tag{3.30}$$

and time-averaged shear stress

$$\bar{\sigma} = \frac{2}{l_s^* \tau} \int_0^{\tau/2} \sigma(t^*)\, dt^*, \tag{3.31}$$

for $\tau/T \in [0.013, 10]$. Decreasing the valve period increases the maximum instantaneous shear stress σ_{max}, at first gradually and then steeply. The time-averaged shear stress also increases, but more gently. For $\tau/T = 0.013$, a maximum instantaneous shear stress of 0.027 Pa is attained, which is more than twice as large as the maximum shear stress of 0.011 Pa attained in the shear-promoting static configuration, with all other parameters kept constant.

3.6 Summary

In this chapter we have considered the regime in which the Strouhal number is order one, and the reduced Reynolds number is small. In this regime the timescale of valve-driven axial flow is comparable to that of gravity-driven flow. By exploiting the small aspect ratio of the bioreactor, we have employed the lubrication approximation for the Navier-Stokes equations, which we have solved subject to no-slip and continuity of normal velocity and pressure at the scaffold-channel interfaces, and no-slip on the rigid walls. We have similarly reduced Darcy's law under a long wavelength approximation. We have obtained equations relating the flux through each cross-section of bioreactor tubing to axially-dependent pressure gradients, via cross-sectional conductivities. The upper and lower channels are coupled via their interface with the scaffold. The full three-dimensional time-dependent system of PDEs has been reduced to a one-dimensional quasi-steady system of PDEs.

We have tested different static valve configurations, and predicted their effects on fluxes and scaffold shear stresses. Having computed the flux along the upper channel, lower channel, and the scaffold, we have demonstrated that there are some static valve configurations that should be avoided, as they induce significant backflow in the scaffold. Additionally, we have ranked static configurations in order of highest to lowest scaffold shear stress, and shown that the greatest scaffold shear stress arises from an open upper inlet and lower outlet, and closed upper outlet and lower inlet. Only the configurations with the three highest shear stresses reach shear stresses in the ranges given in equation (2.1), and even then they only just reach above the lower bound 0.086 Pa. This suggests that the static configurations used in Shepherd et al. may not have been exerting sufficient shear stress on the megakaryocytes.

As the configuration with only upper inlet and lower outlet valves open maximises shear stress, allows advective transport of nutrients to the scaffold, and washes platelets out of the scaffold to be collected, we could consider redesigning the bioreactor to have only an upper inlet and lower outlet, and no upper outlet and lower inlet. However, given uncertainties in the literature around the best length of time to expose platelets and megakaryocytes to shear, retaining the upper outlet and lower inlet is desirable for providing flexibility in the operating

protocol. For example, we may wish to deliver nutrients to cells while avoiding having a flow through the scaffold continuously as it may risk activating platelets, or may increase the collection volume too much. In this case, the upper inlet to outlet flow can enhance diffusive transport of nutrients to the scaffold, without contributing to flow through the scaffold.

We have characterised the effect of various geometric parameters on shear stress. The shear stress increases linearly with the upper reservoir height, which provides the driving pressure for the flow. We see this from the scaffold velocity scaling (2.18), which is linearly proportional to the valve-driven velocity scaling U, which for this chapter is equal to the gravity-driven velocity scale, U_g. Since the gravity-driven velocity U_g is linearly proportional to the upper reservoir height, it follows that the scaffold shear stress is linearly proportional to the upper reservoir height.

In contrast, the scaffold permeability and bioreactor length appear in the dimensionless model via the permeability parameter, and have nonlinear influence on the solution. Increasing the bioreactor length while maintaining a constant driving pressure has different effects on shear stress, depending on which part of the bioreactor is lengthened. At small permeabilities (10^{-15} m$^2 - 10^{-12}$ m^2), increasing the scaffold permeability by an order of magnitude increases the shear stress by approximately an order of magnitude; at larger permeabilities ($10^{-12}\,\mathrm{m}^2 - 10^{-9}\mathrm{m}^2$), further increasing the permeability has little effect on the shear stress. The scaffold must also be designed to capture megakaryocytes and allow platelets to escape, which sets porosity bounds; if there is room within such design restrictions to tune permeability, then in low permeability ranges, permeability may be an effective way to control shear (see for example [3, 158]).

We have investigated the effect of valve movement on the bioreactor flow. When transitioning between two static valve configurations with valves moving slowly (with period 40 s), fluxes vary monotonically towards/away from an extrema. Therefore, to determine what valve combinations should be used in transitioning between static configurations, it is sufficient to pay attention to any intermediate configurations that are passed through en route (for example, to avoid passing through configurations that induce high backflow).

In contrast, when opening and closing valves more quickly (say with period 0.5 s), time-dependent effects are more significant. When a valve is closing, flow away from it is enhanced, and when it is opening, flow towards it is enhanced. To avoid huge spikes in backflow, and take advantage of large spikes in scaffold shear stress, nutrient transport, or platelet collection, our model can be used to sweep through dynamic valve configurations that transition between static valve configurations. We have illustrated two examples of such transitions, and the model can in future be used to quickly obtain the exact configuration of valve movement that optimises some given function of tubing and scaffold fluxes, and scaffold shear stress.

We have chosen the valve period to match the timescale of flow induced by the pressure head, whereas in the physical bioreactor set-up of Shepherd et al. the valve period may be shorter (see Table 2.1). Thus, in the next chapter we will investigate whether the qualitative behaviour for short valve periods that we have simulated holds for even shorter valve periods, requiring the reintroduction of inertia in the the Navier-Stokes equations. To validate the modelling in this chapter, it will be important for future experimental work to take measurements of fluxes out of the bioreactor outlets, over a period of time, for various valve configurations, and compare these to model predictions.

Chapter 4

Inertial models for the platelet bioreactor with fast valves

In §3.5.1 we showed that in the shear-maximising static valve configuration (with the upper inlet and lower outlet valves open, and the other two valves closed) the shear stresses in the scaffold just reach the lower end of the estimated *in vivo* shear stress range. However, as discussed in §2.7, studies by a number of groups producing platelets *in vitro* [43, 107, 154] have shown that shear stresses higher than the *in vivo* range may further enhance platelet production.

There are a number of options for achieving higher shear stresses. The quasi-steady model in Chapter 3 demonstrated that increasing the inlet reservoir height only linearly increases the scaffold shear stress. Thus, as physical constraints such as ceiling height restrict the inlet reservoir height, increasing the reservoir height alone can only increase the scaffold shear stress by a factor of two or three. Within the range of physically relevant scaffold permeabilities, we similarly showed in §3.5.1 that there is only scope to increase scaffold shear stress to approximately double the *in vivo* minimum.

There are two velocity scales for axial flow in the system: that of gravity-driven flow, $U_g = \epsilon^2 \rho g h_u^* l^* / \mu$, and that of valve-driven flow, $U = a l^* / T$, introduced in equation (2.15). In Chapter 3 we looked at the regime where the dimensionless valve amplitude a was O(1), and U and U_g were comparable and small enough for inertial terms to be absent from the leading-order governing equations. These conditions constrained the reduced Reynolds number $\mathcal{R} = \epsilon^2 \rho U l^* / \mu = \epsilon^2 \rho a l^{*2} / (\mu T)$ to be small, and the Strouhal number $\mathcal{S} = l^* / (UT) = 1/a$ and dimensionless upper

inlet pressure p_u^{in} to be order unity. Within these constraints, we could decrease the valve period from 40 s to 0.5 s so as to increase the maximum shear stress by a factor of approximately five.

In this chapter the valves are moving sufficiently quickly that the flow speed is dominated by valve movement, $U \gg U_g$, so that the dimensionless inlet pressure p_u^{in} is of o(1) (however as mentioned in §2.8 we do not exploit this fact, because it makes no difference to the ease of solution, and because we use gravity-driven flow as a baseline for comparisons in results). We consider two regimes, depending on the dimensionless valve amplitude, a. In §4.1-§4.7 we assume that the valves can move with order one amplitude oscillations, $a = \mathrm{O}(1)$, so that the Strouhal number $\mathcal{S} = \mathrm{O}(1)$, and the valves are moving quickly enough that the reduced Reynolds number satisfies $\mathcal{R} = \mathrm{O}(1)$. In §4.8 we consider only small amplitude valve oscillations, $a = \mathrm{o}(1)$. We work in the regime where the amplitude of valve oscillations are small enough that $\mathcal{R} = \mathrm{o}(1)$, but the valve period is short enough that the system has an order one Womersley number, $\mathcal{RS}$ (which measures the ratio of the timescale of viscous diffusion to that of valve movement). In the first regime, both linear and non-linear inertia are retained at leading-order, motivating the use of *ad hoc* modelling assumptions to simplify the analysis, whereas in the second regime, only linear inertia is retained and the model is systematically reduced.

Through looking at these two regimes we can investigate valve speed control as a means of attaining shear stresses within the higher target ranges of equation (2.1), for sustained periods of time (i.e. seconds, minutes). Specifically, we address the following questions:

- After a valve stops moving, how long do the effects of enhanced (or diminished) shear stresses last for?
- How does the shear stress in the scaffold depend on the valve speed and amplitude?
- Are there negative effects of moving valves quickly that should be mitigated?

The modelling for the bioreactor with large amplitude valve oscillations is detailed in §4.1−§4.7. In §4.1 we review one-dimensional models for flow in networks of tubes that include inertia. The model is presented in §4.2−§4.5, and in §4.6 we discuss the numerical solution method. We address the questions raised above in §4.7. Following this, §4.8 considers small amplitude valve oscillations: §4.8.1−§4.8.4 presents the model, §4.8.5 uses it to validate the *ad hoc* model of §4.1−§4.7, and §4.8.6 compares fluxes and shear stresses from small and large amplitude valve oscillations. Finally in §4.9 we provide a summary and discussion of results.

4.1 One-dimensional models for tube networks with inertia

We first consider the case of fast, large amplitude valve oscillations. Given the geometrical constraints of the bioreactor, purely gravity-driven flow in the bioreactor has reduced Reynold's number $\mathcal{R} = \mathrm{o}(1)$. However, when the valve-driven flow dominates gravity-driven flow, we may have $\mathcal{R} = \mathrm{O}(1)$, so that the nonlinear inertial terms appear at leading-order in the governing equations. Thus the leading-order problem involves transverse as well as axial velocities and, in contrast to the case of slow valves, we can no longer easily solve for the axial velocity. Instead, we will use a method commonly used in vascular flow [48] and collapsible tube modelling [65], namely prescribing a velocity profile $s(x, y, z, t)$ (or its associated integrated coefficients described below) and integrating the system over the cross-section. This reduces the 3D system to a 1D system where the axial coordinate is the only spatial coordinate. The axial velocity $w_i(x, y, z, t)$ in a tubing system is then related to the axial flux $q_i(z, t)$ and cross-sectional area $A_i(z, t)$ by the postulated relationship

$$w_i = \frac{q_i s}{A_i}, \tag{4.1}$$

and it is then possible to obtain a system relating the pressures and axial fluxes in the bioreactor tubing.

The velocity profile appears in the integrated system through two coefficients: the momentum-flux coefficient,

$$\alpha(z,t) = \frac{1}{A_i} \int_{\Omega(z,t)} s^2 dxdy, \tag{4.2}$$

measuring the strength of non-linear inertia, and the friction coefficient,

$$\mathcal{K}(z,t) = - \int_{\partial\Omega(z,t)} \nabla s \cdot \boldsymbol{n}^{\perp} \, d\xi, \tag{4.3}$$

measuring the strength of viscous dissipation. Here Ω is the tube cross-section, ξ is the arclength coordinate around the boundary $\partial\Omega$, and $\boldsymbol{n}^{\perp} = \boldsymbol{n} - (\boldsymbol{n} \cdot \boldsymbol{e}_z)\boldsymbol{e}_z$ is the cross-sectional projection of the outward-pointing unit normal to $\partial\Omega$.

In the literature there have been multiple approaches to choosing the velocity profile so as to be able to compute these coefficients. The velocity profile can be prescribed *ad hoc* to be a power law function of the transverse coordinates [48], for which experimental data can be used to inform the power [143]. Alternatively, the velocity profile may be taken to be completely flat or flat with a boundary layer, as used for flow in slightly tapered vessels by [114]. More systematically, Azer and Peskin [7] used a Womersley velocity profile, which is valid for unidirectional flow in an infinite channel subject to no slip and driven by an imposed, time-dependent pressure gradient. Their solution method iterates between this Womersley problem and the integrated system for axial flow. The pressure gradient obtained from solving the integrated system is imposed on the Womersley problem, to solve for the Womersley velocity profile at each axial coordinate. Others have used three-dimensional simulations of the Navier-Stokes equations [131] to choose the momentum-flux and friction coefficients directly, without explicitly specifying a velocity profile. As a simplest initial approach, we use power law functions for the velocity profile, and consider a range of possible powers.

When modelling deformable tubes, a constitutive law describing wall mechanics is required to close the system. One-dimensional models for tubes have typically been used to model vascular networks, for which the (visco)elastic nature of the walls is important [48, 114, 138]. Assuming that walls reach equilibrium rapidly, an algebraic relation can be specified relating fluid pressure and cross-sectional

area, resulting in a hyperbolic system of equations for flux, area, and pressure. More complex models incorporate wall inertia, viscoelasticity, or pre-stress relating pressure and cross-sectional area via differential equations [48]. In contrast to these fluid-structure interaction systems, we will simply prescribe the cross-sectional area everywhere in the bioreactor; in particular in the valves we assume that the solenoid pinch valve mechanism completely controls the wall movement.

Since we are prescribing a velocity profile, the above modelling approach is necessarily approximate and *ad hoc* in nature. There have been a number of studies investigating the validity of various velocity profile choices, by comparing one-dimensional and three-dimensional modelling of blood flow in a range of domains and with a range of wall mechanics [30, 61, 164]. Grinberg et al [61] compared two models with rigid walls: a one-dimensional model with prescribed power-law velocity profile, and the full three-dimensional Navier-Stokes equations. The domain was a patient-specific intracranial vasculature domain obtained through MRI imaging, and patient-specific inlet flow-rates and constant outlet pressures were prescribed. Good agreement in the prediction for the pressure drop from inlet to outlet between the one-dimensional and three-dimensional models was found. Flow rates generally agreed well between the two models, with some larger discrepancies in flow rates at locations far from the inlets. These discrepancies were hypothesised to arise from three approximations made in the one-dimensional model: prescribing the velocity profile, assuming a constant cross-sectional area along individual vessels (whereas the three-dimensional model retained variation in cross-sectional area along individual vessels), and neglecting vessel branching angles at vessel bifurcations.

Xiao et al. [164] compared a one-dimensional model and a three-dimensional model, both with compliant walls. They considered an idealised aorta domain and its first generation of main branches, involving eight vessels with varying diameters, tapering, regions of high curvature, and vessel bifurcations. They imposed inlet fluxes on both one-dimensional models, and unidirectional flow with axisymmetric inlet profiles on the three-dimensional model. At the outlets of both models, a Windkessel model was implemented as a boundary condition; this is a lumped-parameter model for flow through large artieries, which incorporates compliance of the artery walls and resistance of smaller downstream blood vessels. Averaging

the pressure and fluxes over one cardiac cycle, they found the average relative error in pressure and fluxes between the one-dimensional and three-dimensional models on the full aorta domain was less than 5% at all inlets and outlets of the constituent vessels. The authors hypothesised that the error was due to neglecting the influence of the external tissue on the arterial walls in the one-dimensional model (but not in the three-dimensional model), or from the assumption of a velocity profile in the one-dimensional model.

Carson et al. [30] compared clinical measurements of pressure drops across stenoses in coronary arteries to those predicted by both one-dimensional models with compliant (but fairly stiff) walls and a three-dimensional model with rigid walls. They used patient-specific coronary vessel geometries, and found that the one-dimensional model with a viscoelastic constitutive law for walls and a near-flat velocity profile gave results closest to clinical measurements.

The above studies [30, 61, 164] of vascular domains considered more complex modelling geometry than the bioreactor yet still yielded results fairly representative of corresponding three-dimensional models or clinical data. However, the tubes in these models had walls that were either rigid or undergoing small (visco)elastic deformations. In contrast, in the bioreactor system we consider, the valves may have imposed large wall deformations. Models in the collapsible tube literature that couple internal flows to large deformations of elastic tube walls often study a simpler domain with just one tube [118]. In these systems, two regions of rigid tube wall sandwich an elastic tube. One-dimensional models of these systems have shown qualitative agreement with experimental results and higher-dimensional theoretical models [148].

Motivated by good agreement between one-dimensional models and three-dimensional models in vascular and collapsible tube modelling, we adopt a similar approach here. We consider a network model consisting of channels, tubes, valves, and a porous scaffold, with prescribed large deformation of valve walls. Inertia is included in the channels, tubes, and valves, and is neglected in the scaffold where we compute the pore Reynolds number *a posteriori*.

Table 4.1: Parameters used for fast and large amplitude valve oscillations.

Name	Symbol	Formula	Value(s)
valve amplitude	a	–	0.95
valve period	τ	–	$0.0026 - 1$ s
typical valve period	T	–	0.04 s
dimensionless valve timescale	–	τ/T	$0.065 - 25$
valve-driven axial velocity scale	U	al^*/T	35 m/s
reduced Reynolds number	$\mathcal{R}$	$\epsilon^2\rho l^* U/\mu$	1
Strouhal number	$\mathcal{S}$	$l^*/(UT) = 1/a$	1

4.2 Model set-up for bioreactor with fast, large amplitude valve oscillations

We work in the regime in which the typical valve period is small enough that the reduced Reynolds number $\mathcal{R} = \mathrm{O}(1)$, and with $a = \mathrm{O}(1)$, the Strouhal number $\mathcal{S}$ is of O(1).

The valve geometry is as described in §2.4 and equation (2.5), with quintic polynomials (A.3) and (A.4) for the valve closure function. As explained in Appendix A, this ensures that system coefficients are continuous in time, when moving between static/opening/closing valves. The qualitative behaviour of the valve area and valve closure in this chapter are the same as shown in Figure 2.5.

The parameters described above are summarised in Table 4.1, along with values used for simulations; all other parameters are as given in Table 2.2. Although we use a valve amplitude slightly less than one ($a = 0.95$) so as to avoid dividing by zero in simulations, when computing U, $\mathcal{R}$ and $\mathcal{S}$ we use $a = 1$ for convenience. Then the Strouhal number is simply $\mathcal{S} = 1$.

4.3 Leading-order governing equations

Here we present the leading-order system of equations (2.23) for the current regime where the reduced Reynolds number $\mathcal{R} = \mathrm{O}(1)$ and the Strouhal number $\mathcal{S} = \mathrm{O}(1)$

as $\epsilon \to 0$, as motivation for the utility of the *ad hoc* modelling approach we use in the rest of this chapter. Accordingly, we expand u_i, v_i, w_i and p_i as power series of the form $\phi_i = \phi_{0i} + \epsilon^2 \phi_{1i} + \mathrm{O}(\epsilon^4)$, for $\phi = u, v, w, p$, to obtain from (2.23) the leading-order governing equations given by

$$\frac{\partial p_{0i}}{\partial x} = 0, \tag{4.4a}$$

$$\frac{\partial p_{0i}}{\partial y} = 0, \tag{4.4b}$$

$$\mathcal{R}\left(\frac{\partial w_{0i}}{\partial t} + u_{0i}\frac{\partial w_{0i}}{\partial x} + v_{0i}\frac{\partial w_{0i}}{\partial y} + w_{0i}\frac{\partial w_{0i}}{\partial z}\right) = \frac{\partial^2 w_{0i}}{\partial x^2} + \frac{\partial^2 w_{0i}}{\partial y^2} - \frac{\partial p_{0i}}{\partial z}, \tag{4.4c}$$

$$\frac{\partial u_{0i}}{\partial x} + \frac{\partial v_{0i}}{\partial y} + \frac{\partial w_{0i}}{\partial z} = 0. \tag{4.4d}$$

These leading-order equations do not provide us with a closed system for u_{0i}, v_{0i}, w_{0i} and p_{0i}. To obtain a closed system, we consider the $\mathrm{O}(\epsilon^2)$ version of the x-and y-momentum equations, namely

$$\mathcal{R}\left(\frac{\partial u_{0i}}{\partial t} + u_{0i}\frac{\partial u_{0i}}{\partial x} + v_{0i}\frac{\partial u_{0i}}{\partial y} + w_{0i}\frac{\partial u_{0i}}{\partial z}\right) = -\frac{\partial p_{1i}}{\partial x} + \frac{\partial^2 u_{i0}}{\partial x^2} + \frac{\partial^2 u_{0i}}{\partial y^2}, \tag{4.5a}$$

$$\mathcal{R}\left(\frac{\partial v_{0i}}{\partial t} + u_{0i}\frac{\partial v_{0i}}{\partial x} + v_{0i}\frac{\partial v_{0i}}{\partial y} + w_{0i}\frac{\partial v_{0i}}{\partial z}\right) = -\frac{\partial p_{1i}}{\partial y} + \frac{\partial^2 v_{0i}}{\partial x^2} + \frac{\partial^2 v_{0i}}{\partial y^2}. \tag{4.5b}$$

We additionally integrate the mass equation (4.4d) over the cross-section, then apply the kinematic boundary condition (2.25) to obtain the leading-order global conservation of mass condition

$$\frac{\partial A_i}{\partial t} + \frac{\partial q_{i0}}{\partial z} = J_i, \tag{4.6}$$

where A_i is the cross-sectional area of tube cross-sections Ω_i, q_{i0} is the leading-order axial flux through Ω_i, and J_i is the net flux leaving the scaffold through the scaffold-channel interface Γ_i. These quantities are given by

$$A_i(z,t) = \iint_{\Omega_i} dx\, dy, \tag{4.7a}$$

$$q_{i0}(z,t) = \iint_{\Omega_i} w_i\, dx\, dy, \tag{4.7b}$$

$$J_i(z,t) = -\mathcal{B}\int_{\Gamma_i} \frac{\partial p_{\mathrm{s}}}{\partial n}\, ds. \tag{4.7c}$$

Equations (4.4c)-(4.6) for $u_{0i}, v_{0i}, w_{0i}, p_{0i}$ and p_{1i} are coupled partial differential equations that appear to be unamenable to analytical progress, necessitating a numerical approach. Solving five coupled partial differential equations in a domain with a moving boundary is computationally expensive, and we see that so far our systematic reduction has not presented many advantages over solving the full Navier-Stokes equations. This motivates the use of an *ad hoc* modelling method that only involves axial velocities, as described in §4.1, and detailed as follows.

4.4 Model incorporating *ad hoc* assumptions on the velocity profile

In the following, we omit the zero subscripts denoting leading-order variables to simplify the notation. In the tube systems we use the leading-order z-momentum equation (4.4c) and integrated mass equation (4.6):

$$\mathcal{R}\left(\frac{\partial w_i}{\partial t} + u_i\frac{\partial w_i}{\partial x} + v_i\frac{\partial w_i}{\partial y} + w_i\frac{\partial w_i}{\partial z}\right) = -\frac{\partial p_i}{\partial z} + \frac{\partial^2 w_i}{\partial x^2} + \frac{\partial^2 w_i}{\partial y^2}, \tag{4.8a}$$

$$\frac{\partial A_i}{\partial t} + \frac{\partial q_i}{\partial z} = J_i, \tag{4.8b}$$

and prescribe an axial velocity profile $s(x, y, z, t)$ such that we can write $w_i = sq_i/A_i$ (see equation (4.1)). We are then able to average (4.8a) so as to eliminate u_i, v_i from the system (see §4.5).

Before averaging the axial momentum equation, we start by discussing the form of s. We consider power-law velocity profiles that satisfy the no-slip condition

$$w_i = 0 \quad \text{on} \quad \partial\Omega_i \tag{4.9}$$

on the walls, together with the requirement, following from equation (4.1), that $\int_\Omega s\, dxdy = A$. As has been widely used in the literature [48], in tubes with circular cross-section of radius b, we use a profile of the form

$$s(r;\gamma) = \frac{\gamma+2}{\gamma}\left(1 - \frac{r^\gamma}{b^\gamma}\right), \tag{4.10}$$

where $\gamma = 2$ corresponds to Poiseuille flow and we recover a plug flow in the limit $\gamma \to \infty$ (see Figure 4.1 a)). Similarly, in valves with elliptical cross-section with

semi-minor and semi-major axes $a(z,t)$ and $b(z,t)$, we choose the velocity profiles to be

$$s(x,y,z,t;\gamma) = \frac{\gamma+2}{\gamma}\left(1-\left(\frac{x^2}{a(z,t)^2}+\frac{y^2}{b(z,t)^2}\right)^{\frac{\gamma}{2}}\right), \tag{4.11}$$

where $\gamma = 2$ is Poiseuille flow through a tube of elliptical cross-section. The velocity profile at a valve midpoint while closing, at a time $\tau/8$ after starting to close, is shown in Figure 4.1 b). In channels, which have rectangular cross-sections $2b_c \times 2c$, we compute the Poiseuille velocity profile, plotted in Figure 4.1 c), to be

$$\begin{aligned} s_p(x,y) = 4b_c c\Bigg(&-\frac{4}{\pi^3}\sum_{n=1}^{\infty}\frac{\sinh\beta_n(x+b_c)+\sinh\beta_n(b_c-x)}{(2n-1)^3\sinh(2\beta_n b_c)}\sin\beta_n(y+c) \\ &+\frac{(y+c)(c-y)}{2}\Bigg)\left(\frac{(2b_c)(2c)^3}{12}-\frac{16(2c)^4}{\pi^5}\sum_{n=1}^{\infty}\frac{\cosh(2\beta_n b_c)-1}{(2n-1)^5\sinh(2\beta_n b_c)}\right)^{-1}, \end{aligned} \tag{4.12}$$

where $\beta_n = (2n-1)\pi/b_c$. In computing this profile we have neglected flux exchange between the channels and the scaffold, and simply used no-slip and no-flux on the channel walls, the first condition of which is valid at leading-order even adjacent to the scaffold, for the same reason as in §3.1. We then use the Poiseuille profile s_p to compute a velocity profile that is Poiseuille at $\gamma = 2$ and becomes increasingly plug-like as γ increases:

$$s(x,y,z,t) = k\max(s_p)\left(1-\left(1-\frac{s_p}{\max(s_p)}\right)^{\frac{\gamma}{2}}\right), \tag{4.13}$$

where $\max(s_p)$ is the maximum value that s_p takes over the rectangle, and k is a numerically computed constant ensuring that $\int_\Omega s\,dxdy = A$ as required by equation (4.1).

There are other forms that we could have used in place of those given in (4.10), (4.11) and (4.13), that would also have corresponded to Poiseuille at $\gamma = 2$, become more plug-like as γ increases, and satisfied $\int_\Omega s\,dxdy = A$; we have chosen (4.10) because of its successful use in the literature. For simplicity, we will take the power law coefficient γ to be constant throughout the tubing, though it may be expected that in different regions of the bioreactor different values of γ will be suitable. For example, in the valves we may expect a higher value of γ than in

the rest of the tubing. Appropriate values of γ could be computed by conducting 3D numerical Navier Stokes simulations of flow through a sequence of valve tubing, a valve and resistor tubing at fixed valve speeds. We would then sweep through values of γ in each of the three regions with the *ad hoc* model to find values of γ that best match the results of 3D numerical simulations. To make the 3D simulations computationally feasible it may be necessary to restrict the valve amplitude, so as to avoid the extreme geometry of a closed valve. Alternatively, we could take experimental measurements of the bioreactor outlet fluxes for a range of valve speeds, and choose values for γ for which our model most closely reproduces experimental outlet fluxes.

As in Chapter 3, in the scaffold domain Ω_s we drop the $\mathrm{O}(\epsilon^2)$-terms in Darcy's equation (2.24) and solve (3.5) subject to continuity of normal stress at scaffold-channel interfaces Γ_i, and no flux on scaffold walls $\partial\Omega_s \setminus (\Gamma_u \cup \Gamma_\ell)$ (3.6) to get

$$p_s(y,z,t) = (p_u(z,t) - p_\ell(z,t))\frac{y}{h_s} + p_\ell(z,t). \tag{4.14}$$

Using (4.7c) we then see the fluxes J_u and J_ℓ in equation (4.8b) are given by

$$J_u = -J_\ell = \begin{cases} -\dfrac{2c\mathcal{B}}{h_s}\big(p_u - p_\ell\big) & \text{for} \quad z_4 < z < z_5 \\ 0 & \text{otherwise.} \end{cases} \tag{4.15}$$

4.5 Averaged governing equations

In this section we derive the averaged governing equations for a general cross-section in the tube system, which are almost identical to those for axisymmetric tubes, as given for example in [127]. We have already averaged the mass equation, when deriving the leading-order system of equations in §4.3. Here we average the axial momentum equation. Consider a small volume $\mathcal{V}$ of tubing occupying the axial region $z \in [z^* - dz/2, z^* + dz/2]$, whose boundary $\partial\mathcal{V}$ consists of the section of tube wall $\partial\Omega_i$ in $z \in [z^* - dz/2, z^* + dz/2]$, and tube cross-sections Ω^- and Ω^+ at either end. Integrating the momentum equation (4.8a) over this volume,

$$\int_{\mathcal{V}} \mathcal{R}\left(\frac{\partial w_i}{\partial t} + u_i\frac{\partial w_i}{\partial x} + v_i\frac{\partial w_i}{\partial y} + w_i\frac{\partial w_i}{\partial z}\right) dV = \int_{\mathcal{V}} \frac{\partial^2 w_i}{\partial x^2} + \frac{\partial^2 w_i}{\partial y^2} - \frac{\partial p_i}{\partial z}\, dV, \tag{4.16}$$

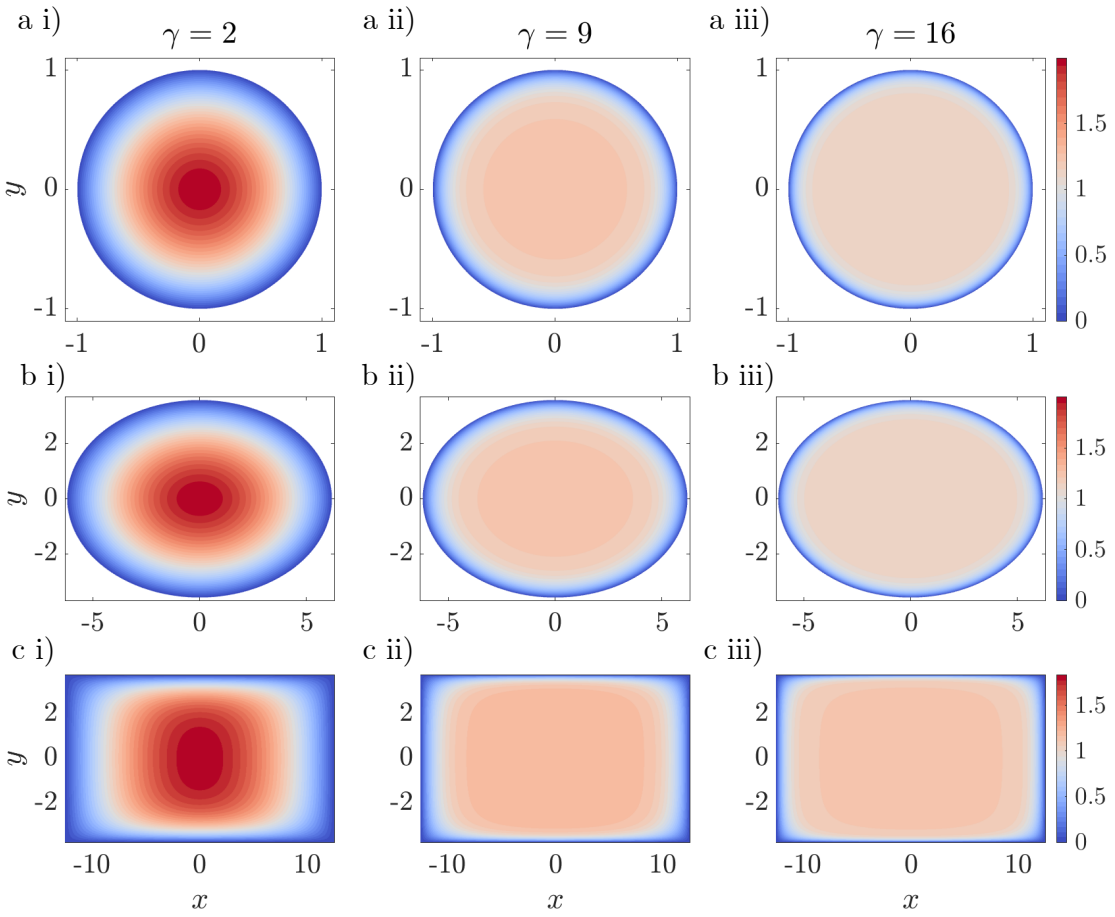

Figure 4.1: Prescribed velocity profiles in a) resistor tubing (equation (4.10)), b) a valve midpoint, at time $\tau/8$ after starting to close (equation (4.11)), and c) a channel (equation (4.13)), for the powers i) $\gamma = 2$, ii) $\gamma = 9$, and iii) $\gamma = 16$ used for results in §4.7. Dimensionless parameters are in Table 2.2.

and taking the limit as $dz \to 0$, we obtain the cross-sectionally averaged system, as follows. First, applying Reynolds transport theorem to the linear inertia term in (4.16) gives

$$\int_{\mathcal{V}} \frac{\partial w_i}{\partial t}\, dV = \frac{\partial}{\partial t} \int_{\mathcal{V}} w_i\, dV - \int_{\partial \mathcal{V}} w_i\, \boldsymbol{U}_i \cdot \boldsymbol{n}_i\, dS, \tag{4.17}$$

where $\boldsymbol{U}_i$ is the velocity of the boundary (equation (2.25)), and $\boldsymbol{n}_i$ is the outward-pointing unit normal to the boundary. Since $w_i = 0$ on the walls, and the rest of

the boundary $\partial\mathcal{V}$ has zero normal velocity, the integral around $\partial\mathcal{V}$ is zero, so that

$$\int_{\mathcal{V}} \frac{\partial w_i}{\partial t}\, dV = \frac{\partial}{\partial t}\int_{\mathcal{V}} w_i\, dV = \frac{\partial q_i}{\partial t}(z^*, t)\, dz + \mathrm{o}(dz). \tag{4.18}$$

Application of the divergence theorem to the non-linear inertia term in (4.16) yields

$$\int_{\mathcal{V}} u_i\frac{\partial w_i}{\partial x} + v_i\frac{\partial w_i}{\partial y} + w_i\frac{\partial w_i}{\partial z}\, dV = \int_{\partial\mathcal{V}} w_i \boldsymbol{u}_i \cdot \boldsymbol{n}_i\, dS. \tag{4.19}$$

As $w_i = 0$ on the walls, and the outward normals of $\Omega^{\pm}$ are $\pm\boldsymbol{e}_z$, we find

$$\int_{\mathcal{V}} u_i\frac{\partial w_i}{\partial x} + v_i\frac{\partial w_i}{\partial y} + w_i\frac{\partial w_i}{\partial z}\, dV = \int_{\Omega^+} w_i^2\, dS - \int_{\Omega^-} w_i^2\, dS. \tag{4.20}$$

Using the prescribed velocity profile $s(x, y, z, t)$, with the axial velocity rewritten as $w_i = q_i s/A_i$ (equation (4.1)), and the momentum-flux correction coefficient given in equation (4.2) and restated here,

$$\alpha = \frac{1}{A_i}\int_{\Omega} s^2 dx dy, \tag{4.21}$$

the non-linear inertia term (4.20) is rewritten as

$$\int_{\mathcal{V}} u_i\frac{\partial w_i}{\partial x} + v_i\frac{\partial w_i}{\partial y} + w_i\frac{\partial w_i}{\partial z}\, dV = dz\left[\frac{\alpha q_i^2}{A_i}\right]_{z^*-dz/2}^{z^*+dz/2}. \tag{4.22}$$

We compute the momentum-flux correction coefficient for ellipses using the velocity profile (4.11) in (4.21) to be

$$\alpha = \frac{\gamma+2}{\gamma+1}, \tag{4.23}$$

while in the channels, α is computed numerically using the velocity profile (4.13) in (4.21). We see from Figure 4.2 a) that α in the channels has the same qualitative dependence on γ as α in the tubing or valves.

Applying the divergence theorem to the viscous term in (4.16) gives

$$\int_{\mathcal{V}} \frac{\partial^2 w_i}{\partial x^2} + \frac{\partial^2 w_i}{\partial y^2}\, dV = \int_{\partial\mathcal{V}} \left(\frac{\partial w}{\partial x}, \frac{\partial w}{\partial y}, 0\right) \cdot \boldsymbol{n}_i\, dS. \tag{4.24}$$

The right-hand side is zero on the end cross-sections $\Omega^{\pm}$, and on the walls we use $w_i = q_i s/A_i$ to obtain

$$\int_{\mathcal{V}} \frac{\partial^2 w_i}{\partial x^2} + \frac{\partial^2 w_i}{\partial y^2}\, dV = -\mathcal{K}_i \frac{q_i}{A_i}\bigg|_{z=z^*} dz + \mathrm{o}(dz^2). \tag{4.25}$$

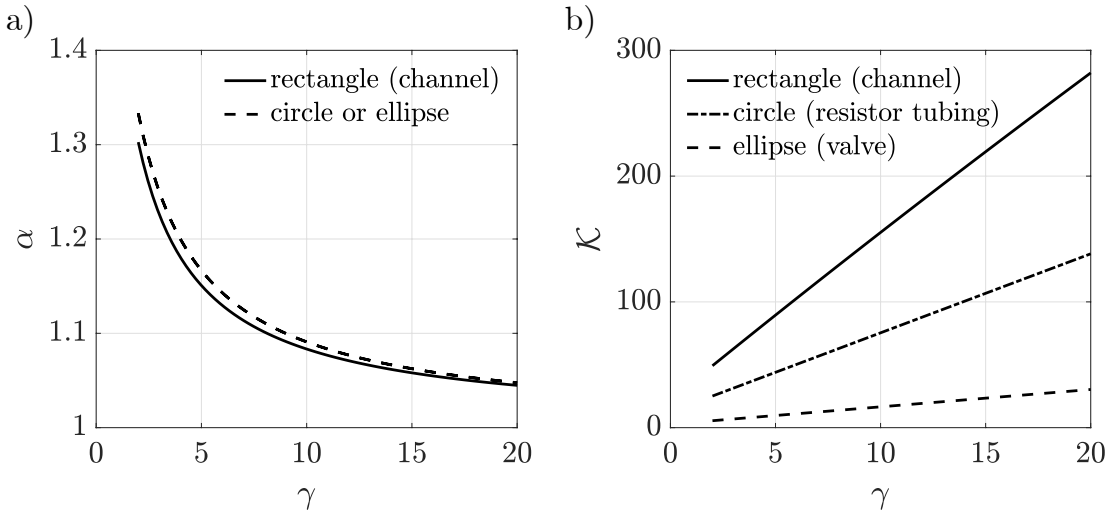

Figure 4.2: a) The momentum-flux coefficient α and b) friction coefficient $\mathcal{K}$ plotted against the power law exponent γ. Three cross-sectional shapes are considered: a channel, with rectangular cross-section (solid line); resistor tubing, with circular cross-section (dashed lined); and a closing valve, with elliptical cross-section at time $\tau/8$ after the valve starts to close (dashed line in a), dash-dot in b)). Dimensionless parameters are in Table 2.2.

Here, the friction coefficient is given in equation (4.3) and restated here,

$$\mathcal{K}_i(z,t) = -\int_{\partial\Omega_i(z,t)} \nabla s \cdot \boldsymbol{n}_i^{\perp}\, d\xi, \tag{4.26}$$

where, as in equation (4.3), ξ is the arclength coordinate and $\boldsymbol{n}_i^{\perp} = \boldsymbol{n}_i - (\boldsymbol{n}_i \cdot \boldsymbol{e}_z)\boldsymbol{e}_z$ is the cross-sectional projection of the outward-pointing unit normal to the wall. Using the velocity profile (4.11) in (4.26), we compute the friction coefficient in tubes with elliptical cross-sections with semi-minor and semi-major axes a_i and b_i to be given by

$$\mathcal{K}_i = \frac{(\gamma+2)\pi(a_i^2+b_i^2)}{a_i b_i}. \tag{4.27}$$

The friction coefficient in the channels, which have rectangular cross-section, are computed numerically using the velocity profile (4.13) in (4.26). Figure 4.2 b) plots the friction coefficient $\mathcal{K}$ as a function of the power law exponent γ in the channels, resistor tubing, and in a valve that is closing, at a time $\tau/8$ after it has

started closing. We see that in the channels the friction coefficient is also linear in γ.

Finally, again using the divergence theorem, the pressure term in (4.16) is

$$\int_{\partial\mathcal{V}} \frac{\partial p_i}{\partial z}\, dV = \int_{\partial\mathcal{V}} p_i \boldsymbol{e}_z \cdot \boldsymbol{n}_i\, dS. \tag{4.28}$$

Using $\int_{\partial\mathcal{V}} \boldsymbol{e}_z \cdot \boldsymbol{n}_i\, dS = 0$ to rewrite the integral over the walls in equation (4.28) as integrals over the end sections $\Omega^{\pm}$ yields

$$\int_{\partial\mathcal{V}} \frac{\partial p_i}{\partial z}\, dV = [A_i(z)(p_i(z) - p_i(z^*))]_{z^*-dz/2}^{z^*+dz/2} + \mathrm{o(dz)}. \tag{4.29}$$

Substituting the terms (4.18), (4.22), (4.25) and (4.29) back into the axial momentum equation (4.16), dividing through by dz and letting $dz \to 0$, we arrive at the following equation relating flux, pressure, and area:

$$\mathcal{R}\frac{\partial q_i}{\partial t} + \mathcal{R}\frac{\partial}{\partial z}\left(\frac{\alpha q_i^2}{A_i}\right) + \frac{\mathcal{K}_i}{A_i} q_i + A_i \frac{\partial p_i}{\partial z} = 0. \tag{4.30}$$

To close the system formed by equations (4.8b), (4.15), and (4.30), we apply the leading-order stress conditions in (2.26), specifying inlet and outlet pressures as

$$p_u(0,t) = p_u^{in}(t), \quad p_u(1,t) = 0, \quad p_\ell(0,t) = p_\ell^{in}(t), \quad p_\ell(1,t) = 0. \tag{4.31}$$

The initial condition for the flux is

$$q_i(z,0) = q_{ib}(z). \tag{4.32}$$

In simulations we choose to start with zero inlet pressures and zero valve movement, and zero flux in the bioreactor. This mean we have a numerically-convenient gradual start-up of flow, stepping in time towards the inlet conditions imposed by the gravitational pressure head of the inlet reservoirs. Specifically, we take the upper inlet pressure to be

$$p_u^{in}(t) = \begin{cases} p_{max}^{in}\left(\dfrac{1-\cos \pi t}{2}\right) & \text{for} \quad 0 \le t < 1 \\ p_{max}^{in} & \text{for} \quad t \ge 1 \end{cases}, \tag{4.33}$$

and the lower inlet pressure to be $p_\ell^{in} = p_u^{in}/2$, where $p_{max}^{in} = U_g/U = \epsilon^2 \rho g h_u^* T/\mu$ is the dimensionless pressure head provided by the height of the upper inlet reservoir. We use the initial condition

$$q_{ib} = 0, \tag{4.34}$$

in simulations, because the initial boundary pressures (4.33) are zero and there is zero initial valve movement. In physical experiments, the inlet pressure p_u^{in} is always at p_{max}^{in}, therefore when presenting results in §4.7 we will only start moving valves and investigating flow behaviour when a steady state has been reached, after $t = 1$ when $p_u^{in} = p_{in}^{max}$. As mentioned in §4.2, valve area is prescribed via equation (2.5) with the valve closure functions (A.3) and (A.4) prescribing the time-dependency of valve area.

In summary, as in Chapter 3 we solve for the fluxes q_i and pressures p_i in each region of the upper and lower tubing systems (black lines in Figure 4.3). To do so, we solve the integrated mass equation given by (4.8b) and (4.15), together with the integrated momentum equation (4.30), subject to initial fluxes (4.32), and prescribed inlet and outlet pressures (4.31) (dark grey nodes in Figure 4.3). We additionally impose continuity of flux and pressure at the junctions (light grey nodes in Figure 4.3), where there can be jump discontinuities in cross-sectional area and thus the long wave-length approximation breaks down and the flow is 3D at leading-order. The flux condition at junctions is systematically derived from the integrated mass equation (4.8b). The pressure condition at junctions is an *ad hoc* condition, chosen for its simplicity and its wide use in the vascular modelling literature, where comparison with 3D numerical simulations suggest that pressure drops at junctions do not significantly contribute to mean pressure drops across a system (see e.g. discussion in [130]). In our system, the junctions are all located far from the scaffold region, which is the region whose flow dynamics we are most interested in, and we therefore expect this *ad hoc* condition to have relatively little impact on the flow in the scaffold.

4.5.1 Resistor tubing, valve tubing and enclosed channels

In the following three sections we simplify the governing equations, integrating PDEs to obtain ODEs where possible. The regions of the bioreactor are shown

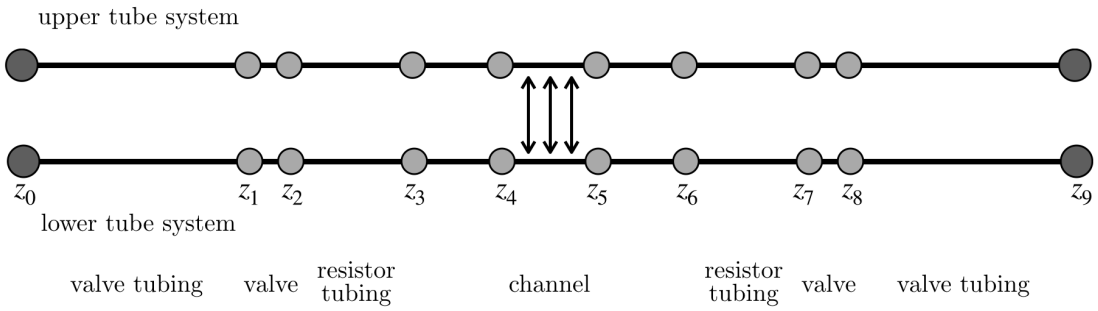

Figure 4.3: Network diagram of the bioreactor system, showing axial coordinates. At the edges we solve (4.8b) and (4.15), together with (4.30). The edges are joined by continuity of pressure and flux (light grey nodes), and pressure (4.31) is prescribed at the inlets and outlets (dark grey nodes). The upper and lower tube systems are coupled due to the scaffold in (z_4, z_5), see equations (4.8b), (4.15).

in simplified form in Figure 4.3. In the resistor tubing, valve tubing and enclosed channels (the regions of channel that do not adjoin the scaffold), there is no wall movement or flux into the scaffold, so that A_i is constant and $J_i = 0$. From the integrated mass equation (4.8b), the flux through each of these regions therefore has no z-dependence, so that the non-linear term in the integrated momentum equation (4.30) is zero. We denote the flux in $z \in (z_k, z_{k+1})$ by q_{ik} for $k = 0, 2, 3, 5, 6, 8$, and the pressure at $z = z_k$ by p_{ik}. Integrating (4.30) over the length of each region of resistor tubing, valve tubing, and enclosed channel, we obtain the expression

$$\mathcal{R}\frac{dq_{ik}}{dt} + \frac{\mathcal{K}_{ik}}{A_{ik}}q_{ik} + \frac{A_{ik}[p_i]_k}{[z]_k} = 0, \tag{4.35}$$

for $k = 0, 2, 3, 5, 6, 8$ and $i = u, \ell$. Here $[\phi]_k = \phi(z_{k+1}) - \phi(z_k)$ is the change in ϕ across the length of the region, and we have defined A_{ik} and $\mathcal{K}_{ik}$ to be the cross-sectional area and friction coefficient in $z \in (z_k, z_{k+1})$; these are both taken to be independent of z as the cross-section has no axial dependence.

4.5.2 Valves

In the valves, we use the integrated mass equation relationship (4.8b) to write the flux as the sum of the flux at the left-most valve boundary, and a correction to

account for valve movement:

$$q_i(z,t) = q_{ik}(t) - \tilde{A}_{ik}(z,t), \tag{4.36}$$

where

$$\tilde{A}_{ik}(z,t) = \int_{z_{k+1}}^{z} \frac{\partial A_i}{\partial t}\, dz, \tag{4.37}$$

for $z \in (z_{k+1}, z_{k+2})$, and $k = 0, 6$. Then the integrated momentum equation (4.30) can be written as an equation for the flux q_{ik} at the left-most valve boundary and the pressure p_i in the valve,

$$\mathcal{R}\frac{dq_{ik}}{dt} + F_{ik}q_{ik} + G_i(q_{ik})^2 + H_{ik} + A_i\frac{\partial p_i}{\partial z} = 0, \tag{4.38}$$

where

$$F_{ik}(z,t) = -2\alpha\mathcal{R}\frac{\partial}{\partial z}\left(\frac{\tilde{A}_{ik}}{A_i}\right) + \frac{\mathcal{K}_i}{A_i}, \tag{4.39a}$$

$$G_{ik}(z,t) = \alpha\mathcal{R}\frac{\partial}{\partial z}\left(\frac{1}{A_i}\right), \tag{4.39b}$$

$$H_{ik}(z,t) = -\mathcal{R}\frac{\partial \tilde{A}_i}{\partial t} + \alpha\mathcal{R}\frac{\partial}{\partial z}\left(\frac{\tilde{A}_{ik}^2}{A_i}\right) - \frac{\mathcal{K}_i\tilde{A}_{ik}}{A_i} \tag{4.39c}$$

are all prescribed through the specification of valve area and velocity profile. Integrating (4.38) over the length of each valve gives

$$\overline{1}_{ik}\mathcal{R}\frac{dq_{ik}}{dt} + \overline{F}_{ik}q_{ik} + \overline{G}_{ik}(q_{ik})^2 + \overline{H}_{ik} + [p_i]_{k+1} = 0, \tag{4.40}$$

for $k = 0, 6$, where

$$\bar{\phi}_{ik}(t) = \int_{z_{k+1}}^{z_{k+2}} \frac{\phi_{ik}}{A_i} dz \tag{4.41}$$

for $\phi \in \{1, F, G, H\}$.

4.5.3 Regions of channel adjoining the scaffold

Adding and subtracting the integrated mass equation (4.8b) for $i = u, \ell$, gives

$$\frac{\partial q_-}{\partial z} = -\frac{4c\mathcal{B}}{h_s}p_-, \qquad\qquad \frac{\partial q_+}{\partial z} = 0, \tag{4.42a, 4.42b}$$

where $q_\pm = q_u \pm q_\ell$ and $p_\pm = p_u \pm p_\ell$. From (4.42b) we see that $q_+(z,t) = q_+(t)$ is just a function of time. We also add and subtract the integrated momentum equations (4.30) in the two channels. Since the cross-sectional area A_i and friction coefficient $\mathcal{K}_i$ are constant in the upper and lower channels (thus denoted here as A and $\mathcal{K}$), this yields

$$\frac{\partial q_-}{\partial t} + \frac{\alpha}{A} q_+ \frac{\partial q_-}{\partial z} + \frac{\mathcal{K}}{A\mathcal{R}} q_- - \frac{h_s A}{4c\mathcal{B}\mathcal{R}} \frac{\partial^2 q_-}{\partial z^2} = 0, \tag{4.43}$$

$$\frac{dq_+}{dt} + \frac{\alpha}{A} \frac{\partial}{\partial z} \left(\frac{q_-^2}{2} \right) + \frac{\mathcal{K}}{A\mathcal{R}} q_+ + \frac{A}{\mathcal{R}} \frac{\partial p_+}{\partial z} = 0. \tag{4.44}$$

Equation (4.43) is a parabolic PDE whose hyperbolic term increases with the total flux q_+ through the upper and lower channels. Since $q_+ = q_+(t)$ we can integrate (4.44) across the channel length $z \in (z_4, z_5)$ to obtain

$$\frac{dq_+}{dt} + \frac{\alpha [q_-^2]_4}{2A[z]_4} + \frac{\mathcal{K}}{A\mathcal{R}} q_+ + \frac{A[p_+]_4}{\mathcal{R}[z]_4} = 0, \tag{4.45}$$

where we recall that $[\phi]_k$ denotes $\phi(z_{k+1}) - \phi(z_k)$.

4.5.4 Continuity and boundary conditions

Continuity of flux at the valve left-hand boundaries is

$$q_{i0} = q_{i1} \quad \text{and} \quad q_{i8} = q_{i9}. \tag{4.46}$$

Continuity of flux at the valve right-hand boundaries is

$$q_{i1} - \tilde{A}_{i0}(z_2) = q_{i2} \quad \text{and} \quad q_{i7} - \tilde{A}_{i6}(z_8) = q_{i8}, \quad i = u, \ell. \tag{4.47}$$

Continuity of flux between resistor tubing and channels is

$$q_{i2} = q_{i3} \quad \text{and} \quad q_{i5} = q_{i6}. \tag{4.48}$$

Continuity of flux between sections of channel that do not adjoin the scaffold and sections that do, is

$$q_{i3} = q_{i4} \quad \text{and} \quad q_{i5} = q_{i6}. \tag{4.49}$$

Continuity of flux at the channel entrances and exits are

$$q_{u3} = \frac{q_+(z_4) + q_-(z_4)}{2}, \quad q_{\ell 3} = \frac{q_+(z_4) - q_-(z_4)}{2}, \tag{4.50a}$$

$$q_{u6} = \frac{q_+(z_5) + q_-(z_5)}{2}, \quad q_{\ell 6} = \frac{q_+(z_5) - q_-(z_5)}{2}. \tag{4.50b}$$

Continuity of pressure at the channel entrances and exits are

$$p_{u4} = \frac{p_+(z_4) + p_-(z_4)}{2}, \quad p_{\ell 4} = \frac{p_+(z_4) - p_-(z_4)}{2}, \tag{4.51a}$$

$$p_{u5} = \frac{p_+(z_5) + p_-(z_5)}{2}, \quad p_{\ell 5} = \frac{p_+(z_5) - p_-(z_5)}{2}, \tag{4.51b}$$

where $p_{ik} = p_i(z_k)$. Boundary pressures (4.31) are applied via prescribed functions

$$p_{\ell 0} = p_u^{in}(t), \quad p_{\ell 0} = h_\ell p_\ell^{in}(t), \quad p_{\ell 9} = 0 = p_{u9}. \tag{4.52}$$

4.5.5 Summary

To compute the fluxes and pressures in the bioreactor, in the valve tubing, in the resistor tubing, and in the enclosed channels, we solve for the fluxes $q_{ik}(t)$ and the nodal pressures $p_{ik}(t)$ ($i = u, \ell$ and $k = 0, ..., 9$). In the channels that adjoin the scaffold we solve for fluxes $q_+(t)$ and $q_-(z,t)$, pressures $p_-(z,t)$ and nodal pressures $p_+(z_4,t)$ and $p_+(z_5,t)$. In total these are 43 time-dependent unknowns and two space and time-dependent unknowns.

The system consists of the ODEs (4.35) for $k = 0, 2, 3, 5, 6, 8$ and $i = u, \ell$ in the valve tubing, resistor tubing, and enclosed channels, the ODEs (4.40) for $k = 0, 6$ and $i = u, \ell$ in the valves, the PDEs (4.42a) and (4.43), and ODE (4.45) in the regions of channel adjoining the scaffold, subject to the continuity conditions $(4.46) - (4.51)$, boundary pressures (4.52), and initial condition (4.32). This gives a total of 45 ODEs, boundary conditions, and continuity conditions, 43 of which determine the time-dependent unknowns. The remaining two of these equations act as boundary conditions for the PDE (4.43) for $q_-(z,t)$. Once q_- is known, p_- can be directly calculated using the PDE (4.42a).

4.6 Numerical solution

We use the method of lines to solve equation (4.43) for q_- by spatially discretising the channel into N segments with nodes labelled by $j = 1, ..., N$, and step-sizes $\Delta z = (z_5 - z_4)/(N-1)$. We let q_-^j denote the approximation to q_- evaluated at the j^{th} node, and use central differences for the second-order spatial derivative. To discretise the hyperbolic term in equation (4.43), we choose a well-established semi-discrete second-order central scheme proposed by Kurganov and Tadmor [90] using a five-points stencil for nodes $j = 3, ..., N-2$, that is easily implemented in MATLAB using the method of lines, and has small numerical dissipation relative to other central schemes (we also trialed simpler schemes such as upwinding but these did not reach convergence within the tolerances). At nodes $j = 1, 2$ and $j = N-1, N$ we use third order forwards and backward differences, respectively, to compute the first spatial derivative of q_-. Equation (4.43) is thus discretised for $j = 2, ..., N-1$ as

$$\frac{dq_-^j}{dt} + \frac{\alpha}{A}\left(q_+\frac{\partial q_-}{\partial z}\right)^j + \frac{\mathcal{K}_i}{A\mathcal{R}}q_-^j - \frac{h_s A}{4c\mathcal{B}\mathcal{R}}\left(\frac{q_-^{j+1} - 2q_-^j + q_-^{j-1}}{(\Delta z)^2}\right) = 0. \tag{4.53}$$

The hyperbolic terms are discretised for $j = 2$ as

$$\left(q_+\frac{\partial q_-}{\partial z}\right)^j = q_+\left(\frac{4q_-^3 - 3q_-^2 - q_-^4}{\Delta z}\right), \tag{4.54}$$

for $j = N-1$ as

$$\left(q_+\frac{\partial q_-}{\partial z}\right)^j = q_+\left(\frac{3q_-^{N-1} - 4q_-^{N-2} + q_-^{N-3}}{\Delta z}\right), \tag{4.55}$$

and for $j = 3, ..., N-2$ as

$$\left(q_+\frac{\partial q_-}{\partial z}\right)^j = \frac{\mathcal{H}^{j+1/2} - \mathcal{H}^{j-1/2}}{\Delta z}. \tag{4.56}$$

Here the midpoint numerical fluxes $\mathcal{H}^{j+1/2}$ are

$$\mathcal{H}^{j+1/2} = \frac{1}{2}\left(q_+\left(q_p^{j+1/2} + q_m^{j+1/2}\right) - |q_+|\left(q_p^{j+1/2} - q_m^{j+1/2}\right)\right), \tag{4.57}$$

the intermediate values of q_-^j are

$$q_p^{j+1/2} = q_-^{j+1} - \frac{dz}{2}(q'_-)^{j+1} \quad \text{and} \quad q_m^{j+1/2} = q_-^j + \frac{dz}{2}(q'_-)^j, \tag{4.58}$$

and the approximate derivative $(q'_-)^j$ is

$$(q'_-)^j = \text{minmod}\left(\theta\frac{q_-^j - q_-^{j-1}}{\Delta z}, \frac{q_-^{j+1} - q_-^{j-1}}{2\Delta z}, \theta\frac{q_-^j - q_-^{j-1}}{\Delta z}\right). \tag{4.59}$$

In (4.59), the minmod limiter operator is defined as

$$\text{minmod}(a,b,c) = \begin{cases} \max(a,b,c) & \text{if} \quad a,b,c > 0, \\ \min(a,b,c), & \text{if} \quad a,b,c < 0, \\ 0 & \text{otherwise,} \end{cases} \tag{4.60}$$

and $\theta \in [1,2]$ is the minmod limiter coefficient, which we set to be 2, as in the literature. The minmod limiter aims to reduce spurious oscillation in the numerical solution. It does this by approximating the derivative at node j to be the shallowest of the three minmod arguments, if they have the same sign. Otherwise, if the three arguments have different sign then the derivative at node j is approximated to be zero.

We rewrite p_-^1 and p_-^N in terms of fluxes q_- using (4.42a):

$$p_-^1 = -\frac{h_s}{4c\mathcal{B}}\left(\frac{4q_-^2 - 3q_-^1 - q_-^3}{\Delta z}\right), \tag{4.61a}$$

$$p_-^N = -\frac{h_s}{4c\mathcal{B}}\left(\frac{3q_-^N - 4q_-^{N-1} + q_-^{N-2}}{\Delta z}\right). \tag{4.61b}$$

Using (4.61b), discretised continuity of pressure conditions (4.51) at the channel entrances and exits are therefore

$$p_{u4} = \frac{1}{2}\left(p_+^1 - \frac{h_s}{4c\mathcal{B}}\left(\frac{4q_-^2 - 3q_-^1 - q_-^3}{\Delta z}\right)\right), \tag{4.62a}$$

$$p_{\ell 4} = \frac{1}{2}\left(p_+^1 + \frac{h_s}{4c\mathcal{B}}\left(\frac{4q_-^2 - 3q_-^1 - q_-^3}{\Delta z}\right)\right), \tag{4.62b}$$

$$p_{u5} = \frac{1}{2}\left(p_+^N - \frac{h_s}{4c\mathcal{B}}\left(\frac{3q_-^N - 4q_-^{N-1} + q_-^{N-2}}{\Delta z}\right)\right), \tag{4.62c}$$

$$p_{\ell 5} = \frac{1}{2}\left(p_+^N + \frac{h_s}{4c\mathcal{B}}\left(\frac{3q_-^N - 4q_-^{N-1} + q_-^{N-2}}{\Delta z}\right)\right). \tag{4.62d}$$

Discretised continuity of flux conditions (4.50) at the channel entrances and exits are

$$q_{u3} = \frac{q_+ + q_-^1}{2}, \quad q_{\ell 3} = \frac{q_+ - q_-^1}{2}, \quad q_{u6} = \frac{q_+ + q_-^N}{2}, \quad q_{\ell 6} = \frac{q_+ - q_-^N}{2}. \tag{4.63}$$

To further simplify the system, we rewrite the equations in the resistor tubing, valve tubing, valve and enclosed channel regions, in terms of p_{i4}, p_{i5} $(i = u, \ell)$ and the channel variables. To do so, the following equations are combined to eliminate $p_{i0}, p_{i1}, p_{i2}, p_{i3}, q_{i0}, q_{i2}, q_{i3}$ from the system: tubing equation (4.35) for $k = 0, 2, 3$; valve equation (4.40) for $k = 0$; boundary pressures (4.52); and continuity of flux between resistor tubing and channels (4.48), between valve and resistor tubing (4.47), and at channel entrances and exits (4.63). To eliminate $p_{i6}, p_{i7}, p_{i8}, p_{i9}, q_{i5}, q_{i6}, q_{i8}$ from the system, we combine tubing equation (4.35) for $k = 5, 6, 8$; valve equation (4.40) for $k = 6$; continuity of flux between resistor tubing and channels (4.48), between valve and resistor tubing (4.47), and at channel entrances and exits (4.63); and boundary pressures (4.52).

Thus we are left with four ODEs for p_{i4}, p_{i5} $(i = \ell, u)$:

$$\begin{aligned}\frac{dp_{i4}}{dt} = &\left(\overline{1}_{i0} + \mathcal{R}\left(\frac{[z]_0}{A_{i0}} + \frac{[z]_2}{A_{i2}} + \frac{[z]_3}{A_{i3}}\right)\right)^{-1} \left\{\mathcal{R}\left(\frac{[z]_2}{A_{i2}} + \frac{[z]_3}{A_{i3}}\right)\frac{d\tilde{A}_{i0}}{dt} + p_i^{in}(t)\right. \\ &\left. - \left(\left(\overline{F}_{i0} + \frac{\mathcal{K}[z]_0}{A_{i0}^2}\right)q_{u0} + \overline{G}_{i0}q_{u0}^2 + \overline{H}_{i0} + p_{u4} + \left(\frac{\mathcal{K}_{i2}[z]_2}{A_{i2}^2} + \frac{\mathcal{K}_{i3}[z]_3}{A_{i3}^2}\right)q_{i3}\right)\right\}\end{aligned} \tag{4.64}$$

and

$$\begin{aligned}\frac{dp_{i5}}{dt} = &\left(\overline{1}_{i6} + \mathcal{R}\left(\frac{[z]_5}{A_{i5}} + \frac{[z]_6}{A_{i6}} + \frac{[z]_8}{A_{i8}}\right)\right)^{-1} \left\{\frac{\mathcal{R}[z]_8}{A_{i8}}\frac{d\tilde{A}_{i6}}{dt} - p_i^{out}(t)\right. \\ &\left. - \left(\left(\overline{F}_{i6} + \frac{\mathcal{K}_{i5}[z]_5}{A_{i5}} + \frac{\mathcal{K}_{i6}[z]_6}{A_{i6}}\right)q_{i6} + \overline{G}_{i6}q_{i6}^2 + \overline{H}_{i6} - p_{i5} + \frac{\mathcal{K}_{i8}[z]_8}{A_{i8}^2}q_{i8}\right)\right\},\end{aligned} \tag{4.65}$$

in addition to the $N-2$ ODEs (4.53) for q_-^j $(j = 2, ..., N-1)$, one ODE (4.45) for q_+, and four continuity of pressure conditions (4.62) relating $p_+^1, p_+^N, q_-^1, q_-^N$ at channel entrances and exits. This gives a total of $N + 7$ equations to solve for $N + 7$ variables at each timestep, subject to the initial condition (4.32).

To quality-control the code, we construct the numerical scheme in MATLAB piece by piece, first solving the channel equations (4.53) and (4.45) subject to prescribed pressure boundary conditions, and checking results agree with known solutions, before introducing the more complex boundary conditions given by the ODEs (4.64) and (4.65), and continuity equations (4.62).

4.6.1 Validation

As specified by the inlet pressures (4.33), in the initial part of a simulation there is a gradual start-up of flow, before valves start moving. Since the start-up period is not of interest, from here onwards we translate time forward by one unit, so that $t = 0$ is when the upper inlet pressure has reached the constant, positive value p^{in}_{max} and a steady state has been reached, after which the valves first start moving.

We check convergence at the extremes of our valve period ranges, corresponding to valve periods $\tau = 2.6 \times 10^{-3}$ s and $\tau = 1$ s, and at the intermediate period $\tau = 0.04$ s. Additionally, we check convergence for extremes of velocity profile powers $\gamma = 2$ for Poiseuille flow, and $\gamma = 60$ for plug-like flow. The exact solution for each set of (τ, γ) is approximated by $(\tilde{q}_u, \tilde{q}_\ell, \tilde{q}_s)$, which we calculate using a large number of spatial gridpoints, and low absolute and relative tolerances in the time integration. We measure the solution error as the maximum of the L^∞ error in q_u, q_ℓ, and q_s at a fixed time t_1, over the length of the scaffold region:

$$\mathcal{E}_1 = \max_{\substack{z\in(z_4,z_5)\\ \phi\in\{q_u,q_\ell,q_s\}}} \left|\phi(z,t_1) - \tilde{\phi}(z,t_1)\right|. \tag{4.66}$$

Figure 4.4 plots the error $\mathcal{E}_1$ with $t_1 = 3\tau/4$ as we vary the number of spatial steps N, the relative tolerance in the time integration, and the absolute tolerance in the time integration. All valves are initially open in $t < 0$, and at $t = 0$ the upper inlet valve closes by 95% and reopens over the valve period τ, according to equation (2.5). We find that with this valve configuration, the maximum error given by equation (4.66) comes from the upper channel flow q_u, which may be because the upper channel contains the moving valve. Figure 4.4 shows that the error generally decreases as the number of axial steps is increased, or as the absolute or relative tolerances decrease. The log-log convergence plots varying axial steps

have slope of approximately -1.5, which agrees with the L^∞ convergence rates found by Kurganov and Tadmor [90].

We also validate the numerical scheme by comparing results to the quasi-steady model of Chapter 3. In the regime where the valves are moving slowly, with a Poiseuille profile $\gamma = 2$, the reduced Reynolds number $\mathcal{R}$ in equation (4.30) is small, thus inertial terms become negligible and the model in §4.5 should agree with the quasi-steady model. We quantify solutions by computing the fluxes

$$q_{u,\ell}^m = q_{u,\ell}\left(\frac{1}{2}, t\right) \quad \text{and} \quad q_s(t) = -2b_s \int_{z_4}^{z_5} v_s(z,t)\, dz \tag{4.67}$$

through the upper and lower channels at their axial midpoints, and the vertical flux through the scaffold, respectively. Labelling the fluxes from the quasi-steady model with tildes $(\tilde{q}_u^m, \tilde{q}_\ell^m, \tilde{q}_s)$, we report the maximum relative difference between the model with inertia and the quasi-steady model (this yields a reasonable measure of error as the fluxes do not become too small for this range of valve periods),

$$\mathcal{E}_2 = \max_t \left(\frac{|q_u^m - \tilde{q}_u^m|}{\tilde{q}_u^m}, \frac{|q_\ell^m - \tilde{q}_\ell^m|}{\tilde{q}_\ell^m}, \frac{|q_s - \tilde{q}_s|}{\tilde{q}_s} \right). \tag{4.68}$$

In Figure 4.5 we simulate the valve dynamics where the upper inlet valve closes and opens, and the other three valves are open, and use an absolute tolerance of 10^{-5} and a relative tolerance of 10^{-11}. Figure 4.5 shows a decrease in $\mathcal{E}_2$ from 38% to 0.25% as the valve period τ increases from 0.25 s to 40 s, and the system enters the quasi-steady regime. In Figure 4.5 we have used $N = 512$ spatial steps; we have also checked that by increasing N we can reach smaller errors $\mathcal{E}_2$.

Using small amplitude valve oscillations with $a = \mathrm{o}(1)$, in §4.8.5 we will validate the model of §4.4 against the (systematically-derived) model of §4.8.1.

4.6.2 Pore Reynolds number

To determine the range of values for the valve period τ for which inertia in the scaffold may be neglected, and thus Darcy's law is valid, we compute the pore Reynolds number as described in §3.4. We allow pore Reynolds numbers of up to 10, because as mentioned in §2.5, although systematic derivation of Darcy's law requires small pore Reynolds numbers, experimental evidence shows that Darcy's

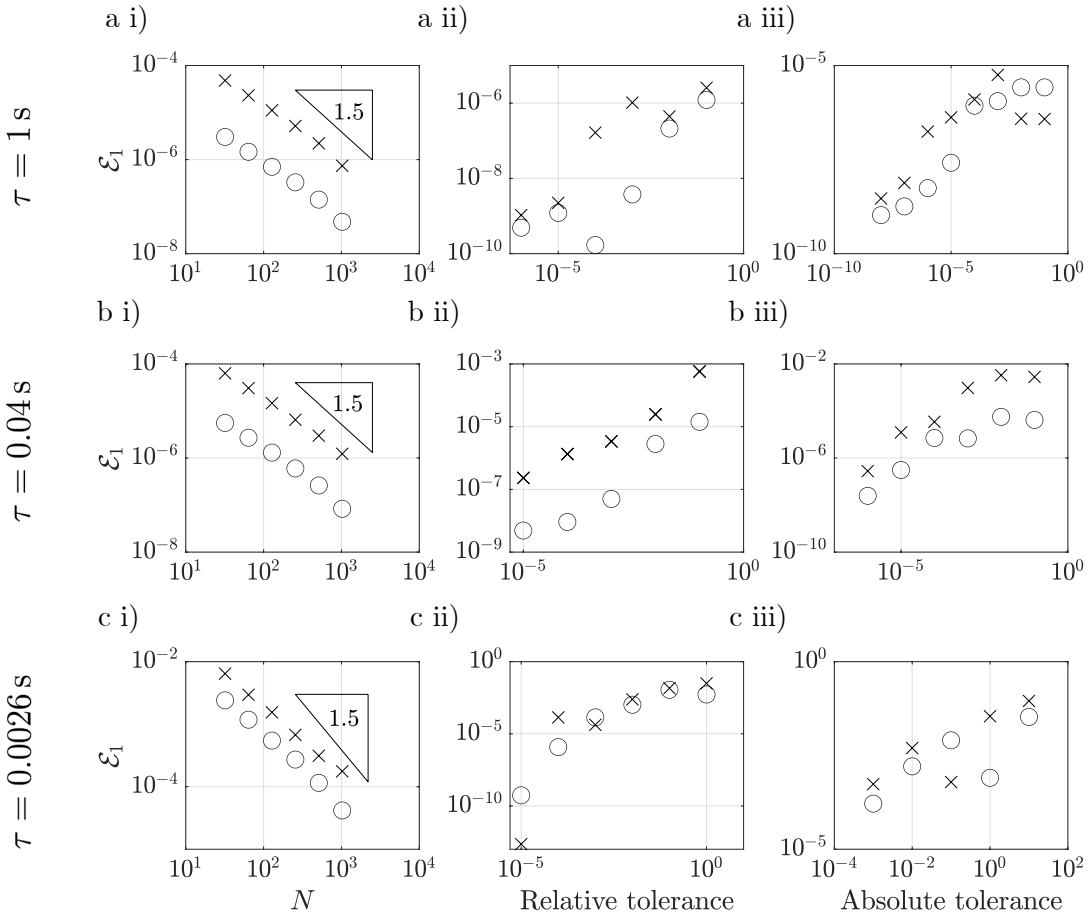

Figure 4.4: Convergence plots varying i) the number of spatial steps N, and ii) relative and iii) absolute tolerances of the time integration scheme, for valve periods a) $\tau = 1$ s, b) $\tau = 0.04$ s, and c) $\tau = 2.6 \times 10^{-3}$ s; and for Poiseuille profile $\gamma = 2$ (crosses) and plug-like profile $\gamma = 60$ (circles). The finest solutions $\tilde{q}_u, \tilde{q}_\ell, \tilde{q}_s$ have been computed using $N = 2048$, a relative tolerance of 10^{-11}, and absolute tolerances 4×10^{-9}, 2×10^{-7}, and 10^{-4} for a), b), and c) respectively. Note that as τ decreases the absolute errors $\mathcal{E}_1$ increase because the absolute value of the solutions increase.

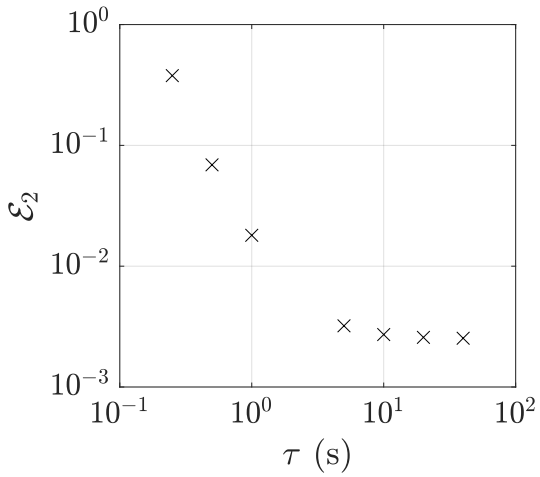

Figure 4.5: The relative difference $\mathcal{E}_2$ in fluxes between the one-dimensional model with inertia of §4.4 and the quasi-steady model of Chapter 3, while the upper inlet valve closes and opens, and the other three valves are open. Lengthscales are $b_v^* = 4.9 \times 10^{-4} = b_c^*$, $b_r^* = 10^{-4}$, and other parameters are as in Table 2.1.

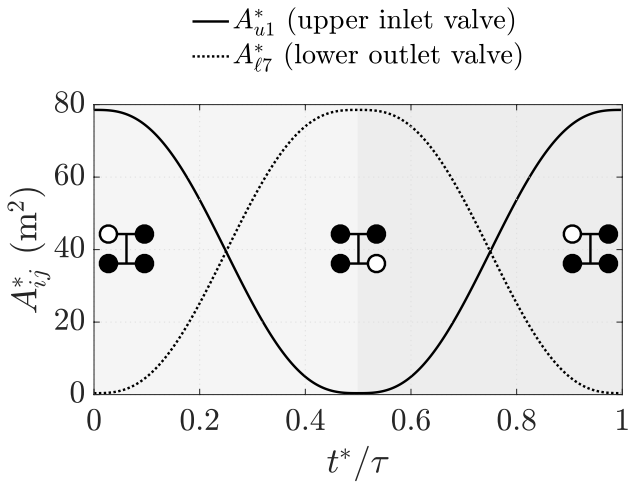

Figure 4.6: Valve cross-sectional areas when pulsing the upper inlet and lower outlet valves once, where black (white) circles on the inset diagrams indicate closed (open) valves. Light (mid) grey shading is the upper valve closing (opening) and lower valve opening (closing). The other two valves are closed. The velocity profile power is $\gamma = 9$; other parameters are as in Tables 2.2 and 4.1.

law is valid for higher pore Reynolds numbers. Additionally, using the average pore diameter as the lengthscale when computing the pore Reynolds number yields a larger pore Reynolds number than would be obtained when using the square root of permeability, thus in using the average pore diameter we are being relatively conservative.

To compute the pore Reynolds number we run simulations cycling between two valve configurations, chosen to maximise scaffold velocity. We refer to the full period of moving from one configuration to the other, and back again, as one valve pulse. Figure 4.6 depicts one pulse, with time t^* scaled by the valve period τ: at the beginning of a pulse, $t^*/\tau = 0$, the upper inlet valve is open and all other valves are closed. Then the upper inlet valve closes simultaneously with the lower outlet opening, to arrive at the configuration with the lower outlet valve open and all other valves closed, at $t^*/\tau = 0.5$. Finally, for $t^*/\tau \in (0.5, 1)$, the upper inlet reopens as the lower outlet closes, while the other two valves are still closed.

We expect the scaffold velocity, and therefore the pore Reynolds number, to increase with decreasing valve period. By computing $\mathcal{R}_p$ for various valve periods τ, we find that $\tau = 0.0026$ s has a pore Reynolds number $\mathcal{R}_p = 10$. Therefore in the following we restrict the valve period to $\tau \geq 0.0026\,\text{s}$.

4.7 Results

Here we show how valves can be used to attain shear stresses in the scaffold that are maintained within a target range for seconds or minutes. We pulse valves as shown in Figure 4.6 and described in §4.6.2. Time t^* is translated forward by T s and plotted scaled by the valve period τ throughout, so that the startup period of equation (4.33) occurs in $-T/\tau < t^*/\tau < 0$, the valves start to move at $t^*/\tau = 0$, and they complete one cycle of opening/closing at $t^*/\tau = 1$. We present results for powers $\gamma = 2, 9, 16$ in the velocity profiles specified in equations (4.11) and (4.13), where $\gamma = 2$ is Poiseuille flow, $\gamma = 16$ is a near-flat profile (with no slip at the walls), and $\gamma = 9$ is also relatively flat and has been chosen because of its use in the literature [127, 143].

Throughout this section we use the numerical scheme described in §4.6, with spatial steps $N = 512$, a relative tolerance of 10^{-7}, and an absolute tolerance

ranging between 10^{-10} and 10^{-5} (with higher absolute tolerances for smaller valve periods τ, because smaller τ give higher fluxes).

4.7.1 One pulse

First, we determine whether a single pulse can provide sustained shear stress within a target range. As mentioned in §3.5.1, the shear stress estimate (2.30) is at leading order

$$\Sigma(z,t) = \frac{8\mu\tau U_s}{\phi d}\,|v_s|\,. \tag{4.69}$$

The spatial mean of the shear stress in the scaffold is

$$\sigma = \frac{1}{l_s}\int_{z_4}^{z_5} \Sigma(z,t)\,dz. \tag{4.70}$$

As an aside, we remark that although we will work with the spatial mean of the shear stress, at each point in time the shear stress is approximately constant in space throughout the scaffold. We see this by plotting the shear stress $\Sigma(z,t)$ for $z \in (z_4, z_5)$ at each point in time (results not shown). The shear stress being spatially uniform also tells us that we expect the upper and lower channel fluxes q_ℓ and q_u to be approximately linear in z, because equations (4.42a), (4.14) and (2.24) say that the scaffold velocity v_s is linearly proportional to $\partial q_-/\partial z$, and equation (4.42b) that q_+ is constant in z. We also verify that q_u and q_ℓ are linear in z in the scaffold by plotting them in space and time.

In Figure 4.7 a) we plot σ for valve periods i) $\tau = 0.04$ s and ii) $\tau = 0.004\,\mathrm{s}$ (black line), and compare each of them to the shear stress achievable when the upper inlet valve and lower outlet valves are fully open, and the other two valves are closed (grey line). Both valve speeds result in spikes in shear stress above the equilibrium value of 0.16 Pa, resulting in time-averaged mean shear stresses of $\sigma = 0.26$ Pa for $\tau = 0.04$ s and $\sigma = 7.1$ Pa for $\tau = 0.004$ s (note that the spikes mirror the scaffold fluxes in Figure 4.7 b), discussed below). This indicates that controlling valve speed may be a good way to attain higher shear stresses.

We must also choose how many times to pulse the valves, and how long a gap to leave between pulses. To this end, we determine how long the dynamical influence of a single pulse remains, beyond the duration of the pulse itself. The relaxation time t_r is defined as the time taken after a single pulse has been completed for the

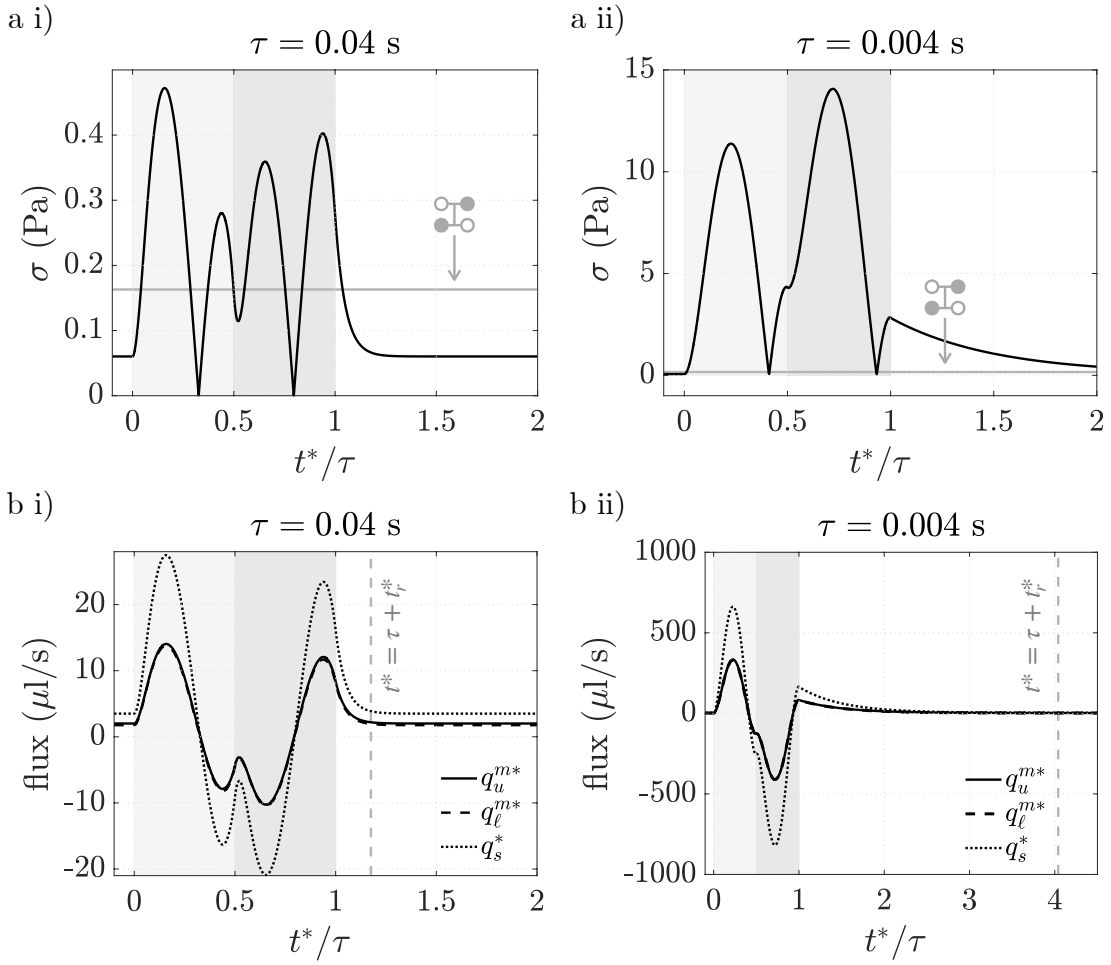

Figure 4.7: Dynamics of the bioreactor when pulsing the upper inlet and lower outlet valves once: the light (mid) grey shaded area is when the upper inlet valve is closing (opening) and the lower outlet valve is opening (closing). a) Spatial mean of the scaffold shear stress over one pulse for i) valve period $\tau = 0.04$ s and ii) $\tau = 0.004$ s, as compared to the grey line showing the mean shear stress for the static configuration depicted in grey. b) Fluxes along the midpoint of the upper and lower channels, and down the scaffold, for i) valve period $\tau = 0.04$ s and ii) $\tau = 0.004$ s. The vertical line marks when the fluxes have relaxed to within 10% of their final values. $\gamma = 9$ and other parameters are as in Tables 2.2 and 4.1.

fluxes q_u^m, q_ℓ^m halfway along the upper and lower channels, and the flux q_s down the scaffold, to return to within 10% of their equilibrium values when the upper inlet valve is open and all other valves are closed:

$$t_r = \min_t \left\{ t > \frac{\tau}{T} : \left| \frac{q(t) - q(t_f)}{q(t_f)} \right| < 0.1 \quad \text{for} \quad q \in \{q_u^m, q_\ell^m, q_s\} \right\} - \frac{\tau}{T}. \tag{4.71}$$

Here t_f is the simulation end time, $t = 0$ is the pulse start time, and τ/T is the dimensionless pulse duration. The equilibrium values $q(t_f)$ when the upper inlet valve is open and all other valves are closed are near to but not quite zero, because valves only close by 95% in the simulations to avoid dividing by zero valve area when computing valve coefficients in equation (4.39c). In Figures 4.7 b i) and ii), we plot the fluxes q_u^{m*}, q_ℓ^{m*} and q_s^* for $\tau = 0.04$ s and $\tau = 0.004$ s, respectively, and mark the time $t^* = t_r^* + \tau$, when the system has relaxed, by vertical dashed lines. For $\tau = 0.04$ s the system is quick to relax, taking only 0.0070 s. For $\tau = 0.004$ s the system takes slightly longer, 0.012 s, to relax, but though this relaxation time is very long relative to the pulse duration, in absolute terms it is still very short. Computing the relaxation times over a range valve periods $\tau \in (0.0026, 1)$ s, as shown in Figure 4.8 for velocity profile powers $\gamma = 2, 9, 16$, we confirm that the relaxation time is always very short: less than 0.022 s for all of the valve period we study, and effectively instantaneous (to within the minimum numerical timestep) for $\tau > 0.13$ s. As shear stress is related to the scaffold flow by equation (4.69), this indicates that the shear stress will only be enhanced for a maximum of approximately 0.022 s beyond the duration of valve movement. Therefore, multiple pulses are required to achieve sustained higher shear stresses.

As an aside, we remark that the qualitative behaviour of fluxes changes between $\tau = 0.04$ s and $\tau = 0.004$ s. Figure 4.7 b i) shows that for both valve periods, just after the upper inlet valve starts to close and the lower outlet valve starts to open (shaded light grey) there are spikes in fluxes in the direction of upper inlet to lower outlet. Similarly, just after the upper inlet starts to open and the lower outlet valve starts to close (shaded mid-grey), there is a spike in flux from outlet to inlet. For the faster valve period $\tau = 0.004$ s these spikes are much larger, relative to the other two peaks/troughs in flux, noticeable just before $t^*/\tau = 0.5$ and $t^*/\tau = 1$. The trough just before $t^*/\tau = 0.5$ and the peak just before $t^*/\tau = 1$

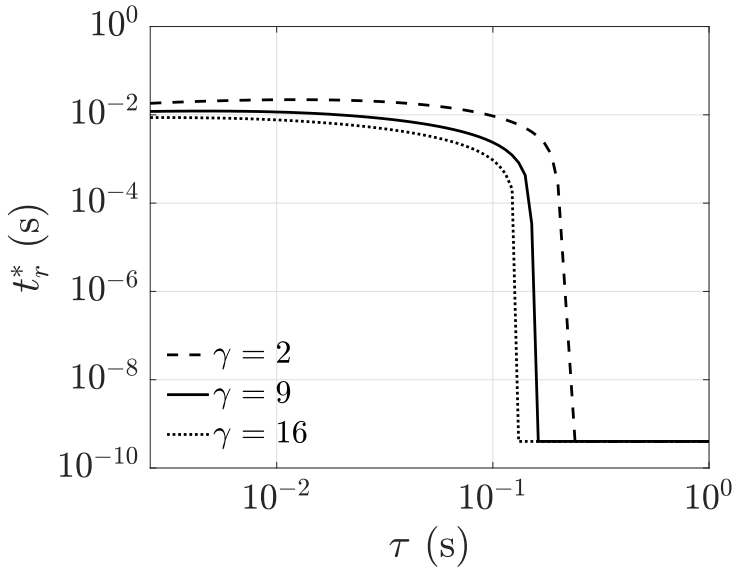

Figure 4.8: Relaxation times for varying valve periods $\tau \in (0.0026, 1)$ s, when pulsing the upper inlet and lower outlet valves once. Parameters are as in Tables 2.2 and 4.1.

are both artefacts of the resistor and valve tubing (between which the valves are situated) having different radii. This is demonstrated by the peaks disappearing when the valve tubing radius is changed to be the same as resistor tubing radius (results not shown).

4.7.2 Multiple pulses

To investigate whether the system behaviour changes greatly over multiple pulses, in Figure 4.9 we plot the time series of shear stress over five valve pulses, demarcated by dashed lines, for i) $\tau = 0.04$ s and ii) $\tau = 0.004$ s. Apart from slight differences between the first and later pulses for $\tau = 0.004$ s, we see there is very little change in shear stress behaviour over the course of the five pulses. To confirm that shear stress metrics vary little between pulses, we measure the maximum shear stress σ_{max} and mean shear stress $\bar{\sigma}$ (both taken over space and time)

$$\sigma_{max} = \max_{\substack{z^* \in (z_4^*, z_5^*) \\ t^* \in (n\tau, (n+1)\tau)}} \Sigma(z^*, t^*), \qquad \bar{\sigma} = \frac{1}{l_s^* \tau} \int_{n\tau}^{(n+1)\tau} \int_{z_4^*}^{z_5^*} \Sigma(z^*, t^*) dz^* \, dt^*, \quad (4.72)$$

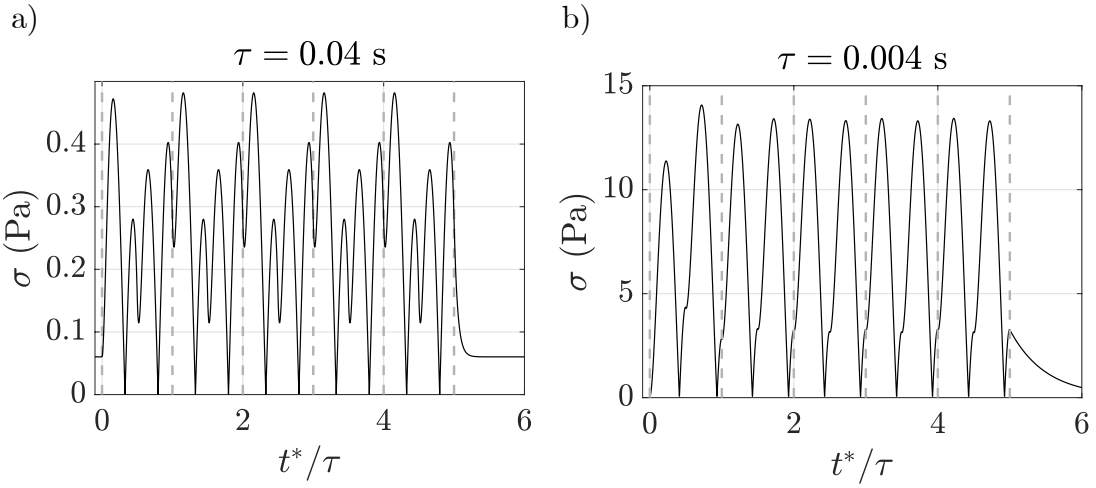

Figure 4.9: Spatial mean of the scaffold shear stress over five pulses, demarcated by dashed lines, for i) $\tau = 0.04$ s and ii) $\tau = 0.004$ s. $\gamma = 9$ and other parameters are as in Table 2.2.

for each pulse over ten pulses for $\tau = 0.004, 0.04, 0.4$ s. We find that after the first pulse, each metric changes by less than 1% between any two pulses, which gives us confidence in using the second pulse when computing shear metrics for Figure 4.10.

In Figure 4.10 we demonstrate how valve period influences the maximum and mean shear stresses for the valve periods $\tau \in (0.0026, 1)$ s. Figure 4.10 shows that for $\tau \in (0.0026, 0.1)$ s, which is when the valve-driven axial flow U dominates the gravity-driven axial flow U_g (see equation (2.15)), the maximum and mean shear stresses, σ_{max} and $\bar{\sigma}$, depend inversely on τ, with power law exponents around -1. For $\tau \in (0.01, 0.1)$ s, the maximum and mean shear stresses decreases slightly more sharply than for $\tau \in (0.0026, 0.01)$ s, and the maximum shear for flow with a plug-like velocity profile $\gamma = 16$ decreases more steeply than for $\gamma = 2, 9$. As may be expected when the valve period is comparable to the timescale of gravity-driven flow, for $\tau \in (0.1, 1)$ s, σ_{max} tails off to become approximately constant, while $\bar{\sigma}$ remains constant. The maximum and mean shear stresses are also plotted in Figure 4.10 a ii) and b ii) relative to their values σ_{stat} at equilibrium when the upper inlet valve and lower outlet valves are open and the other two valves are closed. These plots show that using smaller valve periods can increase the mean

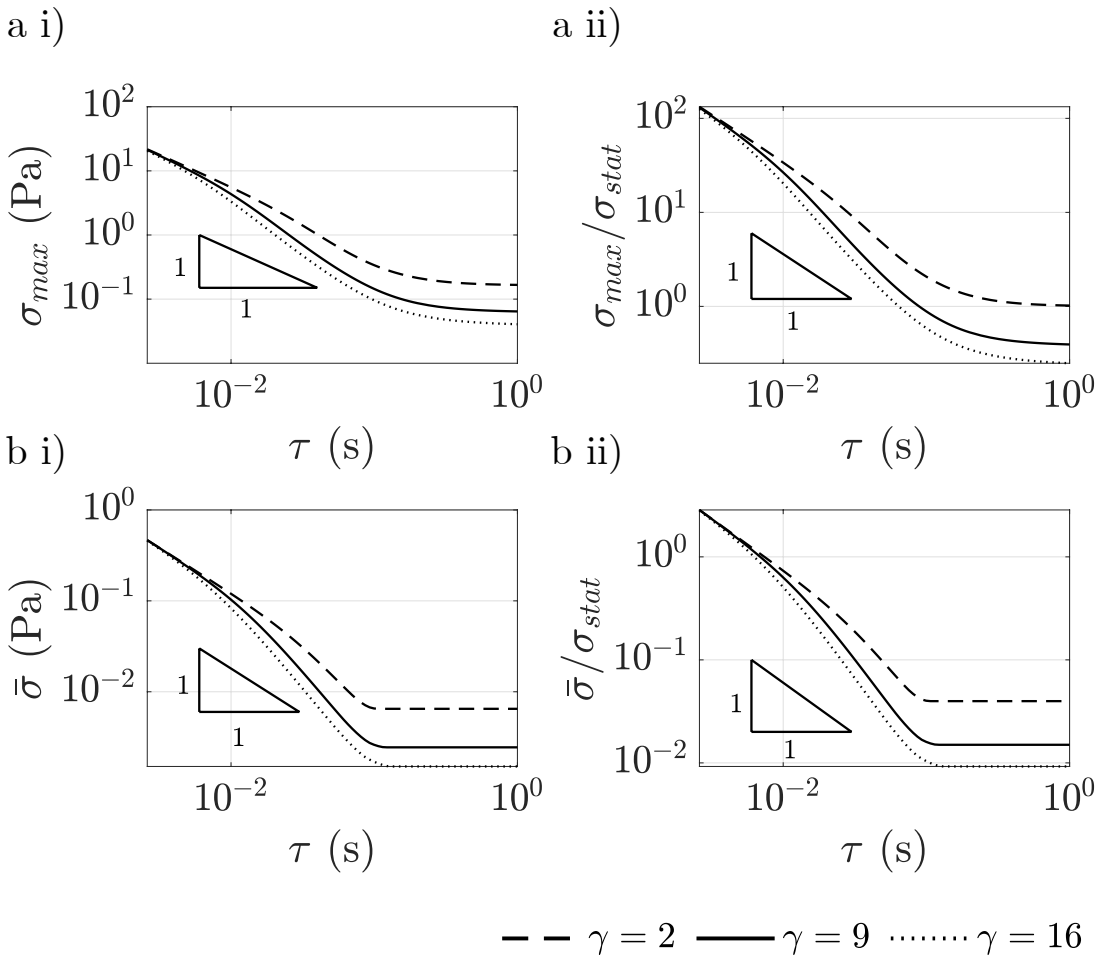

Figure 4.10: The a) maximum σ_{max} and b) mean $\bar{\sigma}$ shear stresses, over the duration of one pulse, for valve periods $\tau \in (0.0026, 1)$ s and velocity profile powers $\gamma = 2, 9, 16$. i) Absolute values of the maximum and mean shear stresses, and ii) their values relative to the shear stress σ_{stat} when the upper inlet and lower outlet valves are open, and the other two valves are closed. Parameters are as in Tables 2.2 and 4.1.

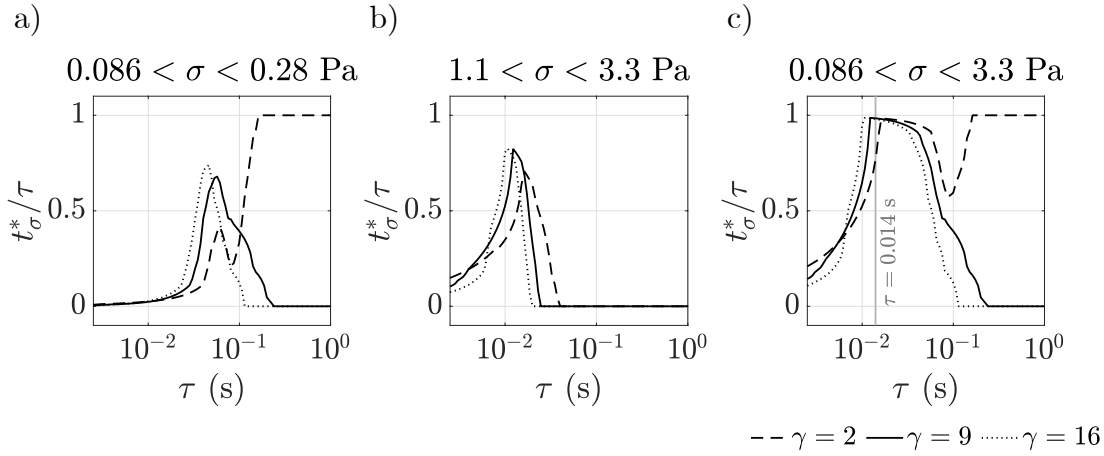

Figure 4.11: The proportion of one pulse spent within the target shear stress range, as the valves are pulsed continuously for a range of valve periods $\tau \in (0.0026, 1)$ s and velocity profile powers $\gamma = 2, 9, 16$, for i) the approximate *in vivo* shear stress range $(0.086, 0.28)$ Pa, ii) higher shear stress range used *in vitro* $(1.1, 3.3)$ Pa, and iii) the lower *in vivo* bound and upper *in vitro* bound. Parameters are as in Tables 2.2 and 4.1.

shear stress by as many as 3 times, and the maximum shear stress by as many as 123 times.

As mentioned in §2.2, it is not known whether controlling instantaneous (as measured for example by σ_{max}) or integrated shear stress (as measured for example by $\bar{\sigma}$ is more important for enhancing platelet production. A perhaps more informative integrated measure of the shear stress is the threshold time t^*_σ, measuring the duration during the n^{th} pulse when at least half of the scaffold has shear stresses within a target range (σ_1, σ_2):

$$t^*_\sigma = \int_{n\tau}^{(n+1)\tau} \delta_t(T_\sigma)\, dt^*, \tag{4.73}$$

where $\delta_t(\cdot)$ is the dirac measure function and T_σ is the set

$$T_\sigma = \{t^* \in (n\tau, (n+1)\tau) : \sigma(z^*, t^*) \in (\sigma_1, \sigma_2) \text{ for} \geq 50\% \text{ of } z \in (z_4, z_5)\}. \tag{4.74}$$

We consider the case where valves are being pulsed continuously for a number of seconds, and have reached a steady value of t^*_σ after a number of pulses (at least $n = 6$ pulses for $\tau \in (0.0026, 1)$ s). Figure 4.11 plots the proportion t^*_σ/τ

of time during which at least half of the scaffold is within the target shear stress ranges a) $0.086 < \Sigma < 0.28$ Pa (*in vivo*), b) $1.1 < \Sigma < 3.3$ Pa (*in vitro*) and c) $0.086 < \Sigma < 3.3$ Pa, for velocity profile powers $\gamma = 2, 9, 16$. For all three ranges, the results for $\gamma = 9, 16$ show that if the valve period is either too long or too short, then at all times during the pulse, less than half of the scaffold is within the shear stress range. For the Poiseuille profile with $\gamma = 2$, the shear stress for $\tau > 0.16\,\text{s}$ is high enough that at least half of the scaffold always has shear stress above 0.086 Pa. Given that we have not tested which velocity profile is most accurate, it is safest to choose a valve period that gives a high value of t^*_σ/τ for all of $\gamma = 2, 9, 16$; for instance $\tau = 0.014\,\text{s}$ ensures that there is almost always at least half of the scaffold within the combined shear stress range $(0.086, 3.3)$ Pa, as marked by the grey line in Figure 4.11 c).

As the valve period τ increases, the proportion t^*_σ first rises then falls in all of Figures 4.11 a) - c), bar two cases: $\gamma = 2$ in Figures 4.11 a) and c), where t^*_σ rises, falls, and rises again. We explain this difference for Figure 4.11 a), which has target shear stress range $0.086 < \Sigma < 0.28$ Pa; the reasoning for Figure 4.11 c) is analogous. Figures 4.12 a i) - iii) plot the scaffold flux q^*_s against time for different valve periods τ. They all show that as τ increases (solid lines to dashed lines), the scaffold flux q^*_s decreases in magnitude. Going from $\tau = 0.04$ s (solid line) to $\tau = 0.05$ s causes t^*_σ to increase (as shown in Figure 4.11 a)): looking at Figures 4.12 a,b i), we see this is due to the decrease in the volume of backflow ($q^*_s < 0$) causing a higher proportion of time to be spent within the shear range, shaded in grey. As the valve period is increased from $\tau = 0.065$ s to $\tau = 0.075$ s, t^*_σ decreases, because the volume of backflow has decreased enough to cause t^*_σ to decrease, while the forward flow has not decreased enough to cause t^*_σ to increase, as shown in Figures 4.12 a, b ii). Finally, increasing from $\tau = 0.085$ s to $\tau = 0.1$ s causes t^*_σ to increase, because the forward flow has now decreased sufficiently, as shown in Figure 4.12 a, b iii). For $\tau = 0.1$ s there is no backflow.

4.7.3 Lower outlet flow and scaffold backflow

In choosing a valve period, there are two other metrics we may wish to consider: the flux out of the lower outlet, and the backflow through the scaffold. Both of

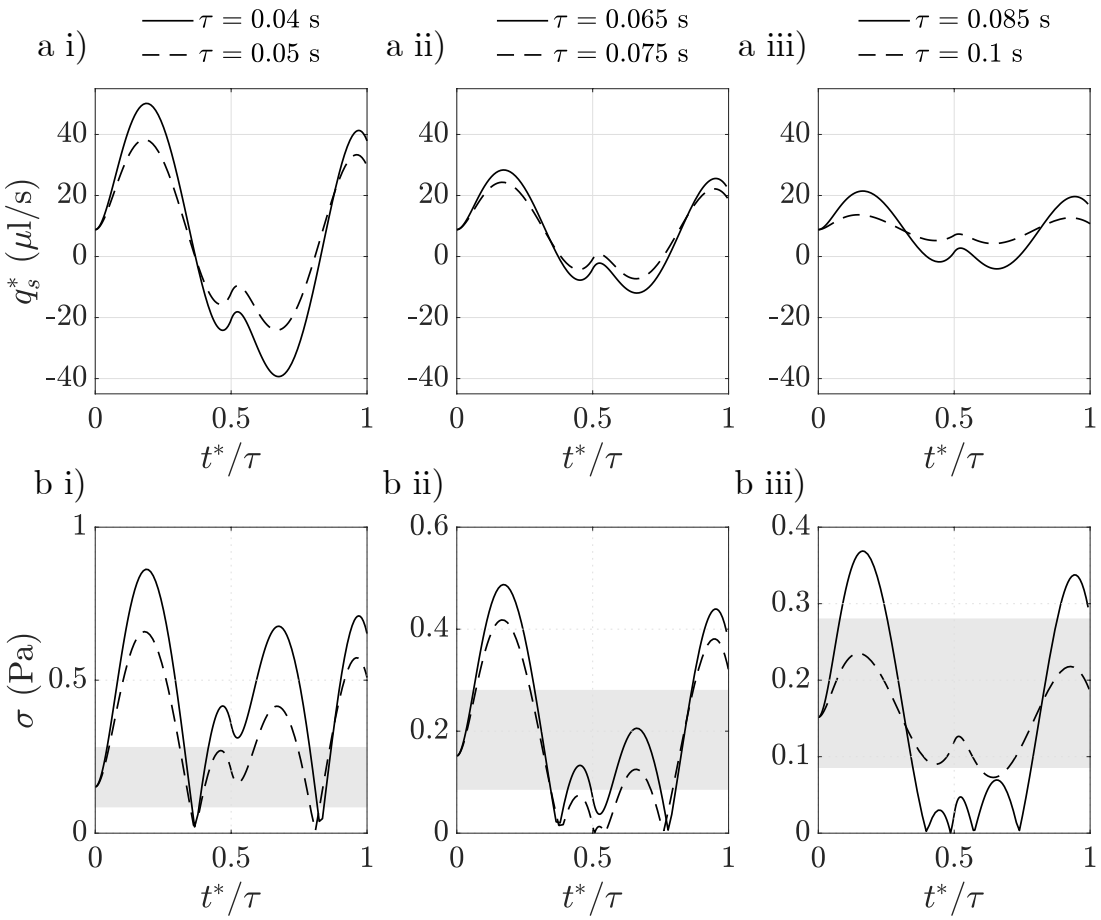

Figure 4.12: The a) vertical flux q_s^* and b) spatial mean of the shear stress σ in the scaffold over one valve pulse, with $\gamma = 2$, explaining the behaviour of t_σ^* for $\gamma = 2$ in Figure 4.11 a). The solid and dashed lines are i) $\tau = 0.04, 0.05\,\text{s}$, ii) $\tau = 0.065, 0.075\,\text{s}$, iii) $\tau = 0.085, 0.1\,\text{s}$, respectively. All other parameters are as in Tables 2.2 and 4.1.

these should be kept low; the first so as to avoid having to reconcentrate the final product too much, which is an expensive process, and the second so as to avoid megakaryocytes and platelets being washed out of the scaffold and transported along the upper tube system, which may disrupt platelet production by megakaryocytes, and delay platelets from leaving the bioreactor. Megakaryocytes may originally be lodged in a pore of the scaffold, and begin to extend proplatelets into flow, but then by being moved out of and back into a pore again, proplatelets may no longer end up extending into the flow, but could become jammed between a megakaryocyte and the scaffold.

We compute the flux out of the lower outlet during one second, and while valves are continually pulsing, *viz.*

$$Q^*_{\ell 9} = \int_{n\tau}^{n\tau+1} q^*_{\ell 9}(t^*)\, dt^*. \tag{4.75}$$

where the flux is computed after n pulses have elapsed, when the flux has become (approximately) periodic. The flux $Q^*_{\ell 9}$ is compared to the flux $Q^*_{\ell 9,stat}$ out of the lower outlet when the upper inlet and lower outlet valves are open and static, and the other two valves are closed. Figure 4.13 a) plots the $Q^*_{\ell 9}/Q^*_{\ell 9,stat}$ against $\tau \in (0.0026, 1)$ s. We take $n = 25$ in equation (4.75), because after 25 pulses the total flux per pulse out of the lower outlet has equilibrated to within 1% of that of neighbouring pulses, for $\tau \in (0.0026, 1)$ s with $\gamma = 2, 9, 16$. For $\tau > 0.02$ s (marked in grey) the relative flux is approximately constant and bounded just above one, and for $\tau < 0.02$ it decreases as the valves speed up. Using valve pulses to exert shear stress will therefore result in roughly equal or less outlet flux than would result from using the static valve configuration with upper inlet and lower outlet valves open. Thus, using pulsed valves with the configuration of Figure 4.6 instead of static valves will not cause extra product dilution, and for fast valves will even lead to a more concentrated product.

Figure 4.13 b) plots the volume of backflow during the longest period (t_0, t_1) of continuous scaffold backflow during a pulse:

$$Q_s = \int_{t_0}^{t_1} q_s(t)\, dt, \tag{4.76}$$

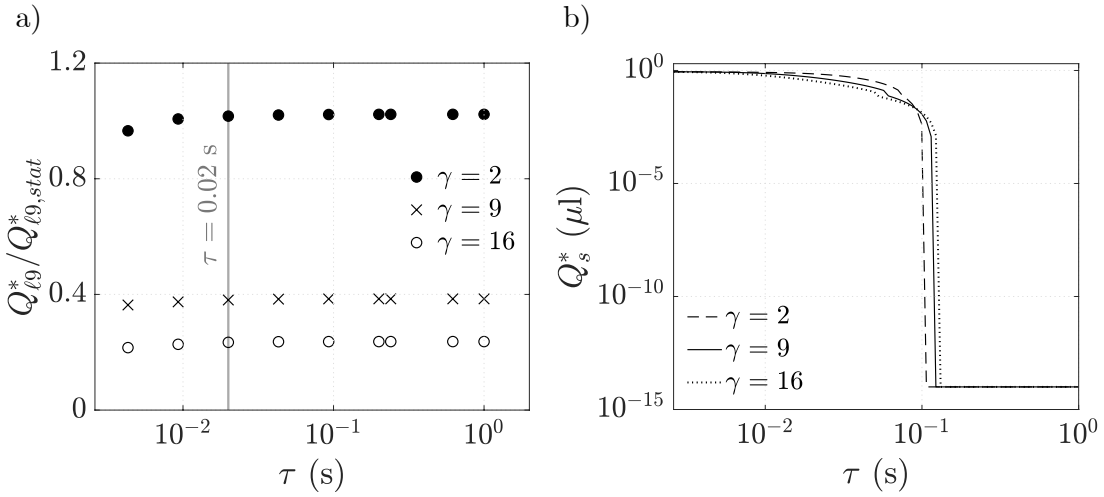

Figure 4.13: a) The total flux, $Q^*_{\ell 9}$, out of the lower outlet over one period for a valve moving with period $\tau \in (2.6 \times 10^{-3}, 1)$ s, relative to that, $Q^*_{\ell 9,stat}$, when the upper inlet and lower outlet valves are open, with the other two valves closed. For $\tau < 0.02$ marked in grey, the flux decreases as τ decreases. b) The volume Q^*_s of backflow up the scaffold during the longest period of continuous backflow in a pulse, for $\tau \in (2.6 \times 10^{-3}, 1)$ s. The velocity profile powers are $\gamma = 2, 9, 16$ and parameters are as in Tables 2.2 and 4.1.

where the instantaneous scaffold flux q_s is given in equation (4.67). We consider that each period of backflow is an isolated event, rather than accumulating them, because they are separated by periods of flow down the scaffold. The scaffold backflow is computed after 6 pulses, by which point it has equilibrated to within 1% of that of neighbouring pulses for all values of $\tau \in (0.0026, 1)$ s for $\gamma = 2, 9, 16$. For fast valves with $\tau \in (0.0026, 0.0045)$ s there is the greatest volume of backflow, ranging between $0.8\,\mu$l and $0.89\,\mu$l. As the valve period increases the amount of backflow decreases, until about 0.1 s where it drops off to zero (within machine precision). A volume of 0.89 μl leaving the scaffold into the upper channel corresponds to displacing fluid by approximately 0.1 mm along the upper channel or up the scaffold. This is approximately 5 times the typical diameter of a megakaryocyte ($16.4\,\mu$m$-22.4\,\mu$m [145]), so may disrupt their positions (experiments or cell-scale modelling would be useful to verify this). To ensure that fluid is displaced by backflow by less than the diameter of a megakaryocyte, the volume of backflow should be less than 0.1 μl, which corresponds to requiring a valve period greater than 0.05 s. Figure 4.11 shows that choosing $\tau = 0.05$ s would still result in at least half of the scaffold being within the shear stress range $0.086 < \sigma < 3.3$ Pa for 80% of the time, for velocity profile power $\gamma = 9$. Thus 0.05 s may be a good choice of valve period.

4.7.4 Varying the scaffold permeability

Finally, we check how varying the scaffold permeability affects the shear stress when flow is driven by valve movement. Figure 4.14 a) shows that all permeabilities have a similar qualitative dependence of maximum shear stress σ_{max} on the valve period τ. Specifically, increasing the scaffold permeability increases the maximum shear stress σ_{max} for a given valve period τ; for example increasing K by an order of magnitude from $K = 10^{-15}$ to $K = 10^{-14}$ (bottom line to third from bottom line) increases σ_{max} by approximately an order of magnitude. However, the increase in shear stress saturates at higher permeabilities, as indicated by the lines becoming closer together. This agrees with the corresponding static case (with the upper inlet and lower valves open, and the other valves closed) discussed in §3.5.1, where the scaffold shear stress increased with permeability up to a point

where permeability was no longer the limiting factor; instead, for example, the resistor tubing may have become the limiting factor.

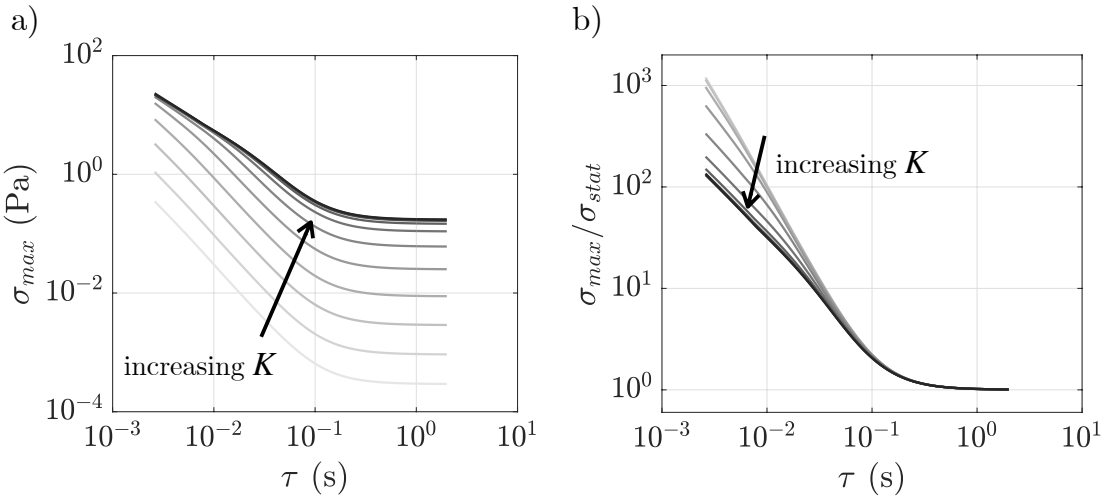

Figure 4.14: a) Maximum shear stress over the second of two pulses, for 13 scaffold permeabilities $K \in [10^{-15}, 10^{-9}]$, equally spaced on a log scale. b) Maximum shear stress relative to that when the upper inlet and lower outlet valves are open, with the other two valves closed. Other parameters are as in Tables 2.1 and 4.1.

We also explore whether the scaffold permeability affects the valve period τ at which valve movement enhances shear stress σ_{max} above the maximum σ_{stat} obtained in a static configuration. This is indicated by the longest period τ below which $\sigma_{max}/\sigma_{stat} > 1$. As shown in Figure 4.14 b), this period is not sensitive to the value of K, but occurs around $\tau = 0.4$ for all K. We do see however that at smaller valve periods, $\sigma_{max}/\sigma_{stat}$ is higher for lower scaffold permeabilities, indicating that decreasing the valve period increases the shear stress in lower permeability scaffolds relatively more than in higher permeability scaffolds.

4.8 Small-amplitude valve oscillations

In both the quasi-steady model of Chapter 3 and the inertial model of §4.1−§4.7, the moving valves have opened and closed almost completely (they do not close completely so as to prevent numerical errors in dividing by zero valve area), corresponding to the regime where the valve amplitude a, appearing in equation (2.5),

is order one. In this section, we consider the regime where the valve amplitude a is small, i.e. $a = \mathrm{o}(1)$ as $\epsilon \to 0$. Consequently there is a separation of timescales between the typical valve period T and the timescale T/a of valve-driven axial flow. By exploiting this separation in timescales, we are able to systematically reduce the model equations presented in Chapter 2. Solutions of this reduced system enable us to explore the dynamics of small-amplitude valve oscillations, and we may use these solutions to verify within this regime the model of §4.1−§4.7, which incorporated *ad hoc* assumptions.

The reduced Reynolds number $\mathcal{R} = a\epsilon^2\rho l^{*2}/(\mu T)$ is smaller than its value in §4.1−§4.7 by a factor of a, and the Strouhal number is $l^*/(UT) = 1/a$. An important dimensionless quantity in this regime is the Womersley number, $\mathcal{RS}$, which is the ratio of the timescale of viscous diffusion to that of valve movement. We work in the regime in which $\mathcal{RS} = \mathrm{O}(1)$, and $\mathcal{R} = \mathrm{o}(1)$. In contrast, many studies in the collapsible tube literature have looked extensively at the regime where the Womersley number is much greater than one, see for example [66], resulting in an inviscid core with Stokes boundary layers. The present regime has not been explored experimentally, but as we show may offer advantages over O(1) amplitude valve oscillations.

4.8.1 Leading order model

In the present regime, non-linear inertia is negligible at leading-order, resulting in a system that is simpler to solve than that of §4.2-§4.7. The leading order governing equations (2.23) are

$$\mathcal{RS}\frac{\partial w_i}{\partial t} = -\frac{\partial p_i}{\partial z} + \frac{\partial^2 w_i}{\partial x^2} + \frac{\partial^2 w_i}{\partial y^2}, \quad \frac{\partial p_i}{\partial x} = 0, \quad \frac{\partial p_i}{\partial y} = 0, \tag{4.77a}$$

$$\frac{\partial u_i}{\partial x} + \frac{\partial v_i}{\partial y} + \frac{\partial w_i}{\partial z} = 0. \tag{4.77b}$$

Integrating the mass equation (4.77b) over the cross-section as usual, we obtain

$$\frac{\partial \hat{A}_i}{\partial t} + \frac{\partial q_i}{\partial z} = J_i, \tag{4.78}$$

where $\hat{A}_i = \mathrm{O}(1)$ as $a \to 0$ and is related to the cross-sectional valve area, $A_i = \pi b_v^2 + a\hat{A}_i(z,t)$. Here A_i is given in equation (2.5), with valve closure functions (that prescribe the time-dependency of valve area) given by equations (A.3)

and (A.4). The flux q_i through the tubing systems and net flux J_i leaving the scaffold through interface Γ_i are again given in equation (4.6). As in §3.2 and §4.4, we solve the leading order Darcy flow equation to obtain J_i, given by equation (4.15) in terms of the pressures p_u and p_ℓ in the upper and lower tubing systems:

$$J_u = -J_\ell = \begin{cases} -\dfrac{2c\mathcal{B}}{h_s}\big(p_u - p_\ell\big) & \text{for} \quad z_4 < z < z_5 \\ 0 & \text{otherwise,} \end{cases} \tag{4.79}$$

We solve equations (4.77a) and (4.78) subject to no-slip on the tubing system walls and scaffold-channel interface (4.9), prescribed pressures (4.31) at the tubing systems' inlets and outlets, and initial condition (4.32) for the flux. As in §4.5 we prescribe pressures at inlets and outlets to be zero initially, with the inlet pressures increasing according to (4.33). Thus there is zero initial flux, as in equation (4.34).

In sections §4.8.2 and §4.8.3 we seek separable solutions of equation (4.77a) in each of the valve, resistor tubing, valve tubing, and channel regions. This allows us to determine the radial dependence of the axial velocity, w_i, and leaves us with integral equations for the pressure, which we solve using numerical methods in §4.8.4.

4.8.2 Valves

To solve equation (4.77b) and (4.78) in the valves, we transform into coordinates in which the valve walls are fixed by writing

$$(\hat{x}, \hat{y}, \hat{z}) = \left(\frac{x}{b_v + ab_1}, \frac{y}{b_v + ac_1}, z\right), \quad \hat{t} = t, \tag{4.80}$$

where b_v is the undeformed valve radius and b_1 and c_1 are the time-dependent perturbations to the semi-minor and semi-major axes of the elliptical valve cross-sections. With this choice of coordinates the valve cross-sections are circles of radius one. The derivatives transform as

$$\frac{\partial}{\partial x} = \frac{1}{b_v + ab_1}\frac{\partial}{\partial \hat{x}}, \quad \frac{\partial}{\partial y} = \frac{1}{b_v + ac_1}\frac{\partial}{\partial \hat{y}}, \quad \frac{\partial}{\partial z} = \frac{\partial}{\partial \hat{z}}, \tag{4.81}$$

and

$$\frac{\partial}{\partial t} = \frac{\partial}{\partial \hat{t}} + \frac{a\hat{x}}{b_v + ab_1}\frac{\partial b_1}{\partial \hat{t}}\frac{\partial}{\partial \hat{x}} + \frac{a\hat{x}}{b_v + ab_1}\frac{\partial c_1}{\partial \hat{t}}\frac{\partial}{\partial \hat{x}}. \tag{4.82}$$

Expanding $1/(b_v + ab_1) = 1/b_v + \mathrm{O}(a)$, and $1/(b_v + ac_1) = 1/b_v + \mathrm{O}(a)$, and setting J_i to be zero in the mass equation (4.78) because the valves do not interface with the scaffold, we find that the leading order equations are simply given by

$$\mathcal{RS}\frac{\partial \hat{w}_i}{\partial \hat{t}} = -\frac{\partial \hat{p}_i}{\partial \hat{z}} + \frac{1}{b_v^2}\left(\frac{\partial^2 \hat{w}_i}{\partial \hat{x}^2} + \frac{\partial^2 \hat{w}_i}{\partial \hat{y}^2}\right), \quad \frac{\partial \hat{p}_i}{\partial \hat{x}} = 0, \quad \frac{\partial \hat{p}_i}{\partial \hat{y}} = 0, \tag{4.83}$$

with

$$\frac{\partial \hat{A}_i}{\partial \hat{t}} + \frac{\partial \hat{q}_i}{\partial \hat{z}} = 0, \tag{4.84}$$

where hatted functions have hatted variables as arguments, obeying $\hat{w}_i = w_i$, $\hat{p}_i = p_i$ and $\hat{q}_i = b_v^2 \int_{\hat{\Omega}} \hat{w}_i d\hat{x} d\hat{y}$, with $\hat{\Omega}$ being the unit disc. Thus the valve movement only enters at leading order through the $\partial \hat{A}_i/\partial \hat{t}$ term in the integrated mass equation. After transforming to cylindrical polar coordinates, $(\hat{x}, \hat{y}, \hat{z}) = (r\cos\theta, r\sin\theta, \hat{z})$, the $z-$momentum equation is

$$\mathcal{RS}\frac{\partial w_i}{\partial t} = -\frac{\partial p_i}{\partial z} + \frac{1}{b_v^2 r}\frac{\partial}{\partial r}\left(r\frac{\partial w_i}{\partial r}\right), \tag{4.85}$$

where we have dropped hats. Seeking a separable solution

$$w_i = f_i(r) g_i(z, t), \tag{4.86}$$

we find the radial components of the solution to be the Bessel functions of the first kind, with order zero:

$$f_{i,n}(r) = J_0(\beta_n r), \tag{4.87}$$

where β_n are the zeros of $J_0(r)$ with $n \in \mathbb{N}$ (positive integers), enforcing the no-slip condition (4.9). Substituting

$$w_i(r, z, t) = \sum_{n=1}^{\infty} f_{i,n}(r) g_{i,n}(z, t) \tag{4.88}$$

into equation (4.85) and projecting on the n^{th} mode yields

$$\mathcal{RS}\frac{\partial g_{i,n}}{\partial t} = -C_n \frac{\partial p_i}{\partial z} - \frac{\beta_n^2}{b_v^2} g_{i,n}, \quad n \in \mathbb{N}. \tag{4.89}$$

The coefficients C_n come from expanding the pressure term in (4.85) in terms of $f_{i,n} = J_0(\beta_n r)$, and are defined as

$$C_n = \frac{2}{J_1(\beta_n)^2} \int_0^1 J_0(\beta_n r)\, r\, dr, \tag{4.90}$$

where J_1 are Bessel functions of the first kind with order one. Note that because the pressure has no radial dependence, we will need to take a large number of terms when truncating the infinite sum (4.88) over the n solution modes. Although this can be avoided by instead solving for the flow relative to Poiseuille flow (i.e. letting $w_i = w_i^{pois} + w_i^{rel}$, where $w_i^{pois} = [b_v^2(1-r^2)/4]\partial p_i/\partial z$, and solving for w_i^{rel}), we would then obtain an equation involving both spatial and temporal derivatives of pressure, as opposed to only spatial derivatives. As this requires an extra integration, the present method is simpler to implement numerically.

We solve equation (4.89) for the temporal and axial modes $g_{i,n}$ of the solution, in terms of the (as-of-yet unknown) pressure gradient $\partial p_i/\partial z$ and an initial condition $g_{i,n}(z,0)$, and obtain

$$g_{i,n} = e^{-\gamma_n t}\left(g_{i,n}(z,0) - \frac{C_n}{\mathcal{RS}}\int_0^t e^{\gamma_n s}\frac{\partial p_i}{\partial z}(z,s)ds\right) \tag{4.91}$$

where $\gamma_n = \beta_n^2/(b_v^2\mathcal{RS})$. We can now integrate the axial velocity w_i over the cross-section to obtain the flux

$$q_i = b_v^2\sum_{n=1}^{\infty} D_n e^{-\gamma_n t}\left(g_{i,n}(z,0) - \frac{C_n}{\mathcal{RS}}\int_0^t e^{\gamma_n s}\frac{\partial p_i}{\partial z}(z,s)\,ds\right), \tag{4.92}$$

where

$$D_n = 2\pi\int_0^1 J_0\left(\beta_n r\right)\, r\, dr. \tag{4.93}$$

By substituting the flux (4.92) into the integrated mass equation (4.84), and setting $g_{i,n}(z,0) = 0$ due to the zero-flux initial condition (4.34), we obtain an integro-differential equation for p_i,

$$\frac{\partial \hat{A}_i}{\partial t} - b_v^2\sum_{n=1}^{\infty}\frac{C_n D_n}{\mathcal{RS}}\int_0^t e^{\gamma_n(s-t)}\frac{\partial^2 p_i}{\partial z^2}(z,s)\,ds = 0. \tag{4.94}$$

4.8.3 Resistor tubing, valve tubing and channels

In the resistor tubing, valve tubing and channels, the walls are stationary so we can immediately seek separable solutions of equation (4.77a). The resistor tubing and valve tubing both have circular cross-sections, thus the solutions are identical to those in the transformed valve domains (4.92), with the radius b_v of the valve

tubing swapped for the resistor tubing radius b_r in the resistor tubing, and $\partial \hat{A}_i/\partial t$ set to zero in equation (4.94). We again impose zero initial flow, $g_{i,n}(z,0) = 0$, thus from equation (4.94) we see that in the resistor tubing and valve tubing the pressure p_i is linear in z.

The channels have rectangular cross-sections, and to reflect this we seek separable solutions

$$w_i = f_i(x,y)g(z,t), \tag{4.95}$$

and take f_i to be eigenfunctions of the Laplacian in the rectangular domain $-c \le x \le c, -b_c \le y \le b_c$,

$$f_{i,kn}(x,y) = \cos \lambda_k x \cos \nu_n y, \tag{4.96}$$

where $\lambda_k = (2k+1)\pi/(2c)$ and $\nu_n = (2n+1)\pi/(2b_c)$, for $k, n \in \mathbb{Z}_{\ge 0}$. Thus the no-slip condition (4.9) is satisfied. The temporal/axial mode $g_{i,kn}$ is, in terms of the pressure gradient and initial condition $g_{i,kn}(z,0)$, then given by

$$g_{i,kn}(z,t) = e^{-\gamma_{kn} t} \left(g_{i,kn}(z,0) - \frac{E_{kn}}{\mathcal{RS}} \int_0^t e^{\gamma_{kn} s} \frac{\partial p_i}{\partial z}(z,s)\, ds \right), \tag{4.97}$$

where $\gamma_{kn} = \left(\lambda_k^2 + \nu_n^2\right)/(\mathcal{RS})$, and the coefficients E_{kn} come from expanding the pressure gradient in terms of $f_{i,kn}$

$$E_{kn} = \frac{4(-1)^{k+n}}{b_c c \lambda_k \nu_n}. \tag{4.98}$$

Integrating over the cross-section, we obtain the flux

$$q_i = \sum_{k,n}^{\infty} b_c c E_{kn} e^{-\gamma_{kn} t} \left(g_{i,kn}(z,0) - \frac{E_{kn}}{\mathcal{RS}} \int_0^t e^{\gamma_{kn} s} \frac{\partial p_i}{\partial z}(z,s)\, ds \right), \tag{4.99}$$

which takes the same form as the valve flux in equation (4.92), with different coefficients. In the enclosed channels, with zero initial flow $g_{i,kn}(z,0) = 0$ and constant cross-sectional area, $\partial A_i/\partial t = 0$, substituting the flux into the integrated mass equation (4.84) again shows that the pressure is linear in z, as it is in the resistor and valve tubing. In these regions we therefore write the pressure as

$$p_i = \left(\frac{p_{i,j+1} - p_{ij}}{z_{j+1} - z_j} \right) z + \frac{p_{ij} z_{j+1} - p_{i,j+1} z_j}{z_{j+1} - z_j} \quad \text{for} \quad j = 0, 2, 3, 5, 6, 8, \tag{4.100}$$

where we must solve for the nodal pressures p_{ij}. The fluxes are given by equation (4.92) in the valve and resistor tubing, and equation (4.99) in the enclosed channels. We use these expressions for flux and pressure to enforce continuity of flux and pressure between regions.

In the channels that adjoin the scaffold, we still have $\partial A_i/\partial t = 0$, but now the flux J_i between the channel and scaffold is proportional to the difference in pressures between the upper and lower channels, as in equation (4.79). Substituting the flux (4.99) with zero initial flow $g_{i,kn}(z,0) = 0$ into the mass equation (4.84), we therefore obtain integro-differential equations coupling the pressures in the upper and lower channels,

$$\sum_{k,n}^{\infty} \frac{b_c c E_{kn}^2}{\mathcal{RS}} \int_0^t e^{\gamma_{kn}(s-t)} \frac{\partial^2 p_u}{\partial z^2}(z,s)\, ds = \frac{2c\mathcal{B}}{h_s}\left(p_u - p_\ell\right), \tag{4.101a}$$

$$\sum_{k,n}^{\infty} \frac{b_c c E_{kn}^2}{\mathcal{RS}} \int_0^t e^{\gamma_{kn}(s-t)} \frac{\partial^2 p_\ell}{\partial z^2}(z,s)\, ds = -\frac{2c\mathcal{B}}{h_s}\left(p_u - p_\ell\right). \tag{4.101b}$$

In summary, we must solve equation (4.94) in each of the valves and equations (4.101) in the region of channel adjoining the scaffold, subject to continuity of flux and pressure between regions, and prescribed pressures (4.31) at $z = 0, 1$ as before.

4.8.4 Numerical solution

To solve the integro-differential equations (4.94) and (4.101), we discretise the time integral into M steps of size $\Delta t = t/M$ and take the second derivatives of p_i with respect to z to be piecewise constant in time, and equal in the interval $t \in ((i-1)\Delta t, i\Delta t)$ to their values at $i\Delta t$. Thus at time $t = m\Delta t$, for $m = 1, ..., M$, we compute the integrals in (4.94) and (4.101) to be

$$\int_0^t e^{\gamma s} \frac{\partial^2 p_i}{\partial z^2}(z,s)\, ds = \sum_{k=1}^{m} \int_{(k-1)\Delta t}^{k\Delta t} e^{\gamma s} \frac{\partial^2 p_i}{\partial z^2}(z, k\Delta t)\, ds \tag{4.102}$$

$$= \sum_{k=1}^{m} \left(\frac{1 - e^{-\gamma \Delta t}}{\gamma}\right) \frac{\partial^2 p_i}{\partial z^2}(z, k\Delta t)\, e^{\gamma k \Delta t}. \tag{4.103}$$

Equations (4.94) and (4.101) can at each time $t = m\Delta t$ be written as boundary value problems for $p_i(z, m\Delta t)$, with the pressure at all previous timesteps being

already solved for. We use the MATLAB in-built boundary value problem solver bvp4c to solve for the pressures in the valves and the scaffold-adjoining region of the channel at each timestep. The nodal pressures at the boundaries separating valve tubing, resistor tubing, and enclosed channels are treated as unknown parameters, and enter through boundary conditions of continuity of flux and pressure between each region. Throughout, we use a relative tolerance of 10^{-7} and an absolute tolerance of 10^{-3}. We truncate the infinite sums in equations (4.94) and (4.101) at $k, n = 100$ terms.

We verify the numerical scheme by computing the scaffold shear stress when the valves are static and open, and comparing the results to those of the quasi-steady model in §3.5.1 in the same set-up, finding that answers agree to within 0.1%. We also compare the shear stress to that of the quasi-steady model when the upper valve closes and then opens, and the other three valves are open, for valve amplitudes $a = 0.001, 0.01, 0.1$ and valve period 9.8 s (which is within the quasi-steady regime). The present model and the quasi-steady model are again found to agree to within 0.1%.

We perform convergence tests in the number of timesteps, M, by approximating the true solution to be that with $M = 3200$ timesteps. We pulse the valves once, with the valve sequence in Figure 4.6, using a valve amplitude $a = 0.1$, valve period $\tau = 0.04\,\mathrm{s}$, and Womersley number $\mathcal{RS} = 1$. The L^∞ error $\mathcal{E}_1$, given in equation (4.66), is computed at time $t = 0.8\tau$ for solutions with $M = 50, 100, 200, 400, 800, 1600$, relative to the $M = 3200$ solution. Figure 4.15 plots $\mathcal{E}_1$ against M, and shows that the convergence rate is approximately 1.5.

Another approach to solving equations (4.94) and (4.101) would have been to take Laplace transforms, allowing the transformed second derivatives of the pressure to be taken outside the sums in each equation. We have taken the above approach due to its relative ease of numerical implementation.

4.8.5 Comparison with the *ad hoc* model

We compare results of the systematically-derived model in §4.8.1-§4.8.3 with the model presented in §4.2-§4.7, which includes *ad hoc* assumptions. This allows us to validate the *ad hoc* assumptions, at least in the small-valve amplitude regime.

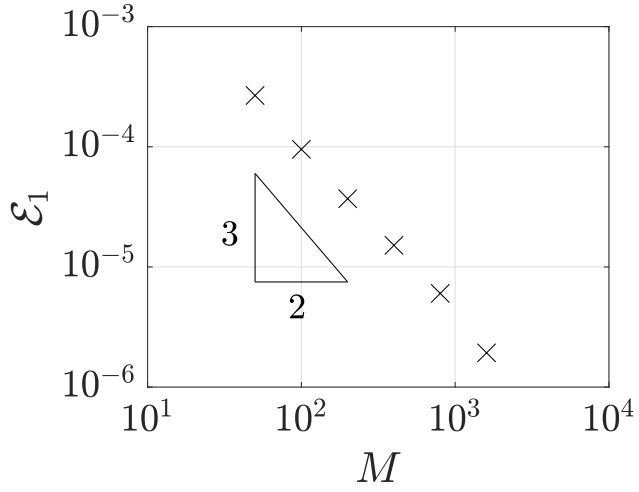

Figure 4.15: Convergence test for the numerical scheme in §4.8.4, plotting the L^∞ error $\mathcal{E}_1$ at time $t = 0.8\tau$ against the number of timesteps. The valve period is $\tau = 0.04$ s, valve amplitude is $a = 0.1$, and Womersley number is $\mathcal{RS} = 1$.

Specifically, labelling the fluxes from the model in §4.2−§4.7 with tildes, we compute the relative difference using the relative L^∞ norm:

$$\mathcal{E}_3 = \max_{\phi \in \{q_u^m, q_\ell^m, q_s\}} \left(\frac{\sum_t \left| \phi - \tilde{\phi} \right|^2}{\sum_t |\phi|^2} \right)^{1/2}, \tag{4.104}$$

while pulsing valves once according to the valve sequence in Figure 4.6. Here, as given in equation (4.67), q_u^m, q_ℓ^m and q_s are the fluxes through the upper and lower channels at their axial midpoints, and the vertical flux through the scaffold, respectively. In Figure 4.16 a) we compute the relative difference $\mathcal{E}_3$ while fixing the valve amplitude at $a = 0.1$, and varying the valve period $\tau = 0.004, 0.008, 0.04, 0.4, 4$ s and power law exponent $\gamma = 2, 9, 16$ for the *ad hoc* velocity profile (which appears in equations (4.11) and (4.13)). Figure 4.16 a) shows that $\gamma = 2$ gives the closest agreement between the model with at most 17% difference. The flux q_u^{m*} through the mid-point of the upper channel is plotted in Figure 4.16 b), where we see that the systematic model and $\gamma = 2$ in the *ad hoc* model do indeed agree closely. It may be expected that as the amplitude a increases or the valve period decreases, the velocity profile may become more plug-like, and higher values of γ may provide

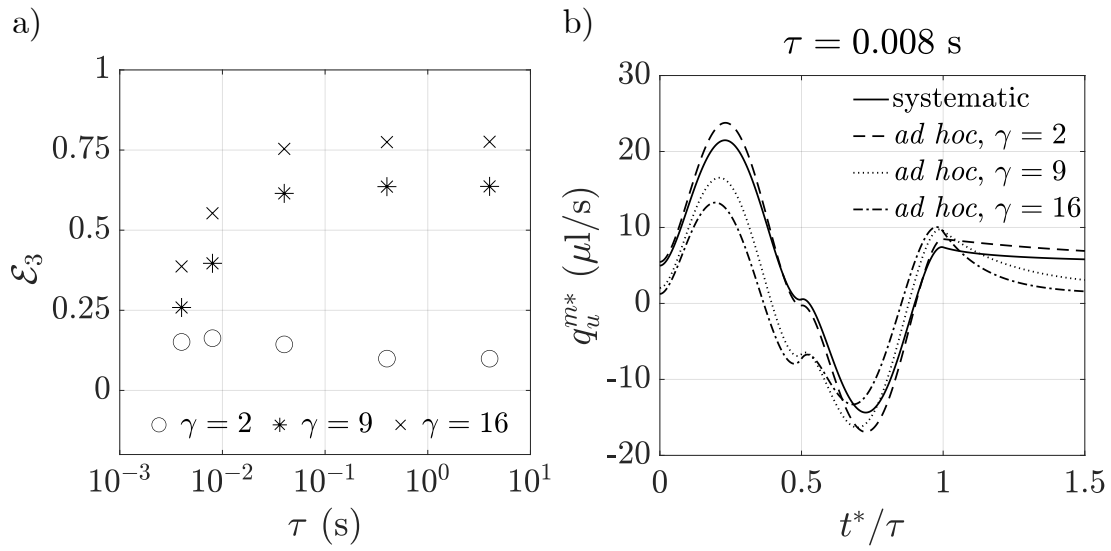

Figure 4.16: a) Relative difference $\mathcal{E}_3$ between the *ad hoc* model of §4.2−§4.7 and the model of §4.8, with valve amplitude $a = 0.1$. The number of timesteps is $M = 3000, 3000, 1000, 1000, 4000$ for $\tau = 0.004, 0.008, 0.04, 0.4, 4$, respectively; other parameters are as in Table 2.1. The power law exponent γ for the *ad hoc* velocity profile is given in equations (4.11) and (4.13).

more accurate results.

We also compute $\mathcal{E}_3$ while varying the valve amplitude $a = 0.001, 0.01, 0.1$ and period $\tau = 0.004, 0.008, 0.04, 0.4, 4$ s, and fixing the power law exponent $\gamma = 2$. Figure 4.17 shows that for $a = 0.001$ or 0.01 the relative difference $\mathcal{E}_3$ between fluxes in the *ad hoc* model and the systematic model is about 0.1. Since the error in the systematic model is of $\mathrm{O}(a)$ (errors from neglecting terms of order $\epsilon^2 \approx 10^{-8}$ are much smaller), this indicates that the *ad hoc* model has errors of approximately 10% for $a = 0.001, 0.01$ arising from the *ad hoc* prescription of the axial velocity profile. For $a = 0.1$, the difference $\mathcal{E}_3$ ranges between approximately $0.15 < \mathcal{E}_3 < 0.17$ for smaller valve periods of $\tau \lesssim 0.1$s, and $\mathcal{E}_3 \approx 0.1$ for longer valve periods of $\tau \gtrsim 0.1$s. Since the systematic model should have at most approximately 10% error, this means that there is at least $5 - 7\%$ error in the *ad hoc* model for smaller valve periods, and doesn't tell us anything about the error for longer valve periods (although we do already know that as τ increases above ≈ 1 s, the reduced Reynolds number $\mathcal{R}$ becomes small enough that the inertial terms, which contain

the *ad hoc* assumption, are small compared to the viscous term, hence we do expect the error in the *ad hoc* model to fall as τ increases).

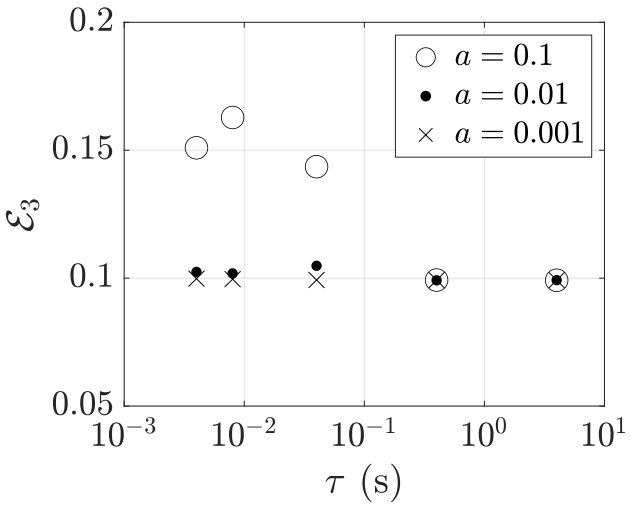

Figure 4.17: The relative difference $\mathcal{E}_3$ between the systematic and *ad hoc* models, for small valve amplitudes $a = 0.001$ (crosses), 0.01 (dots), 0.1 (circles), and valve periods $\tau = 0.004, 0.008, 0.04, 0.4, 4$ s (using $M = 3000, 3000, 1000, 1000, 4000$ timesteps, respectively). The power law exponent is $\gamma = 2$ and other parameters are as in Table 2.1.

4.8.6 Comparing small and large amplitude oscillations

Here we compare fluxes and scaffold shear stresses achieved using small valve oscillations ($a = 0.1$) with those from using large valve oscillations ($a = 0.95$, as in §4.7), again using the valve sequence of Figure 4.6. We compute results for small valve oscillations using the model in §4.8.1-§4.8.4, and those for large valve oscillations using the model of §4.2−§4.7 (i.e. taking the results directly from Figure 4.10). As in §4.7 we pulse the valves multiple times until the flow is periodic in time, i.e. until there is less than 1% change in shear and flux metrics, and use the final pulse to compute the maximum and mean shear stresses (4.72) and the scaffold backflow (4.76). For shear stresses we require 2 pulses, and for backflow 6 pulses. For the large amplitude oscillations, we use the velocity profile power $\gamma = 2$ for illustration; the results for the other powers $\gamma = 9, 16$ are qualitatively similar.

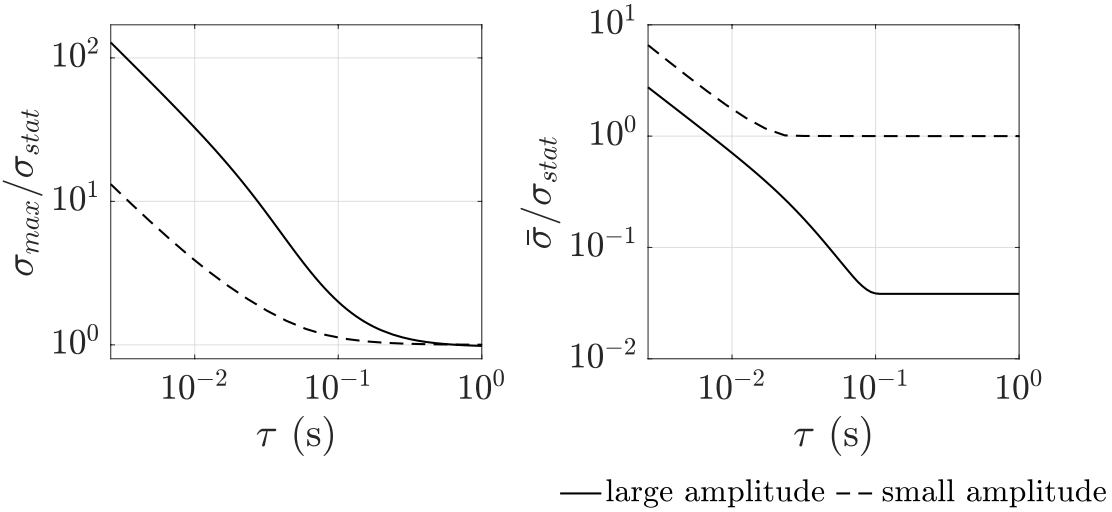

Figure 4.18: Comparing the a) maximum and b) mean shear stresses (equation (4.72)) produced when pulsing the valves with large ($a = 0.95$, solid line) and small ($a = 0.1$, dashed line) amplitude valve oscillations, using the valve sequence in Figure 4.6. The valve period τ takes values in $(0.0026, 1)$s. In the small-amplitude numerical scheme of §4.8.4, 600 timesteps are used; in the large-amplitude numerical scheme of §4.6, 512 spatial steps are used. The power law exponent is $\gamma = 2$ and other parameters are as in Table 2.1.

Figure 4.18 varies the valve period while comparing the maximum and mean shear stresses during one valve pulse, relative to the maximum shear stress achievable with stationary, open valves. Figure 4.18 a) shows that, as may be expected, large amplitude valve oscillations (solid line) always achieve a higher maximum shear stress than small amplitude (dashed line) for all valve periods. However, from Figure 4.19 b) we see that small amplitude valve oscillations achieve higher mean shear stresses than large amplitude valve oscillations. This is because with small amplitude oscillations, the flow through the scaffold never dips too low as valves never close, whereas with large amplitude oscillations the scaffold flux dips to nearly zero at times, thereby reducing the mean shear stress. If a high mean rather than maximum shear stress is desired (motivated for example by the continuous flow of blood past megakaryocytes *in vivo*) then small amplitude valve oscillations may be a good option.

Furthermore, Figure 4.19 shows that the backflow Q_s^* up the scaffold is reduced by using small rather than large amplitude valve oscillations. In particular, in §4.7 we estimated that backflows of more than $0.1\,\mu$l may cause megakaryocytes to dislodge and proplatelet positions to become tangled; and small amplitude valve oscillations always have $Q_s^* < 0.1\,\mu$l for valve periods $\tau \in (0.0026, 1)$ s. This provides another reason to choose small-amplitude oscillations over large amplitude oscillations.

4.9 Summary

In this chapter we have constructed a model of the platelet bioreactor that is valid for fast valve motions, while avoiding the computational expense of time-dependent three-dimensional numerical simulations in a time-dependent geometry with small aspect ratio. This was done by reducing the model of Chapter 2 under the assumption of small aspect ratio, while retaining order one reduced Reynolds and Strouhal numbers, and hypothesising the functional form of the axial velocity profiles throughout the tube systems. This latter simplification is an *ad hoc* assumption common in vascular and collapsible tube modelling, where it has been shown to give results in agreement with higher-dimensional simulations or clinical data. In recognition of the *ad hoc* nature of the assumption, we have presented

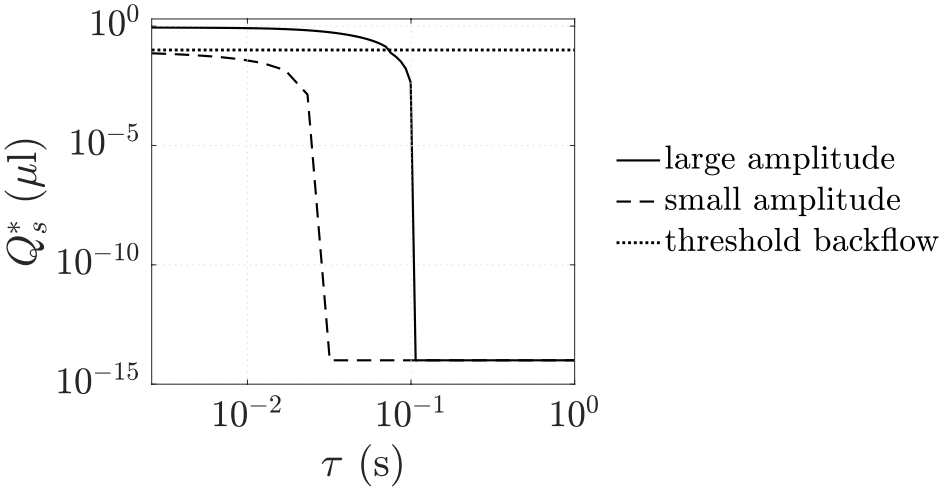

Figure 4.19: Comparison of the greatest continuous volume of backflow Q_s^* up the scaffold when pulsing the valves with large ($a = 0.95$, solid line) and small ($a = 0.1$, dashed line) amplitude valve oscillations, using the valve sequence in Figure 2.2. The valve period τ takes values in $[0.0026, 1]$ s. In the small-amplitude numerical scheme of §4.8.4, 600 timesteps are used; in the large-amplitude numerical scheme of §4.6, 512 spatial steps are used. The power law exponent is $\gamma = 2$ and other parameters are as in Table 2.1.

results that correspond to three different velocity profiles, including Poiseuille flow and flatter profiles. We may expect profiles closer to Poiseuille flow to be more suitable for slower valves, and flatter profiles to be more realistic for faster valves. To validate the model's accuracy for small amplitude valve oscillations, we have compared its results with a systematically-derived model for flow through the bioreactor with small amplitude valve oscillations, and found good agreement. To check the model's accuracy for the bioreactor valves, which may undergo large amplitude imposed valves oscillations (whereas vascular models incorporate compliant walls undergoing small elastic oscillations), it will be essential to perform three-dimensional numerical simulations of the Navier-Stokes equations in the valves in future work.

In Chapter 3 we showed that by using only static valve configurations we cannot reach typical shear stresses desired for *in vitro* platelet production. In this chapter we used our model to show that by continuously pulsing valves at a specified period it is possible to achieve scaffold shear stresses that lie within

target shear stress ranges for sustained periods of time. In contrast, pulsing valves only once was shown to have little effect on shear stress beyond the duration of the pulse itself. For illustrative purposes, we used a sequence of valve configurations expected to enhance shear stress (equivalent results for other sequences of valve configurations can be as readily obtained), and showed how valve period and amplitude can be chosen to target a shear stress range, while avoiding excessive scaffold backflow that disrupts platelet production. For the presented valve sequence, we additionally showed that pulsing the valves continuously at fast speeds gives a more concentrated product solution, relative to the product concentration obtained when valves are static. We conclude that, in comparison to the long periods of static valves punctuated by the isolated valve movements that were used by Shepherd et al. [137], continually pulsing valves therefore has the potential to enhance platelet production.

Another option for achieving higher shear stresses in the scaffold would be to redesign the bioreactor so that the flow is driven by pumps, as has been used in other bioreactors [27]. Peristaltic pumps in particular could be appropriate as they do not place a limit on the volume of cell culture media that can be passed through the bioreactor (in contrast to for example syringe pumps). If the pumps' flux dynamics are known, and the pumps are situated between the valves and inlets (or the valves are removed altogether), then the model in this chapter could be adapted to include pumps by prescribing boundary fluxes instead of prescribing the inlet pressures. The upper inlet pump would have to be removed when seeding the bioreactor to prevent interaction between the pump and cells, and placed far away enough from the scaffold to avoid contact with cells during bioreactor operation [137].

Up until now, we have used the fluid shear stress in a volume-averaged model of the scaffold to characterise the effect of flow on platelet formation. In the next chapter we turn to the cellular and subcellular scales level of platelet formation, to explore how an external flow interacts with cytoskeletal forces within proplatelets to regulate the onset of platelet formation.

Chapter 5

Modelling the elongation of proplatelets in flow

5.1 Introduction

As well as being interesting in its own right, understanding the cellular and subcellular mechanisms governing platelet production is important for developing treatments for platelet-related disorders, and informing the design of bioreactors targeted to support the mechanisms underlying platelet production. In this chapter we therefore turn to cell-scale and subcellular-scale modelling of platelet production. We model proplatelet elongation, which as described in §1.1 is an intermediate process that occurs after megakaryocyte maturation and before platelet release. Specifically, we study the stages of proplatelet elongation where the aspect ratio of proplatelet length to average diameter is small, as depicted in Figure 5.1.

The mechanisms underpinning proplatelet elongation are only partially understood. In particular, while there is evidence that proplatelet elongation is regulated by external flow, the mechanisms underlying this coupling are unknown. Mathematical modelling may be used as a tool to test hypotheses for proposed mechanisms. In this chapter we present preliminary work on two avenues for modelling proplatelets, with the intention of further exploring and extending both avenues in future work. In the first avenue, we take a simplest-first approach to constructing a model of proplatelet elongation that will be able to describe proplatelet shapes and elongation rates while immersed in flow. This avenue takes a more complex form for the subcellular machinery than the second avenue, but sacrifices accuracy

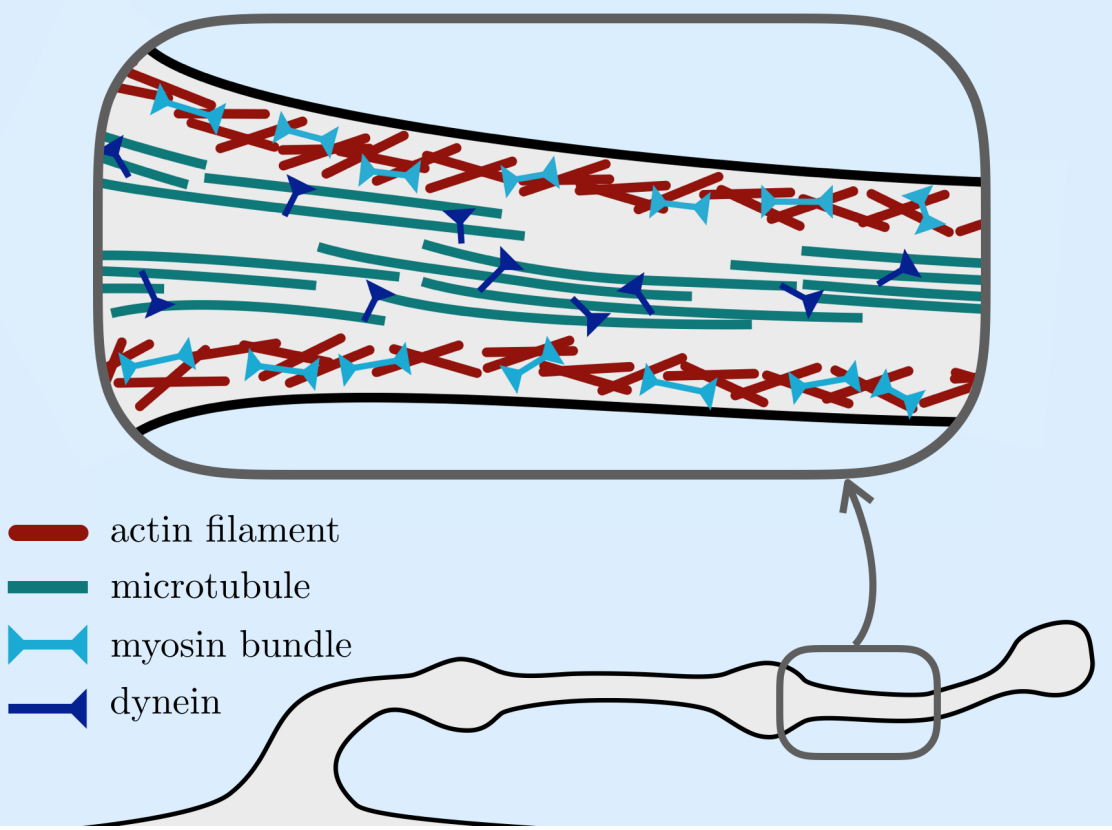

Figure 5.1: Schematic of a proplatelet elongating, showing essential features of the cytoskeletal structure. The inset shows bundles of microtubules (green) lining the proplatelet shaft and cross-linked by dynein (dark blue), and the cortical network of actin filaments (red) crosslinked by bundles of myosin (light blue). The black edge is the cell membrane.

in capturing the forces exerted by the external flow on the proplatelet. In the second avenue, we explore a more accurate method for computing these forces, coupled to a simpler constitutive law for the proplatelet than used in the first avenue. The work in this chapter provides a base for future work on hypothesis testing for mechanisms governing proplatelet elongation. This may for example include testing whether a model with purely mechanical coupling between external flow and the cytoskeleton can qualitatively reproduce experimentally observed proplatelet elongation dynamics, or whether a model including mechanotransductive coupling (where a mechanical stimulus is converted into biochemical signals) is better at mimicking experiment.

In §5.2 we review the biological background of proplatelet formation, focusing on what is known about the role of the cytoskeleton in driving proplatelet elongation. A literature review of modelling cytoskeleton-regulated cellular processes in flow that covers both modelling avenues is provided in §5.3, followed by an overview of the first modelling approach we take in §5.4.1. Details of the model, linear stability analysis, and preliminary numerical solutions are provided in §5.4.2-§5.4.6. An overview of the second modelling approach is given in §5.5.1, with details of the model in §5.5.3-§5.5.8, and results in §5.5.9. We end with a discussion in §5.6.

5.2 The biology of proplatelet formation

Proplatelet formation both *in vivo* and *in vitro* has been shown to involve elongation, pause, and retraction phases [14, 19], as demonstrated by the increase and decrease in proplatelet length over the timescale of minutes in Figure 5.2 a). These phases are thought to be predominantly driven by extensile microtubule bundles and contractile actin networks depicted in the inset of Figure 5.1. Below we discuss details of both of these cytoskeletal elements, and how their behaviour is modulated by flow.

The cell cortex is a contractile actomyosin network

Actin filaments (red in Figure 5.1) are helical polymers made of the protein actin, and are found mainly in the cell cortex, under the cell membrane [2]. The two ends of an actin filament differ structurally, with one denoted as positive and other as negative. They are arranged in a largely isotropic manner [58] and are cross-linked by the motor protein myosin (light blue in Figure 5.1), forming the cortical actomyosin network. Myosin molecules have a motile head domain, a short neck domain that acts as a lever arm, and a long tail domain. They assemble to form symmetric bipolar bundles of approximately 30 myosin molecules, where motor heads on each end of the bundle walk towards the positive end of actin filaments [22]. Although actomyosin networks have the potential to be either contractile or extensile, in practice cellular actomyosin constructs have been observed to be contractile overall [83]. The mechanism behind cellular actomyosin constructs

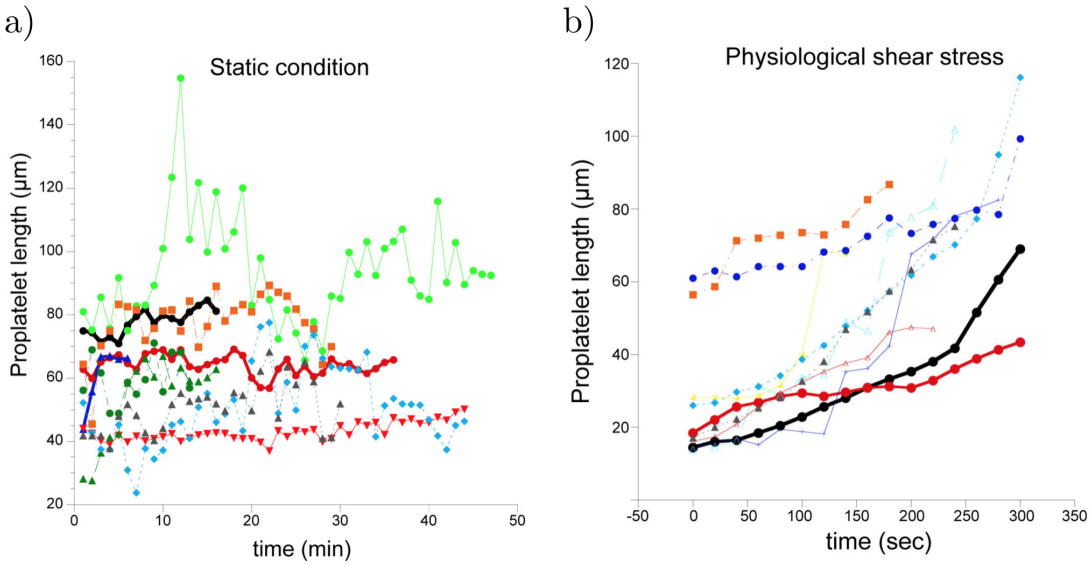

Figure 5.2: a) Proplatelet length against time in static culture, evidencing periods of elongation, pause, and retraction, within the overall elongation process. b) Pause and retraction periods are reduced under shear flow conditions similar to physiological conditions. Each line is a different proplatelet. Note in a) the unit of time is minutes, while in b) it is seconds. Figures are taken with permission from Bender et al. [14] SI Figures 1 c), d). (shear stress is only specified as 'physiological' in the paper [14]; hence we expect it to be in the range $0.086-0.28$ Pa, see equation (2.1)).

being contractile rather than extensile is unclear; multiple mechanisms have been suggested [83].

Actomyosin contraction may be enhanced by shear flow

Myosin-IIA is the myosin isoform that powers actomyosin network contraction [22]. In mice that are deficient in myosin-IIA, proplatelet pause and retraction phases are absent, which indicates that these phases are caused by contraction of the actomyosin cortex [19]. Shear past proplatelets has been shown to decrease phosphorylation of the amino acid Serine-1943 on the myosin tail, from approximately 14% to 5% upon application of 5 Pa of fluid shear stress over 15 min, thus increasing assembly of soluble cytoplasmic myosin-IIA into bipolar bundles [147]. We may therefore expect shear to promote actomyosin contraction and hence pro-

mote pause or retraction phases. However, evidence contradicts this: *in vitro* experiments have shown that pause and retraction phases occur less frequently when proplatelets are in physiological levels of shear flow (Figure 5.2 b)), relative to when they are in static culture (Figure 5.2 a)) [14]. As discussed below, this points to an interesting interaction between contractile and extensile forces in the proplatelet, and the external flow.

Microtubules slide to elongate proplatelets

Microtubules (green in Figure 5.1) are relatively rigid, long, hollow tubes made from the protein tubulin [2]. Similarly to actin filamemts, microtubules are polar, with a positive and negative end. *In vitro* observations have shown that at each proplatelet cross-section, at least four bundles of approximately ten microtubules line the shafts of proplatelets [71]. The microtubules are crosslinked by dynein (dark blue in Figure 5.1), which is an asymmetric motor protein whose motile head walks towards the minus end of microtubules [2]. Dynein causes extensile sliding of microtubules over each other in the proplatelet shaft [14], although the exact mechanisms that cause sliding to be overall extensile are not known. Microtubules polymerise mainly at their plus ends, and have been observed to continuously polymerise towards both the proplatelet tip and base, indicating that microtubule bundles in proplatelets have mixed polarity [117]. Thus one suggestion for the mechanism causing extensile motion is that dynein may mainly slide antiparallel microtubules apart from each other [14].

Microtubule sliding drives proplatelet elongation in static conditions

In the absence of flow, microtubules have been shown to be indispensible for proplatelet elongation: upon application of microtubule depolymerising drugs, megakaryocytes do not extend new proplatelets and retract already extended proplatelets [151]. It is particularly the dynein-driven sliding rather than the polymerisation of microtubules that is crucial [14]; this has been shown by proplatelet elongation being severely impaired after the treatment with dynein inhibitors, whereas treatment with microtubule-polymerisation inhibitors (but not depolymerisers) did not impair proplatelet elongation.

Shear stress enhances proplatelet elongation

As discussed in §1.1 and evidenced in Figure 5.2 b), experimental observations have shown that shear stress may substantially speed up proplatelet elongation. *In vivo*, if mice are deficient in myosin-IIA, proplatelet elongation continues to occur even when microtubules are depolymerised, and occurs at even higher rates than in wild-type mice [19]. Thus the flow of blood past proplatelets may contribute to proplatelet elongation.

Proplatelet elongation *in vitro* under physiological shear rates has been shown to be $30 - 40$ times faster than in static culture [14], with pause and contraction periods greatly reduced, as shown in Figure 5.2 b). It is not known whether faster elongation is caused by direct mechanical action of the flow stretching the cell membrane, or through mechanotransductive pathways, that could for example recruit more dynein to microtubules.

Details of how (shear-enhanced) elongation and contraction interact so as to result in pause, elongation and retraction phases is unclear. It has been suggested that the purpose of pause and retraction phases is to allow time for membrane reserves in the megakaryocyte to enter the proplatelet, or to contribute to enhancing membrane integrity [19]. There may also be cross-talk between microtubules and actin, via the multidomain proteins formin, which may play a role in actin nucleation, elongation, bundling, and alignment, and microtubule alignment, stabilisation, and bundling [170].

Bead formation is accelerated by flow

During proplatelet elongation bead-like swellings form along the length of the proplatelet [17], as shown in Figure 5.3. The formation of these swellings has also been shown to be accelerated by placing megakaryocytes in a flow environment. Recent computational modelling [8] approximated proplatelets as elastic membranes filled and surrounded by fluid, with anisotropic surface stresses to reflect isotropically contractile actomyosin and axially extensile microtubules. Varying the exterior flow conditions showed that a purely mechanical model could reproduce acceleration of bead formation under flow, suggesting that the bead formation may be predominantly mechanically accelerated.

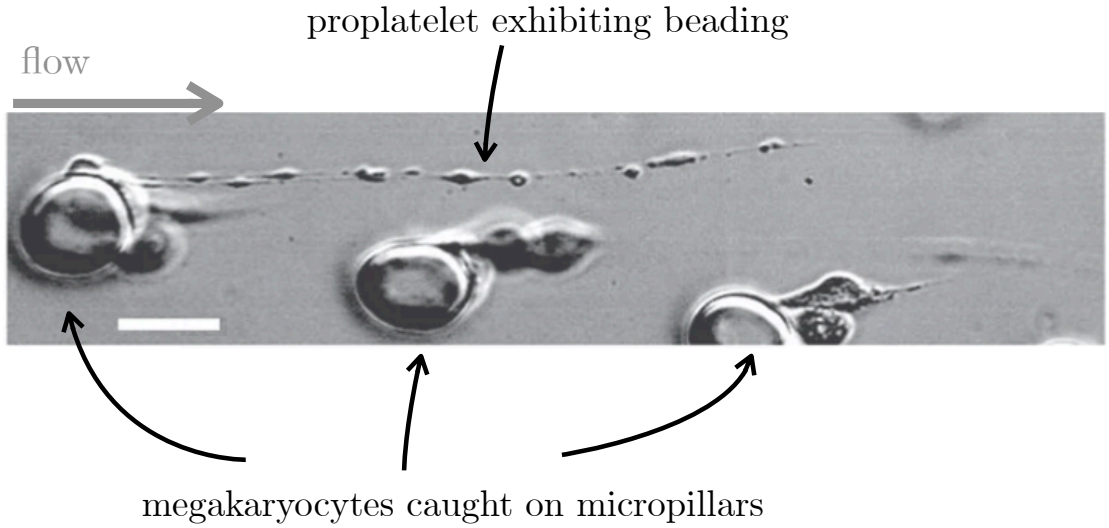

Figure 5.3: Beading on proplatelets: photo of megakaryocytes caught on micropillars in a microfluidic bioreactor, with proplatelets elongating into the flow and beaded structures forming along proplatelets. Image is taken with permission from Figure 3 a) in Blin et al. [17].

Summary of the biology of platelet formation

In the above we have discussed the aspects of the biology of platelet formation that are relevant to our modelling; here and in Figure 5.4 we summarise these aspects. Contractile and extensile forces compete with each other to give rise to phases of pause, extension and retraction, and beading structures along the proplatelet. There is evidence that both contractile and extensile forces may be enhanced by shear stress provided by an external flow: shear stress may increase myosin assembly, thereby increasing the contractility of the actomyosin cortex; shear stress also may increase extensile forces by enhancing the rate of microtubule sliding and/or mechanically stretching the proplatelet membrane. Observations to date *in vitro* generally show that shear stress reduces the duration of retraction and pause phases, suggesting that shear-enhanced extensile forces dominate any shear-enhanced contractile forces.

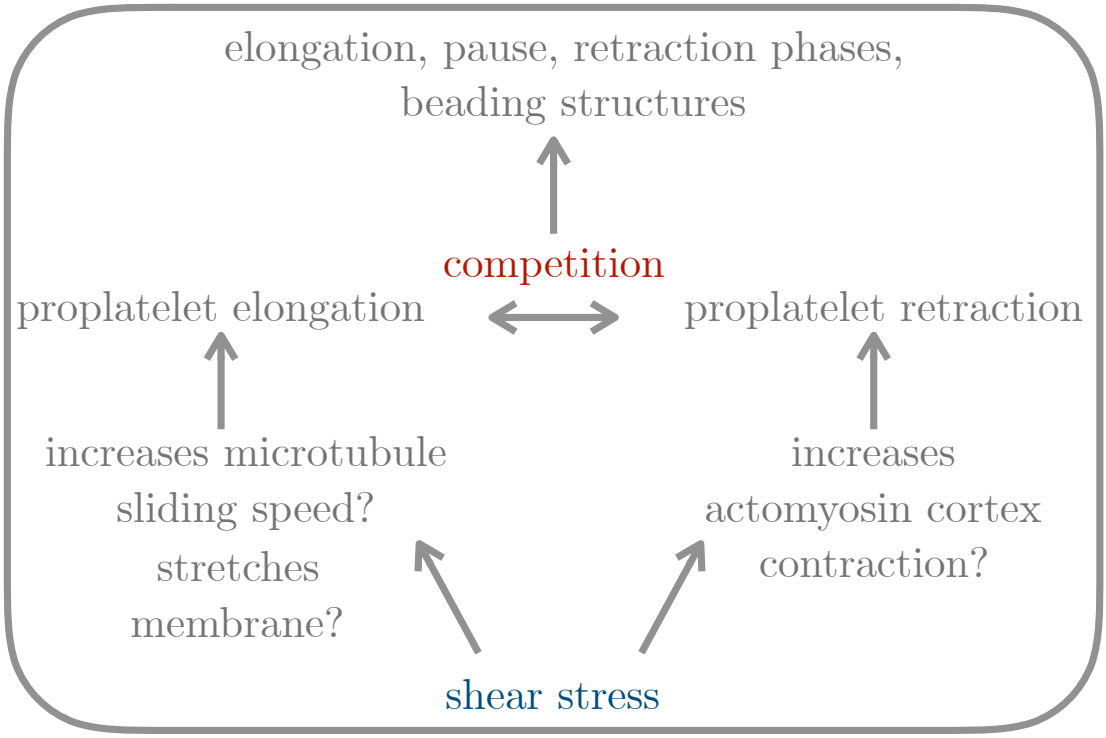

Figure 5.4: Diagram summarising factors regulating the process of proplatelet elongation and the potential impact of shear stress.

5.3 Modelling cytoskeleton-regulated cellular processes immersed in flow

5.3.1 Modelling the cytoskeleton

Many mathematical models of the cytoskeleton model individual actin and microtubule filaments. These models are used to study how the dynamics of actin and microtubule networks are affected by factors including actin filament/microtubule orientation and density, and motor cross-linker density, symmetry (whether each end of a motor walks or is passive), and correlation (the distribution of walking or passive motor ends on an actin filament/microtubule) [4, 38, 39, 166]. Interaction between the cytosol and cytoskeleton is typically modelled via a simple viscous drag law. For example, Zemel and Mogilner [166] modelled individual cytoskeletal filaments as rods in a one-dimensional bundle, moving according to force-velocity laws proportional to motor density and the sign of filament orientation. They compared highly and loosely crosslinked bundles, and explored the sensitivity of their dynamics to the boundary conditions. Others have further broken individual cytoskeletal filaments down into segmented pieces connected by springs, allowing for two-dimensional deformation of filaments. For example, Bidone et al. [15] modelled the transformation of an initially isotropic actomyosin network into a bundled structure using an agent-based model where each actin filament or cross-linker was made up of cylinders connected by elastic hinges. Even more fine-grained models have modelled the molecular structure of cytoskeletal filaments, such as the models of Molodtsov [105], who studied how the biochemical transformations within the tubulin dimers comprising microtubules regulate the dynamic instability of microtubules. Various computational packages have been developed for high resolution modelling of the cytoskeleton, incorporating stochastic chemical reactions, filament (de)polymerisations, cross-linker (un)binding, motor walking, and filament mechanics; see for example [121] and references therein.

In contrast to the above, continuum approaches to modelling the cytoskeleton track fields such as filament density, velocity, and local orientation as a function of space and time, and formulate constitutive laws for cytoskeletal stress in terms of these fields. Using tools from irreversible thermodynamics, general active gel theo-

ries [77] have been developed to act as continuum models that incorporate many of the physical effects relevant to the cytoskeleton [75]. Such theories unite previous modelling approaches that have included either permeation of the cytoskeleton by cytosol [5, 81, 113], where the cytoskeleton and cytosol are described as viscous fluids with the addition of an isotropic active stress in the cytoskeleton; viscoelastic single-phase gel descriptions incorporating nematic and polar active stresses [87, 157] (the descendents of Landau-de Gennes and Ericksen-Leslie liquid crystal models [146]); or poroelastic models considering the cytoskeleton as an elastic network permeated by the cytosol [20, 168]. Active gel theories can lack a clear connection to microscale quantities, hence some authors [51, 53, 88] have coarse-grained phenomenological microscale theories to demonstrate how the gel stress is affected by, for example, cross-linker symmetry or preferential attachment to the positive/negative filament end.

We are faced with a choice of whether to model individual microtubule and actin filaments, to use a continuum approach, or to use a multiscale method that averages over a fine-grained model to derive a continuum constitutive law. In the case of modelling proplatelets, we know the macroscale behaviour we expect to observe: elongation, pause, and retraction periods in static conditions, with an external shear flow enhancing elongation and inhibiting retraction. However, we lack detailed knowledge of characteristics such as the polarity of microtubules, the density and type of all the passive and motor cross-linkers in the cortex and microtubule bundles, and the coupling between external flow and the cytoskeleton. An option for modelling a proplatelet would be to build a high-resolution model containing individual microtubules, actin filaments, and cross-linkers, and see how varying the above quantities affects proplatelet dynamics. This could answer questions such as whether passive (in addition to motor) cross-linkers are required to mimic experimentally observed proplatelet dynamics.

However, to address our research questions it is sufficient to use a computationally lighter continuum model with fewer unknown parameters, where we prescribe the microtubule core to be extensile and the cortex to be contractile. A continuum rather than discrete approach is further justified because each proplatelet contains on the order of hundreds of microtubules [71], with each microtubule having radius

and length approximately 40 and 10 times smaller than the proplatelet, respectively [2], while each actin filament has radius and length approximately 100 and 500 times smaller than the proplatelet, respectively [2], with the cortex having a typical mesh-size of 100 nm [34]. As detailed in §5.4.1, in our first modelling avenue we will use a simple active gel model for the proplatelet, with the aim of making analytical progress while retaining the essential cytoskeletal features of proplatelets. In the second modelling avenue in §5.5.1, where our focus is on a more accurate and flexible method for coupling external flow with the proplatelet, we will simply treat the proplatelet as an inextensible elastic filament.

5.3.2 Reduced active gel models of cells

Proplatelets have small aspect ratios, thus a proplatelet model may be amenable to asymptotic reduction. A number of thin film, one-dimensional, or extensional flow models of the cytoskeleton as an active gel have been studied; here we review a few pertinent examples.

Kruse et al. [87] studied lamellipodia motility, focusing on actosmyosin contraction. They modelled a lamellipodium as a single-phase active gel moving with friction on a plate, with a free upper surface, all actin filaments nematically aligned in the axis of movement, and (de)polymerisation occurring at the surface only. They included a stress term proportional to the nematic tensor, which is a tensor that measures the orientational order of filaments, discussed further in §5.4.1. This term represented the anisotropic contraction of the actin network. In the extensional flow regime, Kruse et al. demonstrated how these contractile forces controlled the lamellipodium velocity. In our first modelling avenue in §5.4 we will similarly work in the extensional flow regime.

Bois et al. [18] modelled the regulation of cortical active stresses by a molecular species obeying reaction-diffusion-advection equations, in a one-dimensional, single-phase model of the cortex. With active stress taken to be an increasing function of the molecular species concentration, Bois et al. demonstrated amplification of molecular species concentration by advective flows driven by active stresses, leading to stable pattern formation. Mietke et al. [103] similarly modelled active stress regulation by molecular species, but in a spherical cell where the cortex was

modelled as a viscoelastic shell with isotropic active stresses, containing a cytosol modelled as a passive fluid. Rather than using a molecular species as an intermediary, we will in §5.4 start with the simpler assumption of relating active stresses directly to the fluid stress at the proplatelet boundary. In the second modelling avenue of §5.5 we will not couple the external flow to the proplatelet material properties.

A one-dimensional model for neurite motility by Recho et al. [129] shares some of the features we model, namely an actomyosin cortex surrounding a microtubule core. The former was modelled as an actively contractile viscous material with contractility proportional to a constant motor protein concentration, and the latter as a morphoelastic rod providing pushing (pulling) stress when the microtubule density was above (below) an equilibrium value. The microtubules in neurites are highly stable and do not undergo sliding as they do in proplatelets, making a purely elastic constitutive law appropriate. Using this model, Recho et al. determined how the occurrence of neurite growth, collapse, and pause are affected by the strength of the applied traction relative to actomyosin and microtubule stresses.

5.3.3 Modelling slender structures in flow

Proplatelets have small aspect ratios of proplatelet diameter to length, and are typically associated with small enough length and velocity scales to ensure that the surrounding flow may be modelled as Stokes flow. Thus to model proplatelet interaction with external flow we look to the large body of literature on the hydrodynamics of slender bodies immersed in Stokes flow, reviewed in [54] and frequently used to model flagella and cilia.

To solve for the forces exerted by Stokes flow on the boundary of the flow domain (which includes the proplatelet boundary), it is convenient to use the boundary integral formulation of Stokes flow: this relates the fluid velocity directly to the force density on the boundary. However, though allowing highly accurate results, it is computationally expensive to use boundary element methods [126] to solve the boundary integral formulation of Stokes flow in domains that contain objects of small aspect ratio.

Whereas the boundary integral formulation of Stokes flow relates the fluid velocity to the force per unit area on the boundary, slender body theories [76, 80, 95] exploit the body's small aspect ratio to relate fluid velocity to the force per unit length along the body centreline. The force per unit length is expressed as a combination of singular solutions (e.g. Stokeslets, rotlets, dipoles, sources) to the forced Stokes equations:

$$\mu\nabla^2\boldsymbol{u}_f = \nabla p_f - \boldsymbol{f}\delta(\boldsymbol{x}), \quad \nabla\cdot\boldsymbol{u} = 0, \tag{5.1}$$

where $\boldsymbol{u}_f$ is the fluid velocity, p_f is the fluid pressure, $\delta(\boldsymbol{x})$ is the delta function, and $\boldsymbol{f}$ is the line force density. It has been shown that slender body theories can be derived from the boundary integral equations using the method of matched asymptotic expansions [84], though originally they were derived by justifying *a posteriori* the positioning of point forces along the object centreline. The versions of slender body theories that are leading-order in the body's aspect ratio are called resistive force theories [60], which relate local body velocities to local fluid forces, neglecting non-local contributions. Due to their analytical tractability, we use a resistive force theory in the first modelling avenue in §5.4.

However, resistive force theories do not account for non-local hydrodynamics and, although they can be made to incorporate boundary effects, have been shown to lack accuracy even with such modifications [161]. In contrast to resistive force theories, higher-order slender body theories take into account non-local hydrodynamic effects and can account for simple boundaries such as a half-space. A difficulty presented by higher-order slender body theories is that they require evaluation of singular line integrals. To circumvent this issue we will in the second modelling avenue use a modified slender body theory developed by Cortez [36] and described in §5.5.1, involving *regularised* fundamental solutions being placed along the body centreline.

We are interested in forces exerted along a proplatelet by an external flow, at each arclength point along the proplatelet. The forces along a rigid rod, attached perpendicularly to a wall in a background shear flow were computed by Pozrikidis [125] using both a boundary element method and a slender body method. In a similar set-up but now allowing the cylinder to bend slightly, Pozrikidis reported the

wall shear stresses along the cylinder arclength [124], computed using a boundary element method.

Bächer et al. [8] have constructed the only mathematical model of a proplatelet that we are aware of, modelling the proplatelet as an active thin shell filled with and surrounded by $3D$ Stokes flow. They incorporated (anisotropic) extensile and (isotropic) contractile stresses on the proplatelet surface, and solved the fluid-structure interaction problem using an immersed-boundary lattice Boltzmann method. In contrast, our approach will be computationally lighter, and will incorporate stresses in the bulk of the proplatelet (not just its boundary), as well as coupling between active stresses and stresses from the external flow, thus providing a framework to contrast the dynamics of proplatelet elongation with and without coupling between these two sources of stress.

5.4 Model of a proplatelet as an axisymmetric active nematic gel immersed in viscous flow

5.4.1 Overview of modelling approach

We model the two main parts of the proplatelet cytoskeleton that regulate proplatelet elongation: the cell cortex and microtubule bundles. The proplatelet is modelled as an active gel with internal uniaxial active stresses caused by microtubule sliding, and active surface tension provided by the actomyosin cortex.

On timescales of up to tens of seconds, actin filaments and cross-linkers are fixed, thus the cortex may be considered as predominantly elastic [34, 133]. Dynamic replacement of proteins constituting actin filaments and crosslinkers occurs on timescales of minutes; on longer timescales the cortex behaves as a primarily viscous material. Microtubules similarly have a turnover time of minutes [25]. The timescale for proplatelet elongation and bead formation depends on the external flow: in static conditions proplatelets elongate over tens of minutes, while in flow they elongate over tens of seconds/minutes [19]. Thus, the timescale of proplatelet elongation under flow is comparable to the threshold timescale separating the elastic and viscous responses of proplatelets.

Motivated by modelling the simplest case first, we neglect elastic forces. We also assume the proplatelet is sufficiently highly cross-linked for momentum exchange via cytoskeletal networks to dominate momentum exchange via the cytosol, so that the cytosol and cytoskeletal networks move at the same speed [52]. As elastic forces and transport of momentum via the cytosol are both accounted for in general active gel theory [77], the model may be extended to incorporate them in future work. We neglect the effect of centreline curvature, and assume the proplatelet is axisymmetric: this is motivated by both the low curvature of the proplatelet centreline that we will observe in results from the second modelling avenue in §5.5.9, and also by approximately axisymmetric experimental set-ups, e.g. one where a microfluidic domain contains a micropillar that catches a megakaryocyte, similarly to in [17] (see Figure 5.3).

The microtubule sliding is incorporated as a uniaxial stress, appearing in the model through a stress term proportional to the nematic tensor [77], which measures the average local orientation of microtubules. We will assume that microtubules are uniaxial and aligned with the proplatelet centreline, in which case the nematic stress term will cause extension in the axial direction and contraction in the radial direction. As outlined by Jülicher et al. [77], in addition to a term directly proportional to the nematic tensor, the general stress tensor for an active nematic gel contains terms derived from the dependence of the system's free energy on the nematic tensor (e.g. using the Landau-de Gennes free energy for nematic liquid crystals [59]). However, as we assume that the nematic tensor has no spatial dependence in our case, these terms do not affect the momentum balance, thus we omit them here.

We model the external flow as an incompressible Newtonian fluid, which as mentioned in §2.5 is appropriate for modelling cell culture media. We assume the Reynolds number is sufficiently small that that we may use Stokes equations to model the fluid flow. This is justified as follows. Given a typical proplatelet length of 100 μm ([14]), cell culture viscosity 10^{-3} Pa s and density 10^3 kg/m^3, we need the typical flow velocity to be much smaller than 10^4 μm/s to ensure that the Reynolds number is much smaller than one. Assuming a typical microfluidic channel depth or scaffold pore diameter of 20 μm (close to for example the microfluidic device of Thon et al. [154], the perfusion chamber of Dunois et al. [43], or scaffold of

Shepherd et al. [137]), the shear rate should therefore be much less than $500\,\mathrm{s}^{-1}$. Hence we are generally modelling shear rates closer to those *in vivo* ($50.5-165\ \mathrm{s}^{-1}$ [98]), rather than the higher shear rates of up to $1800\ \mathrm{s}^{-1}$ [43, 154] used in some *in vitro* experiments. We use slender body theory to compute the forces exerted by the external flow on the proplatelet boundary. In the interest of making as much analytical progress as possible, we use only the leading-order terms in the axisymmetric slender body theory, i.e. we use resistive force theory.

To couple forces exerted by the external flow with the active cortex and microtubules stresses, we could introduce chemical messengers, governed by reaction-convection-diffusion equations similarly to in [103]. More simply, we could prescribe a direct relationship between the surface stress exerted by the fluid, and the active cortex and microtubule stresses. Either approach can be incorporated into the model below, which allows for active coefficients that vary in space and time. However, we will start with the simplest case when presenting preliminary results in §5.4.5 and §5.4.6, and consider constant active stresses that are not coupled to the external flow.

5.4.2 Governing equations and boundary conditions

We model an axisymmetric proplatelet with length $\ell(t)$ and boundary $r = a(z,t)$, as depicted in Figure 5.5. The proplatelet is modelled as an incompressible active nematic gel with viscosity μ, surrounded by a fluid of viscosity μ_f. The fluid

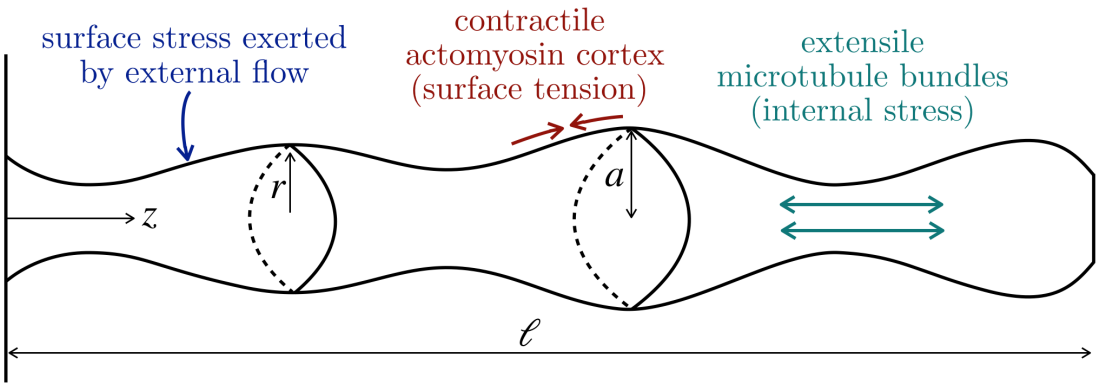

Figure 5.5: Schematic of a proplatelet as an axisymmetric active gel with radius a and length ℓ.

external to the proplatelet is governed by Stokes flow

$$\nabla \cdot \boldsymbol{\sigma}_f = 0, \tag{5.2a}$$

$$\nabla \cdot \boldsymbol{u}_f = 0, \tag{5.2b}$$

where

$$\boldsymbol{\sigma}_f = -p_f \boldsymbol{\mathcal{I}} + \frac{\mu_f}{2}\left(\nabla \boldsymbol{u}_f + \nabla \boldsymbol{u}_f^T\right) \tag{5.3}$$

is the external fluid stress tensor, $\boldsymbol{u}_f$ is the velocity and p_f is the pressure. The conservation of mass equation (5.2b) for an axisymmetric flow $\boldsymbol{u}_f = u_f \boldsymbol{e}_r + w_f \boldsymbol{e}_z$ is satisfied via the introduction of the Stokes streamfunction $\psi(r, z, t)$, in terms of which u_f and w_f are

$$u_f = -\frac{1}{r}\frac{\partial \psi}{\partial z}, \qquad w_f = \frac{1}{r}\frac{\partial \psi}{\partial r}. \tag{5.4}$$

Taking the curl of the momentum equation (5.2a) we can eliminate p_f and obtain an equation for the Stokes streamfunction,

$$\left(\frac{\partial^2}{\partial r^2} - \frac{1}{r}\frac{\partial}{\partial r} + \frac{\partial^2}{\partial z^2}\right)^2 \psi = 0. \tag{5.5}$$

The pressure p_f may be recovered after solving for ψ, by integrating the radial component of equation (5.2a) from r to infinity and prescribing an arbitrary pressure at infinity.

The momentum and mass balance equations inside the proplatelet are

$$\nabla \cdot \boldsymbol{\sigma} = 0 \tag{5.6a}$$

$$\nabla \cdot \boldsymbol{u} = 0, \tag{5.6b}$$

where the stress tensor is

$$\boldsymbol{\sigma} = -p \boldsymbol{\mathcal{I}} + \mu\left(\nabla \boldsymbol{u} + \nabla \boldsymbol{u}^T\right) - \zeta \boldsymbol{\mathcal{Q}}, \tag{5.7}$$

p is the pressure, and $\zeta(r, z, t)$ is the activity coefficient, which we allow to vary in space; for example, it may depend on z through the external stress $\boldsymbol{\sigma}_f$ on the boundary $r = a$. When the active stress is expansive in the direction of microtubule

orientation (as it is in our case), ζ is positive. As described in [77], the nematic tensor $\boldsymbol{\mathcal{Q}}$ is defined as

$$\mathcal{Q}_{ij}(\boldsymbol{x}) = \langle p_i^n p_j^n \rangle - \frac{1}{3}\langle p_k^n p_k^n \rangle \delta_{ij}. \tag{5.8}$$

Here subscripts i, j, k index vector or tensor components, and $\boldsymbol{p}^n$ is the orientation vector of a microtubule, indicating the direction that the plus end of the microtubule points in. The nematic tensor averages local orientations p_i^n of microtubules over all n microtubules in a local volume element through the averaging operation $\langle\cdot\rangle$, and is defined such that $\mathcal{Q}_{ij} = 0$ when the microtubules are isotropically arranged. Since we assume that the microtubules are uniaxial and aligned with proplatelet centreline, in our model $\boldsymbol{p}^n = \pm\boldsymbol{e}_z$ for all microtubules, so that

$$\boldsymbol{\mathcal{Q}} = \boldsymbol{e}_z \otimes \boldsymbol{e}_z - \frac{1}{3}\boldsymbol{\mathcal{I}}. \tag{5.9}$$

Thus with $\zeta > 0$, the active term in the stress tensor (5.7) causes extension in the axial direction and contraction in the radial direction. Writing the gel velocity in axial and radial components $\boldsymbol{u} = u\boldsymbol{e}_r + w\boldsymbol{e}_z$, the momentum balance (5.6a) in component form is

$$0 = \frac{1}{r}\frac{\partial(r\sigma_{rr})}{\partial r} + \frac{\partial \sigma_{rz}}{\partial z} - \frac{\sigma_{\theta\theta}}{r}, \tag{5.10a}$$

$$0 = \frac{1}{r}\frac{\partial(r\sigma_{rz})}{\partial r} + \frac{\partial \sigma_{zz}}{\partial z}, \tag{5.10b}$$

where the components of the proplatelet stress tensor $\boldsymbol{\sigma}$ (5.7) are

$$\sigma_{rr} = -p + 2\mu\frac{\partial u}{\partial r} + \frac{\zeta}{3}, \quad \sigma_{\theta\theta} = \frac{2\mu u}{r}, \tag{5.11a}$$

$$\sigma_{zz} = -p + 2\mu\frac{\partial w}{\partial z} - \frac{2\zeta}{3}, \quad \sigma_{rz} = \mu\left(\frac{\partial u}{\partial z} + \frac{\partial w}{\partial r}\right). \tag{5.11b}$$

Conservation of mass (5.6b) is

$$\frac{1}{r}\frac{\partial}{\partial r}(ru) + \frac{\partial w}{\partial z} = 0. \tag{5.12}$$

We impose the following interfacial and boundary conditions, starting with a kinematic boundary condition at the surface $r = a(z,t)$,

$$u = \frac{\partial a}{\partial t} + w\frac{\partial a}{\partial z}. \tag{5.13}$$

Continuity of velocity is prescribed as

$$(u, w) = \frac{1}{r}\left(-\frac{\partial \psi}{\partial z}, \frac{\partial \psi}{\partial r}\right) \quad \text{on} \quad r = a. \tag{5.14}$$

To model the contractile actomyosin cortex, we introduce a second active coefficient, the active tension $\gamma(z,t)$. This coefficient has no radial dependence but, like the internal activity coefficient ζ, may depend on the external stress $\boldsymbol{\sigma}_f$ on $r = a$ and therefore may vary in z. Following [92], we impose the following stress condition at the proplatelet boundary with surface tension γ:

$$(\boldsymbol{\sigma}_f - \boldsymbol{\sigma})\boldsymbol{n} = \gamma \boldsymbol{n}\,(\nabla \cdot \boldsymbol{n}) - (\nabla - \boldsymbol{n}(\boldsymbol{n} \cdot \nabla))\,\gamma; \tag{5.15}$$

here $\boldsymbol{n} = (\boldsymbol{e}_r - \boldsymbol{e}_z \partial a/\partial z)/\sqrt{(\partial a/\partial z)^2 + 1}$ is the unit normal pointing outwards from the proplatelet and γ may depend on $\boldsymbol{\sigma}_f$ at $r = a(z,t)$. In radial and axial components, equation (5.15) is

$$\sigma_f^r - \sigma_{rr} + \frac{\partial a}{\partial z}\sigma_{rz} = \frac{1}{|\tilde{\boldsymbol{n}}|}\frac{\partial a}{\partial z}\frac{\partial \gamma}{\partial z} + \frac{\gamma}{|\tilde{\boldsymbol{n}}|^3}\left(\frac{|\tilde{\boldsymbol{n}}|^2 a}{a^2} - \frac{\partial^2 a}{\partial z^2}\right), \tag{5.16a}$$

$$\sigma_f^z - \sigma_{rz} + \frac{\partial a}{\partial z}\sigma_{zz} = \frac{1}{|\tilde{\boldsymbol{n}}|}\frac{\partial \gamma}{\partial z} - \frac{\gamma}{a|\tilde{\boldsymbol{n}}|^3}\frac{\partial a}{\partial z}\left(|\tilde{\boldsymbol{n}}|^2 - a\frac{\partial^2 a}{\partial z^2}\right), \tag{5.16b}$$

where $|\tilde{\boldsymbol{n}}| = \sqrt{(\partial a/\partial z)^2 + 1}$, and the radial and axial external tractions are

$$\sigma_f^r = -p_f - 2\mu_f \frac{\partial u_f}{\partial r} - \mu_f \frac{\partial a}{\partial z}\left(-\frac{\partial u_f}{\partial z} + \frac{\partial w_f}{\partial r}\right), \tag{5.17a}$$

$$\sigma_f^z = -\mu_f \frac{\partial u_f}{\partial z} + \mu_f \frac{\partial w_f}{\partial r} - \frac{\partial a}{\partial z}\left(-p_f + 2\mu_f \frac{\partial w_f}{\partial z}\right), \tag{5.17b}$$

with u_f and w_f given in terms of the Stokes streamfunction ψ in equation (5.4). We prescribe symmetry conditions along the centreline

$$u = 0 \quad \text{and} \quad \frac{\partial w}{\partial r} = 0 \quad \text{on} \quad r = 0, \tag{5.18}$$

and a uniform background flow

$$\psi \sim \frac{u_{bg} r^2}{2} \quad \text{as} \quad r^2 + z^2 \to \infty. \tag{5.19}$$

To close the system we will also need boundary conditions at the proplatelet base and tip, and initial conditions. These are stated in §5.4.4 after performing an extensional flow reduction on the system.

5.4.3 Non-dimensionalisation

We non-dimensionalise as follows, so as to balance viscous stresses, active stresses, and active surface tension, and stay in the most general case possible:

$$(r, z) = L(\epsilon\hat{r}, \hat{z}), \;\; a = \epsilon L\hat{a}, \;\; \ell = L\hat{\ell}, \;\; \mu_f = \epsilon^2\mu\hat{\mu}_f \tag{5.20a}$$

$$t = \frac{L}{U}\hat{t}, \;\; (u, w) = U(\epsilon\hat{u}, \hat{w}), \;\; \psi = \epsilon^2 UL^2\hat{\psi}, \;\; u_{bg} = U\hat{u}_{bg} \tag{5.20b}$$

$$p = \frac{\mu U}{L}\hat{p}, \;\; p_f = \frac{\epsilon^2\mu\hat{\mu}_f U}{L}\hat{p}_f, \;\; \zeta = \frac{\mu U}{L}\hat{\zeta}, \;\; \gamma = \epsilon\mu U\hat{\gamma}. \tag{5.20c}$$

Here ϵ is the proplatelet aspect ratio of typical radius to typical length L, U is the typical speed of proplatelet elongation, and $\mu_f = \mathrm{O}(1)$ is the dimensionless external fluid viscosity, enforcing that the external fluid is much less viscous than the proplatelet. After non-dimensionalising, we drop hats.

Equation (5.5) for the Stokes streamfunction becomes

$$\left(\frac{\partial^2}{\partial r^2} - \frac{1}{r}\frac{\partial}{\partial r} + \epsilon^2\frac{\partial^2}{\partial z^2}\right)^2 \psi = 0, \tag{5.21}$$

and the corresponding dimensionless external fluid velocities (5.4) are

$$u_f = -\frac{\epsilon}{r}\frac{\partial\psi}{\partial z}, \;\; w_f = \frac{1}{r}\frac{\partial\psi}{\partial r}, \tag{5.22}$$

The proplatelet momentum equations (5.10) are

$$\frac{1}{r}\frac{\partial(r\sigma_{rr})}{\partial r} + \frac{\partial\sigma_{rz}}{\partial z} - \frac{\partial\sigma_{\theta\theta}}{r} = 0, \tag{5.23a}$$

$$\frac{1}{r}\frac{\partial(r\sigma_{rz})}{\partial r} + \epsilon^2\frac{\partial\sigma_{zz}}{\partial z} = 0, \tag{5.23b}$$

where the dimensionless stresses are defined (with hats dropped) as

$$\sigma_{rr} = -p + 2\frac{\partial u}{\partial r} + \frac{\zeta}{3}, \qquad \sigma_{\theta\theta} = \frac{2u}{r}, \tag{5.24a}$$

$$\sigma_{zz} = -p + 2\frac{\partial w}{\partial z} - \frac{2\zeta}{3}, \quad \sigma_{rz} = \epsilon^2\frac{\partial u}{\partial z} + \frac{\partial w}{\partial r}. \tag{5.24b}$$

The proplatelet mass equation (5.12), kinematic boundary condition (5.13) and the continuity of velocity condition (5.14) are unchanged. The stress boundary

conditions (5.16b) become

$$\epsilon^2\sigma_f^r - \sigma_{rr} + \frac{\partial a}{\partial z}\sigma_{rz} = \frac{\epsilon^2}{|\tilde{\boldsymbol{n}}|}\frac{\partial a}{\partial z}\frac{\partial \gamma}{\partial z} + \frac{\gamma}{|\tilde{\boldsymbol{n}}|^3}\left(\frac{|\tilde{\boldsymbol{n}}|^2 a}{a^2} - \epsilon^2\frac{\partial^2 a}{\partial z^2}\right) \tag{5.25a}$$

$$\epsilon^2\sigma_f^z + -\sigma_{rz} + \epsilon^2\frac{\partial a}{\partial z}\sigma_{zz} = \frac{\epsilon^2}{|\tilde{\boldsymbol{n}}|}\frac{\partial \gamma}{\partial z} - \epsilon^2\frac{\gamma}{a|\tilde{\boldsymbol{n}}|^3}\frac{\partial a}{\partial z}\left(|\tilde{\boldsymbol{n}}|^2 - \epsilon^2 a\frac{\partial^2 a}{\partial z^2}\right) \tag{5.25b}$$

where the dimensionless boundary tractions are

$$\sigma_f^r = \mu_f\left\{-p_f + 2\frac{\partial u_f}{\partial r} - \frac{\partial a}{\partial z}\left(\epsilon^2\frac{\partial u_f}{\partial z} + \frac{\partial w_f}{\partial r}\right)\right\}, \tag{5.26a}$$

$$\sigma_f^z = \mu_f\left\{\epsilon^2\frac{\partial u_f}{\partial z} + \frac{\partial w_f}{\partial r} - \epsilon^2\frac{\partial a}{\partial z}\left(2\frac{\partial w_f}{\partial z} - p_f\right)\right\}. \tag{5.26b}$$

The symmetry conditions (5.18) are unchanged, and the farfield flow condition (5.19) becomes

$$\psi \sim \frac{u_{bg} r^2}{2} \quad \text{as} \quad \epsilon^2 r^2 + z^2 \to \infty. \tag{5.27}$$

To obtain a solvability condition for use in §5.4.4, we integrate (5.23b) in the radial direction, yielding

$$a\left(\sigma_{rz} - \epsilon^2\frac{\partial a}{\partial z}\sigma_{zz}\right)\bigg|_{r=a} + \epsilon^2\frac{\partial}{\partial z}\int_0^a \sigma_{zz}\, r\, dr = 0. \tag{5.28}$$

5.4.4 Asymptotic reduction

We now exploit the small aspect ratio ϵ of the proplatelet to derive a leading-order system of PDEs for the radius a, length ℓ, and axial velocity w of the proplatelet. The derivation is similar to those of previous extensional flow models; see for example [69] for the equivalent reduction of an axisymmetric viscous fiber with surface tension. Since we have derived the relevant solvability condition (5.28) from the cross-sectionally averaged axial momentum equation (5.23b), we do not need to proceed to higher order and therefore do not introduce subscripts, denoting leading-order variables by the variables' original notations.

At leading order, the axial momentum equation (5.23b) is

$$\frac{1}{r}\frac{\partial}{\partial r}\left(r\frac{\partial w}{\partial r}\right) = 0, \tag{5.29}$$

which we solve subject to the symmetry condition (5.18) $\partial w/\partial r = 0$ at $r = 0$ to find that w is independent of the radial coordinate, i.e. the flow is extensional, with

$$w = w(z, t). \tag{5.30}$$

Using the leading-order mass equation (5.12) and the symmetry condition (5.18) that $u = 0$ at $r = 0$, we find that the leading-order radial velocity u in terms of w is

$$u = -\frac{r}{2}\frac{\partial w}{\partial z}. \tag{5.31}$$

Solving the leading-order version of the radial momentum equation (5.23a), namely

$$\frac{\partial p}{\partial r} = \frac{\partial^2 u}{\partial r^2} + \frac{1}{r}\frac{\partial u}{\partial r} - \frac{u}{r^2} + \frac{1}{3}\frac{\partial \zeta}{\partial r}, \tag{5.32}$$

subject to the leading-order version of the radial stress condition (5.25a) on $r = a$,

$$p = 2\frac{\partial u}{\partial r} - \frac{\partial a}{\partial z}\frac{\partial w}{\partial r} + \frac{\zeta}{3} + \frac{\gamma}{a} - \epsilon^2\gamma\frac{\partial^2 a}{\partial z^2}, \tag{5.33}$$

and using equation (5.31) for u, we obtain the solution for p in terms of a and w:

$$p = -\frac{\partial w}{\partial z} + \frac{\zeta}{3} + \frac{\gamma}{a} - \epsilon^2\gamma\frac{\partial^2 a}{\partial z^2}. \tag{5.34}$$

Here we have retained the $\mathrm{O}(\epsilon^2)$ curvature term from equation (5.25a), motivated by its inclusion in similar models for droplet formation, where it is included to stabilize arbitrarily small wavelengths [45].

Using the axial stress boundary condition (5.25b), we find that the first term in the solveability condition (5.28) is, at leading-order,

$$a\left(\sigma_{rz} - \epsilon^2\frac{\partial a}{\partial z}\sigma_{zz}\right)\bigg|_{r=a} = \epsilon^2 a\left(\mu_f\frac{\partial w_f}{\partial r} - \frac{\partial \gamma}{\partial z} + \frac{\gamma}{a}\frac{\partial a}{\partial z}\right). \tag{5.35}$$

Substituting the leading-order pressure (5.34) into the expression (5.24b) for σ_{zz}, we find that

$$\sigma_{zz} = 3\frac{\partial w}{\partial z} - \zeta - \frac{\gamma}{a} + \epsilon^2\gamma\frac{\partial^2 a}{\partial z^2}. \tag{5.36}$$

Finally, substituting equations (5.35) and (5.36) into equation (5.28), and retaining only leading-order terms, we obtain

$$\frac{\partial}{\partial z}\left\{\frac{a^2}{2}\left(3\frac{\partial w}{\partial z} - \frac{\gamma}{a} + \epsilon^2\gamma\frac{\partial^2 a}{\partial z^2}\right) - \int_0^a \zeta\, r\, dr\right\} - a\frac{\partial \gamma}{\partial z} + \gamma\frac{\partial a}{\partial z} + a\mu_f\frac{\partial w_f}{\partial r} = 0. \tag{5.37}$$

where the expression in braces is the leading order tension in the fibre, divided by 2π.

Using the expression (5.31) for u in the kinematic boundary condition (5.13) on $r = a$, we obtain

$$\frac{\partial}{\partial t}(a^2) + \frac{\partial}{\partial z}(a^2 w) = 0. \tag{5.38}$$

We now use slender body theory to derive an expression for the leading-order traction,

$$\sigma_f^z = \mu_f \frac{\partial w_f}{\partial r} = \mu_f \frac{\partial}{\partial r}\left(\frac{1}{r}\frac{\partial \psi}{\partial r}\right), \tag{5.39}$$

exerted on the proplatelet surface by the external flow. This is standard in the literature (e.g. [155]), so we present only a brief outline of the derivation. Slender body theory involves positing a solution for the Stokes streamfunction ψ, consisting of a contribution for the far-field flow, plus a distribution of sources with strengths $q(s,t)$ and Stokeslets with strengths $f(s,t)$ along the proplatelet centreline:

$$\psi(r,z,t) = \frac{u_{bg} r^2}{2} + \int_0^\ell \frac{-q(s,t)(z-s)ds}{4\pi\sqrt{\epsilon^2 r^2 + (z-s)^2}} + \int_0^\ell \frac{f(s,t) r^2 ds}{8\pi\sqrt{\epsilon^2 r^2 + (z-s)^2)}}. \tag{5.40}$$

The two degrees of freedom in f and q are used to enforce continuity of velocity (5.14) at the proplatelet boundary. The integrals in (5.40) are expanded in the limit as $\epsilon \to 0$. As the integrals in (5.40) are singular at $s = z$, this is done by splitting the integration domain into one region near to z, and the remainder of the centreline. Retaining terms up to order unity, the streamfunction $\psi(r,z,t)$ is

$$\psi = \frac{u_{bg} r^2}{2} - r^2 \log\left(\frac{\epsilon r}{2}\right)\frac{f}{4\pi} + \frac{r^2}{8\pi}\fint_0^\ell \frac{f(s,t)}{|z-s|}\,ds + \frac{1}{4\pi}\int_0^\ell q(s,t)\,\mathrm{sgn}(s-z)\,ds. \tag{5.41}$$

We note that the neglected higher-order terms are $\mathrm{O}(\epsilon^2 \log \epsilon)$ and that the third term involves the regular integral

$$\fint_0^\ell \frac{f(s,t)}{|z-s|}ds = \int_0^\ell \frac{f(s) - f(z)}{|z-s|}ds + f(z)\log(1-z^2). \tag{5.42}$$

Using the expression (5.41) for ψ, we compute the leading-order traction (5.39) to be

$$\mu_f \frac{\partial}{\partial r}\left(\frac{1}{r}\frac{\partial \psi}{\partial r}\right) = -\frac{\mu_f f}{2a\pi}. \tag{5.43}$$

Using continuity of velocity, $w = (1/r)\partial\psi/\partial r$ on $r = a$ (from equation (5.14)), we find that the proplatelet axial velocity w and the Stokeslet distribution f are related via

$$w(z,t) = u_{bg} + \left\{2\log\left(\frac{2}{\epsilon a}\right) - 1\right\}\frac{f}{4\pi} + \frac{1}{4\pi}\int_0^\ell \frac{f(s,t)}{|z-s|}ds, \tag{5.44}$$

with an error or $\mathrm{O}(\epsilon^2\log\epsilon)$. The first and third terms in equation (5.44) are of $\mathrm{O}(1)$, while the second term is of $\mathrm{O}(\log(1/\epsilon))$, and therefore dominates as $\epsilon \to 0$. The third term in equation (5.44) also makes the equation substantially more difficult to solve for f in terms of w as it involves an integral; we therefore drop this term in the following, thereby introducing errors of $\mathrm{O}(1/\log(1/\epsilon))$ into the model. Doing so corresponds to using the simplest slender body theory, known as resistive force theory:

$$w(z,t) = u_{bg} + \left\{2\log\left(\frac{2}{\epsilon a}\right) - 1\right\}\frac{f}{4\pi}. \tag{5.45}$$

Using equations (5.43) and (5.45) to write the leading-order axial traction in terms of the proplatelet velocity w, the axial force balance (5.37) becomes

$$\frac{\partial}{\partial z}\left\{\frac{a^2}{2}\left(3\frac{\partial w}{\partial z} - \frac{\gamma}{a} + \epsilon^2\gamma\frac{\partial^2 a}{\partial z^2}\right) - \int_0^a \zeta\, r\, dr\right\} + \gamma\frac{\partial a}{\partial z} - a\frac{\partial \gamma}{\partial z} - \chi(w - u_{bg}) = 0, \tag{5.46}$$

where we have defined the drag coefficient

$$\chi(a) = \frac{2\mu_f}{2\log\left(2/(\epsilon a)\right) - 1} \tag{5.47}$$

The terms in (5.46) that are novel (compared to what is typically seen in the literature for extensional flow modelling) are the terms involving spatial derivatives of γ, and the extensile ζ term. Finally, we prescribe base and tip boundary conditions and initial conditions:

$$w = w_{base} \quad \text{and} \quad a = a_{base} \qquad \text{at} \quad z = 0, \tag{5.48a}$$

$$w = \frac{d\ell}{dt}, \quad \mathcal{T} = \mathcal{T}_\ell, \quad a = 0, \quad \text{and} \quad \frac{\partial a}{\partial z} = 0 \quad \text{at} \quad z = \ell, \tag{5.48b}$$

where w_{base} is the prescribed influx of material from the megakaryocyte body into the proplatelet, a_{base} is the radius at the base, $\mathcal{T}_\ell$ is the prescribed tension at the tip, and $\mathcal{T}$ is the leading-order tension, which is given by

$$\mathcal{T} = \pi a^2\left(3\frac{\partial w}{\partial z} - \frac{\gamma}{a} + \epsilon^2\gamma\frac{\partial^2 a}{\partial z^2}\right) - 2\pi\int_0^a \zeta r\, dr, \tag{5.49}$$

since

$$\mathcal{T} = \int_0^{2\pi} \int_0^a \sigma_{zz}\, r dr d\theta. \tag{5.50}$$

As will be discussed in §5.6, it is not clear how the tension $\mathcal{T}_\ell$ at the tip, where resistive force theory breaks down, should be chosen. We could for example prescribe zero tension, as we may expect the drag in such a small region to be negligible, or we could choose the tension to be that on a sphere with the radius of a platelet, because experimental observations have shown that platelets form at the tip of proplatelets [71]. Since equation (5.46) includes the curvature term involving three spatial derivatives of a, to close the system we have included two boundary conditions on a at $z = \ell$. These correspond to a proplatelet that smooths to zero radius at its tip, as seems to agree with experimental observations.

The initial conditions for the system are

$$a = a_{init} \quad \text{and} \quad \ell = \ell_{init} \quad \text{at} \quad t = 0. \tag{5.51}$$

The reduced systems for (w, a, ℓ) thus consists of equations (5.38) and (5.46), subject to boundary conditions (5.48) at the proplatelet base and tip, and initial conditions (5.51).

5.4.5 Linear stability analysis

In this section we conduct a linear stability analysis of equations (5.38) and (5.46) when the active coefficients ζ and γ are constant, and there is no background flow, $u_{bg} = 0$. In this case, there exists a constant solution $(w, a, \ell) = (0, \bar{a}, \bar{\ell})$. We introduce small amplitude perturbations

$$a = \bar{a} + \delta \widetilde{a} e^{ikz+\lambda t}, \qquad w = \delta \widetilde{w} e^{ikz+\lambda t}, \tag{5.52}$$

where $\delta \ll 1$, $\widetilde{a}$ and $\widetilde{w}$ are constants, k is the wavenumber, and λ is the growth rate of the perturbation. Inserting (5.52) into equations (5.37) and (5.46) gives

$$-3k^2\bar{a}^2\widetilde{w} - 2ik\zeta\bar{a}\widetilde{a} - ik\gamma\widetilde{a} - \epsilon^2 ik^3\bar{a}^2\widetilde{a} = -2ik\gamma\widetilde{a} + 2\chi\widetilde{w}, \tag{5.53a}$$

$$2\lambda\bar{a}\widetilde{a} + ik\bar{a}^2\widetilde{w} = 0, \tag{5.53b}$$

respectively. Combining equations (5.53a) and (5.53b), we obtain the dispersion relation

$$\lambda = \frac{k^2\bar{a}\left(\gamma - 2\zeta\bar{a} - \epsilon^2 k^2\gamma\bar{a}^2\right)}{6k^2\bar{a}^2 + 4\chi}. \tag{5.54}$$

Setting the internal active coefficient $\zeta = 0$ and the external fluid viscosity $\mu_f = 0$ recovers the dispersion relation for a thin axisymmetric filament of viscous fluid [44]. The minus sign in front of ζ in (5.54) indicates that the extensile stress acts as a stabiliser to small perturbations, whereas the contractile surface tension γ destabilises at leading-order, and stabilises at higher-order through the curvature term proportional to ϵ^2.

In Figure 5.6 we plot the dispersion relation (5.54) with active surface tension $\gamma = 1$, and with and without active extensile stress ζ and the higher-order curvature term (the latter of which as mentioned above we have included on an *ad hoc* basis, as is standard in the droplet literature). Figure 5.6 shows that without this higher-order term, the growth rate $\lambda(k)$ remains positive as $k \to \infty$ if there

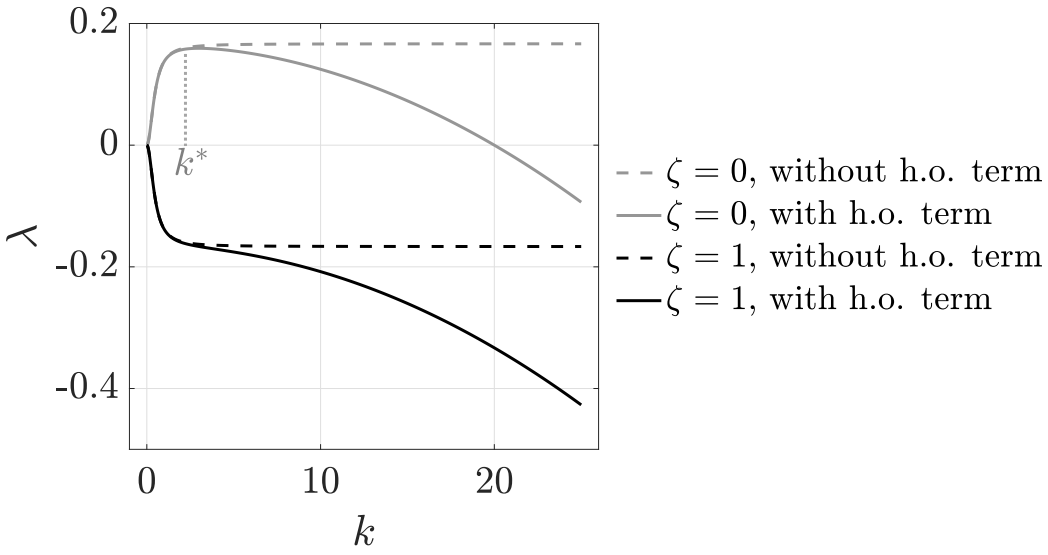

Figure 5.6: Dispersion relation between wavenumber k and growth rate λ for the proplatelet with constant active coefficients, given by equation (5.54). Black lines are $\zeta = 1$, grey lines are $\zeta = 0$, with (solid) and without (dashed) the higher-order curvature term proportional to ϵ^2. The wavenumber k at which maximum growth λ occurs is labelled by k^*. The contractile surface tension is $\gamma = 1$, the base radius is $\bar{a} = 1$ and the proplatelet aspect ratio is $\epsilon = 0.05$.

is no extensile active stress $\zeta = 0$ (grey dashed line), which is unphysical, but is negative for wavenumbers $k \gtrsim 1/\epsilon$ when the higher-order term is included (grey solid line). The wavenumber k^* at which the maximum growth rate λ occurs gives us a prediction, $2\pi/k^*$, of the typical length of a beaded structure on a sufficiently long proplatelet when dynein is inhibited (thereby inhibiting microtubule sliding). This is a model output that we may compare with experimental data in future work. If we set $\zeta = 1$ then λ is negative for all k, though bounded below by $k > (\lambda - 2\zeta\bar{a})/(6\bar{a})$ when the higher-order term is not included (black dashed line), while when including the higher-order curvature term λ is unbounded below as $k \to \infty$ (black solid line).

Figure 5.7 a) demonstrates the effect of increasing the active coefficient ζ: for $\zeta < \gamma/(2\bar{a})$, there is a band of unstable wavenumbers $k^2 < (\gamma - 2\zeta\bar{a})/(\epsilon^2\bar{a}\gamma)$, while for $\zeta > \gamma/(2\bar{a})$ the system is stable to all perturbations. In Figure 5.7 b) we see that increasing the active surface tension γ has a destabilising effect. Due to the presence of positive and negative terms with γ in the dispersion relation (5.54), there is also a stabilising effect for higher wavenumbers as γ increases, with perturbations with wavenumber $k \gtrsim 1/\epsilon$ decreasing more rapidly as γ increases (the dispersion relations cross over at approximately $(k, \lambda) = (1/\epsilon, (\gamma(1 - \bar{a}^2) - 2\zeta\bar{a})/6\bar{a}))$.

We can use this instability analysis, with zero background flow, to make some initial predictions on the typical size of a bead. To do so we compute the wavenumber k^* corresponding to the maximum growth rate, for $\gamma/\zeta \in [10^{-2}, 10^3]$, and find that k^* is positive for $\gamma/\zeta \gtrsim 2$, $k^* > 2.5$ for $\gamma/\zeta \gtrsim 4$, and k^* appears to asymptote to 3 as γ/ζ increases. This indicates that each bead is up to one third the length of a typical proplatelet, which when making comparisons with images of proplatelet formation in static culture [19, 72] at least seems to be approximately correct (with the caveat that proplatelets are relatively tangled and certainly not axisymmetric in [19, 72]).

This basic instability analysis indicates that the active coefficients have the capacity to control instabilities of the homogeneous proplatelet, suggesting a route for platelet formation. It would be interesting to see whether, after calibrating ζ and γ, the maximum growth rate predicted by the model is observed in practice. It is unclear however how this instability mechanism is affected by the dynamics of the elongating proplatelet.

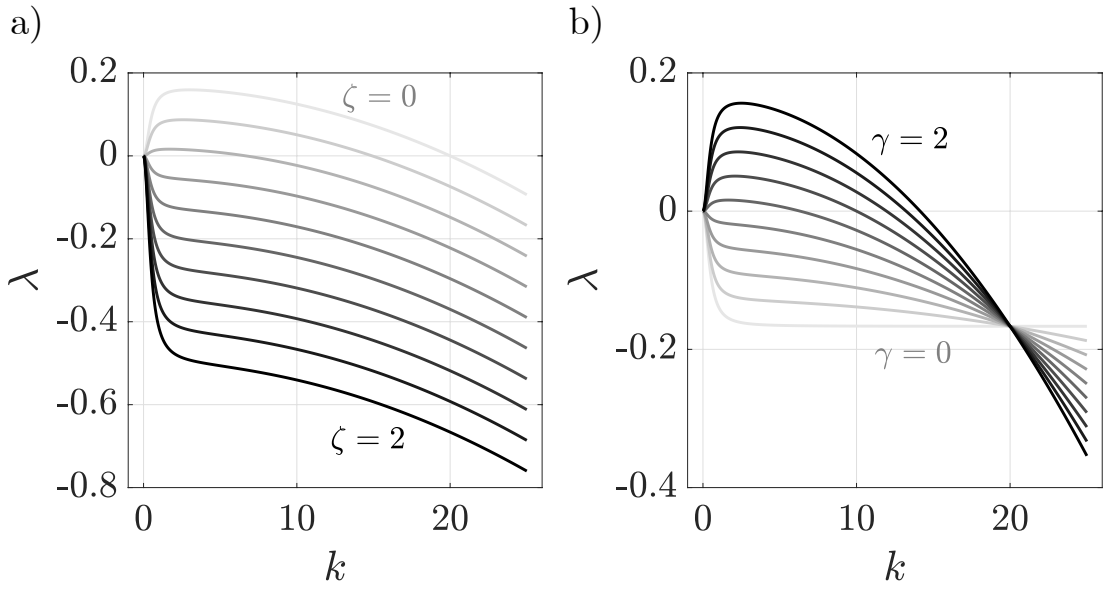

Figure 5.7: Dispersion relation for the proplatelet with constant active coefficients, given by equation (5.54), varying a) the extensile coefficient ζ and b) contractile coefficient γ from zero (grey) to two (black), at regular intervals. In a) $\gamma = 1$ and in b) $\zeta = 0.5$, and in both the base radius is $\bar{a} = 1$ and the proplatelet aspect ratio is $\epsilon = 0.05$.

5.4.6 Preliminary numerical simulations

5.4.6.1 Transformation to a fixed domain

In this section, we conduct some preliminary numerical investigations into the effect of a constant active extensile coefficient and a constant background flow on the proplatelet dynamics. To do so, we first transform to a fixed domain for the proplatelet length. We define $Z(z,t) = z/\ell$, $T = t$, and $w(z,t) = \ell W(Z,T) + \dot{\ell} Z$, where dot denotes differentiation with respect to time. We do not transform the radial coordinate r, and we slightly abuse notation to write $a(z,t)$ as $a(Z,T)$, $\ell(t)$ as $\ell(T)$, $\gamma(z,t)$ as $\gamma(r,Z,T)$, and $\zeta(r,z,t)$ as $\zeta(r,Z,T)$. The proplatelet is now located in $Z \in [0,1]$ and $r < a(Z,T)$. The kinematic condition (5.38) transforms to

$$\frac{\partial}{\partial T}(\ell a^2) + \frac{\partial}{\partial Z}(\ell a^2 W) = 0, \tag{5.55}$$

so that ℓa^2 is now the conserved quantity (c.f. equation (5.37)), while the axial momentum balance (5.46) transforms to

$$\frac{\partial}{\partial Z}\left\{\frac{a^2}{2}\left(\frac{3\dot{\ell}}{\ell}+3\frac{\partial W}{\partial Z}-\frac{\gamma}{a}+\frac{\epsilon^2\gamma}{\ell^2}\frac{\partial^2 a}{\partial Z^2}\right)-\int_0^a \zeta\, r\, dr\right\} + \gamma\frac{\partial a}{\partial Z}-a\frac{\partial \gamma}{\partial Z}-\chi\ell(\dot{\ell}Z+\ell W-u_{bg})=0. \quad (5.56)$$

The boundary conditions (5.48) become

$$W=\frac{w_{base}}{\ell} \quad \text{and} \quad a=a_{base} \quad \text{at} \quad Z=0, \quad (5.57a)$$

$$W=0 \quad \text{and} \quad \mathcal{T}=\mathcal{T}_\ell \quad \text{at} \quad Z=1, \quad (5.57b)$$

where the tension $\mathcal{T}$ in terms of the transformed variables is given by 2π times the expression in braces in equation (5.56). The initial conditions (5.51) remain the same, i.e.

$$a=a_{init} \quad \text{and} \quad \ell=\ell_{init} \quad \text{at} \quad t=0. \quad (5.58)$$

5.4.6.2 Numerical scheme

In this section, we work with equation (5.55) in the form

$$\frac{\partial}{\partial T}(a^2)+\frac{\partial}{\partial Z}(a^2W)=-\frac{\dot{\ell}a^2}{\ell}, \quad (5.59)$$

and we will solve a simpler version of equation (5.56), namely

$$\frac{\partial}{\partial Z}\left\{\frac{a^2}{2}\left(\frac{3\dot{\ell}}{\ell}+3\frac{\partial W}{\partial Z}-\frac{\gamma}{a}-\zeta\right)\right\}+\gamma\frac{\partial a}{\partial Z}-\chi\ell(\dot{\ell}Z+\ell W-u_{bg})=0, \quad (5.60)$$

where for simplicity we omit the regularisation term proportional to ϵ^2 (hence we may expect numerical simulations to become increasingly stiff as γ increases), and set γ, ζ and u_{bg} to be constants. To solve equations (5.59) and (5.60) subject to boundary conditions (5.57) and initial conditions (5.58), we use a modified version of the code of [165], described below.

We discretise the spatial domain $Z \in [0,1]$ into N segments with $N+1$ nodes and a spatial step size of $\Delta Z = 1/N$, and denote the proplatelet velocity or radius squared at the n^{th} node by $\phi(n\Delta Z, t)=\phi_n$, $n=0,...,N$ for $\phi \in \{W, a^2\}$.

For nodes $n = 2, ..., N-2$, the hyperbolic term in equation (5.59) is discretised in space using the third-order version of the CWENO scheme of Kurganov and Levy [89], which involves a five-point stencil. We use the third-order version of the scheme because it is of similar coding complexity to the second-order CWENO scheme (which also involves a 5-point stencil) but will yield more accurate results for a given number N of spatial segments. For nodes $n = 0, 1$ and $n = N-1, N$, the hyperbolic term in equation (5.59) is discretised using fourth order forward and backward differences, respectively.

The tension boundary condition $\mathcal{T} = \mathcal{T}_\ell$ at $Z = 1$ in equation (5.57) can be written as

$$\dot{\ell} = \frac{2\ell}{3a^2}\left(\frac{\mathcal{T}_\ell}{2\pi} + \frac{a^2\zeta}{2} + \frac{\gamma}{a} - 3\frac{\partial W}{\partial Z}\right) \quad \text{at} \quad Z = 1. \tag{5.61}$$

We spatially discretise the $\partial W/\partial Z$ term at $Z = 1$ in equation (5.61) using fourth order backward differences. This leaves us with an ODE in time for ℓ, which we use to replace the $\dot{\ell}$ term in equations (5.59) and (5.60) with algebraic terms. In total, we have $N + 1$ ODEs in time: N for $(a^2)_n$ from the spatial discretisation of equation (5.59), plus one for ℓ.

The spatial derivatives in equation (5.60) are discretised using fourth-order central differences for nodes $n = 2, ..., N-2$. We use fourth-order finite differences for $N = 1, N-1$, with stencil points at $z = j\Delta Z$, for $j - n \in \{-1, 0, 1, 2, 3\}$ when $n = 1$, and $j - n \in \{-3, -2, -1, 0, 1\}$ when $n = N-1$. The spatial discretisation of equation (5.60) therefore gives us obtain $N - 1$ algebraic equations to solve at each timestep. The boundary conditions $W(0, T) = w_{base}/\ell$ and $W(1, T) = 0$ given in equation (5.57) fix the base and tip nodal velocities to be $W_0 = w_{base}/\ell$ and $W_N = 0$.

In total, we have $N+2$ ODEs in time for ℓ and $(a^2)_n$, $n = 0, ..., N$, supplemented by $N + 1$ algebraic constraints. We solve these equations for the $2N + 3$ variables $(a^2)_n, W_n, \ell,\ n = 0, ..., N$ using the inbuilt MATLAB ODE solver ode15s, with initial conditions (5.58) on $(a^2)_n$ and ℓ.

We validate the numerical scheme for $(\zeta, \gamma, u_{bg}) = (1, 0, 0)$ and $(\zeta, \gamma, u_{bg}) = (0, 0, 1)$, with $w_{base} = 0$ and $\mathcal{T}_\ell = 0$, by computing the L^∞ error

$$\mathcal{E}(t) = \max_{\substack{z\in[0,\ell] \\ \phi\in\{a,w\}}} \left|\phi(z, t) - \widetilde{\phi}(z, t)\right|, \tag{5.62}$$

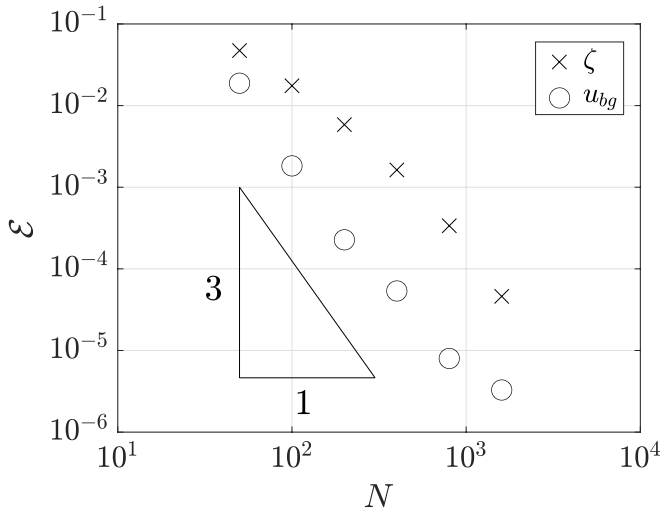

Figure 5.8: The L^∞ error $\mathcal{E}$ against the number of spatial steps N, evaluated at $t = 150$ for $(\zeta, \gamma, u_{bg}) = (1, 0, 0)$ (crosses), and at $t = 4.5$ for $(\zeta, \gamma, u_{bg}) = (0, 0, 1)$ (circles), using the third-order numerical scheme outlined in §5.4.6.2. All simulations have $w_{base} = 0$ and $\mathcal{T}_\ell = 0$.

where $\widetilde{\phi}$ is the finest solution, computed with $N = 3200$ spatial steps, and ϕ has been computed using $N = 50, 100, 200, 400, 800, 1600$. We set both the relative and absolute tolerances in the ode15s options to 10^{-6}, and stop the simulations before the radius a becomes close enough to zero for the simulations to break down, at $t = 180$ for $(\zeta, \gamma, u_{bg}) = (1, 0, 0)$ and at $t = 4.5$ for $(\zeta, \gamma, u_{bg}) = (0, 0, 1)$. Figure 5.8 plots $\mathcal{E}$ against N and shows close to third-order convergence for both $\zeta = 1$ (crosses) and $u_{bg} = 1$ (circles), as should be expected for the above numerical scheme.

5.4.6.3 Results

Here we present some preliminary results investigating the effect of the extensile active coefficient and the background flow on proplatelet dynamics. As we have not yet validated the numerical scheme in §5.4.6.2 for $\gamma \neq 0$, we do not investigate this regime here, and as in §5.4.6.2 we do not include the regularisation term proportional to ϵ^2. Throughout, we focus on the simplest case in which the mass influx from the megakaryocyte body is zero, $w_{base} = 0$, and the tip tension is zero $\mathcal{T}_\ell = 0$.

We first vary the extensile coefficient, ζ. Figure 5.9 plots the proplatelet i) radius, a, and ii) axial velocity, w, against z for active coefficients a) $\zeta = 1$ and b) $\zeta = 10$, until just before the tip of the proplatelet reaches zero radius (and the numerical simulations break down). The lines are plotted at even time intervals between $t = 0$ (blue) and $t = 180$ (red) in a), and between $t = 0$ (blue) and $t = 18$ (red) in b). respectively. We see in Figures 5.9 i) that as time progresses, the proplatelet elongates and becomes thinner overall, but the base at $z = 0$ becomes thicker relative to the tip at $z = \ell$, which tapers off to $a = 0$ for large enough times. This is likely because the tip region experiences a greater resistance to proplatelet extension from the external fluid than is exerted by the drag of external fluid along the surface of the rest of the proplatelet.

The final length ℓ of the proplatelet just before the tip reaches zero radius is approximately $\ell = 14$ for both $\zeta = 1$ and $\zeta = 10$, however the proplatelet with higher extensile stress, $\zeta = 10$, approaches this length more quickly, at around $t = 18$, than the proplatelet with $\zeta = 1$ does, at around $t = 180$. Figures 5.9 ii) show that the proplatelet velocity increases approximately linearly along its length, with a gradient of approximately 0.3ζ at all times. The qualitative similarity between Figures 5.9 a) and b) is explained by the governing equations (5.38) and (5.46) being invariant when ζ, w and t are scaled by a constant factor. Physically, means that if the stress from sliding microtubules increases by a certain factor, then the rate of proplatelet elongation will increase by the same factor.

Next, we investigate the effect of background flow u_{bg} on the elongation of a proplatelet, when neglecting all active contributions, by setting $\gamma = 0 = \zeta$. Figure 5.10 shows the dependence of i) the proplatelet radius, a, and ii) the proplatelet axial, w, over time, for a) $u_{bg} = 0.1$ and b) $u_{bg} = 1$. Lines are plotted at even time intervals between $t = 0$ (blue) and $t = 45$ (red) for a) $u_{bg} = 0.1$, or $t = 4.5$ (red) for b) $u_{bg} = 1$, respectively, i.e. until just before the radius reaches zero anywhere along the proplatelet. The background flow causes the proplatelet radius to decrease at its base, and increase at its tip, as seen in Figures 5.10 i). This occurs because the background flow sweeps exterior fluid from the proplatelet base towards the tip, which exerts a drag on the proplatelet that sweeps the proplatelet fluid from base to tip.

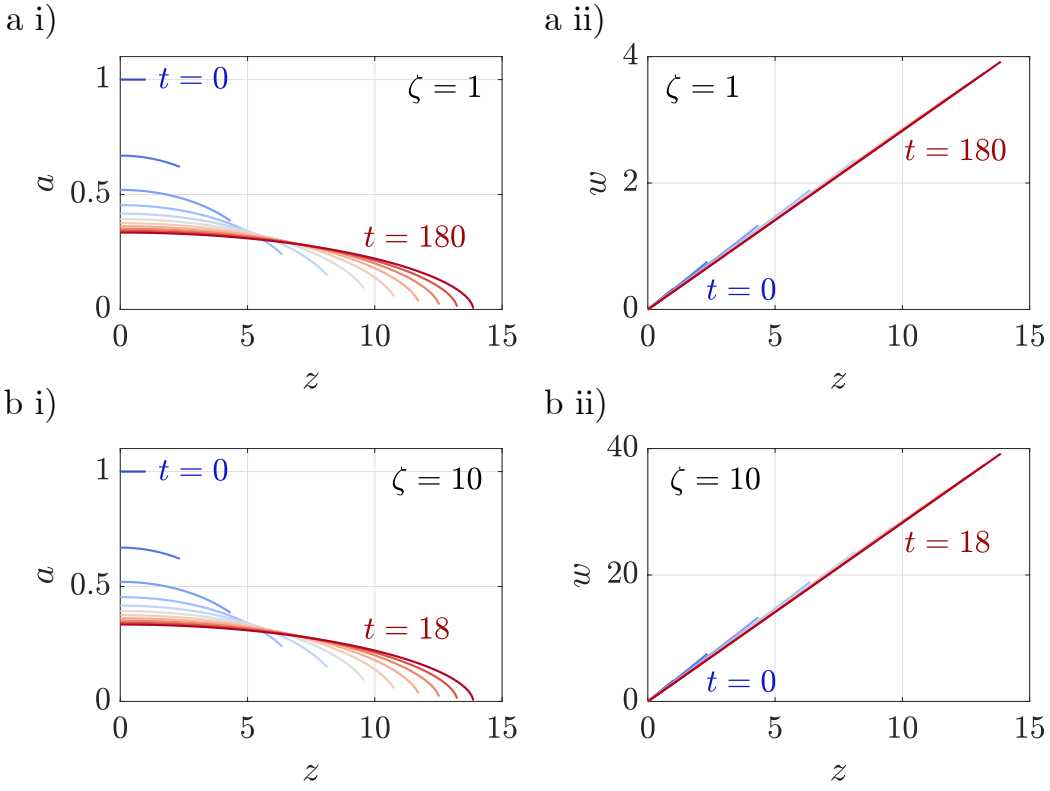

Figure 5.9: The proplatelet i) radius, a, and ii) axial velocity, w, against z while varying the extensile coefficient, a) $\zeta = 1$, and b) $\zeta = 10$. The lines are plotted at even time intervals between $t = 0$ (blue) and $t = 180$ (red) in a), and between $t = 0$ (blue) and $t = 18$ (red) in b), respectively. The w-axis limits vary between a ii) and b ii). In all plots, $\gamma = 0$, $u_{bg} = 0$, $\epsilon = 0.1$, $w_{base} = 0$ and $\mathcal{T}_\ell = 0$; $N = 500$ spatial steps are used, and the relative and absolute tolerances in the temporal ODE solver are 10^{-6}.

Figures 5.10 ii) show that the proplatelet velocity increases in time everywhere but at the base (where it's prescribed to be zero), and that at later times (red) there is a large increase in velocity near the base, and a smaller increase from just beyond the base to the tip. Again, Figures 5.10 a) and b) are qualitatively identical because equations (5.37) and (5.38) are invariant under scaling u_{bg}, w and t by a constant factor.

Finally, we look at the effect of including both a background flow and extensile stress. In Figure 5.11 we vary the ratio ζ/u_{bg} of the extensile coefficient to the background flow and plot the proplatelet radius until just before the radius reaches

zero. The progression from Figure 5.11 a) to c) shows that as ζ/u_{bg} decreases, the pinch-off length of the proplatelet decreases. We observe a combination of tapering at the base and tip caused by the background flow and extensile stress, respectively. As the background flow increases in the direction of elongation, it works to enhance elongation rather than resisting it, so that the tapering at the tip that is seen in Figure 5.9 i) and Figure 5.11 a) and b) is no longer observed.

The results in this section have indicated the individual effects of the extensile stress and background flow. We believe them to be an encouraging first step. Further parameter explorations will be carried out in future work to include the active surface tension γ. This may necessitate the development of the code to take better advantage of ℓa^2 being the conserved quantity. We will also reintroduce the regularisation term proportional to ϵ^2, so as to avoid prohibitive numerical stiffness as γ increases, and apply the physically realistic condition of a smoothly going to zero at the tip.

5.5 Modelling fluid-structure interaction of proplatelets in a half-space

5.5.1 Overview of modelling approach

In this section, we drop the assumption of axisymmetry, and model proplatelets in a half-space. This may allow for comparison with experiments where proplatelets elongate from a wall, as in the bioreactors of Thon et al. [154] or Balduini et al. [9]. A half-space also more closely emulates the *in vivo* environment where proplatelets elongate from a vessel wall into the lumen. Although protrusion into a channel in most cases better reflects a realistic geometry for proplatelet formation, to enforce a no-slip boundary condition in such a geometry would require an infinite image system in the solution method outlined below, which is why we have restricted to a half-space which uses only a finite image system. Though we do not do so in this section, it is easy to use the model to consider a proplatelet in full-space, by removing the image system that enforces the wall no-slip condition.

When a filament moves in a plane perpendicular to a nearby wall, comparisons between resistive force theories and non-local slender body theories have shown

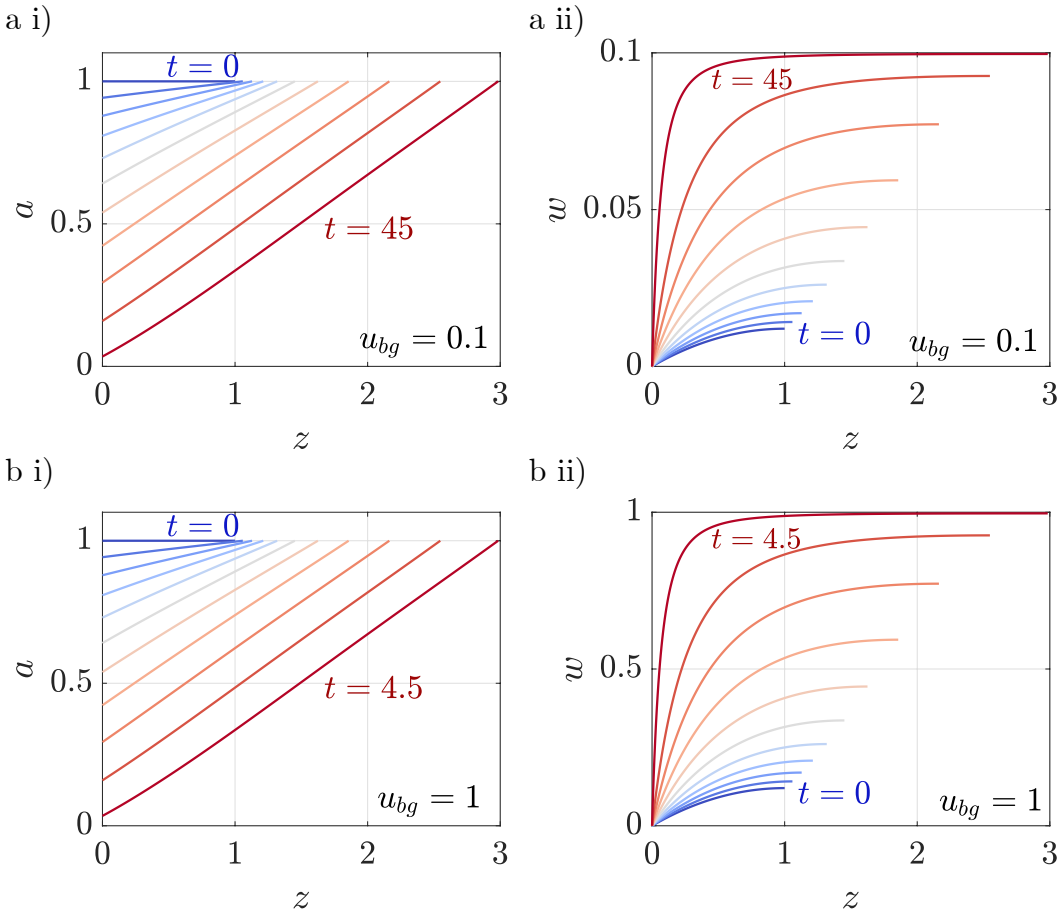

Figure 5.10: The proplatelet a) radius, a, and b) axial velocity, w, against z while varying the background flow i) $u_{bg} = 0.1$ and ii) $u_{bg} = 1$. The lines are plotted at even time intervals between $t = 0$ (blue) and $t = 45$ (red) in a), and between $t = 0$ (blue) and $t = 4.5$ in b). The w-axis limits vary between a ii) and b ii). In all plots, $\gamma = 0$, $\zeta = 0$, $\epsilon = 0.1$, $w_{base} = 0$ and $\mathcal{T}_\ell = 0$, $N = 500$ spatial steps are used, and the relative and absolute tolerances in the temporal ODE solver are 10^{-6}.

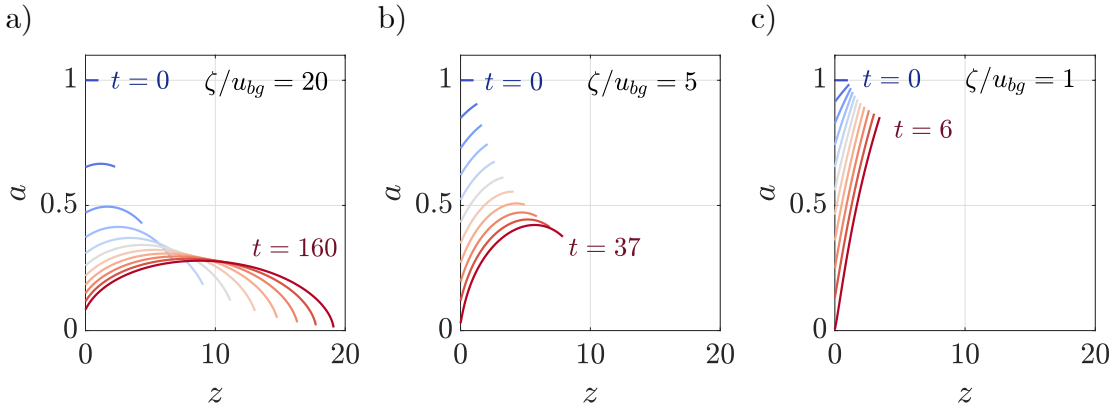

Figure 5.11: The radius a of a proplatelet with the ratio of extensile coefficient to background flow, ζ/u_{bg}, equal to a) 20, b) 5 and c) 1. The lines are plotted at even time intervals between $t = 0$ (blue), and $t = 160, 37, 6$ (red) in a), b) and c), respectively. In all plots, $\gamma = 0$, $\zeta = 1$, $\epsilon = 0.1$, $w_{base} = 0$, $\mathcal{T}_\ell = 0$, $N = 500$ spatial steps are used, and the relative and absolute tolerances in the temporal ODE solver are 10^{-6}.

good agreement when computing the total force along a filament; however pointwise computations of force density along filament centrelines do not show good agreement between the two approaches (e.g. differences of 43% for a filament with aspect ratio 0.01) [161]. Since cell membrane stretching and the strength of active stresses may be affected by pointwise forces along proplatelet centrelines, this motivates the replacement of resistive force theory with a more sophisticated method for computing the forces exerted on a proplatelet, that takes into account non-local effects.

To solve Stokes equations in a domain containing a proplatelet lying in a plane perpendicular to a wall, we use a regularised slender body theory, called regularised Stokeslet segments. Regularised Stokeslet segments is based off Cortez's [36] method of regularised Stokeslets, which we describe first. In this method, point forces along the centreline are smoothed out to be distributed over a region with some chosen lengthscale: rather than populating the centreline with solutions to Stokes flow with a point force (5.1), Cortez instead uses solutions of the regularised Stokes equations

$$\mu\nabla^2\boldsymbol{u}_f(\boldsymbol{x}) = \nabla p_f - \boldsymbol{f}\phi(\boldsymbol{x},\delta), \quad \nabla\cdot\boldsymbol{u}_f = 0. \tag{5.63}$$

Here δ is the regularisation parameter, and $\phi(\boldsymbol{x}, \delta)$ is the cut-off function, or smoothed delta function, which is a smooth, radially symmetric function that integrates to one over $\mathbb{R}^3$. A common choice for the cut-off function $\phi(\boldsymbol{x}, \delta)$ is

$$\phi(\boldsymbol{x}, \delta) = \frac{15\delta^4}{8\pi(|\boldsymbol{x}|^2 + \delta^2)^{7/2}}. \tag{5.64}$$

It is often useful to choose different functional forms of cut-off functions for the Stokeslets, rotlets, dipoles and sources when applying the method of images for a particular geometry [1, 35, 37]. The regularisation parameter δ is commonly chosen to be constant and approximately equal to the radius of the slender body, although more systematic choices of the regularisation parameter have recently been developed [160], where δ is allowed to in space to ensure satisfaction of the no-slip boundary condition on the slender body's surface.

The original form of so-called regularised slender body theories places Stokeslets at discrete nodes along the centreline of the filament [36]. A trade-off exists between choosing the regularisation parameter δ controlling the cut-off function (equation (5.63)) and the distance between nodes. To address errors arising from this trade-off, Cortez [35] replaces discrete distributions of regularised Stokeslets with continuous distributions along line segments, for which Stokes equations can still be solved exactly. We use such a method, in particular we closely follow the method outlined in Walker et al. [161] and use regularised Stokeslet segments. In §5.5.3 below, we provide a method explanation that omits the detailed calculations, and refer the interested reader to the details in [161] and its Supplementary Material.

We choose a simpler route for proplatelet mechanics than in §5.4, and neglect cytosol viscosity and finer cytoskeletal structure. Instead we consider proplatelets to be elastic rods governed by the Kirchoff rod equations. Such a constitutive law facilitates an initial investigation of proplatelet mechanics in a half-space, as the literature contains implementations of the method of regularised Stokeslets integrated with the Kirchoff rod equations. We also assume a proplatelet is inextensible and has constant radius and bending stiffness along its length, motivated by variations in radius being small compared to the proplatelet length. We start with the simplest case by treating elastohydrodynamic effects as occuring on a

much smaller timescale than growth or elongation, although as discussed in §5.4.1 it is possible that their timescales may be comparable.

Given these assumptions, the model can be used to investigate how the forces along proplatelets and their positions are affected by their bending stiffnesses, lengths, intrinsic curvatures, the background flow rate, and the number of proplatelets in an array.

5.5.2 Governing equations and boundary conditions

We model proplatelets lying in a plane spanned by the orthonormal vectors $\boldsymbol{e}_x$ and $\boldsymbol{e}_y$, with $\boldsymbol{e}_z$ lying perpendicular to the plane. The proplatelets lie in a half-space that is perpendicular to a wall at $y = 0$, as shown in Figure 5.12, where the coordinates $\boldsymbol{x} = (x, y)$ are used in the half-space. The K proplatelets have prescribed lengths l^k, a uniform radius a, and centrelines parameterised as $\boldsymbol{x}^k(s^k) = (x^k(s,t), y^k(s,t))$ by arclength coordinates $s^k \in [0, l^k]$. The fluid external to the proplatelet obeys Stokes flow (5.2)-(5.3). Each proplatelet is modelled as an elastic rod, described by the Kirchhoff rod equations, which are one-dimensional equations describing only the centreline of the rod. The Kirchhoff rod equations are obtained

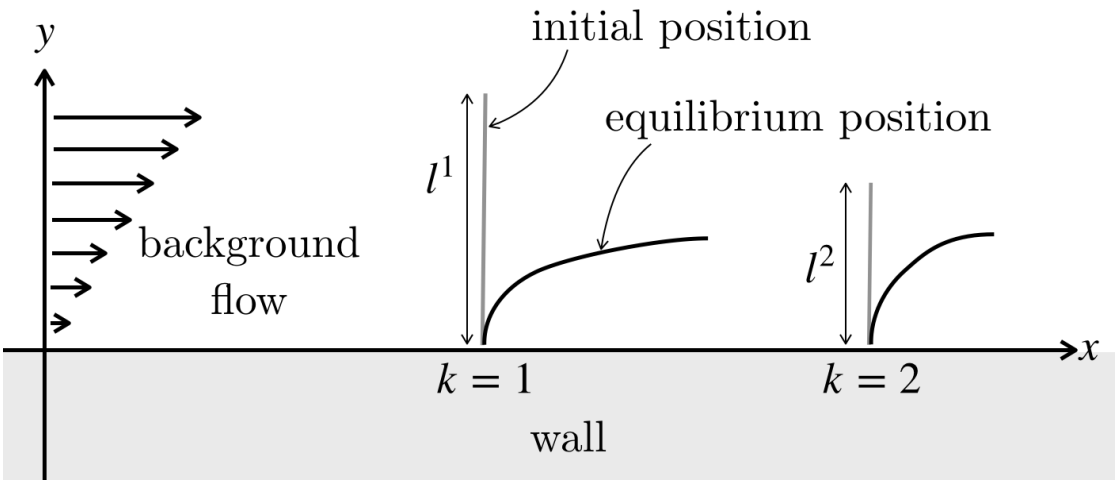

Figure 5.12: Proplatelets are tethered to the wall (grey) of a half-space (white), with a background shear flow. An initial position (light grey) evolves to an equilibrium position (black) when subject to a background flow. The k^{th} proplatelet has length l^k, $k = 1, ..., K$, and in this figure there are a total of $K = 2$ proplatelets.

by balancing forces and moments resulting from internal contact force density $\boldsymbol{n}^k$ (units N), internal contact moment density $\boldsymbol{m}^k$ (units Nm), body force density $\boldsymbol{f}^k$ (units N/m), and body moment density $\boldsymbol{l}^k$ (units N) on proplatelet k [6],

$$\frac{\partial \boldsymbol{n}^k}{\partial s^k} + \boldsymbol{f}^k = \boldsymbol{0}, \tag{5.65a}$$

$$\frac{\partial \boldsymbol{m}^k}{\partial s^k} + \frac{\partial \boldsymbol{x}^k}{\partial s^k} \times \boldsymbol{n}^k + \boldsymbol{l}^k = \boldsymbol{0}. \tag{5.65b}$$

The right-hand sides of (5.65) are zero as there is no acceleration in Stokes flow, and therefore no acceleration of objects in Stokes flow. In the context of proplatelets in flow we have zero body moment, $\boldsymbol{l}^k = \boldsymbol{0}$. As in [64, 161], we assume that proplatelet motion is planar, and that proplatelets do not shear and are inextensible; the internal contact force $\boldsymbol{n}^k$ acts as a Lagrange multiplier enforcing these last two constraints. We assume linear elasticity by using a linear moment-strain constitutive relation

$$\boldsymbol{m}^k = EI \frac{\partial \theta^k}{\partial s^k} \boldsymbol{e}_z, \tag{5.66}$$

where EI is the proplatelet bending stiffness, with units Pa m^4, and $\theta^k(s^k, t)$ is the angle between the x-axis and the tangent to the proplatelet centreline. Each proplatelet is tethered by prescribing a constant location of the proplatelet centreline $\boldsymbol{x}^k$ at its base,

$$(x^k(0,t), y^k(0,t)) = (x_1^k, y_1^k), \tag{5.67}$$

where y_1^k is small but non-zero to avoid numerical degeneracies in the solution method. Proplatelet centrelines have fixed arclength derivatives at their bases,

$$\frac{\partial}{\partial s}(x^k(0,t), y^k(0,t)) = (0,1), \tag{5.68}$$

or equivalently, $\theta^k(0,t) = \pi/2$; proplatelets are therefore assumed to protrude vertically into the half-space from $y = 0$. This is physically reasonable, given that proplatelets are supported by a thicker base, the endothelium through which they protrude *in vivo*, or the walls of a supporting scaffold *in vitro*; however the effect of the clamping angle on results could merit further investigation. Zero contact force and contact moment are imposed at the proplatelet tips,

$$\boldsymbol{n}^k(l^k, t) = \boldsymbol{0} = \boldsymbol{m}^k(l^k, t). \tag{5.69}$$

We prescribe continuity of velocity on the wall, and rather than precisely imposing continuity of velocity at the proplatelet boundaries, we impose the simpler approximate condition of continuity of velocity between the proplatelet centrelines and the fluid:

$$\boldsymbol{u}_f = \boldsymbol{0} \quad \text{on} \quad y = 0, \qquad \boldsymbol{u}_f = \boldsymbol{u}^k \quad \text{on} \quad \boldsymbol{x} = \boldsymbol{x}^k, \quad k = 1, ..., K, \tag{5.70}$$

where $\boldsymbol{u}^k = \dot{\boldsymbol{x}}^k$ is the velocity of the centreline of the k^{th} proplatelet. A shear background flow is prescribed as

$$\boldsymbol{u}_f \sim u_{bg}(y, 0) \quad \text{as} \quad x^2 + y^2 \to \infty, \tag{5.71}$$

where u_{bg} is a constant. The continuity of velocity condition (5.70) contains a time-derivative on $\boldsymbol{x}^k$, necessitating an initial condition on $\boldsymbol{x}^k$. We set the proplatelets to be initially perpendicular to the wall,

$$\theta^k(s^k, 0) = \frac{\pi}{2}. \tag{5.72}$$

In the next section we describe the solution of the model described above using the method of regularised Stokeslets.

5.5.3 Solution of non-local hydrodynamics using regularised Stokeslets segments

Motivated by Cortez's regularised Stokeslet segments and following the method of Walker et al. [161], we discretise each of K proplatelets into N line segments, indexed by lower index i. Each segment has length $v^k = l^k/N$ with angle θ_i^k between the segment and the unit vector $\boldsymbol{e}_x$ parallel to the x-axis, as depicted in Figure 5.13. With this discretisation, the end of segment j on filament k has position

$$\boldsymbol{x}_j^k = \boldsymbol{x}_1^k + \sum_{i=1}^{j-1} (\cos\theta_i^k \boldsymbol{e}_x + \sin\theta_i^k \boldsymbol{e}_y) v^k. \tag{5.73}$$

To facilitate analytical evaluation of the regularised Stokeslet relationship between force density and velocity, we take the force density to be piecewise constant, as

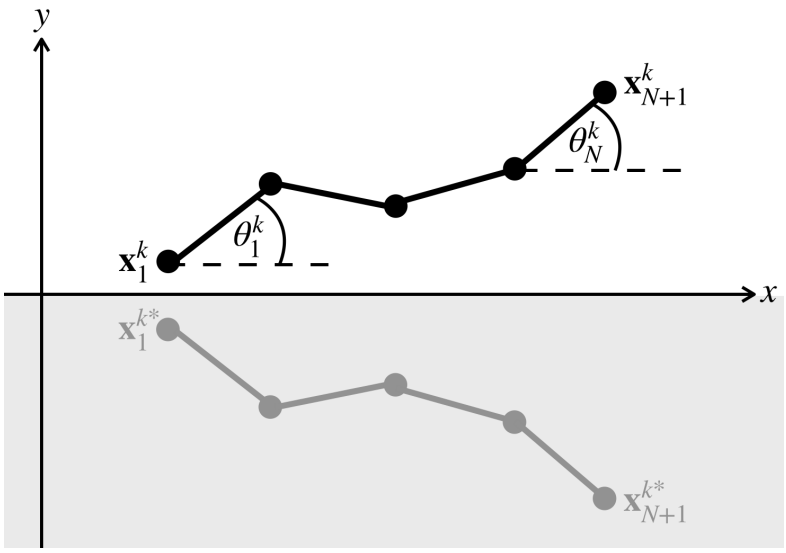

Figure 5.13: Piecewise linear discretisation of the k^{th} proplatelet into N segments in a half-space $y > 0$ with the image proplatelet and wall shown in grey. The proplatelet base $\boldsymbol{x}_1^k$ is a small distance away from the x-axis, to avoid division by zero in the numerical scheme.

in [64]. The force density along segment j of proplatelet k is given by its value at the j^{th} node

$$\boldsymbol{f}^k(s^k) = \boldsymbol{f}_j^k \quad \text{for} \quad s_{j-1}^k < s^k < s_j^k, \quad j = 2, ..., N. \tag{5.74}$$

Numerical investigations in §B.4 show that piecewise constant force density as used above reduces oscillations in computed force densities at the proplatelet endpoints as compared to the piecewise linear force densities used in [35, 161]. Walker et al. [159] also used piecewise constant force density, but with the modification that the force density is not constant along an entire segment, but rather takes the value of the force density at the nearest node, either the $(k-1)^{th}$ or k^{th} node. This eliminates endpoint oscillations, although the reason why it does so remains unclear.

In a set-up with K proplatelets, the velocity $\boldsymbol{u}_f$ at a node $\boldsymbol{x}_j^m$ on filament m

is related to force densities $\boldsymbol{f}^k(s^k)$ via

$$\boldsymbol{u}_f(\boldsymbol{x}_j^m) = \boldsymbol{u}_{bg}(\boldsymbol{x}_j^m) + \frac{1}{8\pi\mu_f}\sum_{k=1}^{K}\int_0^{l^k} S[\boldsymbol{f}^k, \boldsymbol{r}^k] - S[\boldsymbol{f}^k, \boldsymbol{r}^{k*}] - y^2 PD[\boldsymbol{f}^k, \boldsymbol{r}^{k*}] + 2ySD[\boldsymbol{f}^k, \boldsymbol{r}^{k*}] + 2y\left(R_1[\boldsymbol{f}^k, \boldsymbol{r}^{k*}] - R_2[\boldsymbol{f}^k, \boldsymbol{r}^{k*}]\right) ds^k, \quad (5.75)$$

where $\boldsymbol{r}^k = \boldsymbol{x}_j^m - \boldsymbol{x}^k(s^k)$ for $\boldsymbol{x}^k(s^k)$ located on the k^{th} proplatelet, and $\boldsymbol{r}^{k*} = \boldsymbol{x}_j^m - \boldsymbol{x}^{k*}(s^k)$, where $\boldsymbol{x}^{k*}(s^k) = (x^k(s^k), -y^k(s^k))$ is the image point of $\boldsymbol{x}^k(s^k)$ reflected in the x-axis, depicted in grey in Figure 5.13. In equation (5.75), S is the regularised Stokeslet, PD the regularised potential dipole, and SD the regularised Stokeslet doublet. The last two are obtained as solutions to the regularised forced Stokes equations (5.63) with cut-off function (5.64) by using linearity of Stokes equations and applying linear differential operators to the Stokeslet: the directional derivative in the direction $2(\boldsymbol{f}\cdot\boldsymbol{e}_y)\boldsymbol{e}_y - \boldsymbol{f}$ to obtain the Stokeslet doublet, and the negative Laplacian to obtain the potential dipole. The rotlets R_1 and R_2 are each the antisymmetric part of a Stokeslet doublet computed using the cut-off function in equation (5.64) and the cut-off function

$$\psi(\boldsymbol{x}, \delta) = \frac{3\delta^2}{4\pi(|\boldsymbol{x}|^2+\delta^2)^{5/2}}, \quad (5.76)$$

respectively. The two cut-off functions are required to obtain the necessarily cancellation in the image system [1]. Full expressions for the regularised potential dipole, Stokeslet doublet, and rotlets are are given in [35, 161], and [1] contains the full derivation of the image system. As each proplatelet has been discretised into segments with piecewise constant force densities, the integral in equation (5.75) can be split up into integrals over each segment, and computed analytically, as shown in [35, 161]

To convert equation (5.75) from an equation for the fluid velocity $\boldsymbol{u}_f$ to one for node velocities $\dot{\boldsymbol{x}}_j^k$, we use the continuity of velocity condition (5.70). The integral in equation (5.75) has been explicitly computed in [161] at each node on a single proplatelet, and can be readily extended to multiple proplatelets. This results in a linear system relating the velocities at nodes on proplatelet k to force densities at nodes on all proplatelets, taking the form:

$$\dot{\boldsymbol{X}}^k = A^k(\boldsymbol{X}^1, ..., \boldsymbol{X}^K)\boldsymbol{F} + \boldsymbol{U}_{bg}^k, \quad k = 1, ..., K, \quad (5.77)$$

where the matrix A^k (units Pa s) is derived from (5.75) at each node of proplatelet k, which in turn depends on the positions of the $N+1$ nodes of each of the K proplatelets, so that A^k is a $2(N+1) \times 2K(N+1)$ matrix. The vectors $\boldsymbol{X}^k$ and $\boldsymbol{F}$ are given by

$$\boldsymbol{X}^k = (x_1^k, y_1^k, ..., x_{N+1}^k, y_{N+1}^k)^T, \tag{5.78a}$$

$$\boldsymbol{F} = [\boldsymbol{f}^1; \boldsymbol{f}^2; ...; \boldsymbol{f}^K] \tag{5.78b}$$

where the force density at nodes of proplatelet k are

$$\boldsymbol{f}^k = (\boldsymbol{f}_1^k \cdot \boldsymbol{e}_x, \boldsymbol{f}_1^k \cdot \boldsymbol{e}_y, ..., \boldsymbol{f}_{N+1}^k \cdot \boldsymbol{e}_x, \boldsymbol{f}_{N+1}^k \cdot \boldsymbol{e}_y)^T. \tag{5.79}$$

The prescribed background flow at all the nodes of proplatelet k is encoded in $\boldsymbol{U}_{bg}^k$ via

$$\boldsymbol{U}_{bg}^k = (\boldsymbol{u}_{bg}(\boldsymbol{x}_1^k) \cdot \boldsymbol{e}_x, \boldsymbol{u}_{bg}(\boldsymbol{x}_1^k) \cdot \boldsymbol{e}_y, ..., \boldsymbol{u}_{bg}(\boldsymbol{x}_{N+1}^k) \cdot \boldsymbol{e}_x, \boldsymbol{u}_{bg}(\boldsymbol{x}_{N+1}^k) \cdot \boldsymbol{e}_y)^T. \tag{5.80}$$

The full system can be expressed as the concatenation of the K systems (5.77),

$$\dot{\boldsymbol{X}} = A\boldsymbol{F} + \boldsymbol{U}_{bg}, \tag{5.81}$$

where the vectors for each proplatelet position have been combined into the column vector $\boldsymbol{X} = [\boldsymbol{X}^1; ...; \boldsymbol{X}^K]$, the vectors for background velocities at each proplatelet have been combined into the column vector $\boldsymbol{U}_{bg} = [\boldsymbol{U}_{bg}^1; ...; \boldsymbol{U}_{bg}^K]$, and the K matrices encoding hydrodynamics at each proplatelet have been combined into the $2K(N+1) \times 2K(N+1)$ matrix $A = [A^1; ...; A^K]$.

5.5.4 Incorporating proplatelet elasticity

Following [106, 161], the Kirchhoff rod equations (5.65) are integrated along the length of each proplatelet, with zero contact force and contact moment boundary conditions applied at the proplatelet tips. This generates an equation for each node, relating its position to the force densities and moments on all nodes. We concatenate these equations into a linear system relating node positions, force densities and moments at nodes:

$$-B\boldsymbol{F} = \boldsymbol{R}, \tag{5.82}$$

where B depends on the proplatelets' spatial coordinates θ_i^k, x_i^k, y_i^k, and is a $K(N+2) \times 2K(N+1)$ block matrix composed of a copy of the B^k for a single proplatelet from [161], for each of the K proplatelets. The first two rows of each B^k has units m, the rest have units m^2. The vector $\boldsymbol{R}$ is similarly a concatenation of the $\boldsymbol{R}^k$'s in [161],

$$\boldsymbol{R}^k = (\boldsymbol{n}^k(s_1^k) \cdot \boldsymbol{e}_x, \boldsymbol{n}^k(s_1^k) \cdot \boldsymbol{e}_y, m^k(s_1^k), ..., m^k(s_{N+1}^k))^T, \tag{5.83}$$

for each individual proplatelet, where we recall from the constitutive law (5.66) that the moments are $m^k(s^k) = EI\partial\theta^k/\partial s^k$. The first two entries of $\boldsymbol{R}^k$ have units N, and the remaining have units Nm.

5.5.5 Full system

Using the integrated Kirchoff rod equations (5.82) in the discretised hydrodynamic equations (5.81) gives

$$BA^{-1}\dot{\boldsymbol{X}} = -\boldsymbol{R} + BA^{-1}\boldsymbol{U}_{bg}. \tag{5.84}$$

Since the vector $\boldsymbol{X}$ tracks the proplatelet centrelines, which are one-dimensional, we can more concisely formulate the system in terms of the positions (x_1^k, x_1^k) of each proplatelet's first node, and the angles $\theta_j^k, k = 1, ..., K, j = 1, ..., N$, introduced in equation (5.73). Proplatelets' positions can be described by the vectors

$$\boldsymbol{\theta}^k = (X_1^k, Y_1^k, \theta_1^k, ..., \theta_N^k)^T, \quad k = 1, ..., K, \tag{5.85}$$

The two parameterisations are related via

$$\dot{\boldsymbol{X}}^k = Q^k\dot{\boldsymbol{\theta}}^k \quad k = 1, ..., K, \tag{5.86}$$

where each Q^k is a copy of the $2(N+1) \times (N+2)$ matrix Q defined in equation (2.23) of [161]. Each Q^k depends on the angles θ_k^j, $j = 1, ..., N$. We define the $K(N+2) \times 1$ vector $\boldsymbol{\theta} = [\boldsymbol{\theta}^1; ...; \boldsymbol{\theta}^K]$, and the $2K(N+1) \times K(N+2)$ block-diagonal matrix $Q = Q^1 \bigoplus ... \bigoplus Q^K$, so that $\boldsymbol{X}$ and $\boldsymbol{\theta}$ are related via $\dot{\boldsymbol{X}} = Q(\theta)\dot{\boldsymbol{\theta}}$, and equation (5.84) becomes

$$BA^{-1}Q\dot{\boldsymbol{\theta}} = -\boldsymbol{R} + BA^{-1}\boldsymbol{U}_{bg}. \tag{5.87}$$

We non-dimensionalise using the scalings

$$B = L^2\hat{B}, \quad A = \frac{1}{8\pi\mu}\hat{A}, \quad Q\dot{\boldsymbol{\theta}} = \frac{L}{T}\hat{Q}\dot{\hat{\boldsymbol{\theta}}}, \tag{5.88a}$$

$$\boldsymbol{R} = \frac{EI}{L}\hat{\boldsymbol{R}}, \quad \boldsymbol{U}_{bg} = \frac{L}{T}\hat{\boldsymbol{U}}_{bg}, \quad \boldsymbol{F} = \frac{\mu L}{T}\hat{\boldsymbol{F}} \tag{5.88b}$$

where hats denote dimensionless quantities, L is the typical proplatelet length, $T = L/u_{bg}$ is the timescale of background flow past the proplatelet, EI is the proplatelet bending stiffness, and the factor of 8π comes from (5.75). Here we have scaled the force density $\boldsymbol{F}$ exerted by the fluid on the proplatelets with the hydrodynamic scale $\mu L/T$ rather than the elastic scale EI/L^3 as we work in the regime in which the latter is at most comparable to the former. Equation (5.87) becomes

$$E_h\hat{B}\hat{A}^{-1}\hat{Q}\dot{\boldsymbol{\theta}} = -\hat{\boldsymbol{R}} + E_h\hat{B}\hat{A}^{-1}\hat{\boldsymbol{U}}_{bg}, \qquad E_h = \frac{8\pi\mu L^4}{EIT}, \tag{5.89}$$

where we have introduced the elastohydrodynamic number E_h measuring the relative sizes of hydrodynamic and elastic forces.

The non-dimensionalised background flow (5.71) that sets the vector $\hat{\boldsymbol{U}}_{bg}$ through equation (5.80) is simply

$$\hat{\boldsymbol{u}}_{ug} = (y, 0). \tag{5.90}$$

The fixed boundary condition (5.67) is prescribed by setting the right-hand entries of (5.89) corresponding to $\hat{x}_1^1, \hat{y}_1^1, \theta_1^1, ..., \hat{x}_1^K, \hat{y}_1^K, \theta_1^K$ to zero (and we therefore avoid solving for the unknown contact forces $\boldsymbol{n}^k(s_1^k)$ and contact moments $m^k(s_1^k)$ at the proplatelet bases, that appear in expression (5.83) for $\boldsymbol{R}^k$). The $\hat{y}$-component $\hat{y}_1^k$ is chosen to be small but non-zero, $\hat{y}_1^k = 0.01$, so as to avoid dividing through by zero in computations of the integrals (5.75). The intial condition (5.72) is

$$\theta_i^k = \frac{\pi}{2} \quad \text{for} \quad k = 1, ..., K \quad \text{at} \quad t = 0. \tag{5.91}$$

Equation (5.89) is a system of temporal ODEs to solve for the positions $\boldsymbol{\theta}$ of the $K(N+1)$ proplatelet nodes, where the matrices $\hat{A}, \hat{B}, \hat{Q}$ and vectors $\hat{\boldsymbol{R}}, \hat{\boldsymbol{U}}_{bg}$ are all functions of $\boldsymbol{\theta}$. After solving (5.87) with background flow (5.90) subjected to the boundary conditions (5.67) and initial conditions (5.91), we can compute the force density $\boldsymbol{F}$ as described in §5.5.6.

5.5.6 Computing the force density

Knowing the proplatelet positions at a point in time means that $\hat{A}, \hat{B}, \hat{Q}, \hat{\boldsymbol{R}}$ and $\hat{\boldsymbol{U}}_{bg}$ are also known, so that the force density $\hat{\boldsymbol{F}}$ exerted by the fluid on the proplatelets can be computed. The dimensionless version of the hydrodynamic equation (5.81) is

$$8\pi\hat{Q}\dot{\boldsymbol{\theta}} = \hat{A}\hat{\boldsymbol{F}} + 8\pi\hat{\boldsymbol{U}}_{bg}, \tag{5.92}$$

which we combine with (5.89) to compute the force density:

$$\hat{\boldsymbol{F}} = 8\pi\hat{A}^{-1}\hat{Q}\left(\hat{B}\hat{A}^{-1}\hat{Q}\right)^{-1}\left(\hat{B}\hat{A}^{-1}\hat{\boldsymbol{U}}_{bg} - \frac{\hat{\boldsymbol{R}}}{E_h}\right) - 8\pi\hat{A}^{-1}\hat{\boldsymbol{U}}_{bg}, \tag{5.93}$$

where $BA^{-1}Q$ is a $K(N+2) \times K(N+2)$ matrix.

5.5.7 Numerical implementation

We solve the system (5.89) using the MATLAB code of Walker et al. [161], which solves the equivalent system of ODEs (5.92) for one filament in a half-space using MATLAB's in-built stiff ODE solver ode15s, with absolute and relative tolerances 10^{-5}. We make three modifications to the code. The system is enlarged to include multiple proplatelets, so that in the scripts computing $\hat{\boldsymbol{\theta}}, \hat{\boldsymbol{X}}, \hat{\boldsymbol{R}}, \hat{Q}$ and $\hat{B}$ we loop the script for a single proplatelet over the K proplatelets and concatenate. The code producing $\hat{A}$ is looped over all of the $K(N+1)$ nodes now in the system, and while computing each $\hat{A}^k$, an additional loop over the K segments is included to capture the contributions of each node in the entire system on the velocities of nodes on proplatelet k.

To model proplatelets of different lengths, we allow the segment lengths to vary from proplatelet to proplatelet, but fix the number of segments of each proplatelet to be N. In the original code the segment lengths are $1/N$; for proplatelet k we just modify these to be $\hat{l}_k/N$ in the scripts for $\hat{B}, \hat{Q}, \hat{R}$ and $\hat{\boldsymbol{X}}$, where $\hat{l}_k$ is the dimensionless length of proplatelet k.

Finally, instead of piecewise linear force density, we have used piecewise constant force density. As discussed in Appendix B.4 and more extensively in [159], this reduces the oscillations in the force density near the endpoints, although the

reason it does so is unclear. Some endpoint oscillations are still present so we cut off the first and last five segments when presenting results in §5.5.9.

Validation for the numerical scheme is provided in Appendix B.

5.5.8 Hydrodynamic number and regularisation parameter

For the regularisation parameter δ we use a typical proplatelet radius of $0.8\,\mu$m [19], which when non-dimensionalised on a typical proplatelet length of $L = 100\,\mu$m gives a dimensionless regularisation parameter $\hat{\delta} = 0.008$. The results presented in §5.5.9 do not depend qualitatively on the regularisation parameter.

We estimate a range for the hydrodynamic number E_h, defined in equation (5.89), as follows. As mentioned in §5.2, approximately four bundles of ten microtubules line the core of proplatelets. Assuming the bending stiffness is additive, we estimate the stiffness EI of a bundle by multiplying the stiffness of a single microtubule [57] by ten, to get $EI = 2 \times 10^{-22}$ Nm^2. We use this as an estimate for the minimum proplatelet bending stiffness, and estimate typical proplatelet bending stiffness to be four times this (8×10^{-22} Nm^2). Following the discussion of shear rates in §5.5.1, we use shear rates of up to $100\,s^{-1}$. With the characteristic proplatelet lengthscale of $100\,\mu$m [14], and blood viscosity $\mu = 1.2 \times 10^{-3}$ Pas [8] (also the same order of magnitude as cell culture viscosity 10^{-3} Pa s), we therefore look at hydrodynamic numbers in the range $E_h = [0, 1.5 \times 10^6]$, and will for illustration often use a typical value of $E_h = 4 \times 10^5$, computed using bending stiffness $EI = 8 \times 10^{-22}$ Nm^2.

5.5.9 Initial investigations into proplatelet-flow interaction

In the following sections we use the model described above to investigate how the forces exerted on a proplatelet by an external flow depends on the elastohydrodynamic number, proplatelet length, proplatelet intrinsic curvature, and the number of proplatelets in an array.

5.5.9.1 Varying the elastohydrodynamic number

Higher values of the elastohydrodynamic number, $E_h = 8\pi\mu L^4/EIT$, correspond to decreased proplatelet bending stiffness EI, increased proplatelet length L, or

increased background flow shear rate $1/T$. Figure 5.14 demonstrates the effect of E_h on the equilibrium position of a proplatelet in shear flow, and the tangential and normal components of force density along the proplatelet. As E_h increases, Figure 5.14 b) shows that the tangential force component at first increases (dotted to dash-dot/dashed lines) as the proplatelet aligns more closely with the flow direction, before decreasing (dash-dot/dashed lines to solid) as the proplatelet at equilibrium is situated closer to the wall and therefore in a region of slower background flow as prescribed by equation (5.90). As E_h increases, Figure 5.14 c) shows that the normal force component generally decreases, again because the proplatelet becomes more aligned with the flow direction. At lower values of E_h, we see from Figures 5.14 b, c) that the force components increase with arclength, because the proplatelet protrudes out into areas of faster flow. In contrast, at higher values of E_h, the tangential force components are approximately constant along the proplatelet length, while normal components have one or two dips in normal force components, possibly due to there being regions where the proplatelet is perfectly aligned with the flow.

With regards to platelets in flow, $E_h = 1.5\times10^4$ (dashed line) and $E_h = 1.5\times10^6$ (solid line) lie within the expected range of values for E_h, and a key point for both of these is that the tangential force component is approximately one order of magnitude (or more) larger than the normal force component, indicating that proplatelets may primarily experience stress tangential to their surface when in shear flow with shear rates reflecting either *in vivo* or *in vitro* rates. Additionally, Figure 5.14 a) shows that both $E_h = 1.5 \times 10^4$ and $E_h = 1.5 \times 10^6$ have fairly small centreline curvatures apart from near the base. This gives some justification to our assumption of axisymmetry in the model of §5.4.

5.5.9.2 Varying the proplatelet length

By decreasing the dimensionless proplatelet length below 1, we can compare the behaviour of proplatelets with different lengths and the same bending stiffnesses, while fixing the background flow shear rate and velocity (whereas in §5.5.9.1, if we considered decreasing E_h by decreasing L, in fixing $u_{bg} = 1$ we were also either increasing the shear rate or increasing the dimensional background velocity in proportion to L). Figure 5.15 shows the equilibrium positions, and force density

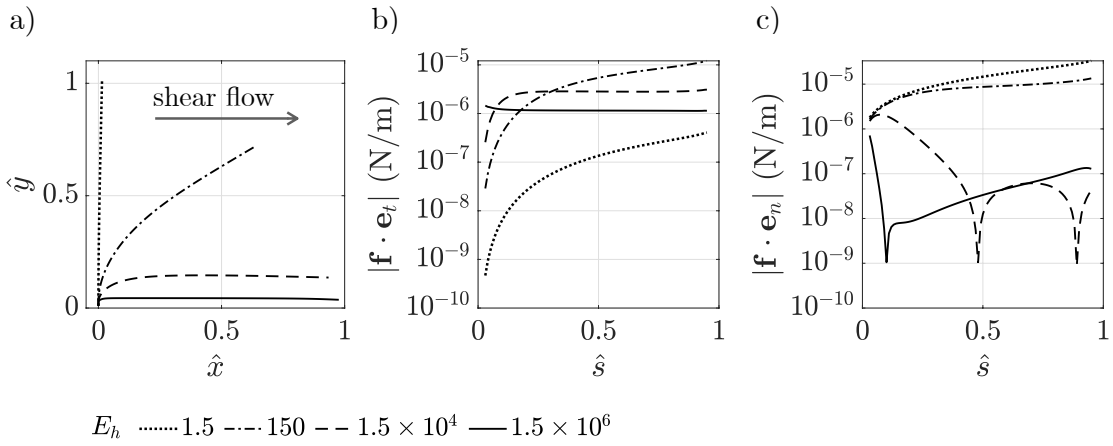

Figure 5.14: Equilibrium a) position, b) tangential force density against arclength, and c) normal force density against arclength, for elastohydrodynamic numbers $E_h = 1.5$ (dotted), 150 (dash-dot), 1.5×10^4 (dashed), 1.5×10^6 (solid), with $N = 100$ segments, dimensionless regularisation parameter $\hat{\delta} = 0.008$, and a unit dimensionless background shear flow.

components for proplatelets of dimensionless lengths $l = 0.5, 0.75, 1, 2$. The main difference is that longer proplatelets experience higher normal forces, with Figure 5.15 c) showing that $l = 2$ experiences normal force densities of up to one order of magnitude higher than $l = 0.5$.

5.5.9.3 Multiple proplatelets

Next we investigate the extent to which neighbouring proplatelets shield each other from flow, i.e. whether a proplatelet has reduced forces acting on it due to the presence of the neighbouring upstream proplatelet. Figure 5.16 b) and c) show that any shielding effects are minimal, as the force densities on upstream and downstream proplatelets have the same order of magnitude, and indeed at some arclength locations the downstream proplatelet even has higher normal force density than the upstream proplatelet. We have checked that for up to 30 proplatelets in an array, shielding is minimal enough that force density components are of the same order of magnitude for each proplatelet. This is fairly unsurprising given the slenderness of the proplatelets, each occupying very little volume relative to the $3D$ flow surrounding them. Perhaps if the proplatelets were placed closer to

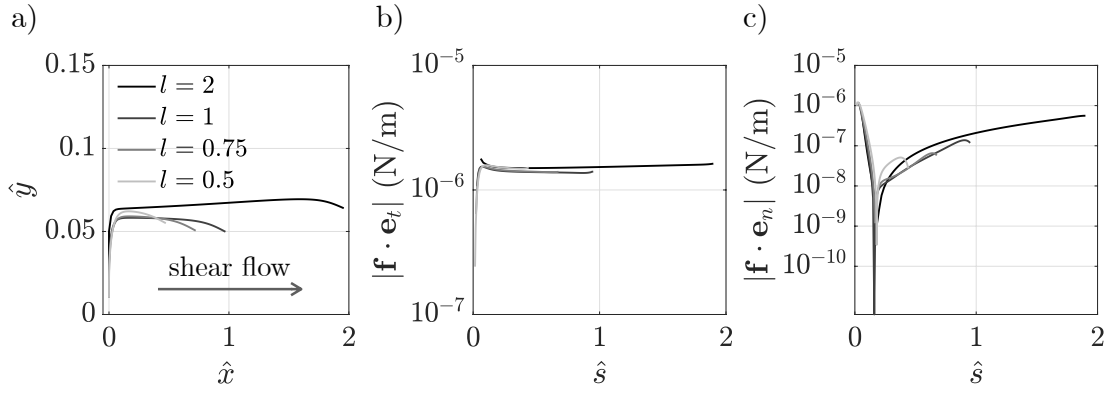

Figure 5.15: Equilibrium a) position, b) tangential force density against arclength, and c) normal force density against arclength, for dimemsionless lengths $l = 0.5, 0.75, 1, 2$ (light to dark), with $E_h = 4 \times 10^5$, $N = 100$ segments, dimensionless regularisation parameter $\hat{\delta} = 0.008$, and a unit dimensionless background shear flow.

each other more shielding would occur, however it is not possible to investigate this within the framework of the method of regularised Stokeslets due to modelling assumptions.

5.5.9.4 Intrinsic curvature

Motivated by studies in static culture indicating that actin causes proplatelets to bend even in the absence of flow [72], we study proplatelets with intrinsic curvatures interacting with shear flow. Intrinsic curvature is incorporated into the moment-strain constitutive relation by subtracting the intrinsic curvature from the current curvature in equation (5.66). Motivated by images in the supplementary material in [72], we choose three examples of intrinsic curvatures, shown in Figure 5.17 a) alongside a straight proplatelet. Their corresponding equilibrium positions under a shear flow are plotted in Figure 5.17 b). Under a shear flow, assigning an intrinsic curvature can cause up to two orders of magnitude fluctuations in normal force density, but causes minimal fluctuations in tangential force density away from that of a proplatelet with no intrinsic curvature, as shown by Figures 5.17 c) and d), respectively. It may be possible that regions of increased normal force density contribute to proplatelet fission, and hence that intrinsic curvatures

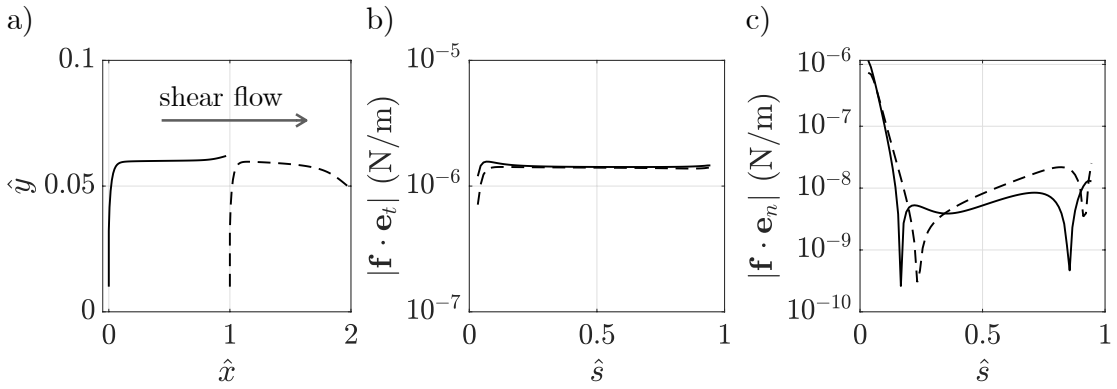

Figure 5.16: Equilibrium a) position, b) tangential force density against arclength, and c) normal force density against arclength for two adjacent filaments, with $E_h = 4\times10^5$, $N = 100$ segments, dimensionless regularisation parameter $\hat{\delta} = 0.008$, and a unit dimensionless background shear flow.

contribute to proplatelet fission.

5.6 Discussion

In this chapter we have explored two avenues of modelling of proplatelet formation. First, we modelled the proplatelet as an axisymmetric active gel, immersed in a viscous fluid. Active cytoskeletal stresses were incorporated through an isotropic surface tension term modelling the actomyosin cortex, and a nematic stress term capturing the extensile bundles of microtubules that are aligned with the proplatelet axis. We exploited the small aspect ratio of the proplatelet to derive a reduced model for its axial velocity, radius, and length. To model interaction with the external flow, we used resistive force theory, which is the leading-order slender body theory where the force exerted by the external fluid on the proplatelet depends only on their local relative velocities. Through a linear stability analysis we demonstrated that contractile surface tension is destabilising, while extensile nematic stress is stabilising. We conducted preliminary numerical simulations that looked individually at the effects of extensile nematic stress and the background flow, on proplatelet dynamics. These simulations demonstrated that the extensile nematic stress and the background flow both elongate the proplatelet. However, their effects differ in that the extensile nematic stress causes the proplatelet to

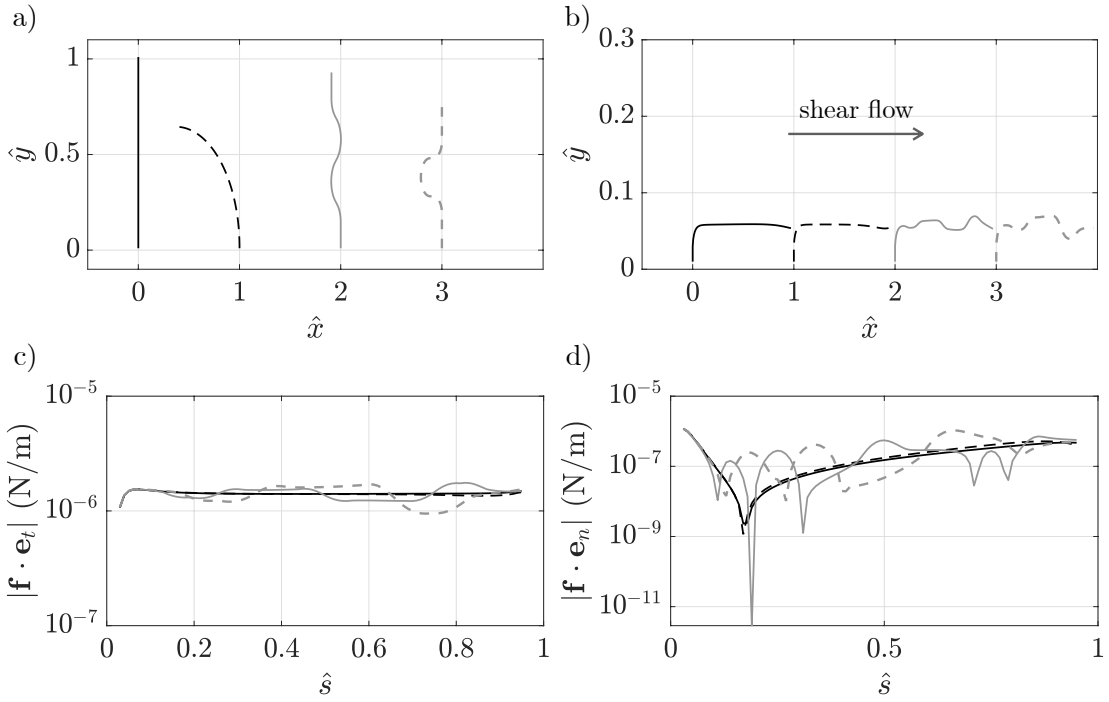

Figure 5.17: a) Intrinsic position, and equilibrium b) position, c) tangential force density against arclength, and d) normal force density against arclength, with $E_h = 4\times10^5$, $N = 100$ segments, dimensionless regularisation parameter $\hat{\delta} = 0.008$, and a unit dimensionless background shear flow. Note in a) the proplatelets are plotted side by side but each simulation is run for each proplatelet alone.

taper from base to tip, while the background flow causes the proplatelet to taper from tip to base.

The next steps with this model are to include the active surface tension and solve the governing equations numerically in wider parameter ranges, and to explore how the external flow and the contractile and extensile active stresses control proplatelet elongation, pause, and retraction phases. This would involve positing relationships between the active coefficients and the background flow, one route for which would be directly prescribing the former as functions of the latter; another option is to couple active coefficients to the concentration of unbound motor proteins or biochemical messengers, themselves governed by advection-reaction-diffusion equations (see for example [18, 82]).

More experimental observations could be incorporated into the active coef-

ficients. We could prescribe the extensile microtubule active coefficient to vary with the radial coordinate in regions where beading is occurring, motivated by experimental observations that microtubules locate nearer the cell cortex in beaded regions [71]. The extensile coefficient could also be prescribed to vary with the proplatelet length, reflecting observations of more loosely arranged microtubules (i.e. not all aligned in tight bundles) in the earlier stages of proplatelet formation [23], that may be expected to slide less effectively. This could be more directly modelled by modifying the nematic tensor to account for heterogeneity in microtubule orientations, i.e. not all being aligned with the centreline. More broadly, using established active gel theory [77], it may be appropriate to modify the model to include the effects of cytoskeleton elasticity, permeation of the cytoskeleton by the cytosol, and the (dis)assembly of cytoskeletal filaments. The simplicity of this first model makes it an ideal candidate for testing out possible biological mechanisms, while retaining the possibility of making analytical progress and/or conducting fast numerical solutions.

It is not clear how to prescribe the tension boundary condition at the proplatelet tip, where the resistive force theory is not valid. To proceed systematically, we would consider an inner region around the tip. However as such a region would have aspect ratio of O(1), this would necessitate solving the full Stokes flow equations in the external fluid coupled to the full active gel equations in the tip, requiring computationally expensive numerical simulations. Given that observations have shown platelets forming at the proplatelet tip [71], another option is to prescribe the tip tension as that on a sphere with radius equal to that of a typical platelet. Alternatively we could just set the tip tension to zero, as the tip region is small so the drag there may be expected to be relatively small.

A limitation of the first model is its assumption of axisymmetry. Some microfluidic devices may be able to mimic a near-axisymmetric domain, and hence provide relevant single-cell observation of proplatelet elongation for comparison with the model. However most settings where proplatelet formation occurs will be far from axisymmetric, with multiple proplatelets and platelets (and other blood cells if *in vivo*) in close proximity to each other, within curved vessels or pores. The first model is furthermore limited in its fluid-structure interaction by only retaining the leading-order terms in the drag exerted by the external fluid. The

higher-order terms were of $O(1/\log(1/\epsilon))$, where ϵ is the proplatelet aspect ratio, thus by neglecting them we introduced logarithmic errors; for example errors of $O(0.43)$ for $\epsilon = 0.1$ or of $O(0.2)$ for $\epsilon = 0.01$.

The second model goes some way in addressing these two limitations: firstly by replacing an axisymmetric free-space with a half-space, and tethering proplatelet bases to the wall to imitate proplatelets protruding from a vessel wall or a microfluidic channel wall; secondly, by using a non-local slender body theory, called the method of regularised Stokeslets. However, the second model uses a simpler constitutive law for proplatelets, modelling each proplatelet as an inextensible elastic rod of uniform radius using the Kirchoff rod equations, without incorporating any active stresses. The model is characterised by one dimensionless parameter, the elastohydrodynamic number, describing the relative strengths of hydrodynamic and elastic effects, in terms of the typical length and bending stiffness of a proplatelet, and the background flow shear rate and viscosity. We varied the elastohydrodynamic number, the number of proplatelets in an array, their relative lengths in an array, and their intrinsic curvatures, and computed their equilibrium positions, and the forces along each proplatelet. We found that under flow rates typically used for platelet production, the predominant force along a proplatelet is tangential rather than normal to its centreline, and that the proplatelet bends sharply near its base to align with the direction of flow. The latter has been observed *in vitro*, see for example [154]. Varying the intrinsic curvature resulted in spikes in normal force of up to two orders of magnitude compared to an intrinsically straight proplatelet, which may possibly contribute to proplatelet fission. Here we simply prescribed the intrinsic curvature based on representative images in the literature.

The model makes the (standard) *ad hoc* choice of regularisation parameter as equal to a characteristic proplatelet radius, and applies the no-slip boundary condition on the proplatelet centreline. Recent advances [159, 160] have replaced a constant regularisation parameter with one that systematically varies with the non-uniform radius, resulting in the no-slip boundary condition being algebraically accurate in the aspect ratio, when evaluated on the boundary.

One way to combine the advantages of the two models would be to replace the drag term from resistive force theory in the first model, with a drag term from

the method of regularised Stokeslets (it is easy to modify the half-space in the second model to a free-space). Such a drag term would be numerically computed, and updated with changes in proplatelet length, as well as changes in proplatelet radius if the modifications of [159, 160] are included in the regularised Stokeslet method.

A more consistent way of combining the two models would be to replace the Kirchhoff rod equations in the second model with the reduced active gel equations of the first model, perhaps first in an axisymmetric geometry and then modified to account for arc-length curvature. To make use of the analytically-computed expressions that relate drag at discretised nodes to the velocity of the node, we would need to coarse-grain the active gel equations, which may not be straightforward.

The longer-term aim is to make direct comparisons with experimental results. With suitable models and experimental results, possibly involving inhibition of select motor proteins and/or depolymerisation of microtubules/actin filaments, this next step would involve statistical inference of activity coefficients and/or laws relating activity coefficients to external stress.

Chapter 6

Conclusions and future work

In this thesis we have developed mathematical models to study platelet production across scales. Here, we summarise each of these models in turn, and discuss potential avenues for future work.

6.1 Bioreactor modelling

6.1.1 Summary of work

In Chapters 2-4, we constructed a model of a novel perfusion bioreactor designed by Shepherd et al. [137] for platelet production. This bioreactor contains a porous scaffold where platelets are produced by megakaryocytes, and two tube systems carrying cell culture media that sandwich the scaffold from above and below. Flow can enter and exit the scaffold through the interfaces between the scaffold and tube systems. The flow in the bioreactor is driven by the gravitational pressure head of the inlet reservoirs, and by the motion of four valves near the inlets and outlets of the tube systems. Cross-flow through the scaffold between the upper and lower tube systems exerts a shear stress on cells in the scaffold.

Our model can be used to predict how the bioreactor fluxes and scaffold shear stress depend on the bioreactor operating conditions and geometrical parameters, to aid experimentalists to mimic the *in vivo* production environment and as a result, to increase the clinical and commercial viability of *in vitro* platelet production. Using modelling, we have explored the range of operating protocols possible in the bioreactor. This included testing whether the operating protocol used by

Shepherd et al., where the flow was driven through the scaffold predominantly using the gravitational pressure head rather than by pulsing the valves, was able to obtain shear stresses in the range required for platelet production.

In Chapter 2, we introduced the full model for the bioreactor. This consisted of the Navier-Stokes equations in the tube systems, and Darcy's law and the continuity equation in the scaffold, coupled via appropriate interface conditions. The model incorporated the opening and closing of the four valves by prescribing the boundary positions of the valve walls to be time-dependent functions. At the inlets and outlets of the tube systems we prescribed unidirectional flow and normal stress boundary conditions, the latter of which enforced the gravitational pressure heads. By idealising the scaffold pores as cylindrical tubes, we obtained an expression of the scaffold shear stress in terms of the scaffold velocity and geometrical parameters characterising the scaffold.

In Chapter 3 we reduced the model of Chapter 2 under the quasi-steady and long wavelength assumptions, by exploiting the small aspect ratio of the bioreactor, and the small size of the reduced Reynolds number. Physically, this corresponded to the regime where the valves were either static or moving slowly. We solved the model to obtain analytical expressions for the pressures and fluxes throughout the bioreactor that contained 36 unknown coefficients. These were determined by solving an algebraic linear system obtained by imposing continuity of fluxes and pressures between different regions of the bioreactor, using matrix inversion in MATLAB at each timestep of valve motion.

We ranked the various static valve configurations in terms of greatest to least scaffold shear stress, and found that by using static valves we were only able to reach the lower end of the target shear stress range for platelet production. We also characterised the dependence of scaffold shear stress on various geometrical parameters, such as the lengths of different regions of the bioreactor, and the scaffold permeability. Finally, we investigated the effect of valve motion on the fluxes and shear stress in the bioreactor, although due to the assumption of a small reduced Reynolds number we were limited to considering relatively slowly moving valves. We found that as valve speeds increased, the maximum scaffold shear stress attained in the scaffold was able to rise above its value when valves were static. The results in this chapter indicated that static valves are only sufficient

for reaching the lower shear stress range, and that faster valve motion may drive a faster flow through the scaffold and hence allow us to reach the higher scaffold shear stresses that may be beneficial for platelet production.

Accordingly, Chapter 4 studied the model of Chapter 2 in the 'fast-valve' regime. We treated the cases of large and small-amplitude valve motion separately. Large-amplitude valve motion corresponded to order one reduced Reynolds and Strouhal numbers, meaning that both unsteady and non-linear inertia was retained in the Navier-Stokes equations. To be able to treat the non-linear inertia term in a relatively computationally light manner, and motivated by modelling methods for flow through blood vessels and collapsible tubes, we made the *ad hoc* assumption of prescribed axial velocity profiles throughout the tube systems. This allowed us to obtain a system of ordinary and partial differential equations for the axial fluxes and pressures in the bioreactor, which we solved using the method of lines in MATLAB. In the small-amplitude valve motion regime, the reduced Reynolds number was small and the Strouhal number was large. Their product, the Womersley number, was order one, so that only linear inertia was retained at leading-order. No *ad hoc* assumptions were required. The resulting integral equations were discretised and solved using MATLAB.

We investigated the use of fast valves with large-amplitude motion to control the shear stress in the scaffold. By using sufficiently fast valves, we could obtain maximum scaffold shear stress of $O(10^2)$ greater than the maximum obtainable with static valves. We suggested that continuously pulsing valves in an appropriate configuration (e.g. closing and opening the upper inlet valve, while opening and closing the lower outlet valve, and keeping the other two valves closed) could be a way to obtain shear stresses in the desired range over seconds or minutes. However, we found that using faster valves increased backflow in the scaffold, which could potentially dislodge megakaryocytes and disrupt the proplatelet elongation process. Using the model to measure the dependence of scaffold backflow on valve period, we were able to recommend a range of valve periods that would be able to avoid excessive backflow while still reaching higher shear stresses.

We found that with small-amplitude valve motion we could achieve lower scaffold backflow and higher mean shear stresses (although lower *maximum* shear stresses) than with large-amplitude valve motion. Continuous small-amplitude

valve oscillations may therefore provide a good compromise between reaching higher shear stresses and avoiding excessive backflow in the scaffold.

6.1.2 Future work

We made assumptions when constructing the bioreactor model that may affect its efficacy in predicting suitable operating protocols to improve platelet yields. There are several ways we could validate and modify the model, outlined below.

Firstly, it is important to validate the model against experimental data. To do this we propose experiments that measure the total flux through the bioreactor outlets after a fixed bioreactor operation time, both for static valves and pulsing valves in a variety of valve configurations. Since we can compute the outlet fluxes using the model, we could then make direct comparisons between this experimental data and the model predictions. It would also be interesting to see whether continuously pulsing the valves quickly with either small-amplitude or large-amplitude valve motion gives higher platelet yields than was achieved by Shepherd et al. using static valves with intermittent solitary valve movements.

In §4.2-§4.7 we prescribed the axial velocity profiles in the tube systems in an *ad hoc* manner, and validated the model in the small-amplitude valve motion regime. To determine the validity of this *ad hoc* assumption in the large-amplitude valve motion regime, we could use computational methods to solve the full three-dimensional Navier-Stokes equations in the valve region, and compare flux and pressure predictions with those from our model.

In Chapter 3 we presented initial investigations into how valve dynamics could be chosen to optimise quantities such as scaffold shear stress and backflow. To develop this work further we could use the computationally cheap models of both Chapters 3 and 4 within more sophisticated optimisation frameworks, to inform experimentalists' choices of precise valve dynamics.

A restriction that may quite readily be lifted is the scaffold being long and thin. In the bioreactor of [137] the scaffold has an aspect ratio of a half, which could be made larger in our model without excessive additional computational burden, i.e. by solving a three-dimensional Laplace's equation in the scaffold (instead of the two-dimensional reduction currently considered).

A significant assumption we made in the model was neglecting the scaffold elasticity and heterogeneity by using Darcy's law with a constant permeability throughout the scaffold. We could easily modify the model to include a two-layered scaffold with higher permeability in the upper layer than in the lower layer, as is present in the bioreactor of Shepherd et al. To incorporate scaffold elasticity, we could use Biot's equations for poroelasticity [16], which couple Darcy's law to the solid mechanics of the scaffold. Microtomography images of scaffolds of the type used in the bioreactor have been taken by Mohee et al. [104]. These images could be used as modelling domains to compute the scaffold shear stress using computational fluid dynamics in the style of Porter et al. [122]. We could use these results to validate the predictions of scaffold shear stress given by our model.

An obvious avenue of further exploration is modelling the nutrient transport in the bioreactor to determine the operating conditions under which megakaryocytes receive sufficient nutrients. This would involve solving advection-reaction-diffusion equations for each nutrient, as has been done frequently in the bioreactor literature [26].

Finally, another extension to the work would involve coupling the bioreactor model to the cellular and subcellular-scale mechanics of platelet formation. We discuss such a possibility in §6.2.2.

6.2 Cellular and subcellular-scale modelling

6.2.1 Summary of work

In Chapter 5 we modelled platelet production at the cellular and subcellular scales, looking at the onset of platelet formation, when cytoskeletal forces drive proplatelets to elongate and form beaded shapes. We constructed two models of this process. The first model used a simple active gel theory to describe the proplatelet as an axisymmetric viscous gel with internal extensile stresses in the axial direction caused by the sliding of microtubule bundles, and contractile surface tension caused by the actomyosin cortex. We modelled the external fluid using Stokes flow and derived a resistive force theory relationship between the axial proplatelet

velocity and the force exerted on it by the external flow. By exploiting the small aspect ratio of the proplatelet, we derived a reduced set of equations governing the proplatelet axial velocity, radius, and length. A linear stability analysis showed that extensile stress is stabilising and, as in a Rayleigh-Taylor instability, surface tension is destabilising. Preliminary numerical simulations showed that internal extensile stresses cause elongation and tapering from the proplatelet base to tip, while a background flow (aligned with the proplatelet axis) causes elongation and tapering from the proplatelet tip to base.

The second model we constructed improved upon the first in that it dropped the assumption of axisymmetry, and used a more accurate method to derive a relationship between external fluid drag and proplatelet velocity, namely the method of regularised Stokeslets. Both *in vitro* and *in vivo*, proplatelets often protrude from a perforated wall into a region of flow, which motivated our choice of modelling domain as a half-space with the base of the proplatelet tethered to the wall. We neglected the viscous character of the proplatelet and its active cytoskeletal forces, and modelled the proplatelet as an elastic rod.

The model consisted of ordinary differential equations in time for the discretised proplatelet centreline position and forces along the proplatelet, which we solved using numerical ODE solvers in MATLAB. Our results showed that in the typical physiological or experimental parameter regimes for flow past proplatelets, the forces on the proplatelet are predominantly in the direction tangential to the proplatelet centreline. We also demonstrated that lining proplatelets in arrays did not result in significant deviations in forces along the proplatelets as compared to when they are isolated, and that the prescription of an intrinsic curvature in the proplatelet may cause large fluctuations in normal stress along the proplatelet away from the intrinsically straight case, but comparatively smaller deviations in tangential stress.

6.2.2 Future work

An obvious next step in the active gel model would be to include the active surface tension in the numerical simulations, and conduct simulations for a range of values of active coefficients and background flow. This would reveal how the shape and

length of a proplatelet depend on its cortical tension and microtubule extensile stress. Mechanotransduction mechanisms could then be incorporated to model the response of the active coefficients to the external flow. Using the existing framework of active gel theory, the constitutive law in the active gel model could be modified to account for proplatelet elasticity, permeation of the cytoskeleton by cytosol, and deviations of the nematic tensor from being purely axially extensile. We could furthermore specify mechanisms for the addition of mass from the megakaryocyte body to the proplatelet, which occurs in the active gel model through a prescribed axial velocity at the proplatelet base. Although biological understanding of mechanisms regulating this aspect of growth is limited, we could trial simple hypotheses relating mass transfer to the external flow rate.

To combine the two models of this chapter, we could quite easily use the method of regularised Stokeslets in an axisymmetric domain to replace the resistive force theory used to compute hydrodynamic drag in the active gel model. Alternatively, we could drop the assumption of axisymmetry and replace the elastic proplatelet in the second model with the active gel proplatelet from the first model.

Comparisons with experiments are necessary to calibrate either model, and to suggest what further mechanisms should be included. Appropriate experiments could include fixing a megakaryocyte in place in a bioreactor with a background flow. We could then monitor the length and shape of a protruding proplatelet over time, while varying the background flow, inhibition of dynein or myosin, and depolymerisation of microtubules between experiments so as to isolate the effects of contractile and extensile forces, and their coupling with the external flow. As the models are relatively computationally cheap to solve, when calibrating the models we may be able to use methods from statistical inference that require the models to be solved many times.

Finally, a key goal would be to bridge the gap between the bioreactor, cell-scale, and subcellular-scale models. By coupling the bioreactor model to transport equations for megakaryocytes and platelets, we could predict the distribution of megakaryocytes and platelets in the scaffold. The bioreactor model could inform background flow conditions in a cell-scale model, while a cell-scale model that incorporates subcellular machinery could predict the rate of platelet production from megakaryocytes, thereby coupling back to cell transport equations. After

calibrating the model against experimental data quantifying platelet yields, such a multiscale model could reduce the burden on experimental trial and error by allowing experimentalists to systematically choose a suitable operating regime to achieve high platelet yields.

In summary, we have used mathematical modelling to gain mechanistic insight into a complex bioreactor for platelet production, and to suggest improved operating regimes for the bioreactor. We have also constructed relatively simple mathematical models that incorporate the key mechanics behind proplatelet elongation. In future work it will be crucial to validate both the bioreactor and cell-scale models against experimental data, and to use experimental insights to guide the next steps in model development. Ultimately, this modelling framework may be used to advance platelet production for therapeutic uses.

Appendix A

Valve closure functions

The valve closure function c_v appears in the equation (2.5) for valve cross-sectional area. We choose c_v in Chapters 3 and 4 as follows.

The system of equations in Chapter 3 contains coefficients only involving the first time derivative of A_i^*. This means that when choosing c_v we require only that dc_v/dt^* is continuous when switching between a moving valve and a static valve, i.e. that $dc_v/dt^* = 0$ when a valve is fully open or closed. We use the following forms for c_v, which satisfy $dc_v/dt^* = 0$ when a valve is open or closed:

$$c_v(t^*;\tau) = \frac{1}{2}\{1 - \cos(2\pi s(t^*,\tau))\} \tag{A.1}$$

where $s = (t^* - t_0^*)/\tau$, the valve starts closing at time t_0^*, and $t^* \in (t_0^*, t_0^* + \tau/2)$;

$$c_v(t^*;\tau) = \frac{1}{2}\{1 + \cos(2\pi s(t^*,\tau))\} \tag{A.2}$$

where the valve starts opening at time t_0^*; $c_v = 0$ when the valve is open; and $c_v = 1$ when the valve is closed.

The system of equations in Chapter 4 contains coefficients involving the first and second time derivatives of A_i^*. We therefore require that both dc_v/dt^* and d^2c_v/dt^{*2} are continuous when switching between a moving valve and a static valve, i.e. that $dc_v/dt^* = 0 = d^2c_v/dt^{*2}$ when a valve is open or closed. We choose a piecewise quintic polynomial in time for c_v, that ensures that the aforementioned condition is satisfied. The valve closure function takes one of the forms:

$$c_v(t^*;\tau) = 16\left(12s(t^*,\tau)^5 - 15s(t^*,\tau)^4 + 5s(t^*;\tau)^3\right) \tag{A.3}$$

where the valve starts closing at time t_0^* and $t^* \in (t_0^*, t_0^* + \tau/2)$, or

$$c_v(t^*;\tau) = 16\left(12\left(\frac{1}{2} - s(t^*,\tau)\right)^5 - 15\left(\frac{1}{2} - s(t^*,\tau)\right)^4 + 5\left(\frac{1}{2} - s(t^*,\tau)\right)^3\right) \tag{A.4}$$

when the valve starts opening at time t_0^* and $t^* \in (t_0^*, t_0^* + \tau/2)$. As before $c_v = 0$ when the valve is open, and $c_v = 1$ when the valve is closed. While the valve is closing (opening), $c_v(s)$ is a quintic polynomial with stationary inflection points at $s = 0$, corresponding to a fully open (closed) valve, and $s = 1/2$, corresponding to a closed (open) valve.

Appendix B

Validation of model of §5.5

Here we validate the model in §5.5 against a number of examples in the literature. All plotted quantities are the dimensionless hatted variables in §5.5, although here we omit hats.

B.1 Tethered fibre in shear flow

We first omit elasticity and rather assume the fibre is rigid, so as to validate the regularised Stokeslet method against the boundary element method used by Pozrikidis [125]. The force density along the a single fibre aligned perpendicularly to the wall and tethered to the wall at one end is computed for regularisation parameters $\epsilon = 0.001, 0.005, 0.01$, and $E_h = 27.3$, under a shear flow in the x dimension with dimensionless shear rate of 1. Good agreement between our results and the force density in the x direction obtained by Pozrikidis is shown in Figure B.1 a) for $0.01 < s < 0.94$. We see increasing fluctuations in force density near the endpoints as the regularisation parameter increases, in line with the observations of Cortez [35].

B.2 Tethered elastic fibre in shear flow

Next we validate the method of regularised Stokeslets against the boundary element method of Pozrikidis [124] in the case of a single elastic filament tethered to the wall of a half-space. This comparison has been done by Walker et al. [161], using piecewise linear force density, whereas we use piecewise constant force density

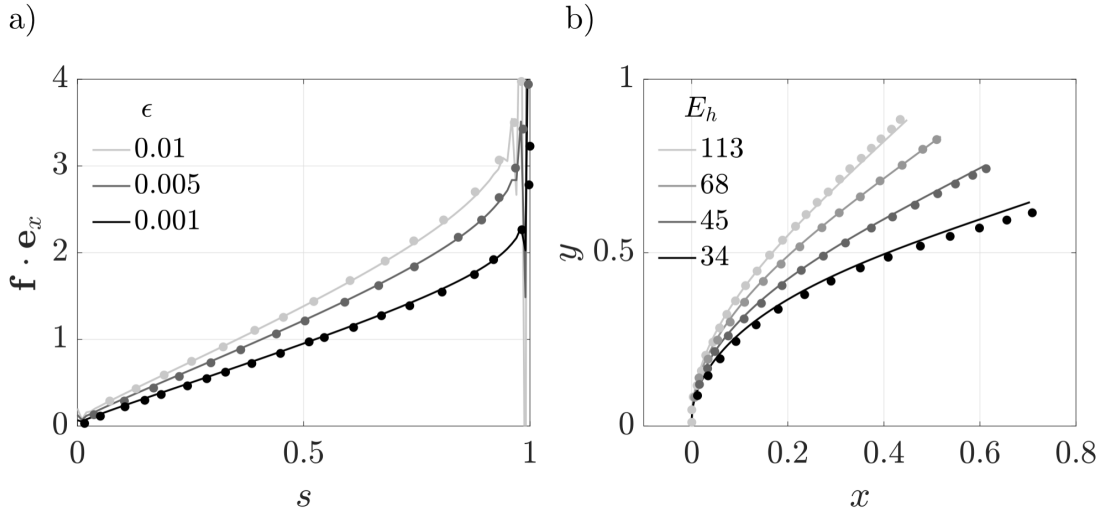

Figure B.1: a) Tethered fibre in shear flow. Dimensionless force density $\boldsymbol{f}$ in the x direction against arclength s, computed by us using the regularised stokeslet method (lines) with piecewise linear force density and by Pozrikidis [123] using the boundary element method (dots), for $E_h = 27.3$, $\epsilon = 0.001, 0.005, 0.01$ (left to right), $N = 50$ segments, and background shear flow $\boldsymbol{u}_{bg} = y\boldsymbol{e}_x$. b) Tethered elastic fibre in shear flow. Equilibrium states of a fibre tethered to the wall of a half-space, for elastohydrodynamic numbers $E_h \approx 34, 45, 68, 113$.

along the filament. Figure B.1 b) shows filament positions computed for elastohydrodynamic number $E_h \approx 34, 45, 68, 113$, $N = 80$ segments, and regularisation parameter $\epsilon = 0.05$. The filament is initially perpendicular to the wall, and is moved by the dimensionless shear flow $\boldsymbol{u} = y\boldsymbol{e}_x$ before eventually settling in an equilibrium state, plotted in Figure B.1 b). The closeness of the dots (data from [124]) and the lines (our data) indicate good agreement between computation via the boundary element method [124] and the method of regularised Stokeslets.

B.3 Single free fibre in shear flow

We validate our implementation of the method of regularised Stokeslets against that of Hall-McNair et al. [64], with the example of a single filament moving freely under shear flow. The filament is initially situated with its midpoint at the origin, and is perturbed from being straight so as to give rise to buckling, with perturbed

tangent angles given by

$$\theta_n(0) = 0.9\pi + 0.1\left(\frac{\tilde{s}_n^3}{3} - \frac{\tilde{s}_n^4}{4} + \frac{\tilde{s}_n^5}{5}\right), \tag{B.1}$$

where $\tilde{s}_n$ is the arclength midway along the n^{th} segment. Hall-McNair et al. use the dimensionless viscous-elastic parameter

$$\mathcal{V} = \frac{\mu\dot{\gamma}L^4}{EI}, \tag{B.2}$$

where $\dot{\gamma}$ is the shear rate. For our computations this is converted to our elastohydrodynamic parameter $E_h = 8\pi\mu L^4/(EIT)$ by multiplying through by 8π. Figure

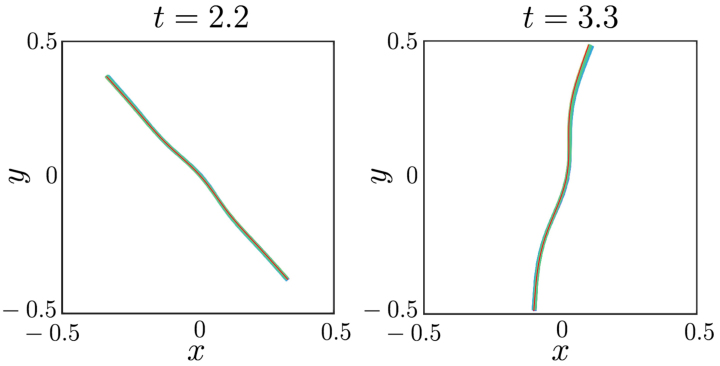

Figure B.2: Single free fibre in shear flow. $\mathcal{V} = 4\times10^3$, $E_h = 32\pi\times10^3$, $N = 40, 80$, $\epsilon = 0.01$. Red lines are our data for $N = 40$, green and blue (hardly visible) lines are data from Figure S3 in Hall-McNair et al [64], for $N = 80$ and $N = 40$ segments, respectively.

B.2 shows agreement between our filament configurations (red) and those of Hall-McNair et al (green), plotted in the $x-y$ plane at $t = 2.2, 3.3$ for $E_h = 3.2\pi\times10^3$.

We also look at agreement in tangent angles in the body frame, which are tangent angles shifted by the mean tangent angle at time t:

$$\theta^i_{\text{body}}(t) = \theta^i(t) - \frac{1}{N}\sum_{j=1}^{N}\theta^j(t). \tag{B.3}$$

Figure B.3 plots the tangent angles along the arclength s of a filament with elastohydrodynamic number $E_h = 4\pi\times10^4$ and $N = 40$ segments, at times $t = 2.2, 3.3, 4.4$. We observe good agreement between our results (lines) and those

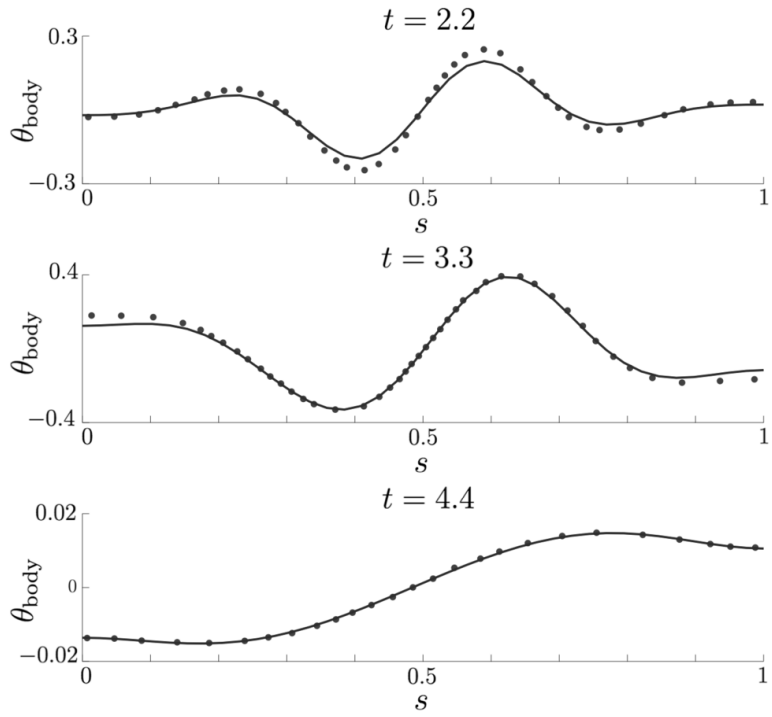

Figure B.3: Single free fibre in shear flow. $\mathcal{V} = 5 \times 10^3, E_h = 4\pi \times 10^4, N = 40$, $\epsilon = 0.01$. Circles are data from Hall-McNair et al [64] Figure 5a), lines are our data, computed using piecewise linear force density.

of Hall-McNair et al. (circles). Similarly, Figure B.4 shows agreement in tangent angles for $E_h = 32\pi \times 10^4$ and $N = 80$, with results plotted at $t = 2.2, 3.3$. Note however that more segments than for $E_h = 4\pi \times 10^4$ were required to obtain visibly close agreement (80 segments rather than 40).

B.4 Comparing linear force density and constant force density

When choosing force density to be piecewise linear in the method of regularised Stokeslets, oscillations in computed force density are observed near filament end-points. By instead using piecewise *constant* force densities along each filament segment (as we do in §5.5), the oscillations are made less severe, as shown in Figure B.5. As discussed in [159], the reason for this is unclear.

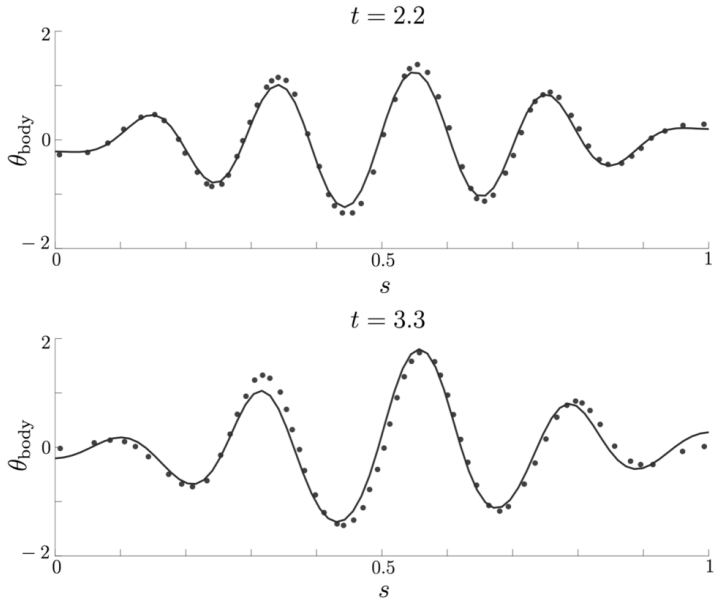

Figure B.4: Single free fibre in shear flow. Lines are our data, with $E_h = 32\pi \times 10^4, N = 80$, $\epsilon = 0.01$, computed using piecewise linear force density. Circles are data from Hall-McNair et al [64] Figure S4, with $\mathcal{V} = 4 \times 10^4, N = 80$, $\epsilon = 0.01$.

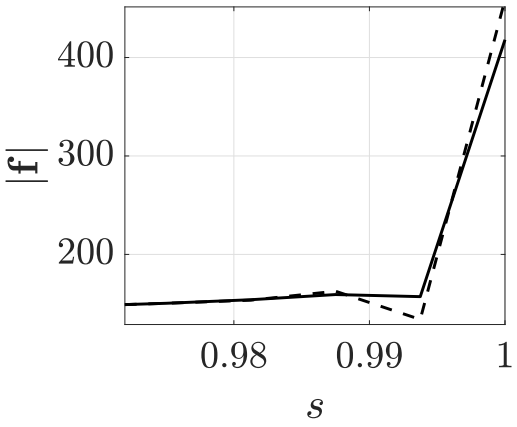

Figure B.5: Comparison of oscillations in force density near filament endpoint, for constant force density (solid) and linear force density (dashed). The filament is in full-space under a uniform flow aligned perpendicularly to fibre. ($\epsilon = 0.001, N = 160, E_h = 2000$)

Bibliography

[1] J. Ainley et al. “The method of images for regularized Stokeslets”. In: *Journal of Computational Physics* 227.9 (2008), pp. 4600–4616.

[2] B. Alberts. *Molecular Biology of the Cell*. WW Norton & Company, 2017.

[3] D. Ali and S. Sen. “Finite element analysis of mechanical behavior, permeability and fluid induced wall shear stress of high porosity scaffolds with gyroid and lattice-based architectures”. In: *Journal of the Mechanical Behavior of Biomedical Materials* 75 (2017), pp. 262–270.

[4] J. Allard et al. “Bidirectional sliding of two parallel microtubules generated by multiple identical motors”. In: *Journal of Mathematical Biology* 79.2 (2019), pp. 571–594.

[5] W. Alt and M. Dembo. “Cytoplasm dynamics and cell motion: two-phase flow models”. In: *Mathematical Biosciences* 156.1-2 (1999), pp. 207–228.

[6] S. S. Antman. “Nonlinear Plasticity”. In: *Nonlinear Problems of Elasticity*. Springer, 1995, pp. 603–628.

[7] K. Azer and C. S. Peskin. “A one-dimensional model of blood flow in arteries with friction and convection based on the Womersley velocity profile”. In: *Cardiovascular Engineering* 7.2 (2007), pp. 51–73.

[8] C. Bächer, M. Bender, and S. Gekle. “Flow-accelerated platelet biogenesis is due to an elasto-hydrodynamic instability”. In: *Proceedings of the National Academy of Sciences* 117.32 (2020), pp. 18969–18976.

[9] A. Balduini et al. “Adhesive receptors, extracellular proteins and myosin IIA orchestrate proplatelet formation by human megakaryocytes”. In: *Journal of Thrombosis and Haemostasis* 6.11 (2008), pp. 1900–1907.

[10] K. Bardsley et al. “Current state-of-the-art 3D tissue models and their compatibility with live cell imaging”. In: *Multi-Parametric Live Cell Microscopy of 3D Tissue Models* (2017), pp. 3–18.

[11] J. Bear. *Modeling Phenomena of Flow and Transport in Porous Media*. Vol. 1. Springer, 2018.

[12] G. S. Beavers and D. D. Joseph. “Boundary conditions at a naturally permeable wall”. In: *Journal of Fluid Mechanics* 30.1 (1967), pp. 197–207.

[13] O. Behnke and A. Forer. “From megakaryocytes to platelets: platelet morphogenesis takes place in the bloodstream”. In: *European Journal of Haematology* 60.S61 (1998), pp. 3–23.

[14] M. Bender et al. “Microtubule sliding drives proplatelet elongation and is dependent on cytoplasmic dynein”. In: *Blood* 125.5 (2015), pp. 860–868.

[15] T. C. Bidone et al. “Morphological transformation and force generation of active cytoskeletal networks”. In: *PLoS Computational Biology* 13.1 (2017), e1005277.

[16] M. A. Biot. “General theory of three-dimensional consolidation”. In: *Journal of Applied Physics* 12.2 (1941), pp. 155–164.

[17] A. Blin et al. “Microfluidic model of the platelet-generating organ: beyond bone marrow biomimetics”. In: *Scientific Reports* 6 (2016), p. 21700.

[18] J. S. Bois, F. Jülicher, and S. W. Grill. “Pattern formation in active fluids”. In: *Physical Review Letters* 106.2 (2011), p. 028103.

[19] A. Bornert et al. “Cytoskeletal-based mechanisms differently regulate in vivo and in vitro proplatelet formation”. In: *Haematologica* 106.5 (2021), p. 1368.

[20] D. C. Bottino and L. J. Fauci. “A computational model of ameboid deformation and locomotion”. In: *European Biophysics Journal* 27.5 (1998), pp. 532–539.

[21] P. E. Bourgine, I. Martin, and T. Schroeder. “Engineering human bone marrow proxies”. In: *Cell Stem Cell* 22.3 (2018), pp. 298–301.

[22] C. Brito and S. Sousa. “Non-muscle myosin 2A (NM2A): structure, regulation and function”. In: *Cells* 9.7 (2020), p. 1590.

[23] E. Brown et al. “Multiple membrane extrusion sites drive megakaryocyte migration into bone marrow blood vessels”. In: *Life Science Alliance* 1.2 (2018), e201800061.

[24] M. A. Brown, R. K. Iyer, and M. Radisic. “Pulsatile perfusion bioreactor for cardiac tissue engineering”. In: *Biotechnology Progress* 24.4 (2008), pp. 907–920.

[25] K. S. Burbank and T. J. Mitchison. “Microtubule dynamic instability”. In: *Current Biology* 16.14 (2006), R516–R517.

[26] I. Burova, I. Wall, and R. J. Shipley. “Mathematical and computational models for bone tissue engineering in bioreactor systems”. In: *Journal of Tissue Engineering* 10 (2019), p. 2041731419827922.

[27] C. K. Byun et al. “Pumps for microfluidic cell culture”. In: *Electrophoresis* 35.2-3 (2014), pp. 245–257.

[28] B. Cameron et al. “Evaluation of platelet transfusion triggers in a tertiary-care hospital”. In: *Transfusion* 47.2 (2007), pp. 206–211.

[29] R. L. Carrier et al. “Perfusion improves tissue architecture of engineered cardiac muscle”. In: *Tissue engineering* 8.2 (2002), pp. 175–188.

[30] J. M. Carson et al. “Non-invasive coronary CT angiography-derived fractional flow reserve: A benchmark study comparing the diagnostic performance of four different computational methodologies”. In: *International Journal for Numerical Methods in Biomedical Engineering* 35.10 (2019), e3235.

[31] N. Castro et al. “Physically active bioreactors for tissue engineering applications”. In: *Advanced Biosystems* 4.10 (2020), p. 2000125.

[32] A. Charlton et al. “Where did platelets go in 2012? A survey of platelet transfusion practice in the North of England”. In: *Transfusion Medicine* 24.4 (2014), pp. 213–218.

[33] G. Cheng, P. Markenscoff, and K. Zygourakis. “A 3D hybrid model for tissue growth: the interplay between cell population and mass transport dynamics”. In: *Biophysical Journal* 97.2 (2009), pp. 401–414.

[34] P. Chugh and E. K. Paluch. “The actin cortex at a glance”. In: *Journal of Cell Science* 131.14 (2018), jcs186254.

[35] R. Cortez. “Regularized stokeslet segments”. In: *Journal of Computational Physics* 375 (2018), pp. 783–796.

[36] R. Cortez. “The method of regularized Stokeslets”. In: *SIAM Journal on Scientific Computing* 23.4 (2001), pp. 1204–1225.

[37] R. Cortez and D. Varela. “A general system of images for regularized stokeslets and other elements near a plane wall”. In: *Journal of Computational Physics* 285 (2015), pp. 41–54.

[38] E. M. Craig, S. Dey, and A. Mogilner. “The emergence of sarcomeric, graded-polarity and spindle-like patterns in bundles of short cytoskeletal polymers and two opposite molecular motors”. In: *Journal of Physics: Condensed Matter* 23.37 (2011), p. 374102.

[39] E. M. Craig et al. “Polarity sorting of axonal microtubules: a computational study”. In: *Molecular Biology of the Cell* 28.23 (2017), pp. 3271–3285.

[40] L. J. Cummings and S. L. Waters. “Tissue growth in a rotating bioreactor. Part II: fluid flow and nutrient transport problems”. In: *Mathematical Medicine and Biology* 24.2 (2007), pp. 169–208.

[41] C. A. Di Buduo et al. “Programmable 3D silk bone marrow niche for platelet generation ex vivo and modeling of megakaryopoiesis pathologies”. In: *Blood* 125.14 (2015), pp. 2254–2264.

[42] E. Dolgin. “Bioengineering: doing without donors”. In: *Nature* 549.7673 (2017), S12–S15.

[43] C. Dunois-Lardé et al. “Exposure of human megakaryocytes to high shear rates accelerates platelet production”. In: *Blood* 114.9 (2009), pp. 1875–1883.

[44] J. Eggers and T. F. Dupont. “Drop formation in a one-dimensional approximation of the Navier–Stokes equation”. In: *Journal of Fluid Mechanics* 262 (1994), pp. 205–221.

[45] J. Eggers and E. Villermaux. “Physics of liquid jets”. In: *Reports on Progress in Physics* 71.3 (2008), p. 036601.

[46] P. R. Fernandes et al. “Multiscale modelling on bone mechanics–application to tissue engineering and bone quality analysis”. In: *IFAC Proceedings Volumes* 45.2 (2012), pp. 1013–1017.

[47] R. T. Ferrell and D. M. Himmelblau. “Diffusion coefficients of nitrogen and oxygen in water”. In: *Journal of chemical and engineering data* 12.1 (1967), pp. 111–115.

[48] L. Formaggia, D. Lamponi, and A. Quarteroni. “One-dimensional models for blood flow in arteries”. In: *Journal of Engineering Mathematics* 47.3 (2003), pp. 251–276.

[49] L. E. Freed and G. Vunjak-Novakovic. “Cultivation of cell–polymer tissue constructs in simulated microgravity”. In: *Biotechnology and Bioengineering* 46.4 (1995), pp. 306–313.

[50] A. Fritsch, C. Hellmich, and P. Young. “Micromechanics-derived scaling relations for poroelasticity and strength of brittle porous polycrystals”. In: *Journal of Applied Mechanics* 80.2 (2013).

[51] S. Fürthauer, D. J. Needleman, and M. J. Shelley. “A design framework for actively crosslinked filament networks”. In: *New Journal of Physics* 23.1 (2021), p. 013012.

[52] S. Fürthauer and M. J. Shelley. “How Cross-Link Numbers Shape the Large-Scale Physics of Cytoskeletal Materials”. In: *Annual Review of Condensed Matter Physics* 13 (2022), pp. 365–384.

[53] S. Fürthauer et al. “Self-straining of actively crosslinked microtubule networks”. In: *Nature Physics* 15.12 (2019), pp. 1295–1300.

[54] E. A. Gaffney, K. Ishimoto, and B. J. Walker. "Modelling motility: the mathematics of spermatozoa". In: *Frontiers in Cell and Developmental Biology* 9 (2021).

[55] C. J. Galban and B. R. Locke. "Effects of spatial variation of cells and nutrient and product concentrations coupled with product inhibition on cell growth in a polymer scaffold". In: *Biotechnology and Bioengineering* 64.6 (1999), pp. 633–643.

[56] L. Geris et al. *Computational Modeling in Tissue Engineering*. Springer, 2013.

[57] F. Gittes et al. "Flexural rigidity of microtubules and actin filaments measured from thermal fluctuations in shape." In: *The Journal of Cell Biology* 120.4 (1993), pp. 923–934.

[58] S. Go et al. "Super-resolution imaging reveals cytoskeleton-dependent organelle rearrangement within platelets at intermediate stages of maturation". In: *Structure* 29.8 (2021), pp. 810–822.

[59] E. F. Gramsbergen, L. Longa, and W. H. de Jeu. "Landau theory of the nematic-isotropic phase transition". In: *Physics Reports* 135.4 (1986), pp. 195–257.

[60] J. Gray and G. Hancock. "The propulsion of sea-urchin spermatozoa". In: *Journal of Experimental Biology* 32.4 (1955), pp. 802–814.

[61] L. Grinberg et al. "Modeling blood flow circulation in intracranial arterial networks: a comparative 3D/1D simulation study". In: *Annals of Biomedical Engineering* 39.1 (2011), pp. 297–309.

[62] Y. Guyot et al. "Coupling curvature-dependent and shear stress-stimulated neotissue growth in dynamic bioreactor cultures: a 3D computational model of a complete scaffold". In: *Biomechanics and Modeling in Mechanobiology* 15.1 (2016), pp. 169–180.

[63] Y. Guyot et al. "Immersed boundary models for quantifying flow-induced mechanical stimuli on stem cells seeded on 3D scaffolds in perfusion bioreactors". In: *PLoS Computational Biology* 12.9 (2016).

[64] A. L. Hall-McNair et al. "Efficient implementation of elastohydrodynamics via integral operators". In: *Physical Review Fluids* 4.11 (2019), p. 113101.

[65] M. Heil and O. E. Jensen. "Flow in collapsible tubes and past other highly compliant boundaries". In: *Flow Past Highly Compliant Boundaries and in Collapsible Tubes* 72 (2003).

[66] M. Heil and S. L. Waters. "Transverse flows in rapidly oscillating elastic cylindrical shells". In: *Journal of Fluid Mechanics* 547 (2006), pp. 185–214.

[67] D. Hellums. “1993 Whitaker Lecture: Biorheology in thrombosis research”. In: *Annals of Biomedical Engineering* 22.5 (1994), pp. 445–455.

[68] J. R. Hess. “Conventional blood banking and blood component storage regulation: opportunities for improvement”. In: *Blood Transfusion* 8.Suppl 3 (2010), s9.

[69] P. D. Howell. “Extensional thin layer flows”. University of Oxford, 1994.

[70] L. Hyndman et al. “Mathematical modelling of fluid flow and solute transport to define operating parameters for in vitro perfusion cell culture systems”. In: *Interface Focus* 10.2 (2020), p. 20190045.

[71] J. Italiano Jr, S. Patel-Hett, and J. Hartwig. “Mechanics of proplatelet elaboration”. In: *Journal of Thrombosis and Haemostasis* 5 (2007), pp. 18–23.

[72] J. E. Italiano Jr et al. “Blood platelets are assembled principally at the ends of proplatelet processes produced by differentiated megakaryocytes”. In: *The Journal of Cell Biology* 147.6 (1999), pp. 1299–1312.

[73] Y. Ito et al. “Turbulence activates platelet biogenesis to enable clinical scale ex vivo production”. In: *Cell* 174.3 (2018), pp. 636–648.

[74] M. J. Jaasma, N. A. Plunkett, and F. J. O’Brien. “Design and validation of a dynamic flow perfusion bioreactor for use with compliant tissue engineering scaffolds”. In: *Journal of Biotechnology* 133.4 (2008), pp. 490–496.

[75] J. Joanny and J. Prost. “Active gels as a description of the actin-myosin cytoskeleton”. In: *HFSP Journal* 3.2 (2009), pp. 94–104.

[76] R. E. Johnson. “An improved slender-body theory for Stokes flow”. In: *Journal of Fluid Mechanics* 99.2 (1980), pp. 411–431.

[77] F. Jülicher, S. W. Grill, and G. Salbreux. “Hydrodynamic theory of active matter”. In: *Reports on Progress in Physics* 81.7 (2018), p. 076601.

[78] T. Junt et al. “Dynamic visualization of thrombopoiesis within bone marrow”. In: *Science* 317.5845 (2007), pp. 1767–1770.

[79] R. M. Kaufman et al. “Circulating megakaryocytes and platelet release in the lung”. In: *Blood* 26.6 (1965), pp. 720–731.

[80] J. B. Keller and S. I. Rubinow. “Slender-body theory for slow viscous flow”. In: *Journal of Fluid Mechanics* 75.4 (1976), pp. 705–714.

[81] L. S. Kimpton et al. “Multiple travelling-wave solutions in a minimal model for cell motility”. In: *Mathematical Medicine and Biology: a Journal of the IMA* 30.3 (2013), pp. 241–272.

[82] L. Kimpton et al. “Approaches to myosin modelling in a two-phase flow model for cell motility”. In: *Physica D: Nonlinear Phenomena* 318 (2016), pp. 34–49.

[83] G. H. Koenderink and E. K. Paluch. “Architecture shapes contractility in actomyosin networks”. In: *Current Opinion in Cell Biology* 50 (2018), pp. 79–85.

[84] L. Koens and E. Lauga. “The boundary integral formulation of Stokes flows includes slender-body theory”. In: *Journal of Fluid Mechanics* 850 (2018).

[85] L. Korson, W. Drost-Hansen, and F. J. Millero. “Viscosity of water at various temperatures”. In: *The Journal of Physical Chemistry* 73.1 (1969), pp. 34–39.

[86] M. Krishnegowda and V. Rajashekaraiah. “Platelet disorders: an overview”. In: *Blood Coagulation & Fibrinolysis* 26.5 (2015), pp. 479–491.

[87] K. Kruse et al. “Contractility and retrograde flow in lamellipodium motion”. In: *Physical Biology* 3.2 (2006), p. 130.

[88] K. Kruse and F. Jülicher. “Actively contracting bundles of polar filaments”. In: *Physical Review Letters* 85.8 (2000), p. 1778.

[89] A. Kurganov and D. Levy. “A third-order semidiscrete central scheme for conservation laws and convection-diffusion equations”. In: *SIAM Journal on Scientific Computing* 22.4 (2000), pp. 1461–1488.

[90] A. Kurganov and E. Tadmor. “New high-resolution central schemes for nonlinear conservation laws and convection–diffusion equations”. In: *Journal of Computational Physics* 160.1 (2000), pp. 241–282.

[91] M. Le Bars and M. G. Worster. “Interfacial conditions between a pure fluid and a porous medium: implications for binary alloy solidification”. In: *Journal of Fluid Mechanics* 550 (2006), pp. 149–173.

[92] G. Leal. *Advanced Transport Phenomena: Fluid Mechanics and Convective Transport Processes*. Vol. 7. Cambridge University Press, 2007.

[93] E. Lefrançais et al. “The lung is a site of platelet biogenesis and a reservoir for haematopoietic progenitors”. In: *Nature* 544.7648 (2017), pp. 105–109.

[94] T. Levy and E. Sanchez-Palencia. “On boundary conditions for fluid flow in porous media”. In: *International Journal of Engineering Science* 13.11 (1975), pp. 923–940.

[95] S. J. Lighthill. *Mathematical Biofluiddynamics*. SIAM, 1975.

[96] K. R. Machlus and J. E. Italiano Jr. “The incredible journey: From megakaryocyte development to platelet formation”. In: *Journal of Cell Biology* 201.6 (2013), pp. 785–796.

[97] K. R. Machlus, J. N. Thon, and J. E. Italiano Jr. "Interpreting the developmental dance of the megakaryocyte: a review of the cellular and molecular processes mediating platelet formation". In: *British Journal of Haematology* 165.2 (2014), pp. 227–236.

[98] I. B. Mazo and U. H. von Andrian. "Adhesion and homing of blood-borne cells in bone marrow microvessels". In: *Journal of Leukocyte Biology* 66.1 (1999), pp. 25–32.

[99] A. D. McCulloch et al. "New multi-cue bioreactor for tissue engineering of tubular cardiovascular samples under physiological conditions". In: *Tissue Engineering* 10.3-4 (2004), pp. 565–573.

[100] H. Melchinger et al. "Role of platelet mitochondria: life in a nucleus-free zone". In: *Frontiers in Cardiovascular Medicine* 6 (2019), p. 153.

[101] A. D. Michelson et al. *Platelets*. Academic press, 2019.

[102] M. Mierzwiczak, A. Fraska, and J. K. Grabski. "Determination of the slip constant in the Beavers-Joseph experiment for laminar fluid flow through porous media using a meshless method". In: *Mathematical Problems in Engineering* 2019 (2019).

[103] A. Mietke et al. "Minimal model of cellular symmetry breaking". In: *Physical Review Letters* 123.18 (2019), p. 188101.

[104] L. Mohee et al. "Investigation of the intrinsic permeability of ice-templated collagen scaffolds as a function of their structural and mechanical properties". In: *Acta Biomaterialia* 83 (2019), pp. 189–198.

[105] M. I. Molodtsov et al. "A molecular-mechanical model of the microtubule". In: *Biophysical Journal* 88.5 (2005), pp. 3167–3179.

[106] C. Moreau, L. Giraldi, and H. Gadêlha. "The asymptotic coarse-graining formulation of slender-rods, bio-filaments and flagella". In: *Journal of The Royal Society Interface* 15.144 (2018), p. 20180235.

[107] Y. Nakagawa et al. "Two differential flows in a bioreactor promoted platelet generation from human pluripotent stem cell–derived megakaryocytes". In: *Experimental Hematology* 41.8 (2013), pp. 742–748.

[108] J. Ng et al. "Biomimetic approaches for bone tissue engineering". In: *Tissue Engineering Part B: Reviews* 23.5 (2017), pp. 480–493.

[109] S. Nishimura et al. "IL-1α induces thrombopoiesis through megakaryocyte rupture in response to acute platelet needs". In: *Journal of Cell Biology* 209.3 (2015), pp. 453–466.

[110] P. Noris et al. “Platelet diameters in inherited thrombocytopenias: analysis of 376 patients with all known disorders”. In: *Blood, The Journal of the American Society of Hematology* 124.6 (2014), e4–e10.

[111] R. D. O’Dea, S. L. Waters, and H. M. Byrne. “A two-fluid model for tissue growth within a dynamic flow environment”. In: *European Journal of Applied Mathematics* 19.6 (2008), pp. 607–634.

[112] R. D. O’Dea, H. M. Byrne, and S. L. Waters. “Continuum modelling of in vitro tissue engineering: a review”. In: *Computational Modeling in Tissue Engineering*. Springer, 2012, pp. 229–266.

[113] J. M. Oliver et al. “Thin-film theories for two-phase reactive flow models of active cell motion”. In: *Mathematical Medicine and Biology: a Journal of the IMA* 22.1 (2005), pp. 53–98.

[114] M. S. Olufsen. “Structured tree outflow condition for blood flow in larger systemic arteries”. In: *American Journal of Physiology-Heart and Circulatory Physiology* 276.1 (1999), H257–H268.

[115] I. Pallotta et al. “Three-dimensional system for the in vitro study of megakaryocytes and functional platelet production using silk-based vascular tubes”. In: *Tissue Engineering Part C: Methods* 17.12 (2011), pp. 1223–1232.

[116] M. A. Panteleev et al. “Wall shear rates in human and mouse arteries: Standardization of hemodynamics for in vitro blood flow assays: Communication from the ISTH SSC subcommittee on biorheology”. In: *Journal of Thrombosis and Haemostasis* 19.2 (2021), pp. 588–595.

[117] S. R. Patel et al. “Differential roles of microtubule assembly and sliding in proplatelet formation by megakaryocytes”. In: *Blood* 106.13 (2005), pp. 4076–4085.

[118] T. Pedley and D. Pihler-Puzović. “Flow and oscillations in collapsible tubes: Physiological applications and low-dimensional models”. In: *Sadhana* 40.3 (2015), pp. 891–909.

[119] R. Penta, D. Ambrosi, and R. J. Shipley. “Effective governing equations for poroelastic growing media”. In: *Quarterly Journal of Mechanics and Applied Mathematics* 67.1 (2014), pp. 69–91.

[120] S. R. Pollack et al. “Numerical model and experimental validation of microcarrier motion in a rotating bioreactor”. In: *Tissue Engineering* 6.5 (2000), pp. 519–530.

[121] K. Popov, J. Komianos, and G. A. Papoian. “MEDYAN: Mechanochemical simulations of contraction and polarity alignment in actomyosin networks”. In: *PLoS Computational Biology* 12.4 (2016), e1004877.

[122] B. Porter et al. “3-D computational modeling of media flow through scaffolds in a perfusion bioreactor”. In: *Journal of Biomechanics* 38.3 (2005), pp. 543–549.

[123] C. Pozrikidis. “Shear flow over a protuberance on a plane wall”. In: *Journal of Engineering Mathematics* 31.1 (1997), pp. 29–42.

[124] C. Pozrikidis. “Shear flow over cylindrical rods attached to a substrate”. In: *Journal of Fluids and Structures* 26.3 (2010), pp. 393–405.

[125] C. Pozrikidis. “Shear flow past slender elastic rods attached to a plane”. In: *International Journal of Solids and Structures* 48.1 (2011), pp. 137–143.

[126] C. Pozrikidis. *A Practical Guide to Boundary Element Methods with the Software Library BEMLIB*. CRC Press, 2002.

[127] A. Quarteroni and L. Formaggia. “Mathematical modelling and numerical simulation of the cardiovascular system”. In: *Handbook of Numerical Analysis* 12 (2004), pp. 3–127.

[128] M. T. Raimondi et al. “Micro fluid dynamics in three-dimensional engineered cell systems in bioreactors”. In: *Topics in Tissue Engineering* 2 (2005), p. 296.

[129] P. Recho, A. Jerusalem, and A. Goriely. “Growth, collapse, and stalling in a mechanical model for neurite motility”. In: *Physical Review E* 93.3 (2016), p. 032410.

[130] P. Reymond et al. “Patient-specific mean pressure drop in the systemic arterial tree, a comparison between 1-D and 3-D models”. In: *Journal of Biomechanics* 45.15 (2012), pp. 2499–2505.

[131] A. M. Robertson and A. Sequeira. “A director theory approach for modeling blood flow in the arterial system: An alternative to classical 1D models”. In: *Mathematical Models and Methods in Applied Sciences* 15.06 (2005), pp. 871–906.

[132] P. G. Saffman. “On the boundary condition at the surface of a porous medium”. In: *Studies in Applied Mathematics* 50.2 (1971), pp. 93–101.

[133] G. Salbreux, G. Charras, and E. Paluch. “Actin cortex mechanics and cellular morphogenesis”. In: *Trends in cell biology* 22.10 (2012), pp. 536–545.

[134] H. M. Saville et al. “A mathematical model of a valve-Controlled bioreactor for platelet production”. In: *Frontiers in Mechanical Engineering* (2022).

[135] T. W. Secomb and A. R. Pries. “Blood viscosity in microvessels: experiment and theory”. In: *Comptes Rendus Physique* 14.6 (2013), pp. 470–478.

[136] C. Selden and B. Fuller. "Role of bioreactor technology in tissue engineering for clinical use and therapeutic target design". In: *Bioengineering* 5.2 (2018), p. 32.

[137] J. H. Shepherd et al. "Structurally graduated collagen scaffolds applied to the ex vivo generation of platelets from human pluripotent stem cell-derived megakaryocytes: enhancing production and purity". In: *Biomaterials* 182 (2018), pp. 135–144.

[138] S. J. Sherwin et al. "One-dimensional modelling of a vascular network in space-time variables". In: *Journal of Engineering Mathematics* 47.3 (2003), pp. 217–250.

[139] R. J. Shipley, S. L. Waters, and M. J. Ellis. "Definition and validation of operating equations for poly (vinyl alcohol)-poly (lactide-co-glycolide) microfiltration membrane-scaffold bioreactors". In: *Biotechnology and Bioengineering* 107.2 (2010), pp. 382–392.

[140] R. J. Shipley et al. "Design criteria for a printed tissue engineering construct: a mathematical homogenization approach". In: *Journal of Theoretical Biology* 259.3 (2009), pp. 489–502.

[141] V. I. Sikavitsas, G. N. Bancroft, and A. G. Mikos. "Formation of three-dimensional cell/polymer constructs for bone tissue engineering in a spinner flask and a rotating wall vessel bioreactor". In: *Journal of Biomedical Materials Research* 62.1 (2002), pp. 136–148.

[142] M. Sladkova and G. M. De Peppo. "Bioreactor systems for human bone tissue engineering". In: *Processes* 2.2 (2014), pp. 494–525.

[143] N. P. Smith, A. J. Pullan, and P. J. Hunter. "An anatomically based model of transient coronary blood flow in the heart". In: *SIAM Journal on Applied Mathematics* 62.3 (2002), pp. 990–1018.

[144] S. Smyth et al. "Platelet functions beyond hemostasis". In: *Journal of Thrombosis and Haemostasis* 7.11 (2009), pp. 1759–1766.

[145] M. C. Sola-Visner et al. "Megakaryocyte size and concentration in the bone marrow of thrombocytopenic and nonthrombocytopenic neonates". In: *Pediatric Research* 61.4 (2007), pp. 479–484.

[146] A. M. Sonnet and E. G. Virga. *Dissipative ordered fluids: theories for liquid crystals*. Springer Science & Business Media, 2012.

[147] K. R. Spinler et al. "Myosin-II repression favors pre/proplatelets but shear activation generates platelets and fails in macrothrombocytopenia". In: *Blood, The Journal of the American Society of Hematology* 125.3 (2015), pp. 525–533.

[148] P. S. Stewart, S. L. Waters, and O. E. Jensen. "Local and global instabilities of flow in a flexible-walled channel". In: *European Journal of Mechanics-B/Fluids* 28.4 (2009), pp. 541–557.

[149] P. Sucosky et al. "Fluid mechanics of a spinner-flask bioreactor". In: *Biotechnology and Bioengineering* 85.1 (2004), pp. 34–46.

[150] D. Suzuki et al. "iPSC-derived platelets depleted of HLA class I are inert to anti-HLA class I and natural killer cell immunity". In: *Stem Cell Reports* 14.1 (2020), pp. 49–59.

[151] F. Tablin, M. Castro, and R. M. Leven. "Blood platelet formation in vitro. The role of the cytoskeleton in megakaryocyte fragmentation". In: *Journal of Cell Science* 97.1 (1990), pp. 59–70.

[152] G. I. Taylor. "A model for the boundary condition of a porous material. Part 1". In: *Journal of Fluid Mechanics* 49.2 (1971), pp. 319–326.

[153] J. N. Thon and J. E. Italiano. "Platelet formation". In: *Seminars in Hematology*. Vol. 47. 3. Elsevier. 2010, pp. 220–226.

[154] J. N. Thon et al. "Platelet bioreactor-on-a-chip". In: *Blood* 124.12 (2014), pp. 1857–1867.

[155] J. Tillett. "Axial and transverse Stokes flow past slender axisymmetric bodies". In: *Journal of Fluid Mechanics* 44.3 (1970), pp. 401–417.

[156] T. F. S. .-. US. *RPMI 1640 Medium, no glutamine, no phenol red*. `https://www.thermofisher.com/uk/en/home/technical-resources/media-formulation.114.html`. (Accessed on 05-11-2020). 2020.

[157] R. Voituriez, J. Joanny, and J. Prost. "Generic phase diagram of active polar films". In: *Physical Review Letters* 96.2 (2006), p. 028102.

[158] P. Vossenberg et al. "Darcian permeability constant as indicator for shear stresses in regular scaffold systems for tissue engineering". In: *Biomechanics and Modeling in Mechanobiology* 8.6 (2009), pp. 499–507.

[159] B. J. Walker and E. A. Gaffney. "Regularised non-uniform segments and efficient no-slip elastohydrodynamics". In: *Journal of Fluid Mechanics* 915 (2021).

[160] B. J. Walker et al. "A regularised slender-body theory of non-uniform filaments". In: *Journal of Fluid Mechanics* 899 (2020).

[161] B. J. Walker et al. "Filament mechanics in a half-space via regularised Stokeslet segments". In: *Journal of Fluid Mechanics* 879 (2019), pp. 808–833.

[162] S. Waters, L. Schumacher, and A. El Haj. "Regenerative medicine meets mathematical modelling: developing symbiotic relationships". In: *NPJ Regenerative Medicine* 6.1 (2021), pp. 1–8.

[163] R. J. Whittaker et al. "Mathematical modelling of fibre-enhanced perfusion inside a tissue-engineering bioreactor". In: *Journal of Theoretical Biology* 256.4 (2009), pp. 533–546.

[164] N. Xiao, J. Alastruey, and C. Alberto Figueroa. "A systematic comparison between 1-D and 3-D hemodynamics in compliant arterial models". In: *International Journal for Numerical Methods in Biomedical Engineering* 30.2 (2014), pp. 204–231.

[165] S. J. Young. "Biomechanical modelling of the gastrointestinal epithelial stem cell niche". University of Nottingham, 2009.

[166] A. Zemel and A. Mogilner. "Motor-induced sliding of microtubule and actin bundles". In: *Physical Chemistry Chemical Physics* 11.24 (2009), pp. 4821–4833.

[167] F. Zhao, R. Chella, and T. Ma. "Effects of shear stress on 3-D human mesenchymal stem cell construct development in a perfusion bioreactor system: Experiments and hydrodynamic modeling". In: *Biotechnology and Bioengineering* 96.3 (2007), pp. 584–595.

[168] C. Zhu and R. Skalak. "A continuum model of protrusion of pseudopod in leukocytes". In: *Biophysical Journal* 54.6 (1988), pp. 1115–1137.

[169] G. Ziegler, A. Benado, and S. Rizvi. "Determination of mass diffusivity of simple sugars in water by the rotating disk method". In: *Journal of Food Science* 52.2 (1987), pp. 501–502.

[170] M. Zuidscherwoude et al. "Loss of mDia1 and Fhod1 impacts platelet formation but not platelet function". In: *Platelets* (2020), pp. 1–12.